Synthesis and Characterisation of Superparamagnetic Nanocomposite Particles for Water Purification and Resources Recovery

Dissertation zur Erlangung des
naturwissenschaftlichen Doktorgrades
der Julius-Maximilians-Universität Würzburg

durchgeführt am
Fraunhofer-Institut für Silicatforschung ISC
Würzburg

Fraunhofer ISC

vorgelegt von

Karl Mandel
aus München

Würzburg 2013

Eingereicht bei der Fakultät für Chemie und Pharmazie am:

Gutachter der schriftlichen Arbeit:

1. Gutachter: Prof. Dr. Gerhard Sextl
2. Gutachter: Prof. Dr. Matthias Franzreb (Karlsruhe, KIT)

Prüfer des öffentlichen Promotionskolloquiums:

1. Prüfer: Prof. Dr. Gerhard Sextl
2. Prüfer: Prof. Dr. Matthias Franzreb (Karlsruhe, KIT)
3. Prüfer:

Datum des öffentlichen Promotionskolloquiums:

Doktorurkunde ausgehändigt am:

Synthesis and Characterisation of Superparamagnetic Nanocomposite Particles for Water Purification and Resources Recovery

PhD Thesis

Karl Mandel

Würzburg 2013

Julius-Maximilians-University
Würzburg

Fraunhofer-Institute for Silicate
Research ISC Würzburg

JOURNAL PUBLICATIONS IN CONTEXT OF THIS WORK

Major parts of this PhD thesis have been published during the time of origin of the PhD work (which started in January 2011) in peer-reviewed journals:

1. Karl Mandel, Frank Hutter, Carsten Gellermann, Gerhard Sextl
   Synthesis and stabilisation of superparamagnetic iron oxide nanoparticle dispersions
   Colloids Surf., A, 2011, **390**, 173.

2. Karl Mandel, Frank Hutter
   The magnetic nanoparticle separation problem
   Nano Today, 2012, **7**, 485.

3. Karl Mandel, Wojciech Szczerba, Andreas F. Thünemann, Heinrich Riesemeier, Matthias Girod, Gerhard Sextl
   Nitric acid-stabilized superparamagnetic iron oxide nanoparticles studied with X-rays
   J. Nanopart. Res., 2012, **14**, 1066.

4. Karl Mandel, Frank Hutter, Carsten Gellermann, Gerhard Sextl
   Modified Superparamagnetic Nanocomposite Microparticles for Highly Selective Hg(II) or Cu(II) Separation and Recovery from Aqueous Solutions
   ACS Appl. Mater. Interfaces, 2012, **4**, 5633.

5. Karl Mandel, Asya Drenkova-Tuhtan, Frank Hutter , Carsten Gellermann, Heidrun Steinmetz, Gerhard Sextl
   Layered double hydroxide ion exchangers on superparamagnetic microparticles for recovery of phosphate from waste water
   J. Mater. Chem. A, 2013, **1**, 1840.

6. Karl Mandel, Frank Hutter, Carsten Gellermann, Gerhard Sextl
   Stabilisation effects of superparamagnetic nanoparticles on clustering in nanocomposite microparticles and on magnetic behaviour
   J. Magn. Magn. Mater., 2013, **331**, 269.

7. Karl Mandel, Frank Hutter, Carsten Gellermann, Gerhard Sextl
   Reusable superparamagnetic nanocomposite particles for magnetic separation of iron hydroxide precipitates to remove and recover heavy metal ions from aqueous solutions
   Sep. Purif. Technol., 2013, **109**, 144.

8. Asya Drenkova-Tuhtan, Karl Mandel, Anja Paulus, Carsten Meyer, Frank Hutter, Carsten Gellermann, Gerhard Sextl, Matthias Franzreb, Heidrun Steinmetz
   Phosphate recovery from wastewater using engineered superparamagnetic particles modified with layered double hydroxide ion exchangers
   Water Res., submitted.

Permission for reuse of the article contents has been obtained from all publishers. By courtesy of Elsevier, publications 1, 2, 6, and 7 are reused. Publication 3 is reused by courtesy of Springer, publication 4 by courtesy of the American Chemical Society and publication 5 by courtesy of the Royal Society of Chemistry. Chapters in this thesis which are published as articles are marked appropriately by footnotes along the chapter headlines.

The content of publications 1, 2, 4, 5, 6 and 7 was created by Karl Mandel independently; under supervision of Dr. Frank Hutter, Dr. Carsten Gellermann and Prof. Dr. Gerhard Sextl. The experiments on phosphate recovery from waste water, in publication 5, were conducted by Asya Drenkova-Tuhtan, „Institute for Sanitary Engineering, Water Quality and Solid Waste Management ISWA", University Stuttgart.

Publication 3 was performed in cooperation with researchers from the "Bundesanstalt für Materialprüfung BAM" in Berlin. XAFS and SAXS measurements, analyses and modelling were carried out by the researchers of the BAM. The original text for the publication was written by Karl Mandel, Dr. Wojciech Szczerba (BAM) and Prof. Dr. Andreas F. Thünemann (BAM).

Work no. 8, submitted for publication to *Water Research*, arose from a cooperation with the "Institute for Sanitary Engineering, Water Quality and Solid Waste Management ISWA" and the "Karlsruhe Institute of Technology KIT". The majority of experimental concept and work was done by Asya Drenkova-Tuhtan, University Stuttgart. The manuscript was jointly written by Asya Drenkova-Tuhtan (ISWA), Karl Mandel and Anja Paulus (KIT). Data was plotted and modeled jointly by Karl Mandel and Asya Drenkova-Tuhtan (ISWA). Appropriate hints can also be found along the chapters that reuse part of this submitted work.

ACKNOWLEDGEMENTS

It would have been impossible to have created this PhD thesis without the help and support of many people that believed in the topic and my abilities to cope with the task. Although I was an unknown applicant to Prof. Dr. Gerhard Sextl and Dr. Carsten Gellermann when I introduced myself in 2010 in Würzburg (as I have not studied in Würzburg before), I could immediately feel their support and trust in me and I was warmly welcomed at the Fraunhofer ISC in Würzburg. Therefore, I first of all want to express my deep gratitude to Prof. Dr. Gerhard Sextl for always supporting my ideas, plans and my work in such a great extend! And of course, for having accepted me as PhD student by having offered this fascinating topic as PhD thesis to me. It is most appreciated! Thank you!

In the same way, this holds for Dr. Carsten Gellermann. He initially suggested me for the topic of this PhD thesis. He at all times supported me as supervisor so much in every way. Thank you for the many fruitful discussions, your helpful suggestions and advice, your dedication to the research area of magnetic particles and your trust in my work.

Special thanks to Dr. Frank Hutter. He always took his time for any questions, concerns, doubts, hypotheses, etc., I had. Thank you for the countless hours of discussions, arguments about theories, your critical but constructive questions and helpful comments and the high pace and dedication when it came to proofreading texts of mine. Thank you for your sense of humor that I will certainly miss once you are retired!

I want to thank Dr. Uta Helbig who, although not directly having been involved in the topic of my thesis, always had an open ear for my concerns, my plans and who helped me over several points of frustration and uncertainty during my PhD time.

During the course of this project, I got into contact with Prof Dr. Matthias Franzreb (KIT, Karlsruhe, Germany). I want to point out my gratitude that he was happily spending a lot of his time to supervise the pilot-scale experiment and for helping me with questions and concerns in such a friendly and supporting way all the time. Moreover, thank you very much for having kindly accepted to act as second Reviewer of this PhD thesis.

Asya Drenkova-Tuhtan (ISWA, Stuttgart, Germany), who was my partner in the project on phosphate recovery, worked so hard and with such a high dedication on all water related research. Thank you for the great cooperation and for being such a wonderful colleague!

The studies on the nanoparticles were a very exciting excursion for me into the world of X-ray physics, where I learned a lot. I want to thank Dieter Sporn for having got the discussion about the structure of the nanoparticles started and for having established the contact to the researchers of the BAM (Berlin, Germany). Thank you for your brilliant analyses and ideas, Dr. Wojciech Szczerba and Prof. Dr. Andreas F. Thünemann! Also, my thanks go to Dr. Heinrich Riesemeier and Matthias Girod for their great work.

Many thanks to Prof. Dr. Doris Heinrich for her help to improve the theory section in this work and to Dr. Karl-Heinz Haas for the fruitful discussions on various topics of this work.

I want to thank Martina Hofmann very much for having proofread for so many hours all the articles of mine to improve the style of writing.
Thank you, Anja Paulus (KIT, Karlsruhe, Germany) for your hard work and experimental ideas with the pilot-scale test.
Dr. Rolf Ostertag, Prof. Dr. Heidrun Steinmetz (ISWA, Stuttgart, Germany), Dr. Carsten Meyer (ISWA, Stuttgart, Germany), Dr. Sofia Dembski, Dr. Gerhard Schottner, Dr. Peer Löbmann, Thomas Ballweg, Walther Glaubitt and Elisabeth Scheller deserve my acknowledgement for their various kinds of support.
For help with the many devices and measurement systems involved in this thesis, I want to point out the great support by Peter Löschke, who seems to know everything about any measurement system that can be found at the Fraunhofer ISC and who gave me an introduction to VSM and Fraunhofer diffraction. Let me thank Dr. Werner Hopp and Christine Wendler for ICP-OES measurements, Dr. Alexander Reinholdt for TEM, Dr Rüdiger Bertermann for NMR, Peter Michel for BET and Richard Olsowski for DTA-TG-MS measurements and further Kathrin Bracken for FIB cuts. Manfred Römer is acknowledged for the SEM briefing, Johannes Prieschl for the zeta sizer briefing, Peter Tur for the XRD briefing and Dr. Sofia Dembski and Moritz Milde for the TEM briefing. I want to thank Miranda Rothenburger-Glaubitt for the viscosimetry measurements and Katja Scherbaum for the GPC measurements. Many thanks to Doris Hanselmann for her many helpful practical hints in the lab and the FTIR briefing. Thanks to Rainer Jahn and Claudia Köllner for having shared the lab with me and their help getting stuff sorted there. My students Michael Schneider, Benedikt Schug, and Andrej Shvalbe shall be acknowledged for their diligent lab work.
Andreas Flegler, Sebastian Hasselmann, Patrick Schmidt, Tina Oertel, Manuel Röder, Moritz Milde and Bernhard Fichtl: Thank you for many nice and inspiring discussions.
I always had great support when it came to administrative stuff by Gabriele Struppe, Sylvia Schrenker and Ursula Hopf. Thanks a lot that everything always ran so smoothly!
Thanks to my office colleagues Dr. Silke Gholami-Toll and Gabi Ulm for the pleasant time and good atmosphere in our office.
There is a very long list of great colleagues at the ISC of whom some in the meanwhile even became good friends. I want to say thanks to all these people for having made my time at the ISC so joyful.
Very important, thank you, all my friends from school or university time, for the long lasting, fruitful, lively and strong friendships.
And of course, most important, I want to thank my family and particularly, to be pointed out, my parents Anna-Maria Mandel and Dr.phil. Karl-Herbert Mandel. Thank you, for all your support throughout my whole life!

Last but not least: Feodora-Johanna Gabler, thank you for every single wonderful day with you which makes my life so happy and worthwhile!

The *Fonds der Chemischen Industrie (FCI)* is gratefully acknowledged for having financed my work by having awarded me with a *Kekulé-Scholarship*.

The *Baden-Württemberg Stiftung* is acknowledged for the funding of the project on phosphate recovery (*BioSuPaWert*).

ABBREVIATIONS

ADP	adenosine diphosphate
ATP	adenosine triphosphate
BET	Brunauer-Emmett-Teller
CCD	charge-coupled device
CIP	carbonyl iron powder
coth	hyperbolic cotangent
dLA	dispersed lactic acid modified nanoparticles
DLS	dynamic light scattering
DLVO	Derjaguin-Landau-Verwey-Overbeek
dMP	dispersed MELPERS4343 modified nanoparticles
DNA	deoxyribonucleic acid
DRIFT	diffuse reflectance infrared Fourier transformed (spectroscopy)
DTA	differential thermal analysis
EDX	energy dispersive X-ray (analysis)
emu	electromagnetic unit
erf	error function
EXAFS	extended X-ray absorption fine structure
FC	field cooled
FD	Fraunhofer diffraction
FT	Fourier transformation
FTIR	Fourier transformed infrared (spectroscopy)
HGMF	high gradient magnetic filter
HRTEM	high resolution transmission electron microscopy
HSAB	hard and soft acids and bases
ICP-OES	inductively coupled plasma - optical emission spectroscopy
IR	infrared
LA	lactic acid
LASS	lactic acid modified nanoparticles in a sodium silicate based matrix

LATEOS	lactic acid modified nanoparticles in a TEOS based matrix
LDH	layered double hydroxides
LIX84	2-hydroxy-5-nonylacetophenone ketoxime in kerosene
MAS	magic angle spinning
MP	MELPERS4343: polycarboxylate ether polymer
MPSS	MELPERS4343 modified nanoparticles in a sodium silicate based matrix
MPTEOS	MELPERS4343 modified nanoparticles in a TEOS based matrix
MS	mass spectrometry
NMR	nuclear magnetic resonance (spectroscopy)
NZVI	nano zero valent iron
REE	rare earth elements
RKKY	Ruderman-Kittel-Kasuya-Yosida
RT	room temperature
SAXS	small angle X-ray scattering
SEM	scanning electron microscopy
SS	sodium silicate
STEM	scanning transmission electron microscopy
TEM	transmission electron microscopy
TEOS	tetraethoxysilane
TG	thermogravimetry
TIC	total inorganic carbon
VSM	vibrating sample magnetometry
WHO	World Health Organisation
XAFS	X-ray absorption fine structure
XANES	X-ray absorption near edge structure
XRD	X-ray diffraction
ZFC	zero field cooled

LIST OF VARIABLES

A	area
a	unit cell vector
a_p	perpendicular radial distance from a wire
B_i	prefactor
b	fitting constant
B ; $\vec{B}$; B_x	magnetic flux density (magnitude ; vector ; one spacial direction)
bkg	background factor
c	unit cell vector
C_e	equilibrium concentration in solution
γ_d	domain wall energy
γ_A	interfacial surface energy per unit area
d ; d_{hkl}	spacing between lattice planes indexed with the Miller indices *hkl*
D	particle diameter related to the Guinier radius of gyration
δ	chemical shift
ΔE_0	global potential correction factor
$\Delta T_{ir,B}$	difference between the values of T_{ir} and T_B
ΔE_a	energy of the magnetic anisotropy barrier
Δr	lattice disorder parameter
E_0	absorption edge energy
E_{dipol}	dipolar energy
E_{ms}	magnetostatic energy
η	dynamic viscosity
f	fluctuation frequency
$\vec{F}$	total force vector
$\vec{f}$	force density vector
F_B	Brownian force
$\overrightarrow{F_g}$	gravitional force vector
$\overrightarrow{F_d}$	viscous drag force vector
$F_{m,x}$	magnetic force in one spacial direction
$\vec{g}$	gravitational acceleration vector
G	Guinier prefactor
H_{ext} ; $\overrightarrow{H_{ext}}$; $H_{ext,x}$	external magnetic field (magnitude ; vector ; one spacial direction)

hkl	Miller indices
$I(q)$	intensity function of q
I	nuclear spin
J	exchange integral
k_B	Boltzmann's constant
k_{ex}	exchange energy constant (per length)
k	vector (magnitude) in the reciprocal space ($\frac{2\cdot\pi}{\lambda}$)
K_α	(crystalline) anisotropy energy constant (per volume)
K	fitting constant
k_i	rate constant
$\mathcal{L}$	Langevin function
λ	wavelength
m ; $\vec{m}$	magnetic moment (of a nanoparticle) (magnitude ; vector)
$<m>$; $<\vec{m}>$	average magnetic moment (of a nanoparticle) (magnitude; vector)
M ; $\vec{M}$	mass magnetisation (magnitude ; vector)
M_s	saturation magnetisation by mass
M_{TB}	magnetisation at T_B
M_{Tir}	magnetisation at T_{ir}
μ_0	permeability of free space
μ_B	Bohr magneton
n	number of nanoparticles
$\vec{n}$	unit vector normal to a surface s
N_{agg}	aggregation number
N_d	demagnetisation tensor or scalar
N_s	number of surface atoms
N_{tot}	total number of atoms
p	power exponent
q	(scattering) vector (magnitude) in the reciprocal space ($\frac{2\cdot\pi}{\lambda}$)
q_e	equilibrium amount of adsorbed substance
Q_{max}	maximum amount of adsorbed substance
q_t	amount at time t of adsorbed substance
r	particle radius
r_{SD}	critical single domain radius
r^*	radius of the critical particle size

R	R-space: the real space
R^2	correlation coefficient
R_g	Guinier radius of gyration
ρ ; ρ_p ; ρ_f	density (general ; particle ; fluid)
s	surface of a body
$\overrightarrow{S_\iota}$	total atomic spin of an atom
S	saturation (of a solution)
S_c	critical saturation (of a solution)
σ^2	Debye-Waller factor (EXAFS)
T	temperature
$\boldsymbol{T}$	Maxwell stress tensor
t	time
T_B	blocking temperature
T_{ir}	irreversible temperature
τ	fluctuation time
U	Heisenberg-Hamiltonian
u	fitting constant
V	particle volume
v ; $\vec{v}$; v_x	velocity (magnitude ; vector ; one spacial direction)
V_m	molecular volume
x	coordinate
χ_s	magnetic susceptibility
$\chi(k)$	EXAFS fine structure function
y	coordinate
z	coordinate
Ω ; $\vec{\Omega}$	magnetisation by volume (magnitude ; vector)
Ω_s	saturation magnetisation by volume

CONTENT

1. INTRODUCTION

1.1 Purification of water and recovery of resources: A prospect for magnetic particles

Since October 2011, the world's population has been exceeding seven billion, according to the estimates of the United Nations Organisation.[1] Health and prosperity are prevailing in most of the industrialised countries due to the blessings of modern technologies in all important fields of daily life. Also, for the world's poor majority, sustained progress has been achieved over the last decades.[2] Still, according to the Human Development Report 2011, "*equity is inextricably linked to sustainability*"[2] and without a sustainable thinking in terms of environmental, energy and resources issues, "*the global convergence in human development might be reversed*"[2]. Increasing living standards and a growing population are linked to a rising demand of resources. More and more elements from the periodic table are becoming crucial ingredients in modern technologies. While in 1980, only around 12 elements were needed for the manufacturing of "high tech products", already more than 60 elements were involved in the production of multifunctional materials by 2000.[3] Most of these elements are non-regenerative, i.e., natural deposits are increasingly exploited to satisfy the growing industrial demand. Since geological reserves are not infinite, there are serious concerns about resources supply security for industry in the future.[3-5] This not only holds for expensive and rare metals but also for elements such as phosphorous which is not substitutable as essential element of life and needed as fertiliser to grow food.[6,7] Resources are not lost as they remain on our planet; but they are dissipated from high concentrations to drains of all kinds. One kind of these drains is waste / process / mine water, which might be an interesting new source from which to recover substances.[8-14] The recovery of diluted substances from water might not only help to stop dissipative loss, but also to purify water, which, after all, is our most important and most valuable resource. Over one billion people lack access to improved water supply sources.[15] This is directly related to diseases and poverty.[16] Any kind of water use is linked to its contamination. But we all need clean water every day. Only very small amounts of impurities, for instance heavy metals, are acceptable to retain it drinkable.[17] It is therefore a great challenge to remove highly diluted substances from a huge amount of water.

Thinking in terms of "re-cycling", especially of water and inorganic resources, is probably one of the most important tasks of the 21st century. In this context, acting sustainably could include to develop a process that purifies water and at the same time regains the substances dissolved therein for further use. In the present work, it was envisaged to develop a materials basis that could pave the way for such a process.

Physical and chemical principles offer a huge variety of solutions for the task of separating dissolved or dispersed substances from a fluid such as water: Chemically induced precipitation in combination with sedimentation,[18] membrane and other filter technologies[19] are employed, as is the use of adsorbers such as activated carbon, alumina and silica.[20] These methods are typically unselective.[20] For selective extraction of a substance from a fluid, ion exchange is the means of choice.[21,22] Using resins is typically feasible for concentrations of target substances between 1 µg/l to 1 g/l.[21] At higher concentrations (typically 0.5-500 g/l)[21], solvent extraction, a liquid-liquid ion-exchange process, is preferred over flowing water across an immobilised stationary ion exchanger. In that case, a water immiscible solution, such as kerosene, containing an ion-exchanger molecule, is mixed with water. After the target substance has bound selectively to the molecule, the oil and water phase are separated.[21]
Each of the listed methods comes with disadvantages. The most prominent are blocking and fouling problems when using stationary column / filter setups (solid-liquid separation).[23] In case of liquid-liquid separation, drawbacks include the need of large amounts of water immiscible solvent and intense mixing, as well as the problem of cross-contamination.[21] There are suggested solutions to tackle these and other disadvantages but their detailed discussion is beyond the topic of this work.
Instead, a promising and innovative alternative to all these methods is in the focus of this thesis, namely the use of magnetic particles for separation applications.[24] The principal idea is to add engineered magnetic particles with specially modified surfaces to a fluid. It is envisaged that target substances adsorb or react on the particle surfaces by chemical principles. In an ideal case, the particles are highly distributed in the fluid phase and offer myriads of adsorption spots which equals short diffusion pathways for the target substances. As the particles are designed to respond to a magnetic field gradient, they should be separable from a water stream with their load (e.g. after they have freely moved within the stream for the time required for adsorption taking place). Regenerability of the particles by chemical or physical means might allow their reuse. The target substances, formerly attached to the particles, could be collected, concentrated and potentially reused for industrial processes or safely deposited.

In a simplified picture, this method allows to selectively grab a target substance from water rather than having to pass the whole amount of water through a narrow (membrane) filter to eventually obtain the target substance as filter cake. Magnetic separation might be particularly interesting for highly diluted target elements, i.e., for very low concentrations of a valuable or unwanted (e.g. toxic) substance, dissolved in the water which needs to be purified. However, by dosing an adequate amount of particles, the adsorber capacity might easily be adapted to scavenge any given (high) concentration successfully. Figure 1 depicts

the process scheme of magnetic separation of adsorber particles for water purification and resources recovery.

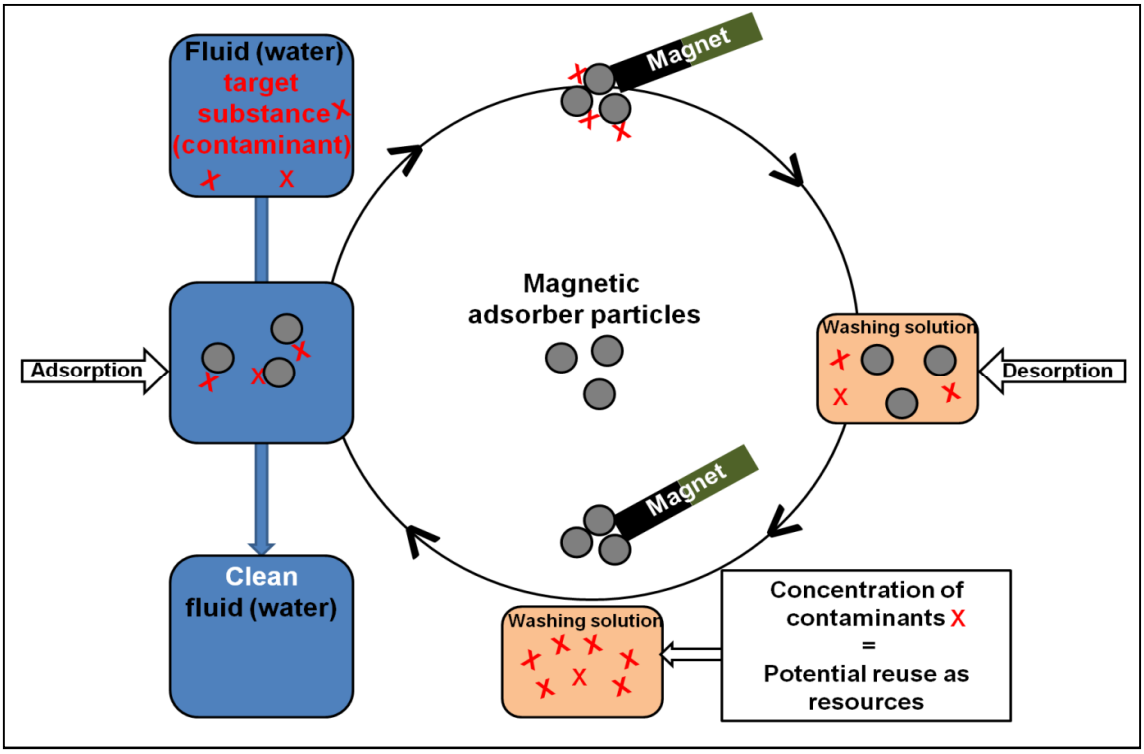

Figure 1: Principle of magnetic separation of adsorber particles for water purification and resources recovery.

The desired property profile of magnetic particles for water purification and resources recovery is as follows:

- The particles should be magnetically responding as strong as possible to an externally applied magnetic field gradient to ensure ideal separability.
- When released into water, the particles should not magnetically agglomerate but stay individually dispersed in the water.
- The particles should have a low density to only slowly sediment.
- They should be small. This yields a high surface to volume ratio, i.e., a maximum surface area, and more adsorption spots per mass of particles.
- The particles' surface affinity should be dedicated to the target substance and ideally, it should be easily modifiable for different targets.
- The particles should have a good (chemical and mechanical) stability in water over a certain range of pH (e.g. from 1-12) plus stability against corrosion and oxidation.
- Toxic materials as particle components or their release to water should be avoided.
- No expensive or rare materials should be part of the particle system.
- The particles should be regenerable and reusable in many separation cycles.

1.2 Design of novel, magnetically switchable, multifunctional scavenger particles[1]

The aim of this work was to develop a particle system to fulfil the requirements as listed in the previous section. The envisaged design is schematically depicted in figure 2, which will be described in the following. The desired micron sized particle is a multifunctional composite consisting of superparamagnetic nanoparticles, confined in a silica matrix with a modified surface, dedicated for selective (and reversible) adsorption of target substances. It was a main task to develop a particle synthesis process that is simple and fast, requiring only inexpensive chemicals in order to pave the way for a large scale applicability of the particles in the field of water treatment.

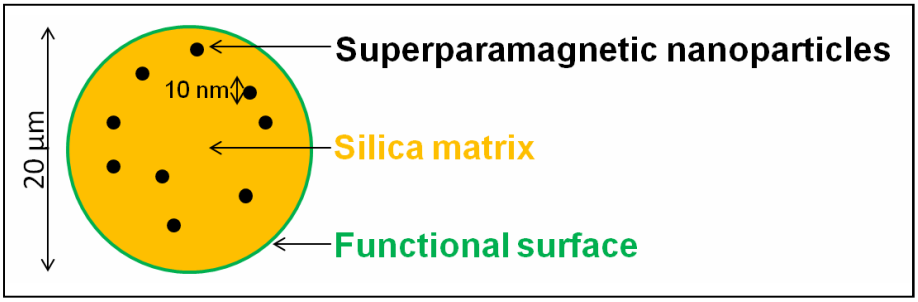

Figure 2: Material composition of a magnetically switchable, multifunctional adsorber particle for water purification and resources recovery (not drawn to scale).

Although magnetic separation has been a well-known process for a long time,[24] nanotechnology offers a new perspective for the design of carrier particles. If magnetic particles are small (e.g. below 20 nm) they can become superparamagnetic.[25] These particles behave like strong magnets in the presence of an external magnetic field (like their bulk counterparts) but lose their magnetisation instantly as soon as the external field is removed; i.e., they have no remanent magnetisation (unlike their bulk counterparts) and therefore can be used as switchable magnets (see *chapters 3.1.3* and *3.2.1*). These particles can be well dispersed in a fluid because they do not agglomerate magnetically. Therefore, if their surface was functionalised properly, they could adsorb target substances selectively and be removed by the gradient of an external magnetic field.[24,26]

Magnetic separation could in principal be simply achieved by a handheld magnet. The magnetic force, directing the particles towards the magnet, is proportional to the magnetic field gradient, to the magnetisation of the particles and to their volume (see *chapter 3.2.1* and [24,26]).

[1] Parts of the text of this chapter have been published and are reused in this work by courtesy of Elsevier and the American Chemical Societey. Original articles: K. Mandel et al., *Nano Today*, 2012, **7**, 485 and K. Mandel et al., *ACS Appl. Mater. Interfaces*, 2012, **4**, 5633.

However, for nanodisperse particles the randomly directed forces of Brownian motion are stronger than the magnetic forces (see calculations in the *Appendix*). Thus, individual nanoparticles are usually not separable in this simple way.

It is therefore a better strategy to increase the particle size without loss of superparamagnetism, to greatly enhance separability, as the magnetic force is proportional to the volume of the particle and the Brownian forces become negligible for larger particles. This may be achieved by assembling nanoparticles into a matrix of diamagnetic material, forming a composite microparticle (nanocomposite)[27]. All nanoparticles in the composite contribute to the magnetic attraction towards an applied field gradient and the whole particle will be separated. However, the high specific surface area of the individual nanoparticles may be lost that way. Therefore, the challenge is to synthesise composite particles that are small and filigree enough to retain a high surface area.

As the surface of the obtained nanocomposite microparticles (usually) needs to be functionalised to turn the particles into selective adsorbers, the microparticle matrix should consist of a material that can be easily modified. Silica is particularly suitable for this purpose, as the material is well understood in terms of its properties, surface reactivity etc. and it is very well known how it can be modified. For instance, a whole toolbox of functional silanes is readily available to equip the particle surfaces with a wide range of functional groups.[28] But not only by silanes, but also by a huge variety of other molecules or compounds, silica can be successfully surface modified.[29]

To demonstrate extraction and recovery of substances with the designed nanocomposite microparticles, four exemplary targets were defined in this work. For each target, a different particle modification was developed. The selected substances and the reasons for having chosen the particular elements are listed in the following:

Phosphate[2]

Phosphorus, in the form of phosphate, is undoubtedly one of most important elements of life – it builds up the backbone of the DNA and is part of the energy carriers ATP and ADP (adenosine triphosphate and adenosine diphosphate) in every cell. Skeletons of vertebrates consist in large part of phosphate. Agriculture relies heavily on phosphate as fertiliser which is needed by every plant to grow.[6] However, the main source of phosphorous, rock-phosphate, is a non-renewable resource. Because of a steadily increasing demand, natural deposits are depleted more and more[6,7] and in the future will

[2] This chapter has been published and is reused in this work by courtesy of the Royal Society of Chemistry. Original article: K. Mandel et al., *J. Mater. Chem. A*, 2013, **1**, 1840.

contain lower phosphate concentrations and a higher content of impurities such as heavy metals, especially toxic cadmium associated with phosphate minerals.[7] If such sources are used, the consequence will be a contamination of soil and ultimately food containing heavy metals.

And yet, on the other hand, phosphate is excreted by every animal and human being. From communal settlements it is collected and transported through the sewer system and finally removed in the waste water treatment plant either by chemical precipitation and withdrawal with the sludge or by enhanced biological phosphorus removal using polyphosphate accumulating micro organisms. It is essential to control the amount of phosphate discharged into surface waters through waste water effluents, because phosphorus is one of the major nutrients contributing to increased eutrophication of rivers and lakes.[30,31] Thus, recovery of phosphate from waste water not only prevents loss of a scarce resource but also protects natural waters from pollution.

Recovering processes of phosphates via precipitation and crystallisation from water (e.g. sewage sludge or extracts of sewage sludge ash) with relatively high phosphate concentration are known. However, they usually lack in selectivity, i.e., contaminants are precipitated with the products.[32,33]

Therefore it is tempting to directly and selectively recover phosphates from raw waste waters where typical concentrations of 4 to 16 mg/l[34] as P with an average concentration in raw municipal waste water of 8 mg/l as P (data for Germany in 2009)[35] are prevailing. Such low concentrations are in the range where ion-exchange processes are most suitable[21] and where the use of magnetic particles could be successful in future.

Mercury

Mercury is a highly toxic element that can ultimately damage the kidney.[18]
It is therefore very important to remove mercury contaminants from water. The WHO guidelines demand that not more than only 6µg/l mercury is present in water.[18] It is a challenging task to completely remove it from water and thus an interesting test for the thoroughness of magnetic particles.

However, mercury is also an important resource and used in many industrial processes.[18] Therefore, it might also be desirable to recover it, once removed from water.

Copper

Copper is an important resource for many industrial processes. The element is becoming more expensive. From 2000 to 2008, prices have risen by 500 %.[4] Interestingly, copper, highly diluted, can also be found in waste water streams.[8,11] Sources are copper materials exposed to weathering conditions, for instance drainage pipes that undergo abrasion.[11] Furthermore the industrial sector discharges copper into water, respective amounts for 2001 were estimated around 46 tons per year in Europe.[13]

As copper mining is often done via leaching (dissolution) processes, copper mine water runoffs are often still very rich in dissolved copper and therefore potentially interesting for copper recovery considerations.[14]

Copper in the environment can accumulate in organisms and might be harmful in too high doses.[4] Therefore, it was tried to demonstrate the selective recoverability of copper as an example of a valuable resource that can be found in water due to human activities.

Heavy metals[3]

Heavy metal ions in general, e.g. from Cd, Cr, Cu, Pb, Zn, As or Hg, originating from natural geological or industrial sources, are hazardous pollutions in water.[36] The water has to be cleaned from these contaminants before being used as drinking water or further being discharged. But, heavy metals may also be valuable elements for industrial applications. It is therefore highly desirable to find processes that not just remove, but also recover dissolved heavy metals in general. Ideally, polluted water is cleaned from highly diluted heavy metal ions and these ions are regained in a concentrated form, allowing their recycling for instance via electrowinning.[37]

The synthesis and functionalisation of magnetically switchable particles and a demonstration of the extraction and recovery of the listed substances was envisaged in this work to yield a proof of concept of the application idea. A manifold applicability of switchable magnetic particles for various separation purposes simply by modifying their surface differently would demonstrate the potential of such a particle system as a technology platform for a broad range of purification and recovery tasks.

[3] This chapter has been published and is reused in this work by courtesy of Elsevier.
Original article: K. Mandel et al., *Sep. Purif. Technol.*, 2013, **109**, 144.

2. STATE OF RESEARCH

To succeed in engineering dedicated nanocomposite particles, knowledge about existing magnetic materials, nanoparticles, nanocomposites and adsorbers is required. The most important developments and results in these fields are summarised in the following sections.

2.1 Magnetic materials (magnetically ordered materials)

There is no simple definition of magnetic or magnetically ordered materials. Magnetical ordering means that the magnetic moments of the atoms in a solid are arranged in parallel or anti-parallel with respect to their neighbouring atoms (see *chapter 3.1.1*), i.e., they are not randomly oriented as in paramagnetic materials. From a rather empirical list of magnetic materials relevant in today's technologies,[38] two groups can be distinguished:

There are materials containing rare or expensive elements such as:[38]
CoPt, MnBi, NiMnSb, Mn, $IrMn_3$, Dy, $SmCo_5$, $Nd_2Fe_{14}B$, Y_2Co_{17}, $TbFe_2$, $Gd_{0.25}Co_{0.75}$, $Sm_2Fe_{17}N_3$, EuO, $SrRuO_3$, $(La_{0.70}Sr_{0.30})MnO_3$, Sr_2FeMoO_6, $Y_3Fe_5O_{12}$, $(Ga_{0.92}Mn_{0.08})As$.

Other materials mostly contain Fe, Co or Ni:[38]
Fe, $Fe_{0.65}Co_{0.35}$, $Fe_{0.20}Ni_{0.80}$, $Fe_{0.40}Ni_{0.40}B_{0.20}$, Co, Cr, Fe_4N, CrO_2, NiO, α-Fe_2O_3, γ-Fe_2O_3, Fe_3O_4, $BaFe_{12}O_{19}$, MnF_2, FeF_3, Fe_7S_8, $Cu_{0.99}Mn_{0.01}$.

Among these, Fe is the most abundant element; it can be found in the earth's crust 40 times as plentiful as all the other magnetically relevant elements together.[39] The base price per kg of iron is only about 0.50 $.[40] The magnetic properties of iron are very good: "*Iron has the highest room temperature saturation magnetisation of any pure element*"[41] which is the second strongest saturation magnetisation (217 emu/g) (see *chapter 3.1.5*) that is known at room temperature at all, after the alloy $Fe_{0.65}Co_{0.35}$ (240 emu/g).[38]

There are furthermore many compounds of iron in form of hydroxides or oxides: The iron hydroxides are bernalite ($Fe(OH)_3 \cdot nH_2O$, $Fe(OH)_2$ and "green rusts" (mixtures of Fe(II) and Fe(III) hydroxide compounds).[42] Iron oxide hydroxides are goethite (α-FeOOH), lepidocrocite (γ-FeOOH), akaganéite (β-FeOOH), feroxyhyte (δ-FeOOH), "high pressure FeOOH" and ferrihydrite (a FeOOH of non-exactly defined formula).[43]

Although some of these hydroxides are interesting for heavy metal adsorption from waste water,[44] they are mostly antiferromagnetic (see *chapter 3.1.1*) i.e. of no "accessible" magnetism.[45] The most interesting iron compounds in terms of magnetic properties are found among the well-known iron oxides: hematite (α-Fe_2O_3), magnetite (Fe_3O_4), maghemite (γ-Fe_2O_3), ε-Fe_2O_3 and wüstite ($Fe_{1-x}O$).[46] Hematite at room temperature is a

very weak (ferro)magnet.[47] Antiferromagnetic (see *chapter 3.1.1*) are wüstite and ε-Fe_2O_3.[45] Magnetite as well as maghemite are ferrimagnetic materials with a remarkable saturation magnetisation of 92-100 emu/g, respectively 60-80 emu/g,[45] which is about one-third of the magnetisation strength of pure iron, however the advantage is that these materials are much less sensitive to oxidation (rusting) compared to pure iron.

2.2 Iron based magnetic nanoparticles

Nanoparticle research on iron based materials yielded tremendous attention in the last years due to their interesting properties (such as superparamagnetism) and potential applications, which were proposed mainly in the field of biomedicine (e.g. contrast agents for magnetic resonance imaging, hyperthermia treatment, drug delivery etc.)[48] but e.g. for nano zero valent iron (NZVI), due to its reactivity, also for environmental remediation.[49] Using top-down approaches, successful synthesis of iron based nanoparticles via milling and wet grinding was reported.[49] However, these methods are very time consuming and energy intensive. More prominent are bottom-up approaches. As there is a huge variety of ways how to obtain iron based nanoparticles from these mainly wet-chemical approaches, only very few of the most important will be mentioned here. More details can be found in an exhaustive review published by B. L. Cushing et al.[50]

Probably the most prominent seminal work on producing nearly monodisperse iron oxide nanoparticle sols in non-polar organic solvents was published in 2002 by S. Sun and H. Zeng who obtained 4 nm magnetite (Fe_3O_4) particles from thermal decomposition of iron(III)acetylacetonate in oleic acid and oleylamine.[51] As an alternative method to get very monodisperse iron based nanoparticles, the synthesis in confined spaces such as micelles was proposed.[48] Typically, oxides are obtained that way.
A prominent bottom-up approach for the synthesis of nano zero valent iron (NZVI) is the so called "$NaBH_4$ method", where Fe ions in solution are reduced to form Fe(0) which nucleates to nanoparticles.[49,52] A variation of the method is the decomposition of $Fe(CO)_5$ by ultrasonication.[49]

For applications where the main aim is to obtain nanoparticles in a simple and reliable way and in high yield, and where it is acceptable that iron based nanoparticles are in an oxidised form and rather polydisperse, coprecipitation is the means of choice.[48] The method was first reported as far back as 1852 - although it was not revealed at the time that the synthesis yields nanoparticles. Instead, the synthesis of a "black material attracting itself" was described, an "*oxide ferroso-ferrique*" from FeO and Fe_2O_3 with "*HO*".[53] Coprecipitation of ferrous and ferric ions from solutions by the addition of an alkali is still very often used to prepare superparamagnetic nanoparticles. The disadvantage is that

agglomerated particles are obtained in the first step. Countless variations of this aqueous precipitation process have been published since then. Slight variations of the actual reaction conditions or addition of stabilising agents to the particle dispersions to obtain a sol were carried out. Among the molecules added for modification were for instance glucose,[54] amino acids (L-glutamic acid and L-lysine,[55] aspartic acid,[56,57] leucine, arginine, cysteine, cystine, aspartate and tyrosine[57]), citric acid,[58] poly acrylic acid,[59] tartaric acid[60] or other carboxylic acids.[61]

Last but not least, it should be mentioned that there is also a very different alternative to obtain iron oxide nanoparticles, namely via biomimetic methods. Bacteria can grow magnetite and also proteins such as apoferritin were used as nanocages to form magnetic iron oxide nanoparticles.[62] Unfortunately, up to now, the bacteria only grow in very dilute media and the nanoparticles production is not economically feasible.

2.3 Magnetic nanocomposite particles for separation applications[4]

As suggested in the introduction (*chapter 1.2*), incorporation of several nanoparticles into a matrix to form nanocomposite microparticles yields improved magnetic separability of these carrier particles from fluids.

Much research has been done on coating magnetic nanoparticles with a diamagnetic material, mainly silica, forming core-shell particles.[63-68] Magnetic multicore composites with a silica[69,70] or polymer[71,72] matrix, as well as hybrid combinations of polymeric and silica matrices,[73-76] have been reported. Typically, the sizes of the composite particles reported are below 200 nm[63-76] and their use is mainly intended for biotechnological separation applications on a laboratory scale.[66-68,70,72-77] Commercially available products, commonly with sizes below a few µm, are also mainly dedicated for the biotechnology market.[26,78,79] Often composite particles are dense spheres,[26,70,71,73,76,78] resulting in a small specific surface area. They are produced typically in small quantities (mg to g). Commercial products often come with a price of a few hundred $/g.
A selection of the most prominent, commercially available magnetic particle systems and their specifications according to the available information from the companies, can be found in table 1. A more exhaustive list of retailers, offering magnetic particle systems to date, can be found elsewhere.[80]

Although most composites developed so far are said to be magnetically separable, their magnetisation is surprisingly low (often below 5 emu/g) which is massively lower than the expected value for magnetite (60 to 80 emu/g).[63,66,68-77] At sizes often below 1 µm, these

[4] A part of this chapter has been published and is reused in this work by courtesy of the American Chemical Society. Original article: K. Mandel et al., *ACS Appl. Mater. Interfaces*, 2012, **4**, 5633.

particles separate from solutions very slowly due to the proportionality of the magnetic forces to their small volume and low magnetisation.[24,26] This is far from ideal because, in large-scale technical applications such as water purification, a fast magnetic separation is necessary for a high throughput.

Higher magnetisations (> 100 emu/g) has been reported for iron[81] or cobalt nanoparticles[82] and iron carbide composites.[83] Unfortunately, these particles show a remanent magnetisation, which leads to magnetic agglomeration, possibly hindering a proper redispersion in water after magnetic separation.

Table 1: Selection of commercially available magnetic particle systems.

Trade name	**Company**	**Micro-particle matrix**	**Super-para-magnetic**	**Particle size**	**Use**	**Com-pany ref.**
Magnetic Beads	Chemagen	Polyvinyl alcohol	yes	0.5–3 µm	Biotech.	[84]
SiMAG	Chemicell	Silica	yes	0.5–1 µm	Biotech.	[85]
MagSilica®	Evonik	Silica	yes	Pyrogen. silica matrix 40 nm nanostructured	Bonding / debonding	[86]
MagSi	Magna-medics	Silica	yes	~ 1 µm	Biotech.	[87]
Estapor®	Merck	Polystyrene	yes	0.7–2 µm	Biotech.	[88]
MagPrep®	Merck	Silica	no	0.1-0.2 µm	Biotech.	[89]
MicroBeads®	Miltenyi-biotech	Antibody	yes	50 nm	Biotech	[90]
MagAttract	Qiagen	Silica	no	0.1–10 µm	Biotech.	[91]
TurboBeads®	Turbo-beads	Primary carbon coating	no	30 nm	Various	[92]

2.4 Binding agents for selected target substances

The following chapter describes possible binding agents for the targets substances defined in this work (see *chapter 1.2*).

2.4.1 Binding molecules for Hg(II) or Cu(II) ions[5]

For Hg(II) removal,[93-98] thiol modified nanoparticles have proven to be good adsorbers.[95,98,99] However, adsorbing Hg(II) selectively turned out to be more difficult. Using dimercaptosuccinic acid, no selectivity for Hg(II) was observed.[99] Poly(3,4-ethylenedioxythiophene) modified magnetic particles showed uptake of Ag(I), Pb(II) and Hg(II).[96] (3-mercaptopropyl)trimethoxysilane modification is suggested to be highly selective for Hg(II); however, it is assumed that this is not due to silane but due to the pore effects of the adsorber material.[98]

Cu(II) removal using magnetic particles has been reported,[100-107] based on amine[100-102] or chitosan modification[103-105] or imprinting methods,[105] among others.[106,107] Selectivity is usually not considered[100-104,106,107] and is only reported for an imprinted material.[105] Modifying magnetic particles with a highly selective Cu(II) binding agent that was originally designed for solvent extraction could result in highly Cu(II) selective magnetic particles that can be used in a process that overcomes the disadvantages of conventional solvent extraction.

Liquid-liquid (solvent) extraction[21,108] of Cu(II) in large-scale mining applications is done by mixing Cu(II) selective ion exchange molecules, such as hydroxy-ketoximes in a water immiscible solvent (e.g. 2-hydroxy-5-nonylacetophenone ketoxime (LIX84, BASF) in kerosene), with water containing Cu(II) ions. Two complexing agents (two LIX84 molecules) are needed to complex one copper ion which leads to a release of two protons.[109,110] The reaction is reversible by acid treatment.[109] Figure 3 schematically shows the complexation mechanism, based on experimental and theoretical findings.[110]
Impregnations of silica gels and membranes with LIX84 have been demonstrated via the anchoring of alkyl groups from aminosilanes[111] or chloroalkylsilanes[109,112,113] on a silica surface, which created a hydrophobic interaction between LIX84 and the alkyl modified surface via van der Waals interactions that promote adsorption / immobilisation of the alkyl chains of LIX84 on the alkyl modified silica surface.[113,114]

[5] This chapter has been published and is reused in this work by courtesy of the American Chemical Society. Original article: K. Mandel et al., *ACS Appl. Mater. Interfaces*, 2012, **4**, 5633.

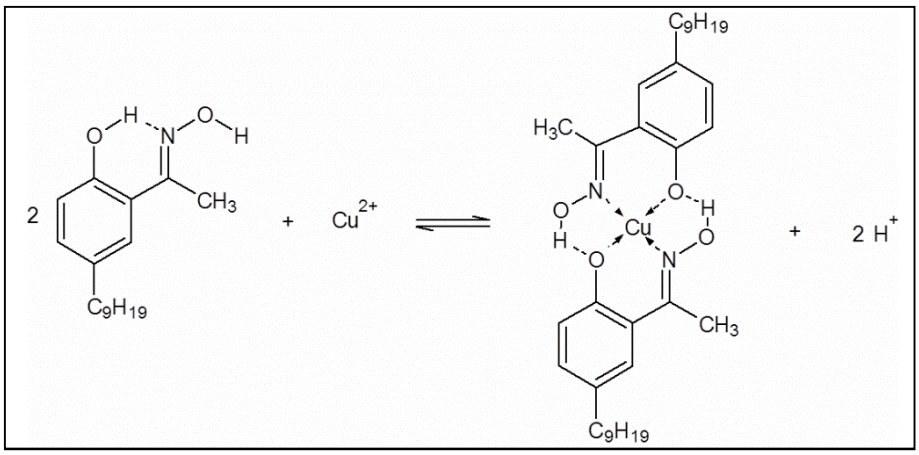

Figure 3: LIX84 molecules (2-hydroxy-5-nonylacetophenone ketoxime) as complexing agents for copper ions via chelating effects of coordinate bonds (arrows). Dashed lines: hydrogen bonds. Binding scheme according to experimental and theoretical findings.[110]

2.4.2 Adsorber and ion exchange materials for phosphate[6]

Various materials were proposed as phosphate adsorbers in waste water. Reported, among others, are akaganéite,[115] alumina oxide hydroxides,[116,117] zirconia based materials[118-120] and other metal hydrous oxides,[121] zeolites,[122] functional polymers,[123,124] and even imprinted polymers.[125]

Besides these materials, anionic clays, so called layered double hydroxides (LDH), have been reported frequently to be promising selective phosphate ion exchange materials.[30,31,126-134] Due to the layered structure of the material, selective intercalation of anions is possible.[135] The prototype of a LDH is hydrotalcite $[Mg_{0.75}Al_{0.25}(OH)_2](CO_3)_{0.125}\cdot 0.5H_2O$ which is similar in structure to brucite $Mg(OH)_2$.[136] Brucite has a CdI_2-type structure, i.e., *"a hexagonal close-packing of hydroxyl ions, with all octahedral sites every two interlayers occupied by Mg^{2+} ions"*.[136] Substitution of Mg^{2+} by Al^{3+} leads to positively charged layers that allow anions to be intercalated between these layers.[136] *"Stacking of the layers can be accomplished in two ways, leading to two polytypes with a rombohedral (3R symmetry) or a hexagonal cell (2H symmetry); hydrotalcite corresponds to* [the] *symmetry 3R* […]".[136] LDH modifications with various metal cations of valence +2, +3 and even +4 were reported,[31,136] which had an influence on the anion selectivity.[136]

[6] This chapter has been published and is reused in this work by courtesy of the Royal Society of Chemistry. Original article: K. Mandel et al., *J. Mater. Chem. A*, 2013, **1**, 1840.

Phosphate adsorption and intercalation into the layers of LDHs were reported either under ideal conditions in deionised water[31,126,127,132,133] or in real waste or sea waters with competitive adsorption of other molecules or ions.[30,128-131,134] When competing molecules or ions were present, the selectivity of phosphate adsorption dropped in comparison to that under ideal conditions but still remained fairly high.[30,128-131,134] Especially, Zr doped LDH systems showed high selectivities in real waste waters.[130,131] Sometimes it is only aimed at prevention of eutrophication.[132-134] Regeneration and reuse of the LDH is often considered. Several adsorption / desorption cycles are examined in many of the works.[126-131] However, a strategy to regain the LDH from solution is seldom proposed; only vaguely it is mentioned that the solid can be filtered from the waste water (which is done at low volumes on a lab scale). LDHs typically consist of flakes in the sub µm to several 100 µm size range and it would be very tedious and almost impossible to regain them by filtration or sedimentation selectively from all other solid substances in a real waste water stream.

The combination of magnetic particles with LDH has been already reported in the literature.[129,137-143] LDHs were typically used as catalysts[140,141] or to adsorb unwanted substances from water such as dyes[138] or arsenates[137]. Coating of magnetic particles with LDH was demonstrated with exfoliated LDH layers obtained in an autoclave process, which is sophisticated, time consuming and expensive.[137-139]

Phosphate removal using magnetic assistance[144-147] has been published in the context of seeded-precipitation[144,145] and in the context of using pure iron particles directly as adsorbers.[146,147] Both techniques are presumably not very selective for phosphate recovery.

2.4.3 Generalised heavy metal removal using flocculation and/or magnetic assistance[7]

A well known process to remove heavy metal ions to clean water is by addition of Fe or Al salts. Flocculation and precipitation of Fe or Al hydroxide colloids lead to adsorption and coprecipitation of other dissolved ions.[18,148] Unfortunately, the flocs are voluminous and mechanically unstable.[148] Therefore they have to be separated by a slow sedimentation generating a still very voluminous sludge, which has to be dried or filtered and eventually deposited as toxic waste.[149] Incineration of the sludge might be harmful due to potential formation of heavy metal chloride gases.

[7] This chapter has been published and is reused in this work by courtesy of Elsevier.
Original article: K. Mandel et al., *Sep. Purif. Technol.*, 2013, **109**, 144.

A much more preferable way of *recycling* heavy metals was recently demonstrated. A filtered and concentrated hydroxide sludge was redissolved through acid treatment and the recovery of heavy metals was achieved by electrowinning.[37] However, separation by filtration is still tedious and impractical. Magnetic separation could be faster and easier.

Some magnetic separation techniques for heavy metal ion removal have been published before.[150-156] A sophisticated and energy-intensive method is the in situ crystallisation of magnetic particles in waste water, the so-called ferrite process.[150,155,156] Fe(II) salt is added and the water temperature risen to about 60 °C. Subsequently, Fe(II) is oxidised by air bubbling and consequently magnetite (Fe_3O_4) is formed together with incorporated heavy metal ions (2 valent heavy metal ions replace Fe(II) in the magnetite lattice).[150] The magnetite (ferrite) crystals can be magnetically separated. Eventually, a waste product has to be deposited.

Another way is the use of magnetic ion-exchange particles, e.g. in the *Sirofloc*[149] or *Miex*[157] process. The complex interactions of the ion-exchanger with the aqueous environment afford a precise adjustment of the process to the specific conditions of the respective targeted purpose.

A direct magnetic separation of precipitated hydroxide flocs seems to be most preferable. As iron hydroxide flocs are only weakly magnetic, precipitation is performed in presence of (usually micron sized) magnetite seed particles.[145,151-154] Seed-grown flocs can be separated magnetically. Magnetite microparticles typically possess a remanent magnetisation, i.e., once separated, they might hardly detach from the separator and remain magnetically agglomerated.[149] Redissolution of the hydroxide precipitate in an acid, without dissolving the magnetite particles, might also be difficult to perform, so that the separated product would be rather deposited with the magnetite added to the amount of waste.
A recovery of the heavy metals and a reuse of magnetic seed particles would therefore be much more beneficial.

3. THEORY[8]

The key item in this work is the "switchable" magnetic (i.e., superparamagnetic) particle. Magnetophysical principles presented in the following chapters are directly related to the magnetic properties and separation behaviour of the engineered particles. Although their magnetic separation can easily be demonstrated, the theory behind the observable process is important for the control of the particle separability.
Synthesis and modifications of the novel nanocomposite microparticles as well as their applications were performed in aqueous systems. The underlying chemical principles will therefore be addressed in a section (*chapter 3.3*) as well.

3.1 Magnetism (Physics)

Magnetism is a highly complex phenomenon that bears many different facets. It is clearly beyond the scope of this work to address all theoretical aspects of the underlying physics of magnetism. In the following, theoretical explanations will be given only with the aim to pave the way towards making the phenomenon of superparamagnetism understandable, as this, along with related effects, will be part of the discussions in the results chapter of this work.

3.1.1 Classes of magnetism

Magnetic properties rely on material composition, in detail on electron spin configuration.[158]

Origin of magnetism in atoms

The magnetic moment of an electron originates from its spin.[159] The magnetic moment of one electron-spin is called the Bohr magneton μ_B and equals $9.2740 \cdot 10^{-24}$ J/T.[159]

An electron confined in an atom furthermore contributes to the magnetic moment with its orbital momentum; moreover, spin-orbit coupling is has to be taken into account.[159]

Considering many electron atoms and molecules, there are two fundamentally different cases:

A) All orbitals of one atom, or the orbitals, obtained from the linear combination of atomic orbitals of atoms that form a chemical bond, are completely filled with electrons.
In that case, the Pauli principle postulates that there is no net magnetic moment originating

[8] Vector multiplication in the chapter is symbolised by * whereas scalar multiplication is indicated by ·.

from the electrons. The reason is that all electrons are paired, i.e., spin and orbital magnetic moments are cancelled.[160]

B) Atomic orbitals are only partly filled.
In that case, net magnetic moments from unpaired electron spins can yield a net magnetic moment for the atom. From the Pauli principle alone, it cannot be explained why electrons should not fill orbitals in pairs and therefore mutually cancel their magnetic moments. However, according to the Hund rules,[161] that were deduced from findings in atomic spectroscopy and that are based on basic electron repulsion considerations, a clear principle how electrons are distributed in the orbitals can be obtained.[161] Resulting magnetic moments can thereby be explained.[161]

Magnetism of materials

Materials, built-up of atoms of case A or B show different magnetisation behaviour in an applied external magnetic field $\overrightarrow{H_{ext}}$. The magnetisation by mass $\vec{M}$, respectively the magnetisation by volume $\vec{\Omega}$ of the material can be related to the external field $\overrightarrow{H_{ext}}$ by:[159]

$$\vec{M} \text{ or } \vec{\Omega} = \chi_s \cdot \overrightarrow{H_{ext}} \quad (1)$$

χ_s is the magnetic (mass respectively volume) susceptibility (which is a tensor, however often taken as a proportionality factor). The susceptibility is different for different types of magnetic materials as will be explained in the following. It is furthermore temperature dependent; however, this aspect is beyond the scope of this brief theory outline.

The sign of χ_s is negative for materials that consist of atoms of type A. This phenomenon is called diamagnetism. Its origin can be explained with Lenz`rule: The external field induces an orbital momentum on the electrons that leads to a magnetisation that is directed antiparallel to this field, i.e., that counteracts it.[162]

For materials built-up of atoms of type B, the magnetic response of the material differs, depending on whether and how magnetic moments of neighbouring atoms couple with each other.

Magnetism of materials: No interaction of neighbouring magnetic atoms: Paramagnetism

If neighbouring magnetic moments are not coupled, they may randomly orient in the material (figure 4a). The phenomenon is called paramagnetism. When the material is exposed to an external magnetic field, the magnetisation directions $\vec{m}$ of the atoms gradually orient towards that magnetic field $\overrightarrow{H_{ext}}$.[163] Therefore, the susceptibility for a paramagnetic material is positive. It is by the order of 10^1-10^2 higher than for diamagnetic

materials.[164,165] The evolution of the average magnetisation $<\vec{m}>$ as function of the strength of the external magnetic field $\overrightarrow{H_{ext}}$ can in classical physics be described by the Langenvin function. Gradually, more and more magnetic moments will orient to parallel direction with the external magnetic field until eventually all magnetic moments are aligned and saturation is reached.[163] The function will be discussed in detail in context of superparamagnetism (*chapter 3.1.3;* also see figure 10 for a depiction of the function).
Quantummechanically, paramagnetism has to be described by the Brillouin function.[163] It takes into account the quantisation of the orbital momentum. When orienting towards the external magnetic field direction, the electron spins, causing the magnetisation of the material, cannot have random but only discrete directions.[163]
Although the physical models are different, both, the Brillouin as well as the Langevin function, describe the shape of the resulting $<m>$ verus H_{ext} curve adequately (the shape is depicted in figure 10).
Considering paramagnetism in metals, moreover unbound conduction electrons, also contributing with their spins towards the magnetisation of a material, have to be considered. This is described by the so-called Pauli paramagnetism model (a detailed discussion is beyond the scope of this text).[163]

Magnetism of materials: Interaction of neighbouring magnetic atoms: Ferromagnetism, antiferromagnetism and ferrimagnetism

In 1928, Heisenberg[166] found that ferromagnetism can be explained by considering a Hamilton operator that only takes into account interaction of effective magnetic spins of neighbouring atoms (taking the sum over all neighbours). The Heisenberg-Hamiltonain *U* can be written as:[167]

$$U = -\sum_{i,j} J \cdot \vec{S_i} * \vec{S_j} \qquad (2)$$

Where *J* is the exchange integral that is related to the overlap of the charge distributions *i* and *j* of neighbouring atoms contributing with their total electronic spins $\vec{S_i}$ and $\vec{S_j}$ (Heisenberg model).[167] The exchange integral originates from considering the difference in energy of a singlet and triplet state in overlapping atomic orbitals.[168] *J* depends on the distance of atoms in a solid as this distance determines which state for the electrons is more favourable (this consideration is often depicted in so-called Bethe-Slater-curves;[168] a detailed discussion is not the scope of this work).

Whether a material is either ferro- or antiferromagnetic is determined by the sign of *J*. In the case of ferromagnetic coupling, *J* is positive. In this case, magnetic moments of neighbouring "magnetic" atoms, pointing in the same direction (figure 4b), yield the lowest exchange energy. Ferromagnetism yields the strongest form of magnetism.

The susceptibility of ferromagnetic materials is by the order 10^2-10^3 higher than for paramagnetic materials.[164]

If *J* is negative, neighbouring atoms will have magnetic moments directed antiparallel to each other to achieve lowest exchange energy. If all the atoms have the same magnetic moments, the total magnetisation will be zero as the magnetic moments of the neighbouring atoms exactly cancel each other; such a material is antiferromagnetic (figure 4c) and has no "accessible" magnetism.[169]
Ferrimagnetism occurs, when magnetic moments of atoms *i* and *j* point antiparallel however differ in magnitude. This is the case if the number of electrons of the atoms *i* and *j* are different. For instance Fe(II) and Fe(III) have a difference of one unpaired electron that contributes with its spin. The opposite spin directions lead to a weakened magnetisation (ferrimagnetic materials, figure 4d).
Almost all magnetically ordered materials (ferro-, antiferro- or ferrimagnets) contain *3d* or *4f* elements,[170] i.e., transition metals or rare earth elements (REE). Seven of the 17 REE are ferromagnetic.[171] However there is no rule to predict what kind of magnetism will be observed in a certain material.[172]
Finally, worth mentioning: For metals, to correctly describe the magnetic phenomena, furthermore a band-model, the so-called itinerant magnetism, has to be considered.[173]

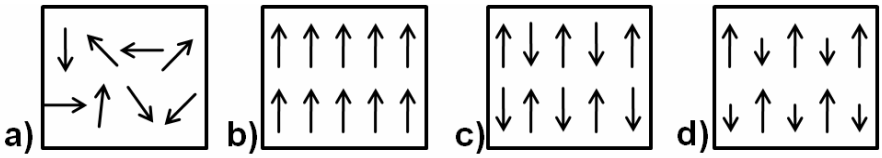

Figure 4: Each arrow represents one atomic magnetic moment. a) In paramagnetic materials, magnetic moments do not couple with each other, i.e., they may point in random directions. b) Moments in ferromagnetic materials all point in the same direction, whereas in antiferromagnetic materials (c), the moment directions of neighbouring atoms are opposed and cancel out each other. For the same arrangement but in case of different atoms with different magnetic moment magnitudes, a weakened magnetism exists (d, ferrimagnetism).

3.1.2 The hysteresis and the concept of domains

The hysteresis

Diamagnetic materials as well as paramagnetic materials (the latter in the region long before saturation is reached) show in a first approximation a linear increase of magnetisation when exposed to a linearily increasing external magnetic field $\overrightarrow{H_{ext}}$; the slope is negative for diamagnetic materials, positive for paramagnetic materials.[164] When a ferri- or ferromagnetic material is exposed to a cyclically reversed external magnetic field, a typical hysteresis can be recorded (see figure 5).

At zero external field ($H_{ext} = 0$), the magnetisation still present in the material is called remanence. The coercitivity is the necessary strength of an external magnetic field which needs to be applied to demagnetise the material.

A bulk ferri- or ferromagnetic material, from which a hysteretic magnetisation behaviour as shown in figure 5 can be recorded, typically consists of many domains. These are regions of the same magnetisation direction, i.e., within a domain (also called "Weiss`scher Bezirk"), all atomic magnetic moments are in parallel.[174] The transition region of one domain to another, where for instance the magnetisation direction might be anti-parallel with respect to the neighbouring domain, is called the domain wall.

When the material is exposed to a magnetic field, the domain walls start to move. This happens in a way that the domains with magnetisation already oriented in the direction of the external field grow larger. Finally, only one single domain will be left, oriented in parallel to the external field. When the external field is removed, the nucleation of domains (figure 5) leads to domain wall formation again. The boundaries will even out over time, finally forming equally sized domains that reduce the stray field (see following sections) to zero. The movement of the wall boundaries can be energetically hampered due to pinning. Pinning by impurities is the main reason for the occurrence of a hysteresis (figure 5). The relaxation rate of a remanent magnetisation strongly depends on the purity of the material, i.e., the domain wall mobility.[175] When relaxation is fast, it is a soft magnetic material; when pinning causes a long lasting remanence, it is a hard magnet.

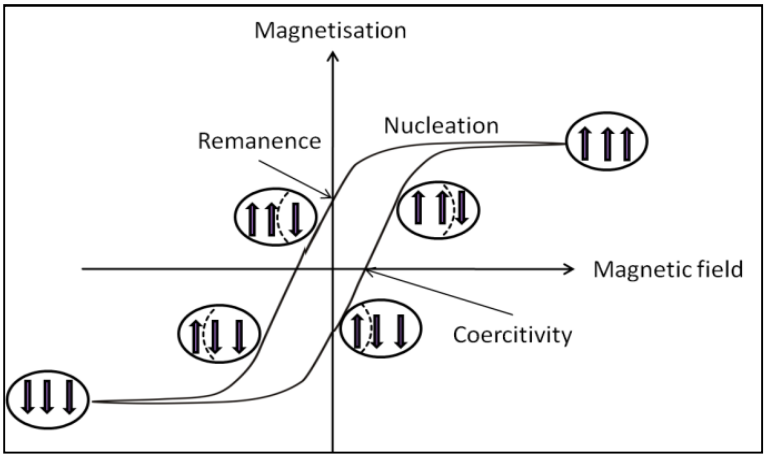

Figure 5: A hysteresis is obtained when a *magnetisation versus external magnetic field* curve is recorded for a ferromagnetic material. The magnetisation direction in the material is changed due to an external field via domain boundary movement. The arrows represent the magnetisation directions of domains in a material (circle) for different situations where a domain wall (dashed line) moves due to an externally applied magnetic field (schematic figure; adapted from[176]).

Domain walls

The thickness of a domain wall is governed by two energy contributions that counteract each other:

Due to the exchange energy of the total electronic spins between neighbouring atoms (compare *equation (2)*), a sharp turn-over of magnetisation direction is not favourable. A rotation e.g. by 180° from one atom belonging to one domain to the next atom belonging to a neighbouring domain is not encountered. The reason is that this would mean counteracting the complete exchange energy at once. Therefore, the magnetisation directions gradually tilt. A complete inversion of magnetisation direction is spread over several atomic layers.[177] Considering only this contribution alone, a domain wall with infinite thickness would be most favourable. Two neighbouring magnetic moments could almost stay parallel and would hardly be twisted, i.e., they could nearly stay in the most favourable exchange direction.
Counteracting this is another energy contribution, which is related to the so-called crystalline anisotropy of a material. A detailed description would go beyond the scope of this work, however, briefly summarised the following can be stated: Atomic orbitals in a crystal are not isotropic, i.e., they arrange with a certain direction that is related to the crystal-system of the solid. An orientation of the magnetisation direction in line with this so-called “easy axis” of the crystal (indifferent if the magnetisation points “up or down”) is the energetically most favourable state.[178] A gradual tilting of the magnetisation directions away from this axis means tilting of the atomic orbitals due to spin-orbit coupling. This tilting however results in a change of overlap of neighbouring orbitals. Consequently, Coulomb interactions are altered. Eventually this leads to a perturbation of the energetically most favourable arrangement of neighbouring (overlapping) orbitals (the “easy axis” orientation).[178] Considering only this energy contribution, a domain wall should be infinitely thin. A direct 180° transition of the magnetic moment from one atom to the next atom would conserve the lowest energy state in terms of crystalline anisotropy energy.
An optimal wall thickness can be obtained from determining the energetic minimum of the sum of the two described energy contributions (as function of atomic layers that take part in the transition region between two neighbouring domains). Thereby, it is also possible to obtain an expression for the energy of the domain wall that can be given per area *A* of a domain wall boundary (the area between two domains) as: [179,180]

$$\frac{\gamma_d}{A} = 2 \cdot \pi \cdot \sqrt{K_\alpha \cdot k_{ex}} \qquad (3)$$

γ_d is the domain wall energy. K_α is the anisotropy energy per volume, originating from the crystalline anisotropy contribution. k_{ex} is the exchange energy per length. It is directly related to *equation (2)* but not equal *J*. It is given per length as it is derived from *J* in a from where it is expressed per lattice constant *a* length in a solid.[181] The values of the energy constants are material dependent.

Single domain versus multi domain magnets

The thermodynamically most favourable domain arrangement in a bulk ferro- or ferrimagnet in the absence of an external field should have an internally closed cycle of magnetisation directions. Achieved by appropriate domain arrangement, this arrangement yields a zero external magnetic stray field (figure 6a). An external magnetic stray field, surrounding a magnetic material, originates from the material itself. It builds-up when the magnetisation direction of a domain points from the solid towards free space. At the surface, i.e., at the transition from solid to free space, magnetic dipoles (sometimes described as "*magnetic surface charges*") are created.[182] An external stray field occurs either if a multi domain magnet does not have an arrangement of domains to yield a closed cycle of magnetisation within the material, or it occurs for single domain magnets (figure 6b).[183] The stray field energy is equal to the magnetostatic energy E_{ms}, that is the energy within the magnetic material. The magnetostatic (or stray field) energy E_{ms} (per volume) of a single domain particle, can be expressed as:[182]

$$\frac{E_{ms}}{V} = \frac{1}{2} \cdot \mu_0 \cdot N_d \cdot \Omega_s^2 \qquad (4)$$

μ_0 is the permeability of free space. Ω_s is the saturation magnetisation by volume of the single domain magnet (magnetic saturation is given as all magnetic moments are aligned in the same direction within the domain). *V* is the particle volume. N_d is the demagnetisation tensor. It results from the consideration that the surface magnetic dipoles cause a demagnetisation within the solid. It has to be considered for small particles.[182] For a (small) spherical particle (that will discussed in the following) it becomes a simple scalar factor, namely 1/3.[184]

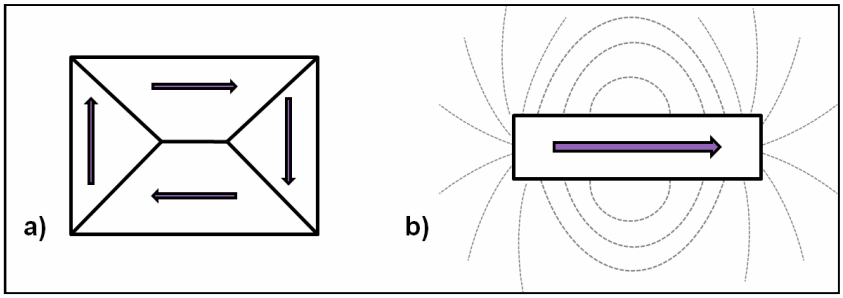

Figure 6: No external stray field exists when magnetic domains arrange in a way to form a closed loop (a). A single domain magnet however possesses an external stray field (dotted lines) (b).

Dividing a single domain particle in two domains reduces the magnetostatic (stray field) energy E_{ms} to roughly the half.[185] However, as thereby a domain wall is created, domain wall energy (*equation (3)*) adds as positive energy contribution.

As it can be seen from *equations (3)* and *(4)*, the domain wall energy is an energy contribution per area between two domains. The magnetostatic energy is a contribution per volume of the domain. It becomes obvious that a decision whether either a single domain or a two domain state is more favourable for a particle can be made by comparing the two absolute energy contributions for a body of given volume (and domain wall area). Considering the case of a spherical particle with radius *r*, the critical single domain radius r_{SD}, can be determined. For particles with $r > r_{SD}$ a two domain particle is energetically more favourable as the volume-energy-contribution scales with r^3 (which dominates for larger *r*):

$$2 \cdot \pi \cdot \sqrt{K_\alpha \cdot k_{ex}} \cdot \pi \cdot r^2 = \frac{1}{4} \cdot \mu_0 \cdot \frac{1}{3} \cdot \Omega_s^2 \cdot \frac{4}{3} \cdot \pi \cdot r^3 \qquad (5)$$

In *equation (5)*, the domain wall energy contribution for a spherical particle with a cross-section of $\pi \cdot r^2$ is set equal to the energy difference gained when a spherical single domain particle of volume $\frac{4}{3} \cdot \pi \cdot r^3$ is divided in two domains (E_{ms} is halved). As the particle is spherical N_d is set to 1/3. Solving *equation (5)* for the critical single domain radius r_{SD} yields:

$$r_{SD} = \frac{18 \cdot \pi \cdot \sqrt{K_\alpha \cdot k_{ex}}}{\mu_0 \cdot \Omega_s^2} \qquad (6)$$

The two energy curves (*equation (5)*), scaling with r^2 and r^3, respectively, and their intersection for $r = r_{SD}$, are graphically represented in figure 7.

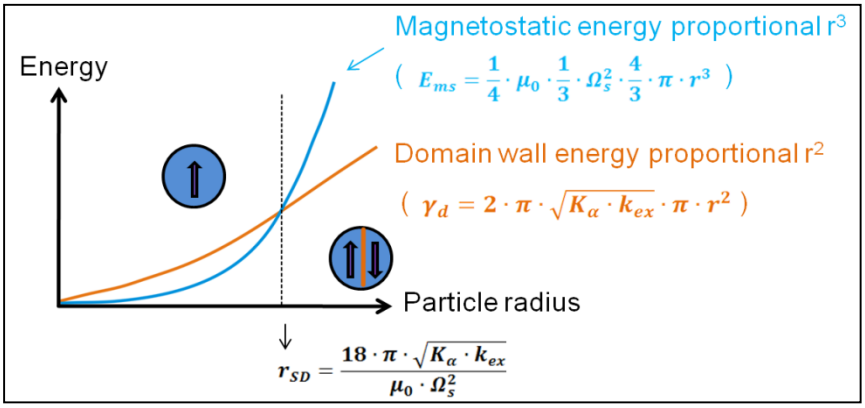

Figure 7: Depending on the size of the magnetic particle single or multi domains are energetically more favourable. Decisive contributions are the domain wall energy and the magnetostatic energy that scale with r^2 and r^3, respectively. The critical single domain radius r_{SD} determines at which size a particle is a single domain or a two domain particle.

3.1.3 Superparamagnetism of single nanoparticles and nanocomposites[9]

Right at the upper size limit for a single domain particle, the measured coercitivity might be larger than for the same material in bulk (figure 8).[186] Other than for multi domain particles, magnetisation directions cannot be changed via domain wall movement.[175] The magnetisation direction can only be changed by rotation of the magnetic moment ensemble of all magnetically coupling atoms of the particle.[175] Single domain particles have a fixed magnetisation direction. It is usually assumed that such particles, in a first approximation, possess an energy barrier originating from the so-called uniaxial anisotropy. If a potential further contribution, that depends on the shape of the particle, is neglected, it equals the crystalline anisotropy (assuming that there is one most favourable magnetisation direction in the particle).[178,187] Due to the anisotropy barrier, the preferred magnetic moment direction is either 0° or 180°. For the particle to switch magnetisation direction from 0° to 180°, a barrier ΔE_a with the energy $K_a \cdot V$ (with K_a the anisotropy energy per volume, which is material dependent and V the particle volume) has to be overcome (see also figure 9).[188] For rotation of magnetic direction, a strong external magnetic field is required.

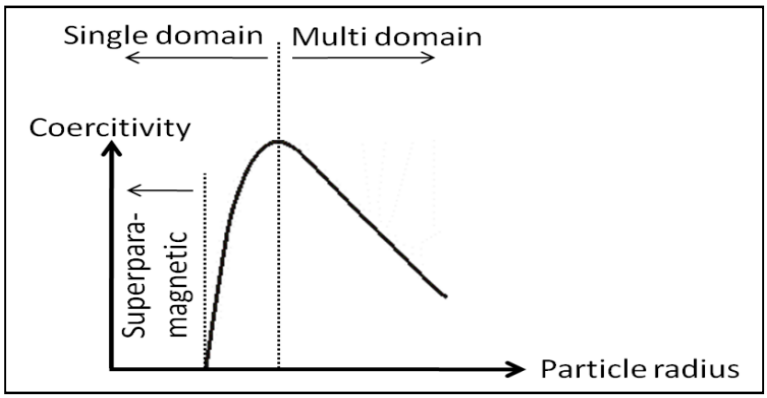

Figure 8: When magnetic particles get smaller, their coercitivity increases up to the point where a single domain particle forms. Reversing this magnetisation demands the highest external magnetic fields (the coercitivity is the highest) as no domain wall movement mechanism is possible anymore. Particles that are even much smaller might behave superparamagnetically, coercitivity shrinks to zero.
(Figure adapted from [189].)

If the size of a single domain particle is further reduced, the anisotropy energy $K_a \cdot V$ (that decreases with the particle size) might eventually become smaller than the prevailing thermal energy $k_B \cdot T$ (k_B: Boltzmann's constant; T: absolute temperature). The magnetic moments of all atoms in the particle still couple for quantum mechanical reasons (the material would be ferri- or ferromagnetic in bulk). However, at this point, the total particle

[9] The discussion on the physics of the blocking temperature has been published and is reused in this work by courtesy of Elsevier. Original article: K. Mandel et al., *J. Magn. Magn. Mater.*, 2013, **331**, 269.

magnetic moment is not fixed in the "energy valley" to either a 0° or 180° direction anymore; it can undergo random fluctuation (see figure 9).[190] This is called the *superparamagnetic effect*.[191] The temperature above which the thermal energy is sufficient to transform a single domain particle with fixed magnetic moment direction to a particle with a randomly fluctuating magnetic moment (see figure 9) is called blocking temperature T_B.[191] Above T_B the magnetic moment of a single domain particle points in a certain direction only for a very short time τ. In 1949, L. Néel, who studied magnetism in single domain grains in the context of geophysics, postulated an expression for the frequency f at which the magnetisation direction fluctuates.[192] It can be formulated as an Arrhenius' equation-like function:[188]

$$f = f_0 \cdot \exp\left(-\frac{K_\alpha \cdot V}{k_B \cdot T}\right) \tag{7}$$

f_0 was estimated by Néel to be in the order of $10^9 \cdot s^{-1}$.[191,193]

To obtain the blocking termperature T_B as value for T from this equation, the „*time scale of the experimental technique*" has to be defined.[188] A typical period of time (by convention) is 100 s for the measurement of magnetisation.[41] If the investigated particle magnetisation direction fluctuates at the given experimental temperature with a frequency higher than 0.01 s^{-1}, it averages out over the time of measurement. No magnetisation is measured and the particle is said to behave superparamagnetically. The absence of a hysteresis when the particle's magnetisation is recorded in a cyclic reversed external magnetic field is characteristic for superparamagnetic particles at a given temperature above T_B.[193-195]

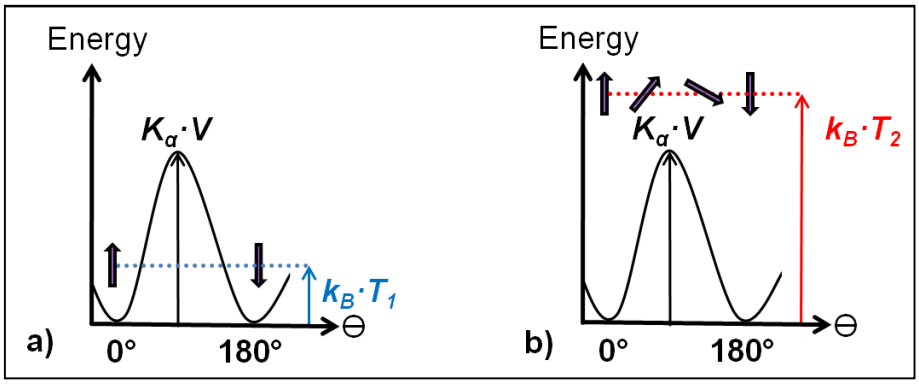

Figure 9: The uniaxial anisotropy in a single domain magnetic particle represents an energy barrier which is proportional to the particle volume. It hinders the particle magnetisation (represented as arrow) to switch its direction if the thermal energy of the particle (at T_1) is not sufficient (a). Above a certain temperature T_B, thermal energy is sufficient to overcome the anisotropy barrier. Therefore, at T_2, the magnetisation direction of the particle can fluctuate freely (b). (The anisotropy barrier is modelled with a $\sin^2\Theta$ function.)[187]

The recorded magnetisation versus $\overrightarrow{H_{ext}}$ curves for superparamagnetic particles can best be described by the Langevin function $\mathcal{L}(x)$. As already mentioned, it is normally used to illustrate paramagnetism in classical physics.[190,193,196] It describes the evolution of the average magnetisation as function of $\overrightarrow{H_{ext}}$. It results from the gradual orientation of randomly directed atomic magnetic moments in a paramagnetic material that is exposed to an external magnetic field. When the Langevin function is used to describe an ensemble of nanoparticles, each nanoparticle is treated as a "large atom". The magnetic moment of such a "large atom" is 10^3-10^5 times higher than the moment of the atoms it is composed of.[193,197] The average magnetic moment $<\vec{m}>$ of a superparamagnetic particle in an ensemble of particles measured as function (and in direction) of $\overrightarrow{H_{ext}}$ is:

$$< \vec{m} > = \vec{m} \cdot \mathcal{L}\left(\frac{\mu_0 \cdot m \cdot H_{ext}}{k_B \cdot T}\right) \tag{8}$$

The function results from the assumption that a dipolar energy E_{dipol} exists for a particle with a magnetisation moment $\vec{m}$ deviating from the $\overrightarrow{H_{ext}}$ direction by an angle θ (which can be 0°-180°):

$$E_{dipol} = -\mu_0 \cdot m \cdot H_{ext} \cdot \cos(\theta) \tag{9}$$

(H_{ext} equals $|\overrightarrow{H_{ext}}|$ and m equals $|\vec{m}|$, i.e., the vector magnitudes).

Using this expression, an average magnetisation $<\vec{m}>$ (that is measured in direction of $\overrightarrow{H_{ext}}$) can be obtained. This is done by weighting the energy contribution (*equation (9)*) with a Boltzmann factor from classical statistical thermodynamics[196] to result in:

$$< \vec{m} > = \frac{\vec{m} \cdot \int_1^{-1} x \cdot \exp\left(\frac{\mu_0 \cdot m \cdot x \cdot H_{ext}}{k_B \cdot T}\right) dx}{\int_1^{-1} \exp\left(\frac{\mu_0 \cdot m \cdot x \cdot H_{ext}}{k_B \cdot T}\right) dx} \tag{10}$$

With *cosθ* being replaced by *x* (the limits of integration are transformed from *θ to x*).

Using a statistical thermodynamic approach is a valid assumption. The average magnetisation is based on a statistical distribution of energy states. It is an expression for the probability to find a particle directed in its magnetisation in parallel to $\overrightarrow{H_{ext}}$.

The integral of e*quation (10)* is well-known and can be looked-up in appropriate tables. It equals a function containing a coth, namely:[196]

$$< \vec{m} > = \vec{m} \cdot \left(\coth\left(\frac{\mu_0 \cdot m \cdot H_{ext}}{k_B \cdot T}\right) - \frac{1}{\left(\frac{\mu_0 \cdot m \cdot H_{ext}}{k_B \cdot T}\right)}\right) \tag{11}$$

The Langevin function from *equation (8)* is the content of the full bracket of *equation (11)*.

The plotted function <m>(H_{ext}) (obtained by ignoring the mathematical discontinuity for $H_{ext} = 0$) is depicted in figure 10.

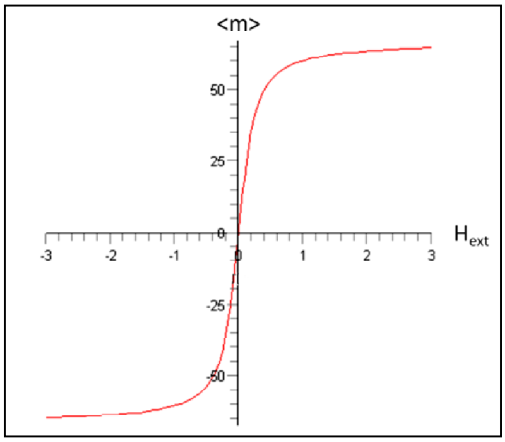

Figure 10: The Langevin function as mathematical description for the magnetisation curve of a superparamagnetic system. The *x*-axis corresponds to the magnitude of $\overrightarrow{H_{ext}}$ and the *y*-axis to the magnitude of $<\vec{m}>$. The average magnetisation measured in direction of $\overrightarrow{H_{ext}}$. (Taking the numerical values of the *x*-axis in units of 10 kOe and of the *y*-axis in units of emu/g, the plot is a model function, resembling measured curves for superparamagnetic nanoparticles synthesised in this work). [10]

The function describes the gradual orientation of initially freely fluctuating magnetic moments of superparamagnetic particles in dependence of an external field $\overrightarrow{H_{ext}}$ parallel to its direction.

When nanoparticles are synthesised, they are never absolutely uniform but have a certain size distribution which can often be approximated by a Gaussian function. Therefore, particles have different magnitudes of *m* depending on the amount of atoms they consists of. Nevertheless, the curves measured for a particle ensemble look like the one shown in figure 10. In order to quantitatively compare magnetisations of different samples (containing *n* nanoparticles), measured curves are weighted by the sample masses. This yields the mass magnetisation *M*:

$$M = \frac{n \cdot <m>}{sample\ mass} \tag{12}$$

A saturation magnetisation M_s (by mass) for a particle sample can be obtained at the point where the measured curve reaches saturation ($\mathcal{L}(x) \to 1$; $< m > \to m$).

In literature, values for the (saturation) magnetisation by mass are often given in cgs units, namely as emu/g. The SI units equivalent is $A \cdot m^2 \cdot kg^{-1}$.

[10] The function that is depicted was calculated and plotted with MAPLE, provided by Maplesoft.

Quite often, practically, the mass magnetisation *M* rather than the volume magnetisation *Ω* (the units of the latter would be emu/cm^3, respectively A·m^{-1}) is considered. This is often beneficial for comparing different particle samples as the mass can easily be obtained experimentally but the volume is often unknown as is the density of the material.

Superparamagnetism not only depends on individual nanoparticle properties. Interactions among ensembles or composites of nanoparticles can further influence superparamagnetic behaviour of the whole system. Nanocomposites, i.e., in a matrix confined superparamagnetic nanoparticles, may also mutually interact within their matrix due to magnetic dipole-dipole interactions.[198,199]

Often, superparamagnetism of nanoparticles or composites is studied by zero field cooled (ZFC) and field cooled (FC) measurements. These can help to understand nanoparticle interactions better. To this effect, a non-magnetised sample is cooled down to a few K and $\vec{M}$ is subsequently measured with increasing temperature (*T*) under a low magnetic field applied ($\overrightarrow{H_{ext}}$, typically a few Oe) to obtain the ZFC curve. After having reached room temperature (RT) the sample is cooled while being exposed to the applied magnetic field $\overrightarrow{H_{ext}}$ and again $\vec{M}$ is recorded in dependence of *T* (FC curve).

A scheme of these measurements together with the direction of $\vec{m}$ for a group of superparamagnetic nanoparticles is shown in figure 11.

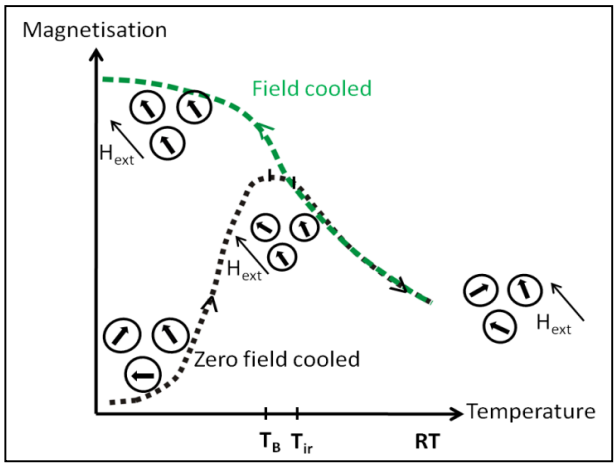

Figure 11: Scheme of zero field cooled (ZFC) and field cooled (FC) measurements; direction of magnetisation $\vec{m}$ of some nanoparticles (black, bold arrows) under applied magnetic field $\overrightarrow{H_{ext}}$.

Heating up a cooled and non-magnetised sample of nanoparticles under $\overrightarrow{H_{ext}}$ gradually leads to an orientation of the magnetisation directions of the single domain particles towards the field, because thermal energy overcomes ΔE_a.[200] Above the temperature T_B, the blocking temperature, thermal energy is higher than ΔE_a and the particles magnetic

energy due to the field $\overrightarrow{H_{ext}}$. The magnetisation direction of the particles freely fluctuates and is no longer oriented parallel to $\overrightarrow{H_{ext}}$. After a maximum at T_B,[201] $\vec{M}$ decreases with increasing T. When the sample is cooled down again while being exposed to the applied $\overrightarrow{H_{ext}}$ (FC curve), all particle magnetisation directions finally align along $\overrightarrow{H_{ext}}$ (highest $\vec{M}$ in the FC curve).

At elevated temperatures, ZFC and FC curves superimpose. The common decline of $\vec{M}$ with increasing T (below RT) is a fingerprint for the superparamagnetism of the system.[202,203] A splitting of ZFC and FC curves is observed below a certain temperature which is assigned as T_{ir} (irreversible temperature). Below T_{ir}, $\vec{M}$ increases further with decreasing T on the FC curve. T_{ir} can coincide with T_B on the ZFC curve or it can be situated at a higher temperature ($T_{ir} > T_B$).[200]

Shapes of the ZFC and FC curves as well as values of T_B and $\Delta T_{ir,B}$ ($\Delta T_{ir,B} = T_{ir} - T_B$) are interpreted in relation to magnetic nanoparticle properties in different ways. If mutual magnetic particle interactions are neglected, the broadness of the ZFC curve is typically correlated to particle size distribution.[199,204-206] ΔE_a increases with the particle volume,[201] i.e., larger particles have higher T_B.[206-209] T_B is either interpreted as the starting temperature of free fluctuation of magnetisation for average-sized particles[210] or for the smallest particles.[200] T_{ir} is considered as the temperature above which the largest particles start to fluctuate freely.[200, 202-210]

In an alternative interpretation, it is the differential quotient $d(M_{Tir} - M_{TB})/dT$ that is related to the particle size distribution.[211]

In other works,[212-215] ZFC and FC curves are interpreted by considering magnetic dipole-dipole interactions. In that case, an increase of T_B is related to an increasing particle interaction intensity[212,213] and particle concentrations in a composite.[214,215] However, the very opposite interpretation was discussed as well.[216] To resolve this contradiction two interaction regimes were postulated.[217] Depending on the intensity of particle interaction, a change in the concentration of magnetic nanoparticles can cause either a higher or lower T_B.[198,217] Nevertheless, it is usually assumed that T_B shifts to higher temperatures with increasing particle interaction.[212-215] This will also be assumed in this work. Taking particle interactions into account, $\Delta T_{ir,B} > 0$ is explained as a random dipolar interaction, as reported.[218] $\Delta T_{ir,B}$ increases with increasing particle interaction.[210]

The influence of different stabilisations and distributions of nanoparticles in a silica matrix and their effects on ZFC / FC measurements will be addressed in this work in *chapter 4.2.2.*

3.1.4 Influence of surface effects on magnetic properties of nanoparticles

The saturation magnetisation M_s of a bulk ferromagnetic material is usually higher than measured for small nanoparticles of the same material.[219] The main reason for the drop of M_s is the high fraction N_s of atoms on the surface of a particle consisting of N_{tot} atoms. The fraction for a spherical particle can be estimated:[220]

$$\frac{N_S}{N_{tot}} = 4 \cdot N_{tot}^{-\frac{1}{3}} \tag{13}$$

For particles with diameters smaller than 10 nm, N_s quickly rises to several ten percent. At the surface, the atoms do have a different coordination as well as dangling bonds. This leads to misalignment of spins (frustrated spins) and thus a shell of atoms that do not contribute to the total magnetisation.[221] Furthermore, surface oxide effects are also encountered which might reduce the total magnetisation of a particle as well.[222] Moreover, a high fraction of surface atoms causes additional surface anisotropy contributions which lead to diverging magnetic moment orientations. For instance, simulations have shown that magnetic moments of surface atoms point in a direction perpendicular to the surface, whereas the magnetic moments inside the particle all point in one parallel direction.[223] If magnetic particles are in contact with surface active agents (surfactants) which might be used to stabilise the particles in dispersion, these organic molecules might also decrease the magnetisation of the particles.

It was reported that the type of anchor group that attaches to the particle determines how dramatically the saturation magnetisation of a particle can be reduced. It was e.g. found that sulfonic and phosphonic groups had stronger impact than mild alcoholic surfactants.[224]

3.1.5 Structure and magnetism of iron and the iron oxides magnetite and maghemite

Iron, at room temperature, has a body centred cubic crystal structure (α-iron) and a very high magnetisation of 217 emu/g[40] as all magnetic moments are ordered in parallel (ferromagnet).

Magnetite (Fe_3O_4) possesses an inverse spinel structure.[225] It has a face centred cubic unit cell (a = 0.839 nm) with 32 O^{2-} closed packed along [111] [225] which yields 8 formula units per unit cell. Remarkably, the iron oxide magnetite contains Fe(II) in its unit cell. The formula can be written as $Fe(III)[Fe(II)Fe(III)]O_4$. One-eighth of the tetrahedral sites are occupied by Fe(III) and one-half of the octahedral sites are occupied by Fe(II) and Fe(III).[226] The atomic magnetic moments of the tetrahedral sites (“A sites”; occupied with Fe(III)) and the octahedral sites (“B sites”; occupied with Fe(II) and Fe(III)), quantum

mechanically interacting via a 127° Fe-O-Fe linkage, align anti-parallel to each other. The B sites (Fe(II) and Fe(III)) align parallel to each other.[227] At 0 K, the magnetic moment of Fe_3O_4 is therefore 4 μ_B ((5 unpaired d-electrons from Fe(III)) – (5 + 4 unpaired d-electrons from Fe(III) and Fe(II)) = 4 μ_B).[226] As already introduced, the Bohr magneton μ_B is the fundamental spin magnetic moment of one electron. The magnetisation of bulk magnetite is 92-100 emu/g.[45] At room temperature, superparamagnetism was reported for magnetite particles with diameters (assumption: spherical particles) smaller than 10-25 nm[228] or 19 nm.[229]

Maghemite (magnet-hematite, γ-Fe_2O_3) is closely related to magnetite. It also possesses an inverse spinel structure with the same oxygen arrangement in the face centred cubic unit cell (a = 0.834 nm).[225] In difference to magnetite, iron ions only prevail as Fe(III). To counterbalance the increased charge, some cation vacancies exist. 21 1/3 Fe(III) ions and 2 1/3 vacancies can be found in the unit cell, where 8 tetrahedral sites are occupied with Fe(III) and the remaining Fe(III) are randomly distributed in the octahedral interstitial sites. The vacancies are confined to the octahedral sites.[225] The magnetic moments of the Fe(III) in the tetrahedral sites are all in parallel with respect to each other and the same holds for the magnetic moments of Fe(III) in the octahedral sites. However, the magnetic moments of the Fe(III) at the tetrahedral sites are anti-parallel to the magnetic moments of Fe(III) at the octahedral sites, therefore, maghemite is a ferrimagnet.[227] Its saturation magnetisation is 60-80 emu/g.[45] Superparamagnetism at room temperature was reported for particles smaller than 10-25 nm.[228]

3.2 Magnetic particle separation in fluids (Process Engineering)

The underlying physical principle for magnetic separation is a force from an external magnetic field that leads to a movement of magnetic particles in a fluid in such a way that the particles are attracted towards the magnet and can therefore be separated from the fluid.

3.2.1 The magnetic force on a particle in a field gradient

The total force (vector) $\vec{F}$ acting on a magnetic body can be explained by the volume integral of a body with volume V over the force density $\vec{f}$:[230]

$$\vec{F} = \int_V \vec{f}\, dV \tag{14}$$

The force density $\vec{f}$, according to Maxwell principles, is equal to the divergence (*div*) of a tensor $\boldsymbol{T}$ and can be written as:[230]

$$\vec{f} = div\boldsymbol{T} = \lim_{V\to 0} \frac{\oint_s \boldsymbol{T}*\vec{n}ds}{V} \tag{15}$$

s is the surface of the body, $\vec{n}$ the unit vector normal to the surface. $\boldsymbol{T}$ is the Maxwell stress tensor and has the form:[230]

$$\boldsymbol{T} = \begin{pmatrix} H_x \cdot B_x - \frac{1}{2} \cdot \vec{H} * \vec{B} & H_x \cdot B_y & H_x \cdot B_z \\ H_y \cdot B_x & H_y \cdot B_y - \frac{1}{2} \cdot \vec{H} * \vec{B} & H_y \cdot B_z \\ H_z \cdot B_x & H_z \cdot B_y & H_z \cdot B_z - \frac{1}{2} \cdot \vec{H} * \vec{B} \end{pmatrix} \tag{16}$$

B is the magnetic flux density, (*H* equals H_{ext}).

Application of several mathematical steps (compare[230]) leads to an expression for the magnetic force. For a one dimensional case, the force $F_{m,x}$ due to a magnetic field gradient (in *x* direction) that acts on a spherical particle with volume *V* and which reached the (volume weighted) saturation magnetisation Ω_S can be given as:

$$F_{m,x} = \mu_0 \cdot \Omega_s \cdot V \cdot \frac{dH_{ext,x}}{dx} \tag{17}$$

μ_0 is the permeability of free space.

In three dimensions, the expression is much more complicated as a gradient in a vector field has to be considered, which results in a second order tensor expression for the magnetic force.[231]

The case of superparamagnetic particles is interesting: Such particles are always in the state of magnetic saturation; however the direction of the magnetic moment of each particle fluctuates freely. Being exposed to an external magnetic field, the dipolar energy (*equation (9)*) comes into play. As demonstrated in *equations (9-11)*, a certain fraction of particles orients its magnetisation directed parallel to the external field as this is the thermodynamically most favourable state. Only then, the magnetic field gradient force (*equation (17)*) acts on these particles. The equation implicitly requires that the particle magnetisation points in the direction of the field gradient. If not, the particle is "switched off" in terms of magnetic separability and in general does not behave like a magnet. That means that the field strength determines the *fraction* of particles that "feels" *at all* the magnetic gradient force. However, as the thermodynamically most favourable state for a particle exposed to a magnetic field is a magnetisation parallel to the field, it is a question of time until the particle gets to that state and the magnetic force acts on it (kinetically

determined). In other words, the weaker the magnetic field at a certain spot, the longer it takes till the whole fraction of particles in solution, dispersed at this spot, is finally separated. For a particle to be separable, it is furthermore required that the magnetic gradient force exceeds other forces. These other forces acting on a particle in solution will be discussed in the next chapter. The magnetic separation force (see *equation (17)*) can be increased by either tweaking the particle properties (size and saturation magnetisation) or by focusing on engineering solutions of the magnetic separator to increase the magnetic field gradient (*chapter 3.2.4*).

3.2.2 Magnetic particles in a fluid exposed to the force field of a magnetic gradient

During magnetic separation, the trajectories of particles in a fluid, other than in case of electrostatics, do not follow the well-known magnetic field lines (i.e. the force lines). Particles rather move perpendicular to magnetic pressure isobars that can be calculated from the gradient vector fields in the respective system.[232] In order to describe the particle behaviour in a fluid more precisely, also several other forces that act on the particle have to be considered:

Gravitational force

A spherical particle with radius r in a fluid underlies the gravitational force $\overrightarrow{F_g}$ that always points down to the ground:

$$\overrightarrow{F_g} = \frac{4}{3} \cdot \pi \cdot r^3 \cdot (\rho_p - \rho_f) \cdot \vec{g} \tag{18}$$

Where ρ_p is the density of the particles, ρ_f the density of the displaced fluid and g is the gravitational acceleration constant prevailing on earth (9.81 m/s^2).

Viscous drag force

It has to be considered that there is a viscous drag when a particle is moved due to a force in a fluid. A very rough but typically[233,234] used approximation is the Stokes viscous drag force for a spherical particle of radius r in a fluid of viscosity η moving with a speed $\vec{v}$ which yields a force $\vec{F}_d$.

$$\vec{F}_d = -6 \cdot \pi \cdot \eta \cdot r \cdot \vec{v} \tag{19}$$

This force always counteracts to the direction of a moving particle.

For a one dimensional case, a velocity v_x for a spherical magnetic particle (that reached magnetic saturation or is a superparamagnetic particle that is "switched on") of radius *r* in a fluid that is attracted *by* and moving *towards* a magnetic gradient (neglecting the susceptibility of the fluid) in *x* direction can be obtained from *equations (17)* and *(19)*:

$$v_x = \frac{\Omega_s \cdot r^2}{6 \cdot \pi \cdot \eta} \cdot \mu_0 \cdot \frac{dH_{ext,x}}{dx} \tag{20}$$

Brownian force

If particles are small enough, they undergo noticeable Brownian motion (random walk) because thermal energy is sufficient to keep the particles in motion. The thermal energy $k_B \cdot T$ is leading to a Brownian force F_B (with random direction) on a particle with diameter $2 \cdot r$. Its scale can (as an order of magnitude estimate) be expressed as:[235-238]

$$F_B \cong \frac{k_B \cdot T}{2 \cdot r} \tag{21}$$

At a certain size of the particles, namely below approximately 1 µm, Brownian motion of the particles is no longer negligible as it influences the particle trajectories.[238,239]

Calculated forces and separation velocities for three model particle systems that are related to the particles considered in this work can be found in the *Appendix*.

3.2.3 Magnetic particle-particle interactions

So far, considerations regarded single particles only. However, in applications not one but many particles are magnetically separated from a fluid. In principle, for correct consideration of particle-particle interaction, weak London - van der Waals forces on the nanoscale as well as Coulomb interactions on the nano- and macroscale have to be taken into account. Here, for reasons of simplicity, these interactions are neglected and only magnetic particle-particle interactions are briefly addressed:

Magnetic particles themselves can – if they are magnetised – be the origin of a strong magnetic gradient that attracts other particles.[235] Therefore, if the particles are not sterically or electrostatically stabilised in a way that is strong enough to lead to mutual repulsion, magnetic agglomeration will normally take place and if the particles are ferromagnetic, this results in large agglomerates that still stick together for a long time after the magnetic field has been removed. A huge particle size increase is the consequence and such particles cannot be individually suspended again once they had been magnetised (figure 12).

Figure 12: Large agglomerates of 500 nm (primary size) magnetite nanoparticles immediately form due to mutual magnetic attraction after shaking up magnetically extracted particles again in solution.

3.2.4 Setups to obtain magnetic gradients for the separation of particles

Inside a solenoid or in the gap between two pole pieces, a magnetic field is uniform and therefore without gradient.[240,241] In high gradient magnetic filters (HGMF) a rather homogenous magnetic field (e.g. the gap between two pole pieces) is dehomogenised by filling the gap with magnetically susceptible (soft ferromagnetic) wires or spheres, resulting in magnetic field gradients pointing towards these objects.[242]

A single wire, when magnetised, produces a magnetic field that drops with $1/(2 \cdot a_p^2)$ in intensity,[242] where a_p is the perpendicular radial distance from the wire. For practical applications it is claimed that the distance a_p at which the force gradient becomes too weak is approximately three times the wire diameter.[243] From these assumptions, an ideal particle capture grid could be constructed.[244] However, the mathematical description of a particle in a fluid flow crossing only one wire capture cross section and thus being attracted by the wire is already sophisticated,[245] although it can be analytically solved for a laminar fluid flow.[245] But as soon as more wires in a flow cross section are used for magnetic particle capture, it is hardly possible even to numerically solve the problem.[245] M. Franzreb worked on the problem for a regular wire grid.[246] Simulations on the deposition of particles on a wire mesh have been published.[247] Still, no proper mathematical descriptions are possible if for instance steel wool is used in a column for magnetic separation.
An alternative to wires for filling of columns are closed packed spheres. It was found that the highest gradients are pointing towards the interstitial space between the spheres, resulting in a very good particle capture,[248] however bearing the problem of eventual blockage of empty spaces after filling with attracted material.[249]

In a simplest case, permanent hand magnets can be used for magnetic separation. They possess a field gradient as their magnetic field roughly drops exponentially with increasing

distance to the magnet. Placing ring-magnets around a narrow column can for instance be a suitable option to separate particles from a fluid stream through this column.

Alternatively, separation using permanent magnets can be done with a drum separator (figure 13)[250] with magnetic fields of typically < 0.2 T.[251] These setups allow a cheap continuous magnetic separation that does not need much energy as no electromagnets are used, however, particles should be well in the µm size range and sufficiently strong magnetic.[250]

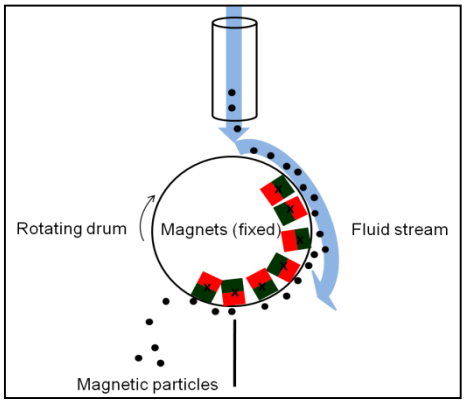

Figure 13: Principle of a magnetic drum separator with permanent magnets (figure after [250]).

3.3 Particle syntheses, surface modifications and sorption principles (Chemistry)

Material synthesis in this work was conducted by wet-chemical techniques. The theoretical fundamentals will be described here, followed by brief considerations of sorption theory that is important for removal and recovery of dissolved substance from fluids.

3.3.1 Wet-chemical synthesis of solids: Bulk and nanomaterials from (co)precipitation

Nanomaterial synthesis can be done using various strategies:[252-254] Top-down methods mainly include lithography techniques (electron or ion beam techniques or chemical etching methods) or physical milling of powders to nanosize. Bottom-up solutions reach from physical methods such as gas condensation, sputtering, evaporation or ablation techniques over physicochemical methods such as molecular beam epitaxy or chemical vapour deposition to purely chemical routes such as thermal decomposition or reduction as well as precipitation.[252- 254]

Precipitation from solution is a facile and effective method to obtain solid products (nano to macro scale) fast and in high yield without advanced equipment.[252] The key condition

for a dissolved substance to precipitate from a solution is its supersaturation.[255] When conditions in solution are changed (e.g. pH variation, reduction etc.), the solubility for a substance may drop below its prevailing concentration which leads to precipitation reactions. Precipitation of several different elements at the same time is called coprecipitation. Precipitates that consist of several elements can be formed when only one element preferentially precipitates (e.g. as an oxyhydroxide) that incorporates other elements which otherwise might still be stable in a dissolved state under the prevailing conditions in solution. A precipitated product can be amorphous or crystalline depending on the thermodynamically most favourable state. However, kinetics might influence the situation in a way that metastable products form.[255]

According to the Stranski / Ostwald Step Rule, the least stable phase in a system nucleates first and might further react until the most stable phase is formed.[255] For instance, amorphous metal hydroxides in a precipitation reaction might form initially, however further condensation reactions (water release) could lead to the evolution of crystalline metal oxides.

Solid formation from liquids always starts with nucleation. Nucleation can be either homogenous or heterogeneous. The latter occurs when nuclei grow on surfaces of any kind, such as impurities or walls of the reaction vessel. Homogenous nucleation happens directly in solution without the need of any surface. Nuclei form as soon as the solid state is thermodynamically more favourable then the liquid state. From thermodynamic constraints it can be deduced that there is a critical size (radius r^*) for a nucleus to be stable. For homogenous nucleation the dependence of the critical radius with the interfacial surface energy per unit area γ_A on the saturation S of a solution is:[256]

$$r^* = \frac{2 \cdot V_m \cdot \gamma_A}{3 \cdot k_B \cdot T \cdot ln(S)} \tag{22}$$

V_m is the molecular volume of the precipitated species.
Only above a critical saturation S_c, nuclei will form (and grow). Sudden supersaturation might lead to a nucleation burst. Subsequently, the concentration of the element in the solution will decrease and eventually, the saturation is too low to create more nuclei. Below S_c only the already existing nuclei will grow from the left atoms / ions in solution.

Nucleation rate above the critical saturation can be as fast as 10^{30} $cm^{-3} \cdot s^{-1}$.[255] A fast nucleation hand in hand with a subsequent fast and strong concentration drop of elements in solution to zero can yield particles that are nano sized.

These particles might agglomerate (also as "hard agglomerates"[257])[11] which is more likely the smaller the particles are and the weaker their mutual repulsion is.[255]

If individually dispersed nanoparticles in solution (i.e. colloidal sols) are desired, agglomeration has to be prevented. This can be achieved by modifying the surface of nanoparticles to repel each other. In polar solvents, electrostatic repulsion takes place: Charged particles in a polar solvent possess a rather rigid layer of ions surrounding the particles, which again is surrounded by a more lose sphere of ions, the electrical double layer. The transition plane between these two regions is called the shear plane. The electric potential at this shear plane with respect to the solvent is designated as the zeta potential, which is an important measurement parameter in colloidal science.[258] The Derjaguin-Landau-Verwey-Overbeek (DLVO) theory[259] describes the balance between repulsion of charged particles due to their electrical double layer and their attraction due to van der Waals forces. Particles with high zeta potential repel each other stronger. Increasing the ion concentration or strength in solution might shrink the double layer and destroy the mutual repelling effect, leading to flocculation (reversible) or coagulation (irreversible) of the colloids.[258]

In non-polar solvents, colloidal sols are obtained by steric stabilisation which is achieved by attaching bulky hydrophobic alkyl chains to the surface of the particles (e.g. fatty acids, bond via the carboxy group to a particle surface)[260]. Repulsion of approaching particles takes place due to entropy reasons that hinder intertwining of the alkyl chains.
Additionally to electrostatic and steric, electrosteric stabilisation mechanisms are possible. It is a combination of both effects, where organic molecules are used that possess both, bulky chains as well as charged functional groups.

3.3.2 Wet-chemical inorganic silica network formation

For synthesis of nanocomposites, nanoparticles need to be incorporated into a solid network, i.e., an inorganic matrix. Wet-chemical methods offer a way to build up such an inorganic network for instance from silica.[261] Typical reactions to form a solid silica network from wet-chemical processing are hydrolysis and condensation. As a classical precursor, tetraethoxysilane (TEOS) is used. It is firstly hydrolysed (*equation (23)*) and then condensated (*equation (24)* or *(25)*) to form a SiO_2 network:[261]

[11] The term "hard agglomerates" is used instead of "aggregates" to avoid confusion of the words agglomerates and aggreagates as it was suggested by G. Nichols et al.[257]

$$\equiv Si\text{-}OR + H_2O \rightleftharpoons \equiv Si\text{-}OH + ROH \quad (23)$$

$$\equiv Si\text{-}OR + HO\text{-}Si\equiv \rightleftharpoons \equiv Si\text{-}O\text{-}Si\equiv + ROH \quad (24)$$

$$\equiv Si\text{-}OH + HO\text{-}Si\equiv \rightleftharpoons \equiv Si\text{-}O\text{-}Si\equiv + H_2O \quad (25)$$

An alternative silica source is sodium silicate (water glass). In a water glass solution silicic acid oligomers[262] and occasionally small silica nanoparticles (up to 2 nm) are present.[263] Repulsion between the species, that hinders their gelation, occurs due to charged oxygen sites from $\equiv Si\text{-}O^-$, resulting from the presence of the sodium hydroxide that "*ionises off*" hydrogen ions.[262] In sodium silicate solution with a molar ratio of SiO_2: Na_2O = 3.1, only 15 % of Si-OX of $Si(OX)_4$ tetrahedrons (with X being Si or H) are charged sites.[262] In principle OH^- can catalyse condensation reactions (*equation (25)*) to form permanent siloxane bonds in the same way as this holds for alkoxysilanes: *"A silicon atom in silicic acid or at a surface normally has a coordination number of 4. The coordination number can be momentarily expanded by adsorption of a hydroxyl ion simultaneously with adsorption of a sixth group such as a silanol group belonging to another silicic acid molecule or colloidal particle. The transition complex is unstable and water condenses out between the two silanol groups to form a permanent siloxane bond. The coordination number drops back to four and the hydroxyl is desorbed, regenerating it to continue its catalytic role in the solution."*[264] However, negatively charged $\equiv Si\text{-}O^-$ repel the OH^- catalysts. Therefore, sodium silicate ions cannot condensate simply by pH increase.[264]

3.3.3 Sorption

The term sorption in general describes immobilisation of substances via another phase. In the following, the phenomenon of adsorption, which is included in the term sorption, will be discussed. Distinction can be made between physisorption, chemisorption and ion-exchange.[265] Physisorption is mainly driven by van der Waals forces: Dipole-dipole interactions lead to adhesive forces between the target substances and the adsorber surface. The forces decrease with the 6^{th} power to distance *substance - surface*. The interactions are rather weak (typical enthalpies are 5-40 kJ/mol)[266]. Chemisorption leads to stronger interactions. Electrons are transferred between the adsorbed substance and the surface.[265] Ion-exchange is a third form of adsorption which concerns Coulomb attractive forces between ions and charged functional groups.[265] Ions are electrostatically attracted[265] by electron donor atoms (for cations) or electron acceptor atoms (for anions) that are part of a ligand[267] which itself may for instance be immobilised on a solid surface. A coordination

complex is formed among the ion and the ligand via *coordinate bonds.*[267] The replacement of one ion, which is more preferentially coordinatively bonded by a ligand, with an already complexed ion is called ion-exchange. The species selectivity / preferential affinity can be explained by the principle of "hard and soft acids and bases" (HSAB).[268] This idea, also known as the Pearson principle, is based on the Lewis acid-base-concept,[269] named after G. N. Lewis,[269] which is a model for the *coordinate bond* that occurs between the electron donating species (Lewis base) and the electron accepting species (Lewis acid).[270] According to the Pearson principle, hard acids form more stable complexes with hard bases and soft acids form more stable complexes with soft bases. A hard acid is a positively charged ion that is hardly polarisable and has a high charge density. A hard base is a ligand atom that is hardly polarisable. Vice versa, a thiol group for instance is a soft Lewis base that preferentially coordinates to a soft Lewis acid such as Hg^{2+}.[271] If a ligand for a metal cation contains several donor atoms that coordinate to the cation, this complex is thermodynamically more stable than a complex composed of many ligands with only one donor atom per ligand. This is called the *chelate effect*.[272] The word is "*derived from the Greek* [word] *for a crab's claw*".[273] A polydentate ligand (the denticitiy is related to the number of atoms of a ligand that form *coordinate bonds* with an ion)[273] "grabs" the ion from several sides like a claw (compare: bidentate in figure 3). The higher thermodynamic stability of a chelate complex is related to an increase in entropy when monodentate ligands, that formerly were coordinated around an ion, are released due to their replacement by the chelate ligand.[272]
A special class of (inorganic) ion-exchangers are layered materials (e.g. clays) that intercalate ions in-between the charged layers of the mineral structures.[136]

All adsorption and subsequent desorption (the reverse equivalent to adsorption) processes underlie kinetical and thermodynamical principles. Often, kinetics, i.e., the change of target substance concentration in solution with time due to immobilisation or release on, respectively from a surface, are described in dependence of concentrations (as function of time) of the dissolved substance by differential equations. Rates are often classified by orders which are related to exponential factors occurring in the differential equations.[274]
After an appropriate adsorption / desorption time, a system (solid-liquid or solid-gas) has reached a dynamic equilibrium of adsorption and desorption which is the regime of thermodynamic considerations. In context of this, isotherm models are established to describe the capacity of an adsorber for a given concentration of a dissolved target substance. Famous isotherm models, that are distinct mainly in different assumptions made on the formation mechanisms of adsorbed molecule layers, are for instance the Langmuir (monolayer molecule adsorption), Henry (multilayer molecule adsorption) and the Brunauer-Emmett-Teller BET (multilayer molecule adsorption) models.[275]

4. RESULTS AND DISCUSSION

Magnetic particle design for water purification and resources recovery involves three steps:

- Identification and development of a suitable *magnetic core material*.
- Incorporation of the magnetic material in *a protective and modifiable matrix*.
- *Modification of the resulting composites* to adsorb dissolved substances.

The particles' performance eventually needs to be evaluated by application in water.

Magnetic core material (chapter 4.1)

Fe based materials were selected to serve as magnetic cores. The other two most prominent magnetic elements Co and Ni were not investigated due to toxicity concerns.[276] No rare elements were used to avoid the creation of a material that does not fulfil sustainability criteria. Micro iron powder as well as nano zero valent iron (NZVI) particles were subject to initial considerations (*chapter 4.1.1)* but major focus was put on iron oxide nanoparticles as magnetic cores for composite particles. Their synthesis and stabilisation is discussed in *chapters 4.1.2* and *4.1.3*. The stabilisation as a sol is an important pre-step before incorporating these nanoparticles into a matrix to form well-defined nanocomposite microparticles.

Protective and modifiable matrix to form nanocomposite microparticles (chapter 4.2)

Silica was chosen as matrix / coating for the iron based particles to protect the particles from oxidation and render subsequent surface modification possible.[28,29] Tetraethoxysilane (TEOS) and sodium silicate (water glass) were investigated as silica sources. The development of nanocomposites is discussed in *chapter 4.2.1* and investigations on their structure and magnetic behaviour are documented in *chapter 4.2.2*.

Composite particle modification to target substances in water (chapter 4.3)

Composite particles were modified in four different ways for four different tasks:

- A silane coupling agent for Hg recovery from water was used to demonstrate the easy and successful modifiability of the particles by silanisation chemistry (*chapter 4.3.1*).
- Cu recovery from water was achieved by composite particles, modified with a ketoxime (LIX84). Silica surfaces were initially rendered hydrophobic via a silanisation reaction with propyl groups that are able to interact via van der Waals forces with nonyl-groups that are part of the LIX84 molecule. This modification uses an impregnation method that exploits hydrophobic interactions (*chapter 4.3.1*).

- Phosphate was recovered by particles modified with layered double hydroxides (LDH) via “electrostatic bonding” (*chapter 4.3.2* and *chapter 4.3.3*).
- General heavy metal removal for water purification was achieved by using the nanocomposite particles as seeds for in situ nucleation of iron hydroxide precipitates in waste water. A process is suggested that allows the recovery of the heavy metals from the purified water (*chapter 4.3.4*).

An overview on the complete syntheses steps is given in figure 14. Investigations on pure iron particles as alternative to iron oxide nanoparticles are not shown in this figure.

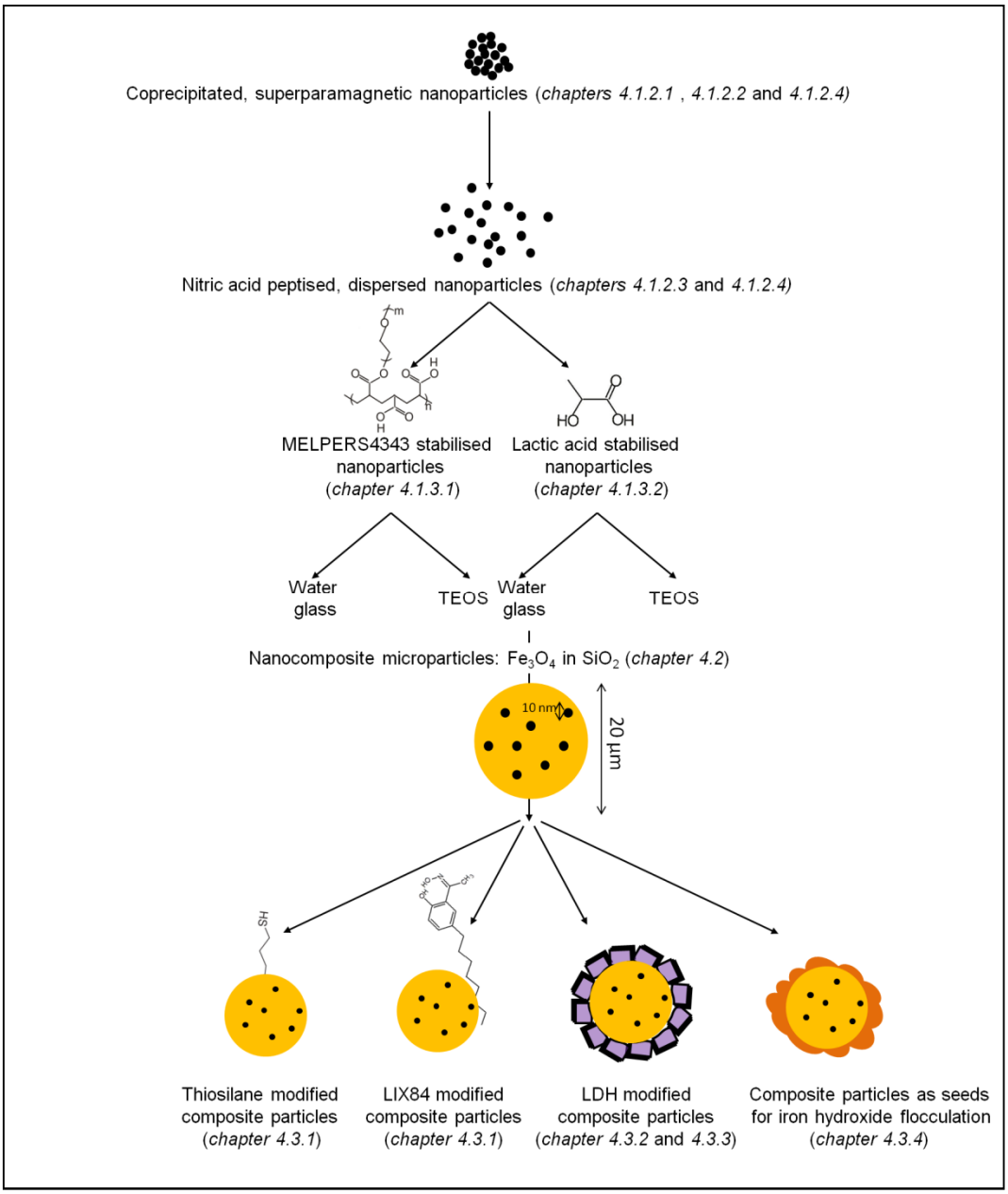

Figure 14: Overview over the synthesis processes discussed in this work.

4.1 Magnetic core material

4.1.1 Highly magnetic iron particles: An alternative to iron oxide nanoparticles?

Using pure iron could be suitable to yield a highly magnetic carrier particle as its saturation magnetisation is about three times higher than of the iron oxide magnetite. Micron sized, highly pure iron is readily commercially available as so-called carbonyl iron powder (BASF, Germany). Its name originates from the synthesis process where iron pentacarbonyl is thermally decomposed to spherical iron particles with diameters of 1-10 µm. The strong magnetisation of the particles is very valuable for magnetic separation applications; however, the challenge is to keep the particles dispersed in water for the adsorption process, i.e., to avoid agglomeration and sedimentation. The particles that are the most suitable to act as magnetic carriers for separation applications in water were selected among all commercially available samples. This was done by comparing the sedimentation speed of formerly magnetised and subsequently redispersed iron particles in water. The slowest sedimentation rates were observed for the particle types with the weakest magnetic agglomeration. A coated, thus oxidation resistant sample type ("CIP SQ") and a very soft magnetic, uncoated iron powder sample ("CIP HS") were identified as the most slowly sedimenting particle types. However, any micron sized iron particle undergoes a comparably fast gravitational settling due to the high density of 7.87 g/cm³ of iron, which is a general drawback that might only be overcome by hollow iron particles, which, however, have not been reported to date.

Fe(0) is highly reactive as it can be easily oxidised.[49] It is often used as a reducing agent for environmental contamination issues.[49] As in this work, iron was chosen for its magnetic properties and not for its reactivity, degradation needs to be avoided to ensure reusability of the particles. A protective particle coating is therefore necessary. The success of this coating can be evaluated from the dissolution rate of a known amount of particles in acid.[277] It will be the slowest for the most dense and most complete protective coating. Pure carbonyl iron powder ("CIP HS") quickly dissolves in an acidic medium (figure 16). Better stability is observed for commercially available silica coated particles ("CIP SQ") (figure 16). It was envisaged to obtain even more stable particles by developing a denser and more resistant coating. Therefore, it was attempted to cover pure iron powder ("CIP HS") with silica as well as with a mixture of silica and precipitated $ZrOCl_2$. SiO_2 from TEOS forms in a hydrolysis and condensation process. It was expected that this "slow growing" would improve the formation of a dense shell around the particles. Reaction of TEOS in presence of "CIP HS" resulted in silica formation on the iron particles. Scanning electron microscopy (SEM) revealed that small silica nanoparticles got

attached to the iron microparticles (figure 15). Energy dispersive X-ray analysis (EDX; not shown) of the iron microparticle surface furthermore indicated a thin silica layer coating.

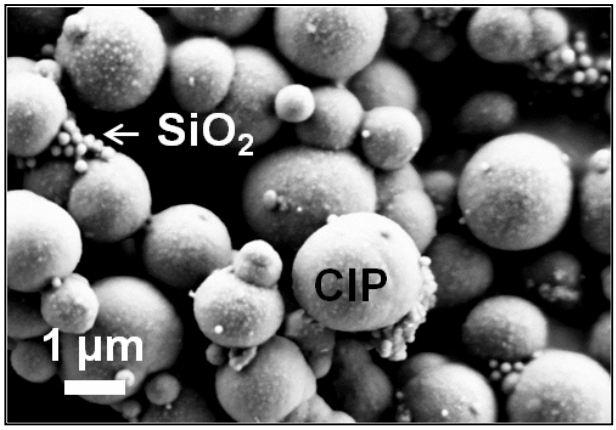

Figure 15: SEM image of small silica particles (SiO_2) attached to carbonyl iron particles (CIP). CIP are furthermore covered with a silica layer which is not visible from SEM but was identified with EDX.

Dispersion of the silica coated particles in 1 M HCl immediately led to a strong bubbling due to H_2 formation from dissolution of the particles. Apparently, it was not possible to achieve a dense coating by using silica alone. Recently, it was reported that ZrO_2 coating improved the acid resistance of Fe particles.[278] Therefore, it was tried to precipitate $ZrOCl_2$ during the silica coating process, additionally. Acid dissolution tests indeed confirmed a better protection of ZrO_2-SiO_2 coated particles (figure 16). Iron dissolution rates were slightly slower than for the commercially coated particles ("CIP SQ").

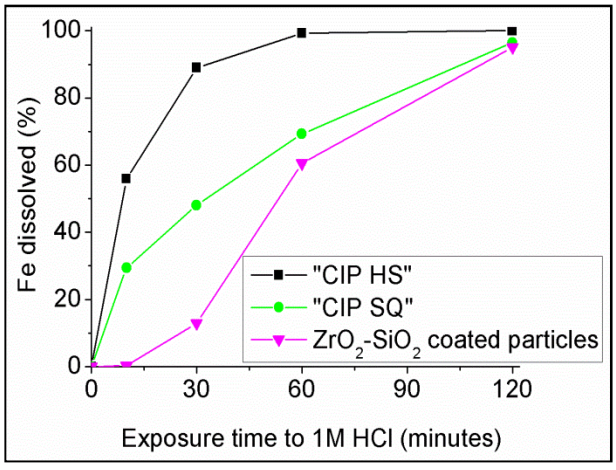

Figure 16: Percent of initially dosed iron (in form of microparticles) dissolved in 1M HCl as a function of time. Examined particles: "CIP HS" (uncoated), "CIP SQ" (commercially coated) and ZrO_2-SiO_2 coated particles.

Figure 17 shows the recorded magnetisation curve of the ZrO_2-SiO_2 coated particles. The saturation magnetisation of the coated particles is 200 emu/g, i.e., close to the value of bulk Fe (217 emu/g). No magnetic remanence was measured for the particles. As the particles are in a range of several µm, superparamagnetic effects can be excluded; they certainly consist of multiple magnetic domains. The only explanation is an excellent purity of the Fe particles. If no pinning or nucleation centres for the domain walls are present, an extremely high mobility of these walls can be assumed, i.e., the magnetic domains of the particles can easily order in a way to yield zero externally measurable magnetisation.

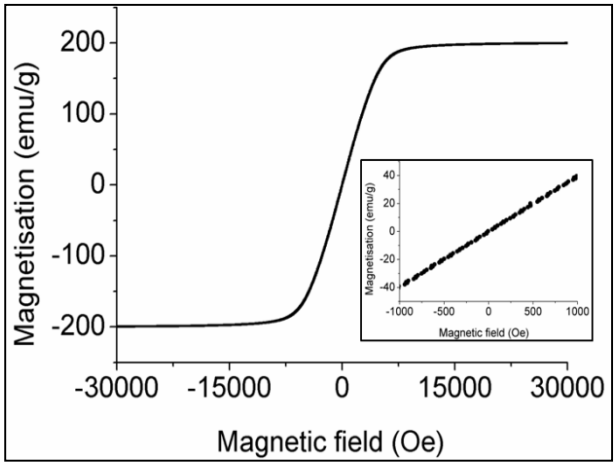

Figure 17: Soft magnetic behaviour of ZrO_2-SiO_2 coated "CIP HS" without hysteresis (Inset: magnification around zero field).

Although the magnetic properties of the particles are attractive due to the strong magnetisation and the non-detectable remanence, they were not subjected to further use. A really dense coating was not achieved as the particles still dissolved remarkably. Using such particles in water has two drawbacks: firstly, they might be reactive and secondly lose their magnetic properties due to slow but continuous oxidation (rusting). Moreover, the problem of relative fast sedimentation due to the high density of the particles, remains unsolved.

An alternative solution to exploit the strong magnetisation of pure iron might be to compose a microparticle that consist of many small iron nanoparticles incorporated into a matrix, i.e., the same schematic nanocomposite particle setup as it was suggested in figure 2. If this was possible using nano zero valent iron (NZVI), a magnetically strongly responding particle might result. Nano zero valent iron (NZVI) can be synthesised by reducing dissolved Fe(III) ions in water with sodium borohydride ($NaBH_4$).[52] Preliminary experiments were carried out using this method. Unfortunately, severe (magnetic) agglomeration of the formed precipitates could not be avoided. It was reported that the

primary size of particles obtained by reduction of iron salts with the "$NaBH_4$ method" is typically in the range of 60-70 nm,[52] well above the superparamagnetic size limit for iron nanoparticles which is below 2-4 nm[209]. Particle sizes of 2-4 nm of pure iron are hardly achievable with standard synthesis methods. As the obtained synthesis product was obviously not advantageous in terms of magnetic properties and as a severe improvement of the product properties with standard methods (that have a chance to be of practical relevance for applications) seemed very unlikely, no further experiments were carried out beyond this stage on NZVI synthesis.

4.1.2 Superparamagnetic iron oxide nanoparticles from coprecipitation[12]

The iron oxides magnetite (Fe_3O_4) and maghemite (γ-Fe_2O_3) possess only about one-third of the magnetisation strength of pure Fe.[45] However, they are easily synthesisable in a size range where they are superparamagnetic. Their production is conveniently possible by precipitation.[53,279]

4.1.2.1 One-pot precipitation of dissolved iron salts

Red-brown precipitates form when ammonia solution is added to an aqueous Fe(III) ion solution. Analogously, blue-green precipitates originate from Fe(II) ions. Fe(III) ions in an alkaline medium react to an (oxy)hydroxide (a FeOOH), Fe(II) ions precipitate as $Fe(OH)_2$ that is oxidised further to a FeOOH.[280] Dried products are X-ray amorphous as measured. Neither of the hydroxides can be separated with ordinary permanent magnets. Also a post-mixing of the precipitates does not lead to a magnetic product (figure 18a). When only Fe(III) ions are precipitated and a fresh Fe(II) ion solution is added to the product, black, magnetically separable particulate matter forms. Considering the reaction educts (iron chlorides, water, ammonia) it can be stated that only iron hydroxide or iron oxide formation is possible and as only two structures possess a noticeably strong magnetisation, the precipitate must be either magnetite (Fe_3O_4) or maghemite (γ-Fe_2O_3).

The formation indicates that the oxidation of $Fe(OH)_2$ is apparently slower than the incorporation of Fe(II) ions into FeOOH to yield an iron oxide. The oxide formation presumably occurs by a fast condensation reaction. Commonly, not a stepwise addition of iron species is used, but a coprecipitation of both iron species in solution is performed to obtain black magnetic precipitates (figure 18b). This synthesis by coprecipitation is a well established process and the reaction is often described as:[48]

$$2\ Fe^{3+} + Fe^{2+} + 8\ OH^- \rightarrow Fe_3O_4 + 4\ H_2O \qquad (26)$$

[12] A part of this chapter has been published and is reused in this work by courtesy of Elsevier.
Original article: K. Mandel et al., *Colloids Surf., A*, 2011, **390**, 173.

Coprecipitation of non-stochiometric ratios of Fe(II) and Fe(III) (in relation to Fe_3O_4, i.e., 1 : 2) results in a mixture of black magnetic precipitates and brown non-magnetic hydroxides. Apparently, the coprecipitation always preferentially takes place with the right ratio of Fe(II) and Fe(III) (1 : 2) followed by hydroxide formation of residual iron ions. It is not very clear and typically not investigated whether oxidation of the magnetic product can cause the transformation to maghemite (γ-Fe_2O_3) if the coprecipitation is carried out in an oxidising environment.[48] Investigations on the structure and oxidation state of the magnetic precipitates were therefore carried out in this work and are discussed in *chapter 4.1.2.4.*

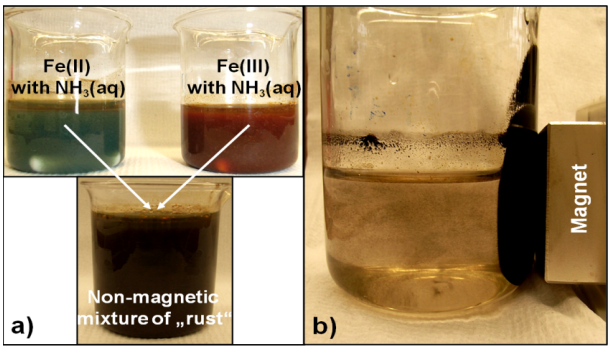

Figure 18: Fe(II) and Fe(III) precipitated alone or a mixture of the two precipitates do not result in a magnetic solid (a); In contrast to this, a coprecipitation of Fe(II) and Fe(III) yields a magnetic precipitate (b).

Transmission electron microscopy (TEM) investigations of the magnetic precipitate reveals that agglomerated nanoparticles of primary sizes in the range of typically (10 ± 2) nm were obtained. Crystallinity of the precipitate was investigated by X-ray diffraction (XRD) (see *chapter 4.1.2.4*), high resolution transmission electron microscopy (HRTEM) analysis and electron diffraction. In the TEM image, figure 19, lattice fringes can be seen. From XRD, crystallite sizes of 9 to 11 nm were determined via the Scherrer equation,[281] which fits to the particle size of about 10 nm (HRTEM). The nanoparticles are single crystals.

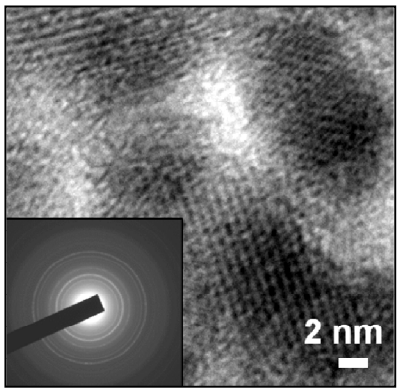

Figure 19: HRTEM image and electron diffraction pattern (inset) of iron oxide nanoparticles.

Vibrating sample magnetometer (VSM) measurements of the dried powder showed that no hysteresis can be observed, i.e., the particles are superparamagnetic (figure 20) with a saturation magnetisation of 77 emu/g.

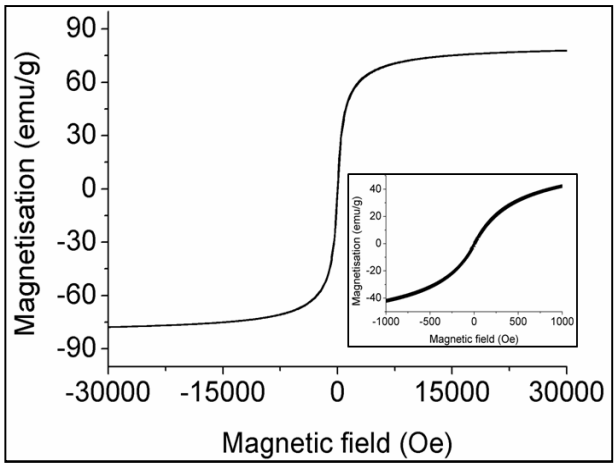

Figure 20: Magnetic curve of as-precipitated, superparamagnetic nanoparticles. (Inset: magnification around zero field).

The very fast nucleation during coprecipitation is the reason why nanosized but agglomerated particles form. Nuclei cannot grow when there is no material left. Agglomerated particles are obtained, because Fe-O^- groups on the surface of the nanoparticles, which in principle could electrostatically stabilise the particles in an alkaline medium, are neutralised by countercations from the base that was used to precipitate the particles (e.g. NH_4^+, Na^+).[279]

4.1.2.2 Continuous synthesis of superparamagnetic iron oxide nanoparticles[13]

The synthesis of superparamagnetic magnetite nanoparticles from coprecipitation of Fe(II) and Fe(III) salts is a well established one-pot process. However, a continuous process is highly desirable for synthesis on a larger scale. Therefore, an easy continuous synthesis procedure without advanced equipment (such as oxygen-free inert chambers) using a Y-connection reactor (principle and photograph see figure 21a and 21b) was developed.

XRD and TEM observations are similar to one-pot precipitated particles. The magnetisation curve for the dried precipitation product shows superparamagnetism and a saturation magnetisation of 67 emu/g (figure 21c). This is to a certain extend lower than the saturation magnetisation observed for one-pot precipitated nanoparticles. A potential explanation might be a partial iron oxyhydroxide formation due to local (in time and space) non-stochiometric conditions during formation in the Y-reactor. Another reason might be

[13] This chapter has been published and is reused in this work by courtesy of the American Chemical Society. Original article: K. Mandel et al., *ACS Appl. Mater. Interfaces*, 2012, **4**, 5633.

that the nanoparticles possess a more defectous structure as the formation conditions might be more kinetically controlled due to the fast throughput and flow process which potentially influences the equilibrium crystal formation. Both assumptions are speculative and were not investigated in further detail.

It should be moreover considered that the magnetisation values are given per weight of particles. Erroneous determination of sample masses (see *experimental section, chapter 7.4*) might lead to significant variation of the calculated saturation magnetisation.

BET measurements reveal a specific surface area of 107 m^2/g of the precipitates, which is in good agreement with the theoretical value of 105 m^2/g for 10 nm spherical magnetite particles. The continuously precipitated nanoparticles are (as the one-pot precipitated ones) agglomerated to sizes between 1 to 200 µm (figure 21d).

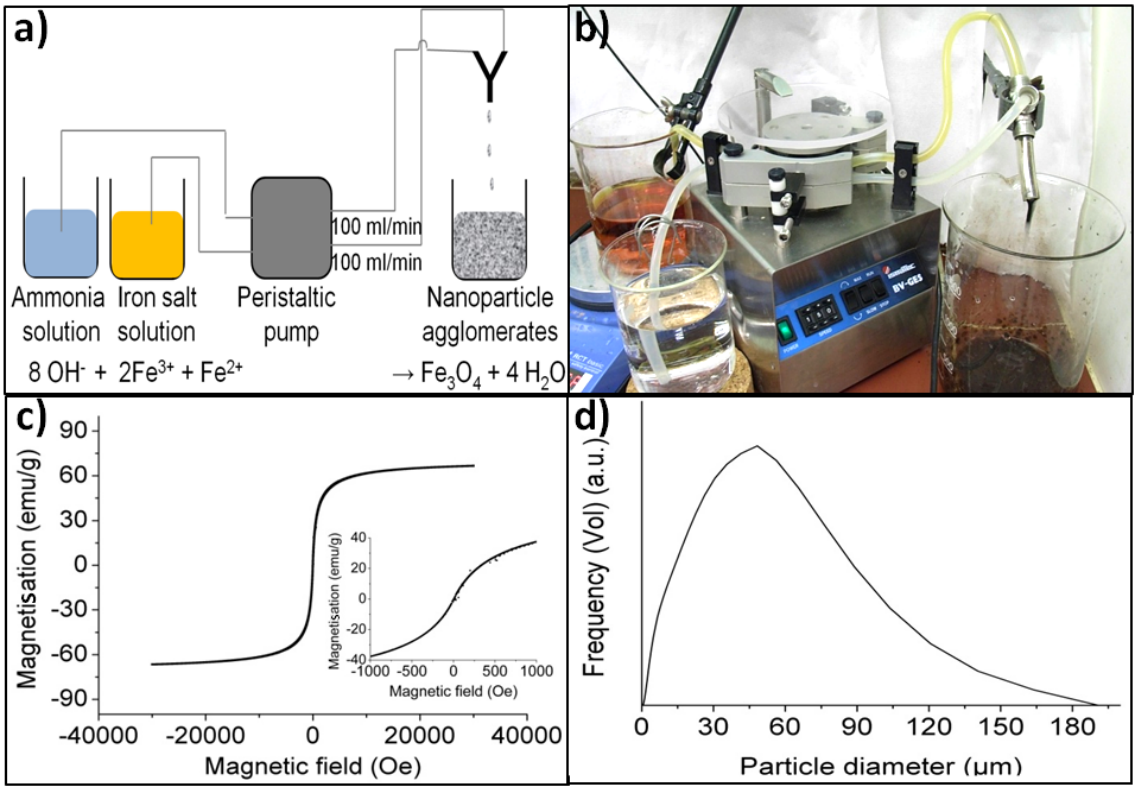

Figure 21: Continuous process for magnetite nanoparticle synthesis (a, b); magnetisation curve of the precipitated product (c) and size distribution (Fraunhofer diffraction) (d).

4.1.2.3 Nanodisperse sols of superparamagnetic iron oxide nanoparticles[14]

In order to form well-defined nanocomposites, i.e., numerous iron oxide nanoparticles in a silica matrix to result in a micron sized particle, it is crucial in the first place to obtain well dispersed nanoparticles in solution. This nanoparticle dispersion or sol can later on be reacted with silica to form composite particles. This is not possible in the same way with as-precipitated nanoparticle agglomerates (see *chapter 4.2*).

To obtain a nanoparticle sol, either agglomeration needs to be prevented during nanoparticle formation or primary agglomerates have to be transferred to a stable dispersion by a post-synthesis treatment. A common way to suppress agglomeration during nanoparticle formation is the in situ presence of surface active molecules (surfactants or stabilising agents). This is a general strategy that is applied when working with thermal decomposition methods.[282,283] It was tried to transfer these principles to the coprecipitation method. As the synthesis is carried out in a polar, aqueous environment, the particles cannot be stabilised by a purely steric mechanism as such surfactants usually cannot be dissolved in water.

Thus, molecules were evaluated that could serve as electrostatic (and with a certain extend steric) repulsion barriers when adsorbed on the surface of the particles. Amine or carboxylic acid groups usually show good affinity towards iron oxide surfaces.[284] In this work, amino acids (L-arginine, L-asparagine, L-glutamine), sugars (D-sucrose, D-glucose) or α-hydroxycarboxylic acids (DL-lactic acid, DL-malic acid, L-tartaric acid) were examined for the purpose of surface modification as previous works reported successful nanoparticle stabilisation by sugars or amino acids (compare *chapter 2.2*, respectively [54-61]). The molecules (in different amounts) were present during coprecipitation of the iron salts with ammonia solution. Only gel-like, brown precipitates formed. Apparently, the functional groups already complexed one of the two iron species or changed its oxidation state in a redox reaction, thus the remaining iron ions precipitated as (oxy)hydroxides and not as magnetic iron oxides. The addition of the stabilising molecules together with ammonia solution, instead of dissolving them with iron ions previously to ammonia solution addition, did not change the outcome either, indicating an apparent very fast complexation of iron ions by the organic molecules.

Consequently, it was tried to post-functionalise the nanoparticles. De-agglomeration of the nanoparticles after precipitation is therefore necessary at first. One way to get a true nanodispersion (sol) of the particles is to add diluted nitric acid (pH = 1-2) as the H^+ charges the particle surface positively. Particles are electrostatically stabilised and a sol is

[14] This chapter in parts has been published and is reused in this work by courtesy of Elsevier.
Original article: K. Mandel et al., *Colloids Surf., A*, 2011, **390**, 173.

obtained (figure 22b). Hydrodynamic particle diameters lie in the range of 10-20 nm (DLS, not shown). The addition of nitric acid was found to be more efficient than e.g. ultrasonication as the latter fails to break all the agglomerates.

The nitric acid stabilised sol is attracted by a magnet as a whole (figure 22b). Such sols are known as ferrofluids.[285] Unlike as-precipitated, agglomerated nanoparticles (figure 22a), the individual nanoparticles of the ferrofluid are not magnetically separated from the fluid as the Brownian forces exceed the magnetic forces in this case (see *Appendix*).

The particles that were dropped from the sol on a TEM grid, and allowed to dry slowly under ambient conditions, showed much smaller particle agglomerates on the grid (figure 22d) than the as-precipitated particle agglomerates dropped on a TEM grid in the same way (figure 22c).

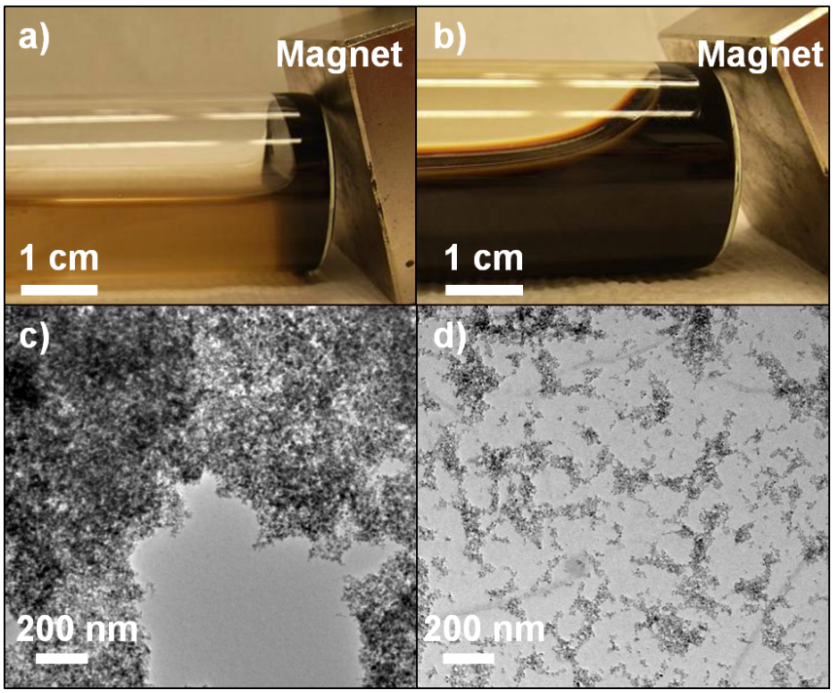

Figure 22: a) As-precipitated nanoparticles separated from the liquid phase; b) nitric acid stabilised sol (ferrofluid); TEM image of a droplet of a) (c) and of b) (d).

Like as-precipitated nanoparticles, nitric acid stabilised ones show superparamagnetic behaviour, however with a lowered saturation magnetisation (57 emu/g; measured for particles obtained from the one-pot synthesis method). Nitric acid treatment might degrade the structure of the nanoparticles and, if magnetite (Fe_3O_4) was prevailing in the first place, further oxidise the particles to γ-Fe_2O_3 (maghemite):[280]

$$2\ Fe_3O_4 + HNO_3 \rightarrow 3\ Fe_2O_3 + HNO_2 \qquad (27)$$

To investigate the influence of the nitric acid treatment, which has proved to be an effective way to nanodisperse the particles, and also to clarify the crystalline structure of the nanoparticles, X-ray as well as HRTEM studies were carried out in more detail and will be discussed in the following chapter.

4.1.2.4 Precipitates / sols of iron oxide nanoparticles: structure and composition[15]

As there is still confusion in literature on the question of the oxidation state of precipitated nanoparticles, i.e., if magnetite or maghemite is obtained, the chemical state of the nanoparticles was investigated by means of X-ray methods. Furthermore, X-ray methods were also applied to study the effect of nitric acid on the particles. Thus, in deep analyses of the particles – precipitated as well as nitric acid peptised – was carried out by means of X-ray diffraction (XRD), X-ray absorption near edge spectroscopy (XANES), extended X-ray absorption fine structure analysis (EXAFS) and small angle X-ray scattering (SAXS). Furthermore imaging investigations were carried out using high resolution transmission electron microscopy (HRTEM).

X-ray diffraction (XRD) results for iron oxide nanoparticles

XRD measurements were carried out on one-pot precipitated (SAMPLE1) and on nitric acid stabilised particles (SAMPLE2). However from the two XRD spectra (figure 23), no decision is possible whether Fe_3O_4 or γ-Fe_2O_3 is prevailing as diffraction patterns of both phases are very similar[286] and fit equally for both X-ray diffractograms that were measured.

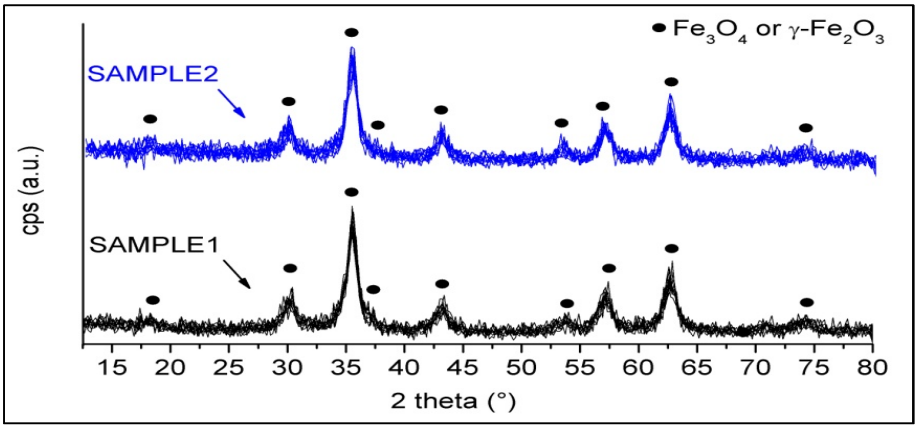

Figure 23: X-ray diffractogram of SAMPLE1, the as-precipitated nanoparticles (bottom graph) and SAMPLE2 the nitric acid treated nanoparticles (upper graph): no distinction from the patterns can be made whether Fe_3O_4 or γ-Fe_2O_3 is the present phase.

[15] This chapter has been published and is reused in this work by courtesy of Springer.
Original article: K. Mandel et al., *J. Nanopart. Res.*, 2012, **14**, 1066. The work was conducted in cooperation with researchers from the "Bundesanstalt für Materialprüfung BAM" in Berlin. XAFS and SAXS measurements, analyses and modelling were carried out by the researchers of the BAM. The original text for the publication was written by Karl Mandel, Wojciech Szczerba (BAM) and Andreas F. Thünemann (BAM).

To get a clearer picture of the type of iron oxide being present before and after peptisation with nitric acid, X-ray absorption studies were carried out.

X-ray absorption spectroscopy results for iron oxide nanoparticles[16]

The analysis of the X-ray absorption near edge (XANES) region of the measured X-ray absorption spectra of the samples, revealed that the absorption edge position of SAMPLE1, the as-precipitated particles, and of SAMPLE2, the nitric acid treated particles, is approximately the same as for magnetite (figure 24), whereas the two iron(III) oxides exhibit a significant shift of their absorption edges toward higher energies. Thus, it can be stated that SAMPLE1 and SAMPLE2 have the same formal valence as magnetite.

It is assumed that the shift of the "white line" (region of 7130-7135 eV in figure 24) to higher energies, similar to that in bulk γ-Fe_2O_3, is caused by the large number of lattice defects, which are the consequence of the particle sizes. This makes the structural part of the XAFS spectrum look in some features similar to bulk γ-Fe_2O_3 that can be regarded in terms of structure as a defective Fe_3O_4 crystal. However, the position of the absorption edge itself indicates magnetite, because of the formal valence, i.e., the Fe(II)/Fe(III) ratio.

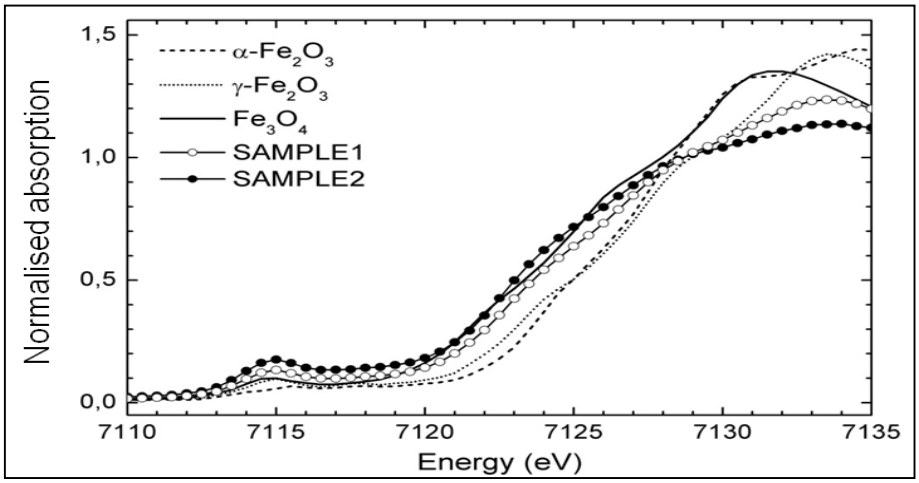

Figure 24: XANES spectra of the samples measured and iron oxide standards normalised to the absorption energy step. The pre-peak visible in the spectra is attributed to tetrahedral iron sites as a result of inversion symmetry breaking. The absorption edge shift being an estimate for the formal valence of the as-precipitated nanoparticles (SAMPLE1) as well as for the nitric acid peptised nanoparticles (SAMPLE2) falls together with that of Fe_3O_4.

The Fourier transformation (FT) of the X-ray absorption fine structure spectra (XAFS) from the *k*-space into the *R*-space, which gives the quasi-radial mean distribution function

[16] This paragraph is first and foremost the work of Wojciech Szczerba, "Bundesanstalt für Materialprüfung BAM", Berlin, published in: K. Mandel et al., *J. Nanopart. Res.*, 2012, **14**, 1066.
It is used here with Wojciech Szczerba's permission.

of the surrounding electron densities and consequently the position of the neighbouring atoms, was performed in the range from 2 to 9 $Å^{-1}$ using the Hannig-type window with a slope parameter of 1. Such settings allowed for a good balance between content of information and noise induced by high *k* signal.

The analysis of the FT EXAFS functions (figure 25) show that the nanoparticles under investigation have in general significantly lower amplitudes. This is a consequence of the small sizes of the particles, elevated surface to volume ratio, and possible disorder.[287] The intriguing fact is that the ratio of the 1st and 2nd coordination shell peaks is inversed in the case of the nanoparticle samples compared to bulk magnetite. This can be explained by the presence of Fe atoms with low coordination number symmetries at the surface which contribute to the amplitude of the first coordination shell peak, but do not influence the signal from farther shells due to a high disorder of the local structure at the surface. This results in a lack of constructive interference of the scattered electron waves and leaves the EXAFS pattern at higher *R* values unaffected.
In order to prove these assumptions *ab intio* calculations using the FEFF 8.4 code were performed. The structural model was established using crystallographic data.[288]
The structure is an inverse spinel, space group Fd3m, with a lattice constant of 8.3958 Å. The Fe ions occupy two different crystallographic sites, at $x = y = z = 1/8$ and $x = y = z = ½$; the oxygen atoms occupy the position $x = y = z = 0.2547$ in the unit cell.[288,289] In bulk magnetite the ratio of octahedral to tetrahedral sites is 2:1. Consequently, FEFF calculations were done for each of the two local symmetries. The two sets of calculated scattering paths were combined by mathematical constraints in the fitting procedure using Ifeffit. FEFF gives to the first scattering paths in both calculations the same amplitude weight of 100.0. Therefore, a correction factor, 6/4×2.0206/1.8861, for the first scattering path of the tetrahedral calculation was introduced, counterweighing the lower degeneracy and taking the closer Fe-O distance into account. This was done to give the two amplitude parameters a more direct meaning of site occupancy in the first shell rather than just that of a correction factor of the scattering amplitude. It was found empirically that such a fine tuning of the model was not necessary for the single scattering paths of the second shell. In the first attempt EXAFS of bulk magnetite was fitted. The free parameters were two Debye-Waller factors (σ^2) for the two atom species, one for each of the coordination symmetries, a global potential correction factor ΔE_0 and four independent amplitude factors for the two shells in each of the coordination symmetries. Preliminary fits showed that the two lattice distortion parameters (Δr) can be set to zero. Only single scattering paths in the range from 1 to 4 Å were used for the fit. The fit gave reasonable parameter values and the expected amplitude ratio of about 2:1 in favour for the octahedral sites. During the refinement of the model it was found that the first and second shell

amplitude parameters of each of the two coordinations could be set equal in the fit. This is a valid assumption for bulk material.

Once a reliable fitting model was established for the bulk structure, fits of the nanoparticle sample were performed (refer to [290] for the fit parameters) (figure 25). The σ^2 parameters obtained for the bulk structure have been used as constants in the fitting models of the two nanoparticle samples. The remaining free parameters from the bulk magnetite model have been kept as variables. Moreover, the amplitude parameters for the first and second shell were allowed to float again. This gave the same number of guessed parameters as in the bulk magnetite fit. For both nanoparticle samples the fit gave for the second coordination shell the expected amplitude ratio of about 2:1 (octahedral / tetrahedral), indicating that the particle core consist of inverse spinel iron oxide. However, for the first shell the ratio was close to 1:1 (see [290] for the fit values). This result seems to support the assumption on the presence of low symmetry coordinated Fe atoms in a disordered surface layer of the oxide particles, as the fitting algorithm sets a higher weight on the scattering path of the tetrahedral coordination.

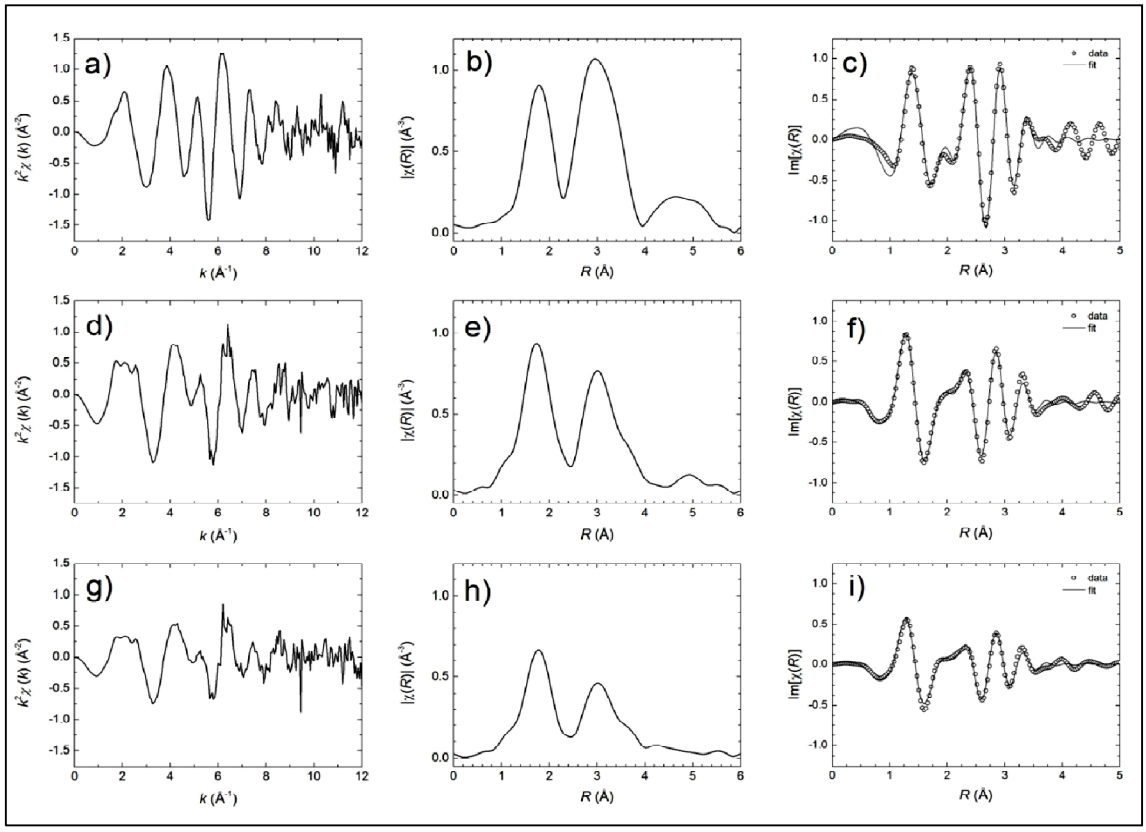

Figure 25: (a-c) Bulk magnetite Fe K-edge EXAFS: a) *χ(k)* weighted by k^2 – EXAFS oscillations after background subtraction; b) Magnitude of FT EXAFS – the two distinctive coordination shells are visible in the spectrum. The first peak is attributed to the nearest Fe-O bonds, whereas the second one is attributed to farther atomic distances, Fe-O and Fe-Fe; c) Imaginary part of FT EXAFS of the experimental spectrum, scattered plot with the best fit line plot. (d-f) Fe EXAFS of the as-precipitated nanoparticles (SAMPLE1), (g-i) Fe EXAFS of the nitric acid peptised nanoparticles (SAMPLE2), plot contents as for bulk magnetite.

The general decrease of the amplitude of the EXAFS signal as seen from SAMPLE1 to SAMPLE2 can be attributed to an increase of the surface to volume ratio by a decrease of mean particle diameters and / or increased surface roughness. This leads to two possible explanations:

1. The nitric acid treated particles of SAMPLE2, are significantly smaller, i.e., an increased fraction of atoms contributing to the surface lead to a signal distortion or

2. The particles have a more distorted surface due to a higher roughness.

The second explanation would mean that the nitric acid treatment leads to a (sub)nano etching effect on the particles making them rougher than the as-precipitated ones. If this was true, it would also add an extra dimension to the picture of dispersing the particles via nitric acid. Potentially, the acid treatment would then dissolve tiny parts of the surface of the agglomerated particles in order to loosen them from each other. However, in that case, then it is also of importance whether the particles get increasingly etched and finally consumed by the nitric acid.

Small angle X-ray scattering (SAXS) results for iron oxide nanoparticles[17]

In order to answer this question, small angle X-ray scattering (SAXS) was carried out on the particles. The technique has the great advantage that primary particle sizes can be measured even when the particles are agglomerated. Other methods such as dynamic light scattering would only measure the size of the agglomerates. Furthermore, agglomeration can be quantified with SAXS and thereby a statement can be made on the dispersion power of nitric acid.

Probing of the in situ nanoparticles' structure was carried out with SAXS on a length scale between π/q_{max} = 0.5 nm and π/q_{min} = 45 nm. The resulting scattering pattern of the as-precipitated, agglomerated nanoparticles (SAMPLE1), the nitric acid peptised, dispersed nanoparticles (SAMPLE2) and also of the particles, stored in nitric acid for long time (SAMPLE3) are depicted in figure 26. It can be seen that the intensity in the low q-range increasingly bends in the line SAMPLE1 SAMPLE2 and SAMPLE3 but all curves superimpose exactly in the high q-range between 0.5 nm^{-1} and 6.0 nm^{-1}. These characteristics are indicative for a decreasing size of structure entities larger than 10 nm while the size of structures smaller than ca. 6 nm is not reduced with increasing nitric acid treatment time. The intensities characteristically scale with q^{-2} in the region around q = 0.2 $nm^{-1}$and with q^{-4} at 0.5 $nm^{-1} < q <$ 3 nm^{-1}. The q^{-4} intensity decay is the classical

[17] This paragraph is first and foremost the work of Andreas F. Thünemann, "Bundesanstalt für Materialprüfung BAM", Berlin, published in: K. Mandel et al., *J. Nanopart. Res.*, 2012, **14**, 1066. It is used here with Andreas F. Thünemann's permission.

Porod scaling, as is valid for nanoparticles with a sharp density transition between a particle and its surroundings.[291] In other words the particles possess a defined Eucledian surface on a length scale between 6 nm and 1 nm. It has to be mentioned here that no differences of the surface roughness on length scales significantly smaller than 1 nm were measurable since the remaining scattering background in the data dominates the scattering intensity at q-values larger than 3 nm^{-1}.

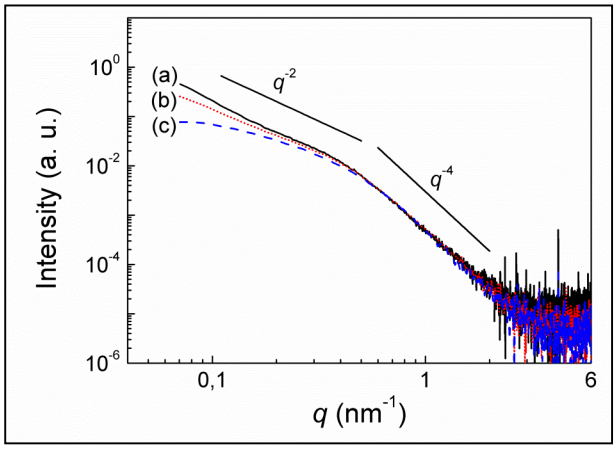

Figure 26: SAXS intensity as a function of the scattering vector for SAMPLE1, the as-precipitated nanoparticles (a), SAMPLE2 the nitric acid peptised particles (b) and SAMPLE3, the peptised particles stored in nitric acid for two months (c). Straight lines indicate the power law behaviour according to a mass fractal (q^{-2}) and Porod's law (q^{-4}).

In contrast to the primary particles, the q^{-2} decay in the low q-region is typical for a mass fractal structure produced e.g. by a diffusion limited aggregation which is equivalent to a three-dimensional random walk.[292] The observed characteristics of the curves are consistent with the presence of agglomerates of discrete nanoparticles whereby the absence of a SAXS peak proves the absence of a periodic arrangement of nanoparticles within the agglomerates. The described qualitative data characteristics allow choosing a suitable model.

G. Beaucage provides a useful equation for quantitative interpretation of the morphology of randomly organised aggregate [18] structures in form of the so-called unified exponential / power-law approach.[292] Therein Guinier and power law regimes are combined for an arbitrary number of structural levels. Applying this approach, two interrelated hierarchical levels are represented, i.e., the level of the primary particles and the level of the aggregates (labelled as 2 and 1, respectively).

[18] The term "aggregate" is used here to be consistent with the primary literature (G. Beaucage) in this context. It could equally be replaced with "agglomerate" as this term is suggested to be used exclusively in general to avoid confusion of different definitions, as discussed by G. Nichols et al.[257]

The scattering intensity for this two-level morphology is given by:[292]

$$I(q) = G_1 \cdot \exp\left(-\frac{q^2 \cdot R_{g1}^2}{3}\right) + B_1 \cdot \exp\left(-\frac{q^2 \cdot R_{g2}^2}{3}\right) \cdot \left\{\left[\mathrm{erf}\left(q \cdot R_{g1} \cdot 6^{-\frac{1}{2}}\right)\right]^3 \cdot q^{-1}\right\}^{p_1}$$
$$+ G_2 \cdot \exp\left(-\frac{q^2 \cdot R_{g2}^2}{3}\right) + B_2 \cdot \left\{\left[\mathrm{erf}\left(q \cdot R_{g2} \cdot 6^{-\frac{1}{2}}\right)\right]^3 q^{-1}\right\}^{p_2} + bkg \qquad (28)$$

Therein the Guinier radius of gyration of the aggregates is R_{g1} and that of the primary particles is R_{g2}. Guinier prefactors are G_1 and G_2. For the power law, the prefactors are B_1 and B_2, the power exponents are p_1 and p_2. Some remaining background scattering resulting from density fluctuations is considered as constant *bkg*.

The scattering data are well-described by *equation (28)* as can be seen in figure 27 (solid and dashed lines, respectively). Therein, for SAMPLE1 (curve a) the single scattering contributions from the primary particles and from the fractal structure is given exemplarily (dotted and dash-dotted line, respectively). The determined primary particles' radii of gyration are (3.2 ± 0.1) nm (SAMPLE1), (3.3 ± 0.1) nm (SAMPLE2) and (3.5 ± 0.1) nm (SAMPLE3). These values show that the size of the primary particles is nearly the same for all samples. Only a small trend towards slightly larger particle seems to appear with increasing nitric acid treatment. The particles' diameters are (10.1 ± 0.3) nm (SAMPLE1, as-precipitated particles), (10.4 ± 0.3) nm (SAMPLE2, nitric acid treated particles) and (11.0 ± 0.3) nm (SAMPLE3 nitric acid treated particles stored for two months in nitric acid) when calculating the diameters as $D = 2 \cdot (5/3)^{1/2} \cdot R_g$ [293] by assuming a spherical shape for simple comparison with TEM results.

The aggregates' radii of gyration are (37.1 ± 2.7) nm (SAMPLE1), (23.2 ± 0.2) nm (SAMPLE2) and (11.2 ± 0.1) nm (SAMPLE3). Obviously, the size of the aggregates strongly decreases by nitric acid treatment. The power law exponents p_1 are 2.05 ± 0.05 (SAMPLE1), 1.61 ± 0.03 (SAMPLE2) and 2.11 ± 0.14 (SAMPLE3). These values are all close to 2 as expected already from simple visual inspection of figure 26 (p_2 was held constant at 4 to prevent unambiguous fit results). The aggregation number N_{agg} can be determined from the aggregates' and primary particles' radii of gyration together with the mass fractal dimension by $N_{agg} = (R_{g1}/R_{g2})^{p1}$.[294] The calculated aggregation numbers for the aggregates are 148 (SAMPLE1, the as-precipitated particles), 23 (SAMPLE2, the nitric acid dispersed particles) and 12 (SAMPLE3, the dispersed particles stored in nitric acid for 2 months). This reduction of the aggregation numbers proves quantitatively how the nitric acid treatment affects the stabilisation of the magnetic nanoparticles.

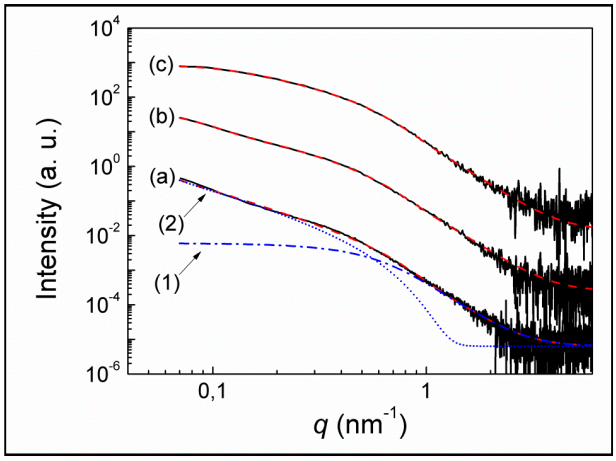

Figure 27: SAXS intensity and curve fits (solid and dashed lines, respectively) for SAMPLE1 (a), SAMPLE2 (b) and SAMPLE3 (c). Exemplarily for SAMPLE1, the arrows (1) and (2) point at the scattering contributions of primary particles (dash-dotted line) and mass fractal structure (dotted line).

Transmission electron microscopy (TEM) investigation results for iron oxide nanoparticles

From SAXS measurements it was found that the particles in all samples possess the same size. This fits well with TEM observations, where particle sizes for as-precipitated and nitric acid treated particles were found in the range of (10 ± 2) nm (longest axis of 100 particles counted) with no significant differences in the samples. A potential explanation for the XANES and EXAFS observations, i.e., the increased surface distortion for the nitric acid treated particles, therefore has to be found in an etching effect of the nitric acid treatment on the particles, leading to a rougher surface without significantly reducing the size of the particles.

High resolution transmission electron microscopy (HRTEM) images reveal evidence for this. Several particles of the nitric acid treated sample showed a very irregular and indented surface. Also, it seems that the crystalline order, approaching the edge of the particles, gets lost. Figure 28 shows three examples of the nitric acid treated - and potentially surface distorted - particles in HRTEM images. The dotted line in figure 28 suggests the originally intact surface of the particles and the solid line shows the remaining intact core. In between the two lines, i.e., at the surface region, it is suggested that the particles' crystalline order is distorted as well as indented due to corrosion.

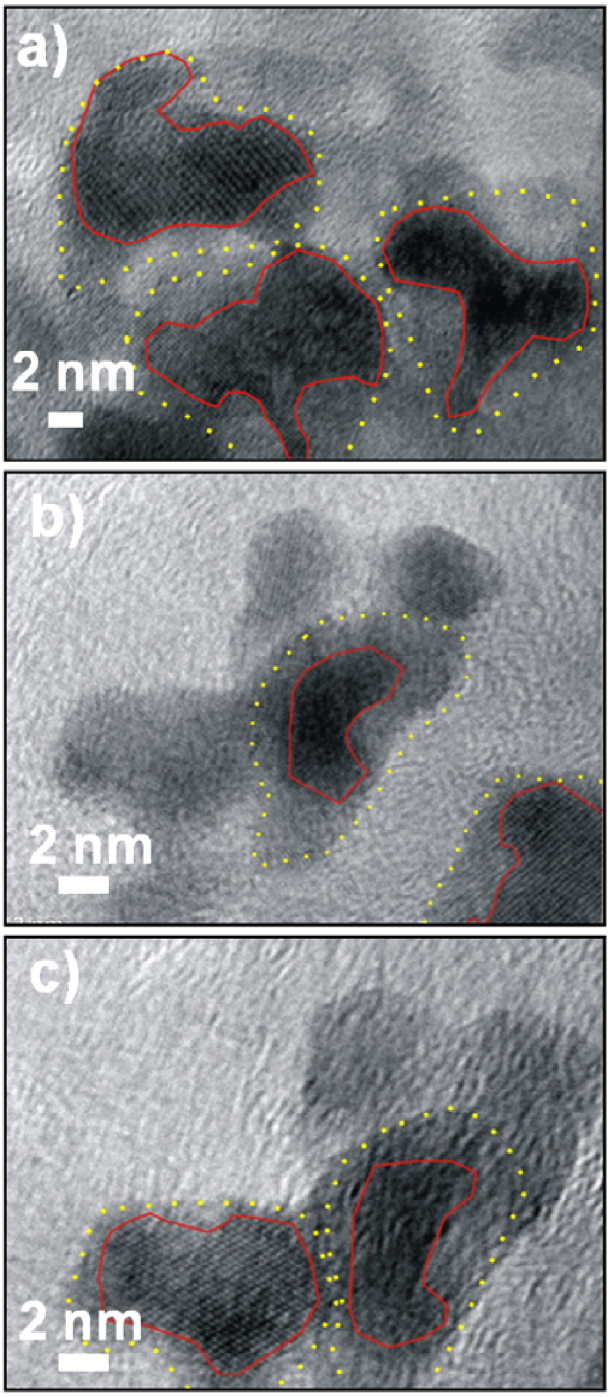

Figure 28 a-c): HRTEM images of nitric acid peptised nanoparticles suggest a distortion of the particles at the edge regions. Potentially distorted regions can be seen between the inner, intact particle part (solid circles) and the outer regions (dotted lines). Note that in figure b) and c) the particle in the middle is the same, just with a slightly different focus, however, it can be seen that the apparent distortion is not just an illumination effect due to different focus.

It can be concluded that with sophisticated X-ray absorption measurements it was possible to show that the coprecipitated particles are – as in many publications just claimed without further investigation – magnetite (Fe_3O_4), even though the synthesis was carried out

without extra prevention from an oxidising atmosphere. Even treatment with a potentially oxidising substance (nitric acid) does not lead to oxidation to maghemite (γ-Fe_2O_3), which is different to an assumption that is often made. Therefore, nitric acid can be used as a simple substance to de-agglomerate the magnetic nanoparticles in a first place for further surface modification processes without severely modifying or destroying the particles. Nevertheless, potential indications were found that nitric acid treatment increases the surface disorder of the nanoparticles probably due to the oxidative corrosive nature of nitric acid. However, it seems that the etching on the (sub)nanolevel stops at a certain point as the particles are not consumed by the acid within two months but rather keep their primary particle size. The potential surface roughening effect of nitric acid, thus the surface distortion might also explain the drop in (saturation) magnetisation that can be observed for magnetite particles that were treated with nitric acid. Thus, not the oxidation of the particles leads to a drop in magnetisation but the surface disorder of the particles which can be connected to a spin disorder.[295]

4.1.3 Functionalisation of iron oxide nanoparticle sols for stable dispersions

Nitric acid treated magnetite nanoparticles behave like a true ferrofluid. However, the electrostatically stabilised dispersion is very sensitive to pH shifts and to addition of salts or other chemicals as these changes immediately lead to agglomeration of the particles. Therefore, functional molecules were investigated to serve as stabilisers for the sol. Stable sols, insensitive to the addition of chemicals, are necessary if the nanoparticles shall be homogenously incorporated into a matrix, e.g. from silica, to form nanocomposite microparticles.

The same molecules as examined for in situ stabilisation experiments, namely amino acids (L-arginine, L-asparagine, L-glutamine), sugars (D-sucrose, D-glucose) and α-hydroxycarboxylic acids (DL-lactic acid, DL-malic acid, L-tartaric acid) were added to nitric acid stabilised nanoparticle sols. It turned out that none of the modifications, except for lactic and malic acid, could prevent agglomeration when the sol was added to ethanol or when the pH of the sol was increased (e.g. with ammonia solution). Lactic acid was selected to be further investigated and used as stabiliser within the following developments (*chapter 4.1.3.2*).

Furthermore, the superplasticiser polymer MELPERS4343 (trade name) was identified as promising to modify the nanoparticle surface. It was more closely examined (see the following *chapter 4.1.3.1*). The initial idea of using this stabiliser for nanoparticles originated from earlier works of Y. de Hazan (group of T. Graule).[296,297]

4.1.3.1 Polycarboxylate ether polymer (MELPERS4343) nanoparticle stabilisation[19]

MELPERS4343 (BASF, Germany) is a commercially available combpolymer used in cement industry as superplasticiser. It has molecular weights of 30 to 40 kg/mol consisting of a polyacrylate backbone and polyethylene oxide side chains with molecular weights of ca. 500 g/mol bound as an ester.[297] T. Graule's group used it for stabilising alumina nanoparticles by an electrosteric mechanism.[296] The polymer binds with its carboxylate backbone to the particles and the polyethylene oxide side chains lead to a steric stabilisation. In the following, stabilisation effects for the magnetite nanoparticles will be discussed. The as-precipitated nanoparticles will be addressed as SAMPLE1, their dispersion as DISPERSION1. Nitric acid peptised particles will be addressed as SAMPLE2 and the sol as DISPERSION2. Melpers4343 modified nanoparticles are assigned as SAMPLE3 and the respective sol DISPERSION3.

As described, the nitric acid stabilised sol is only stable at pH < 4, at higher pH values or higher electrolyte concentrations, e.g. NaCl, particles agglomerate again (figure 29 left). Thus, a further stabilisation of nanoparticles against growth, agglomeration, precipitation or gelation for dispersions at higher pH values, additions of electrolytes (increasing ionic strength) and changes of the dispersion medium, e.g. ethanol instead of water, was tried by reacting them with MELPERS4343. Dynamic light scattering (DLS) measurements (figure 30) confirm that the particle size is much smaller when the reacted dispersion was treated by ultrasound (DISPERSION3). Viscosimetry measurements as well as gel permeation chromatography on DISPERSION3 before and after ultrasonication, however, did not show any changes. Therefore, it is assumed that ultrasonication does not shorten the polymer chains but probably just uncoils them and improves the interaction of individual chains with the particles.

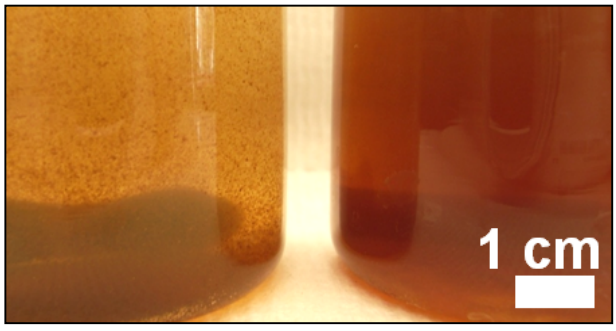

Figure 29: Sols after NaCl addition; left: DISPERSION2 (HNO_3 stabilised); right: DISPERSION3 (MELPERS4343 stabilised).

[19] This chapter has been published and is reused in this work by courtesy of Elsevier.
Original article: K. Mandel et al., *Colloids Surf., A*, 2011, **390**, 173.

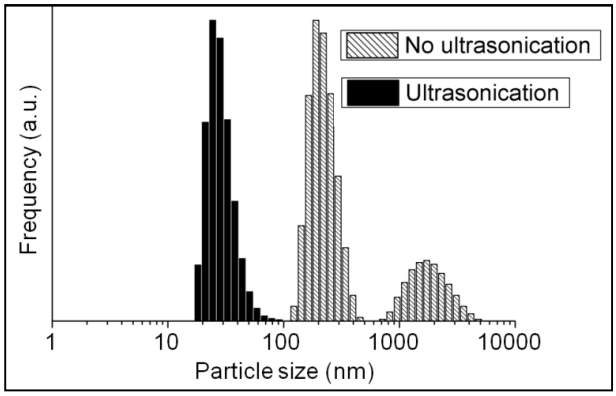

Figure 30: DLS measurements after addition of MELPERS4343 before and after ultrasonication (DISPERSION3).

The particles stabilised with MELPERS4343 (SAMPLE3) still show superparamagnetic behaviour (55 emu/g saturation magnetisation).

To test the stability of the MELPERS4343 functionalised particles, DISPERSION3 was a) titrated with aqueous solutions of sodium and also ammonia solution up to pH 7 and 10 and back to pH 2 and 4 with nitric as well as with hydrochloric acid. Also, DISPERSION3 was added b) to ethanol and to an ethanol / water / ammonia solution mixture. Other than the unstabilised particles of DISPERSION1 or the HNO_3 stabilised DISPERSION2, which flocculates at pH > 4, the MELPERS4343 stabilised particles in DISPERSION3 showed no agglomeration in any of the experiments a) and b). Always the same particles size (around 30 nm, as the ultrasonically treated particles in figure 30) was measured by DLS. Colloidal stability was also tested by addition of 1 g NaCl dissolved in 40 ml water to DISPERSION3. According to the DLVO theory, electrostatically stabilised particles flocculate when electrolytes are added.[259] But as shown (figure 29 right) the sol remains stable, a hint for a steric stabilisation mechanism.

The zeta potential of DISPERSION3 was measured in relation of pH by titrating with a 0.5 M NaOH solution from pH 2 to 13 (figure 31). The stabilised particles show a relatively low zeta potential (10 to -15 mV for pH from 2 to 6). But even at the isoelectric point at pH 3.7, no flocculation was observed and no particle size increase was detected with DLS. The combination of zeta potential and DLS studies allows the conclusion that at least in this pH range, particles are rather sterically than electrostatically stabilised. (The isoelectric point for the only HNO_3 stabilised particles (DISPERSION2) is at pH 6.6, where the sol flocculates).

Increasing the pH over 6, the magnitude of the measured surface potential increases absolutely by deprotonation of the COOH groups; thereby stabilisation may become more electrostatic. At pH > 12 the magnitude of the zeta potential decreases absolutely and particles start to agglomerate.

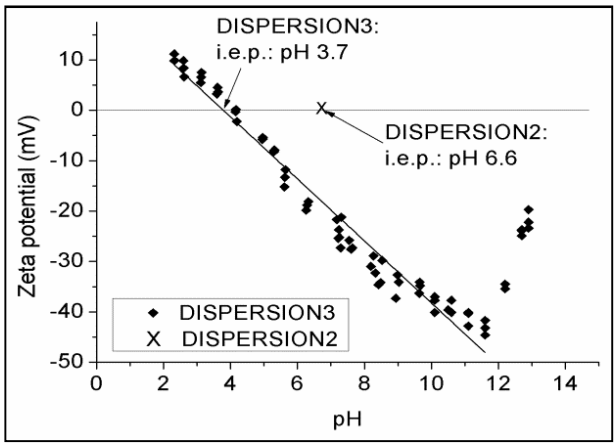

Figure 31: Zeta potential of the MELPERS4343 stabilised sol (DISPERSION3) as function of pH, isoelectric point for DISPERSION2 (nitric acid stabilised).

At pH > 12 hydrolysis of ester groups in MELPERS4343, which connect the polyethylene oxide side chains with the polycarboxylate backbone of the polymer, may occur. Hence steric stabilisation is weakened and electrostatic stabilisation by COO^--groups is not strong enough due to charge neutralisation by Na^+ ions. To prove the assumption of hydrolysis of ester groups, agglomerates formed at pH 13 were magnetically separated, washed with water and ethanol (three times each) and dried (NaOH treated SAMPLE3). IR spectra of these agglomerated particles (figure 32) show reduced intensities of bands for aliphatic C-H (2900 cm^{-1}) and C-O-C (1100 cm^{-1}) stretching vibrations[298] in comparison to spectra of non-agglomerated particles (SAMPLE3) and pure MELPERS4343. Furthermore, in the NaOH treated SAMPLE3, there is almost no evidence for the COOR (1250 cm^{-1}) band,[298] indicating that ester bonds are cleaved. Figure 32 also shows the spectrum of HNO_3 treated particles (SAMPLE2). The NO_3^- band at 1380 cm^{-1} [298] can be seen in all particle spectra indicating that these ions are coordinated to the particle surface in every case. Bands for the iron nanoparticles itself, around 580 and 430 cm^{-1},[299] are observed in SAMPLE2 and the NaOH treated SAMPLE3.

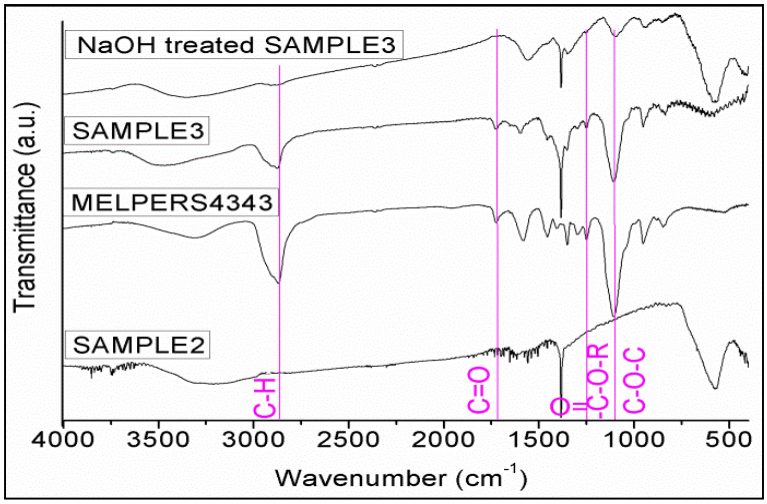

Figure 32: FTIR spectra of SAMPLE2 (nitric acid stabilised), SAMPLE3 (MELPERS4343 stabilised), NaOH treated SAMPLE3 and dried MELPERS4343.

From all these findings, a binding scheme of particle surface to nitrate ions and the stabilising polymer is proposed (figure 33). Hydrogen bridging bonds between the particles surface hydroxyls and carboxylic acid groups of the polymer and coordinative bonds (iron to nitrate ions) are assumed and remain unchanged. The carboxylic groups that coordinate to the particle surface are not deprotonated at higher pH; an indication is the finding of O-H stretching vibrations above 3250 cm^{-1}.[298] For pH 2 to 6 a steric stabilisation of the particles is suggested. From pH 6 to 12 deprotonation of free carboxylic acid groups leads to an electrosteric stabilisation. At pH > 12 ester bonds to polyether side chains are hydrolysed and steric stabilisation is lost. The negative surface charge will be neutralised by Na^+ ions. Electrostatic stabilisation is lost as well. Flocculation of particles starts.

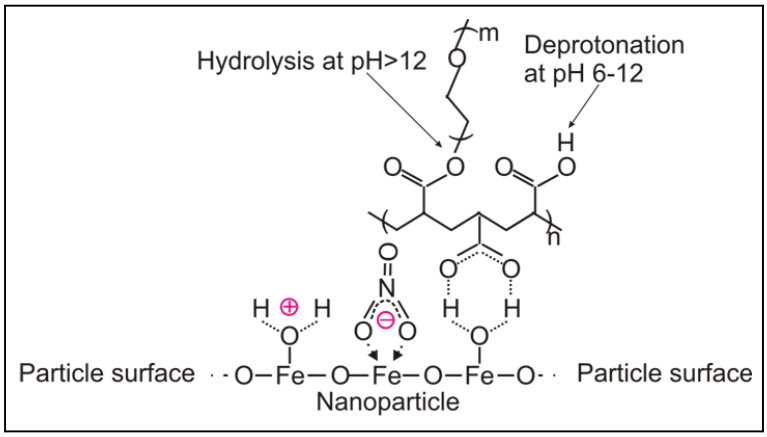

Figure 33: Proposed scheme for iron oxide particle surface with nitrate ions and stabilising polymer in different pH ranges.

4.1.3.2 Stabilisation of nanoparticles with lactic acid

Lactic acid was identified as promising nanoparticle stabiliser besides the polymer MELPERS4343. It is known that α-hydroxycarboxylic acids such as lactic acid can stabilise nanopaticle sols.[300] Nitric acid dispersed nanoparticles can be modified by the addition of lactic acid under stirring. Successful modification of the magnetic particles is indicated by the characteristic FTIR bands of lactic acid for the sample (figure 34).

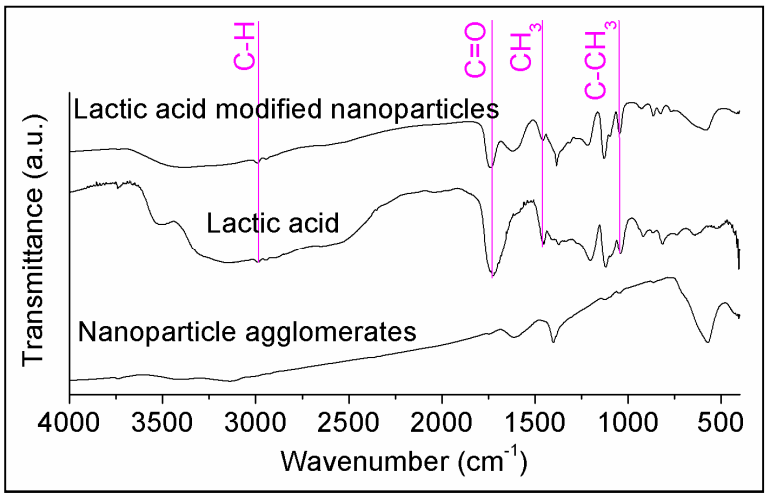

Figure 34: FTIR spectra of as-precipitated nanoparticles, lactic acid and lactic acid modified nanoparticles. Peak assignment according to [298].

A binding scheme of the particle surface to nitrate ions and the stabiliser lactic acid is proposed in figure 35. Lactic acid on the surface of nanoparticles might be considered as a certain kind of steric spacer that hinders agglomeration of approaching nanoparticles. Moreover, at elevated pH, the molecule might be negatively charged due to deprotonation which adds additional repulsion. The negative charge-up can be observed from zeta potential measurements where above pH 9, the particle's surface charge quickly drops to below -30 mV (see figure 42 *chapter 4.2.1*). Increasing the pH of a lactic acid stabilised nanoparticle dispersion e.g. by addition of ammonia (which will be necessary to catalyse silica formation to form composite particles in the next step), leads to a slight particle agglomeration. DLS measurements reveal hydrodynamic diameters of 500-1500 nm. Nevertheless, severe agglomeration after pH increase or addition of other chemicals is inhibited when the nanoparticles are lactic acid modified. As long as the dispersion of modified nanoparticles is stirred, it is acceptably stable and thus suitable as homogenous precursor dispersion for composite particle formation. Furthermore, the particles are well dispersible in ethanolic solutions and behave similar as in water.

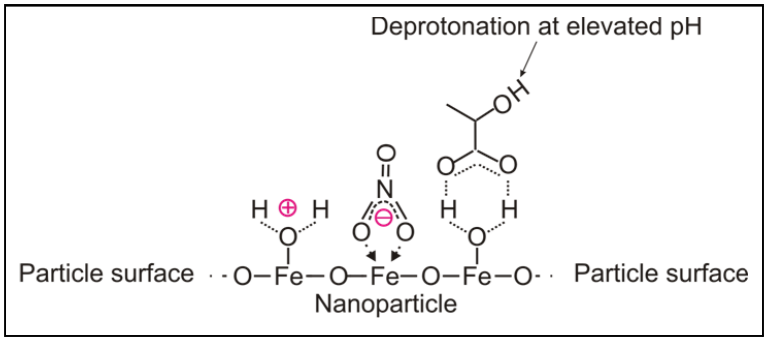

Figure 35: Proposed scheme for iron oxide particle surface with nitrate ions and lactic acid.

4.2 Nanocomposite microparticles[20]

For magnetic separation applications, the adsorber particles should be small, individually dispersible but also highly magnetically separable. Three options are available in principle when working with superparamagnetic nanoparticles: As-precipitated agglomerates can be applied as magnetic carriers, stabilised sols (ferrofluids) could be examined for separation applications or nanoparticles from sols are incorporated into a matrix to form well-defined composite particles that can be applied as magnetic carriers.

It has been known and accepted for a long time that ferrofluids, i.e., sufficiently concentrated sols containing well dispersed magnetic nanoparticles, are attracted by a magnet as a whole.[285] In principle, such ferrofluids can be used for separation applications. To benefit from the nanoparticle attributes (large surface to volume ratio, myriads of individual adsorber spots dispersed in water) but still achieve separation, it might be a solution to add aqueous ferrofluids to contaminated water (i.e. adding a water miscible sol). As such a ferrofluid is attracted by a magnet[301] (figure 36, left), it might act as a "comb" drawn through water containing impurities and adsorbing the target substances. In that case a magnetic *sol-liquid* separation is observed (figure 36, right).

On the other hand, the miscibility of (aqueous) sol and water could become a problem if the ferrofluid gets increasingly diluted by the water and eventually loses its magnetic behavior. Individual nanoparticles (of a few nm in size) are not separable as randomly directed Brownian forces, acting on these particles, are several orders of magnitude larger than directed magnetic forces of a handheld magnet (see *Appendix*).

[20] The introductory chapter (on ferrofluids) has been published and is reused in this work by courtesy of Elsevier. Original article: K. Mandel et al., Nano Today, 2012, **7**, 485.

Ferrofluid separation is a *sol-liquid* separation that seems to be possible, but *solid-liquid* separation is not possible (compare figure 36 left, the whole fluid is attracted; no solid particles are separated).

A water immiscible ferrofluid might be an alternative in which case however, for earning the benefits of nanosize, a nanoemulsion (better known as microemulsion) would have to be produced and the problem of an easy magnetic separability re-arises yet again.

Therefore, it is more practical to use micron sized agglomerates or composites of nanoparticles that are easily magnetically separable as the magnetic force acting on such a micro particle equals the sum of magnetic forces over all nanoparticles that are agglomerated to one larger particle.

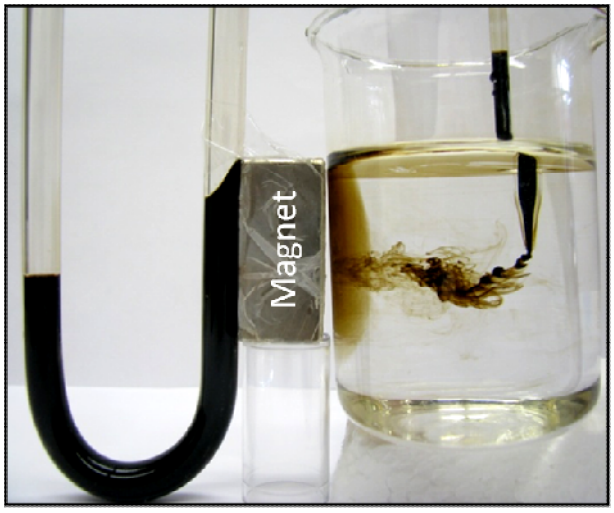

Figure 36: A water miscible ferrofluid (sol), i.e., an aqueous magnetic nanoparticle dispersion (c = 23 g/l, synthesis and discussion in *chapters 4.1.2.3* and *4.1.3.1*) is attracted by a magnet (left). Added to water, it is attracted by the magnet as a cloud (right). This might in principle be used as a "comb" to clean water from contaminants as the miscibility with contaminated water might promote the adsorption of hazardous substances to the nanoparticles in the ferrofluid. *Sol-liquid* separation can be achieved; however, *solid-liquid* separation of individual magnetic nanoparticles does not seem to be possible.

Although the agglomerated nanoparticles obtained from precipitation are micron sized and therefore can be easily separated by a handheld magnet, they cannot be used directly as magnetic carriers. The agglomerates are neither mechanically nor chemically stable and break into lumps of several hundred nanometers in size by ultrasonication or other mechanical shearing. At pH 3 or less, the particles redisperse completely.
To form magnetic carriers stable over a broad pH range, incorporation of the nanoparticles into a protective matrix, e.g. from silica, is therefore necessary.

4.2.1 Development of a superparamagnetic nanocomposite microparticle system[21]

Non-dispersed agglomerates of as-precipitated nanoparticles can be reacted with TEOS to form a silica coating, however, this resulted in the formation of undefined particle agglomerates of sizes between 1 to 200 µm. Figure 37a shows the product obtained by stirring the precipitated and washed nanoparticle agglomerates for ten minutes in ethanol with TEOS and an aqueous ammonia solution. EDX analysis confirms Si in the product (not shown). The particle size distribution is extremely broad ranging from 1 to 200 µm (figure 37b).

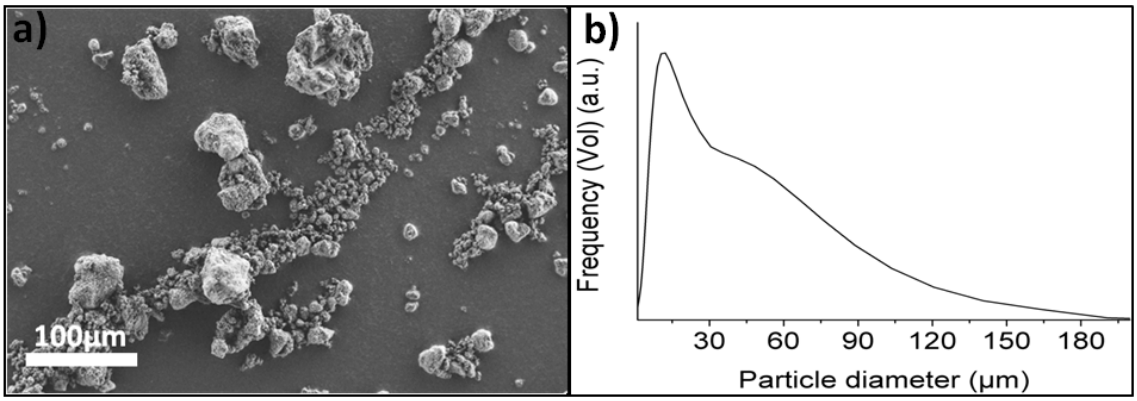

Figure 37: Composite microparticles: agglomerated magnetite nanoparticles in a silica matrix from TEOS. SEM image (a); size distribution measured with Fraunhofer diffraction (b).

Therefore, incorporation of stabilised and dispersed nanoparticles from a sol into a silica matrix (figure 38), rather than nanoparticle agglomerates, in order to obtain more well-defined composite particles, is preferred.

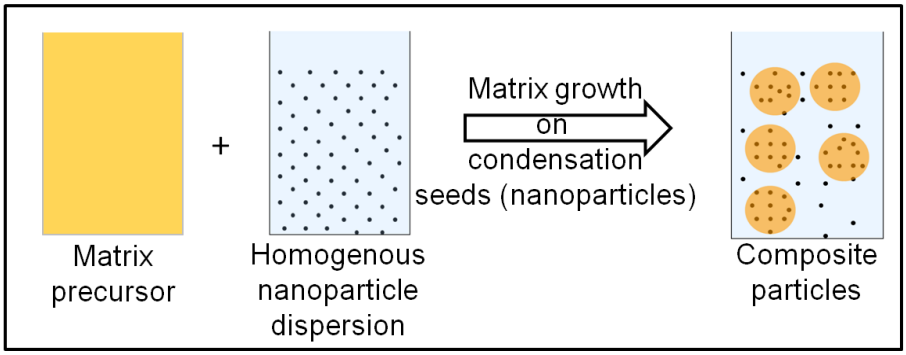

Figure 38: Processing scheme for well-defined composite microparticles formed from a magnetite sol.

[21] The major part of this chapter (except for the part on light microscopy) has been published and is reused in this work by courtesy of the American Chemical Society.
Original article: K. Mandel et al., *ACS Appl. Mater. Interfaces*, 2012, **4**, 5633.

Reaction of TEOS with stabilised nanoparticle sols (see *chapter 4.2.2*) is possible in low quantities (approximately up to 1 g of particles) however, TEOS reaction in larger reactors, designed to produce several grams of particles, leads to severe problems due to uncontrollable gelation. Moreover, for larger scale production, TEOS is a relatively expensive precursor.

Development of a silica matrix from sodium silicate (water glass)

To overcome the problems with TEOS, SiO_2 formation from sodium silicate solution (water glass) using ion exchangers and careful pH adjustment was applied for the coating of magnetic nanoparticles.[302-304] However, this process is sophisticated, slow, and hard to control. A solid silica was also reported to be obtained from simply precipitating water glass in acid.[305,306] This process is well known on an industrial scale where water glass is precipitated with sulphuric acid to obtain, after removing the residual salts by washing (and subsequent drying at elevated temperatures), stable, precipitated silica.[307,308] In this work, nitric acid, rather than sulphuric acid, was investigated for silica precipitation. The reason is that the magnetite nanoparticle sol (to which the silica is meant to be added to form nanocomposite microparticles) is stabilised in a nitric acid solution in the first place.
A silica precipitate is formed when water glass (sodium silicate solution) is added to diluted nitric acid. The filtered (using standard filter paper) precipitate, after having been washed thoroughly for three times with deionised water and subsequently vacuum dried under mild conditions (50 °C, approx. 0.1 mbar, 2 h), was analysed by solid-state ^{29}Si-NMR (figure 39a) and EDX (figure 39b). From NMR analyses it was found that 47 % of Si atoms have a Q3 configuration (three of the four Si bonds are Si-O-Si), 29 % are Q2 (two of the four Si bonds are Si-O-Si) and only 24 % are Q4 (all four bonds are Si-O-Si). The ratio Q4/Q3 is 0.5. Despite having washed the precipitate thoroughly, it contains a remarkable amount of sodium (EDX, figure 39b). Sodium might be attached to the many (possibly partly deprotonated) silanol groups present for the synthesised solid (Q2 and Q3 signals)[309]. Moreover, sodium might even be "*occluded*" as impurities inside the silica network.[310] With the washing steps, as they were performed on a lab-scale here (probably less effective than the washing of precipitated silica, done on an industrial scale in an optimised process with a filter-press)[308], it might not have been possible to thoroughly wash-off all the sodium from the solid, which is therefore left as residual.

Silica precipitation with the described method was carried out in the presence of stabilised and dispersed magnetite nanoparticles. Magnetic composite microparticles were obtained by this precipitation method (figure 39c and figure 39d left). However, unfortunately, these composite particles are destroyed at pH values above 9. The loosened magnetite nanoparticles can no longer be separated in the magnetic field gradient (figure 39d).

A potential explanation for this observation is an insufficient stability of the precipitated silica, i.e., dissolution of the silica particle matrix. The silica precipitate, obtained as described, might redissolve more easily due to the low content of thoroughly connected Si-O-Si (low content of Q4 configuration) and due to the high sodium content. A relation from this observation to another work might be drawn, where it was reported that water glass precipitated in sodium nitrate solutions yields an alkali-containing silica precipitate that is vulnerable to redissolution.[311,312]

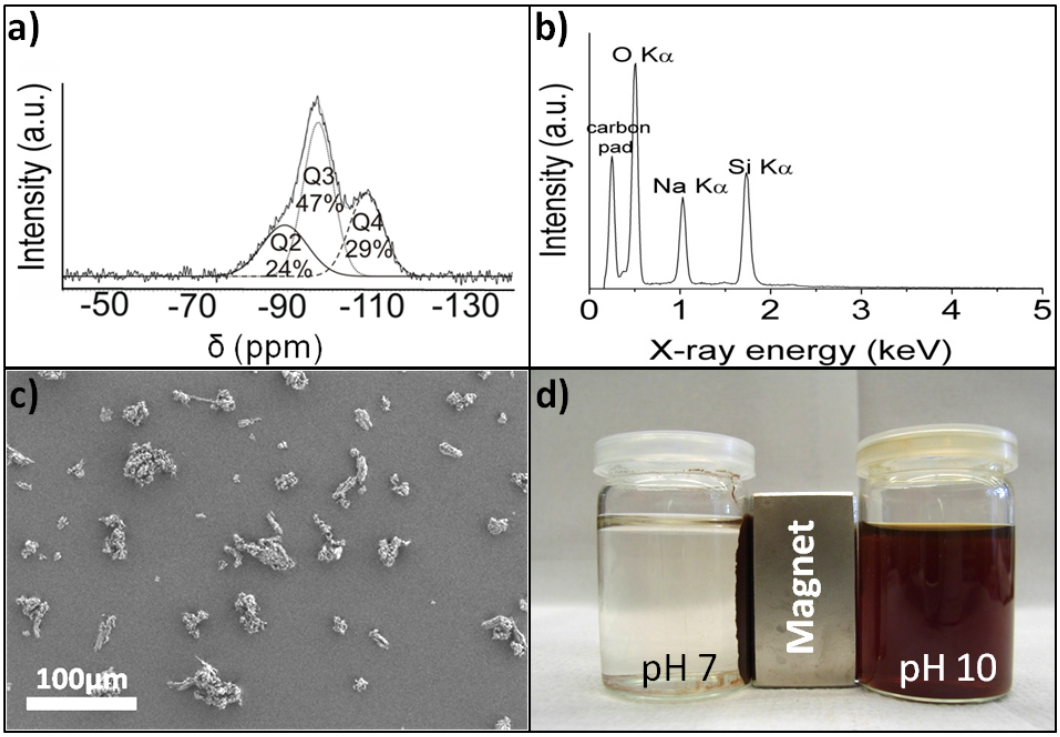

Figure 39: Silica precipitated from water glass solution with diluted nitric acid (a: solid state ^{29}Si-NMR spectrum; b: EDX analysis); magnetic composite microparticles (c: SEM micrograph) from this silica are not chemically stable and dissolve immediately by releasing nanoparticles at elevated pH (d).

Stable nanocomposite microparticles were formed using a modified precipitation process:

If an aqueous ammonia solution (pH 11.5) is added to a water glass solution (pH 12) a slurry forms and quickly redissolves if diluted or stirred. However, reasonably stable and more alkali-resistant silica is precipitated if the same reaction is performed in the presence of NO_3^- ions at RT. At a molar ratio of $NH_3 : HNO_3 : Na_2O{\cdot}3SiO_2 = 27 : 1 : 0.4$, a white, honeycomb-like porous solid forms (SEM; figure 40a). (Its specific surface area is 72 m^2/g (BET)). Analysis of the precipitate, washed and dried in the same manner as the acid precipitated silica, revealed that this time the sodium content within the solid is much lower (EDX analysis; figure 40b). The FTIR spectrum (figure 40c) shows no absorbance for NO_3^- or NH_4^+ ions (i.e., no ammonium or nitrate ions are adsorbed on the silica). Only

negligible amounts of nitrogen (0.43 wt%) and sodium (< 3 wt%) could be detected by ICP-OES. Solid-state ^{29}Si-NMR (figure 40d) analysis results in a Q4:Q3:Q2 ratio of 33:10:1. The silica is fairly stable against dissolution even above pH 9. A silica with an even higher fraction of Si with Q4 configuration is obtained for a precipitation at 80 °C. The obtained solid is composed of many granular-like structures (SEM; figure 40e**)**. The Q4:Q3 ratio increases to 4, and no Q2 groups are present (^{29}Si-NMR; figure 40f). The specific surface area is 110 m^2/g. The temperature increase apparently promotes the formation of siloxane (Si-O-Si) bonds, thereby promoting the SiO_4 tetrahedron network formation.

Some assumptions about the reaction mechanism leading to more stable silica when applying the modified process, are discussed in the following paragraph.

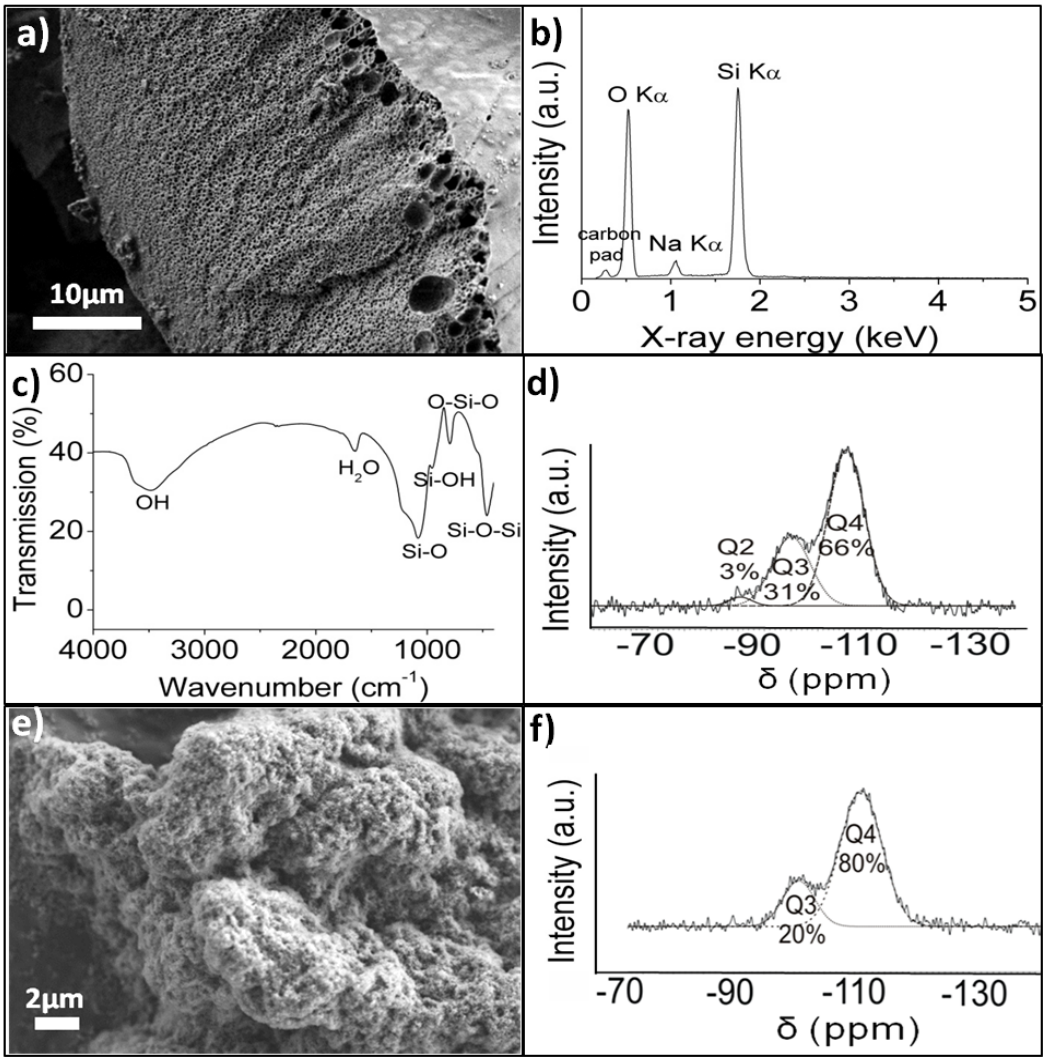

Figure 40: Foam like, stable silica precipitated from a sodium silicate solution with aqueous ammonia in presence of nitrate ions at RT (a: SEM micrograph; b: EDX analysis; c: FTIR spectrum; d: solid state ^{29}Si-NMR spectrum); Silica precipitated with the same chemicals at 80 °C (e: SEM micrograph; f: solid state ^{29}Si-NMR spectrum; EDX and FTIR equal to b) and c)).

Hypothesis on the formation of a solid silica network from water glass solution

Although OH^- groups in an alkaline solution catalyse Si-O-Si condensation reactions (see *chapter 3.3.2*), the promoted deprotonation of silanol groups also increases the negative surface charge of small silica colloids that thereby repel each other,[263] thus hampering further condensation to form crosslinking Si-O-Si bonds. The conditions at higher pH values are complex and it cannot be concluded easily that elevated pH values promote condensation, gelation and precipitation.[313]

However, as in the modified process, several ions are present in the reaction solution, namely nitrate anions, ammonium cations (and sodium cations from the sodium silicate), the ionic strength of the solution is high. The mixture of these ions of positive and negative charge shrink the diffuse double layer around the first silica colloids that form and thereby decrease their mutual repulsion.[314] Thus, the colloids can approach each other more easily and more closely, i.e., their collision is more likely, which is a precondition for the formation of Si-O-Si linkages.[264] Reaction time is drastically shortened, Si-O-Si bond formation is promoted, yielding more Si with Q4 configuration. Elevated temperatures also furthermore promote the condensation reactions.
Thus, a silica network, of which the formation is catalysed by OH^-, can form in presence of electrolytes, to which the nitrate contributes as anion. Due to the highly cross-linked silica Q4 network that thereby forms, less (deprotonated) silanol groups, that are potential spots for sodium to attach, are present at the formed solid. Therefore, silica precipitated with this modified process contains less sodium after washing (figure 40b) and overall is more stable.

Formation of stable superparamagnetic composite microparticles

This process of precipitating a solid silica network can be exploited to synthesise stable superparamagnetic composite microparticles in a simple, fast, and inexpensive way.

The magnetite sol prepared with the dispersing agent HNO_3 and carboxylic acid (lactic acid) stabiliser is mixed with aqueous ammonia. Thereby, pH of the solution rises from 1 to 11.5. Agglomerates, sized up to 1-2 µm (DLS) form if the dispersion is left without stirring. However, as long as the mixture is in motion, i.e. stirred, the sol stays stable and homogenous. After heating to 70 °C, a water glass solution is added under stirring. By precipitation of SiO_2, composite microparticles are formed. The product is separated magnetically after 5 min and washed with water. Up to 100 g of product has been synthesised in one batch.

The composite microparticles show a filigree structure (SEM micrographs: figures 41a and 41b). As shown by TEM (see figures 41c and 41d), a dense covering of SiO_2 surrounds and

protects the magnetite nanoparticles thoroughly. STEM-EDX analysis confirms a mixture of silica and iron oxide inside the microparticle and solely SiO_2 at the surface region. That the surface of the microparticle consists only of silica can also be demonstrated by measurements of the zeta potential in dependence of pH. The results are the same as for pure silica (isoelectric point i.e.p at pH 2)[315] and quite different from those of stabilised magnetite nanoparticles (i.e.p at pH 8; figure 42a). The composition of the microparticle is also confirmed by XRD, FTIR and EDX analyses (figure 42b-d) and by chemical analysis (ICP-OES: 45 wt% Fe_3O_4, 50 wt% SiO_2, 5 wt% water and organic components). On heating the particles to 600 °C, only water molecules are released, and no indication of chemical reactions was found (DTA-TG-MS, see figure 42e-f). Particle size distribution is 1-50 µm with a mean diameter of 20 µm, which was measured by Fraunhofer diffraction in an aqueous suspension (figure 41e). The intrinsic superparamagnetism of the magnetite nanoparticles was maintained in the microparticles (figure 41f). Saturation magnetisation of the composite particles drops to 30 emu/g from 66 emu/g of as-precipitated nanoparticles (continuous synthesis). A magnetisation of 30 emu/g for a micron sized particle is higher than for most composite particle systems published and allows a fast and facile magnetic separation, an inherent precondition for commercial applications.

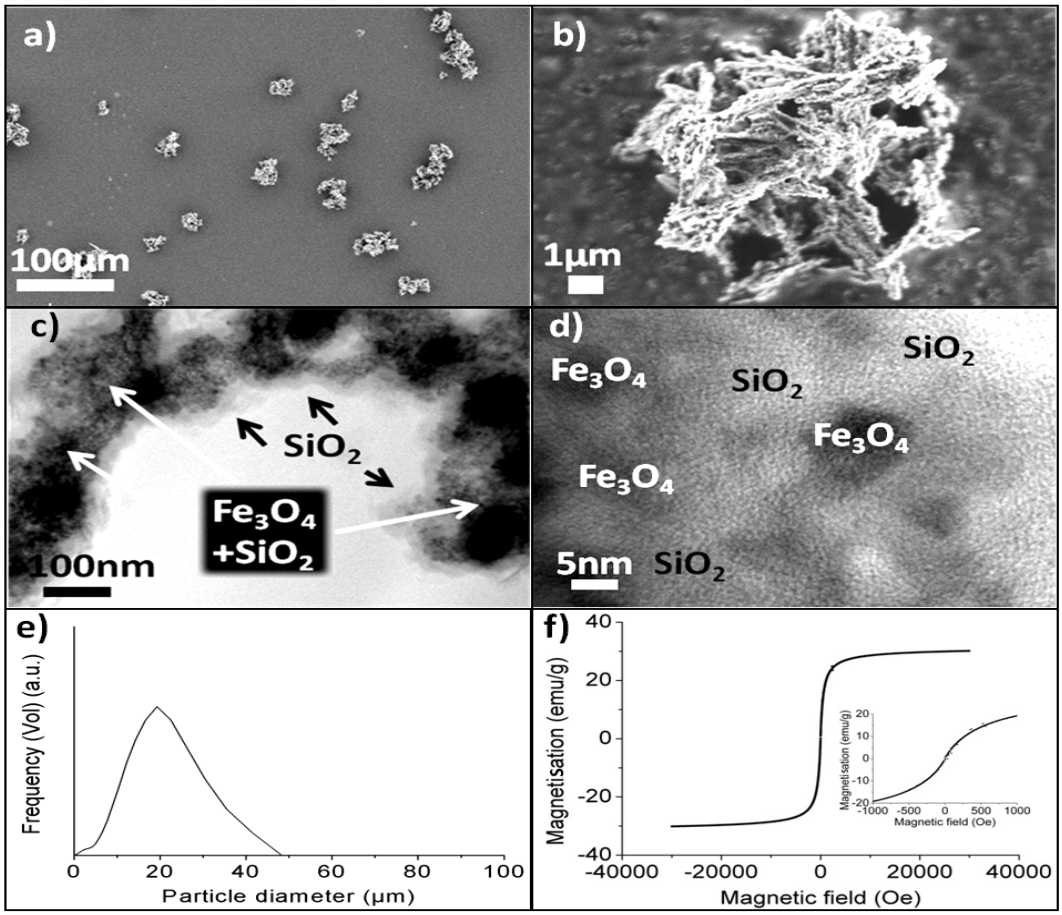

Figure 41: Superparamagnetic composite microparticles (a, b: SEM micrographs; c, d: TEM micrographs and EDX analysis; e: Fraunhofer diffraction on an aqueous suspension; f: VSM measurements).

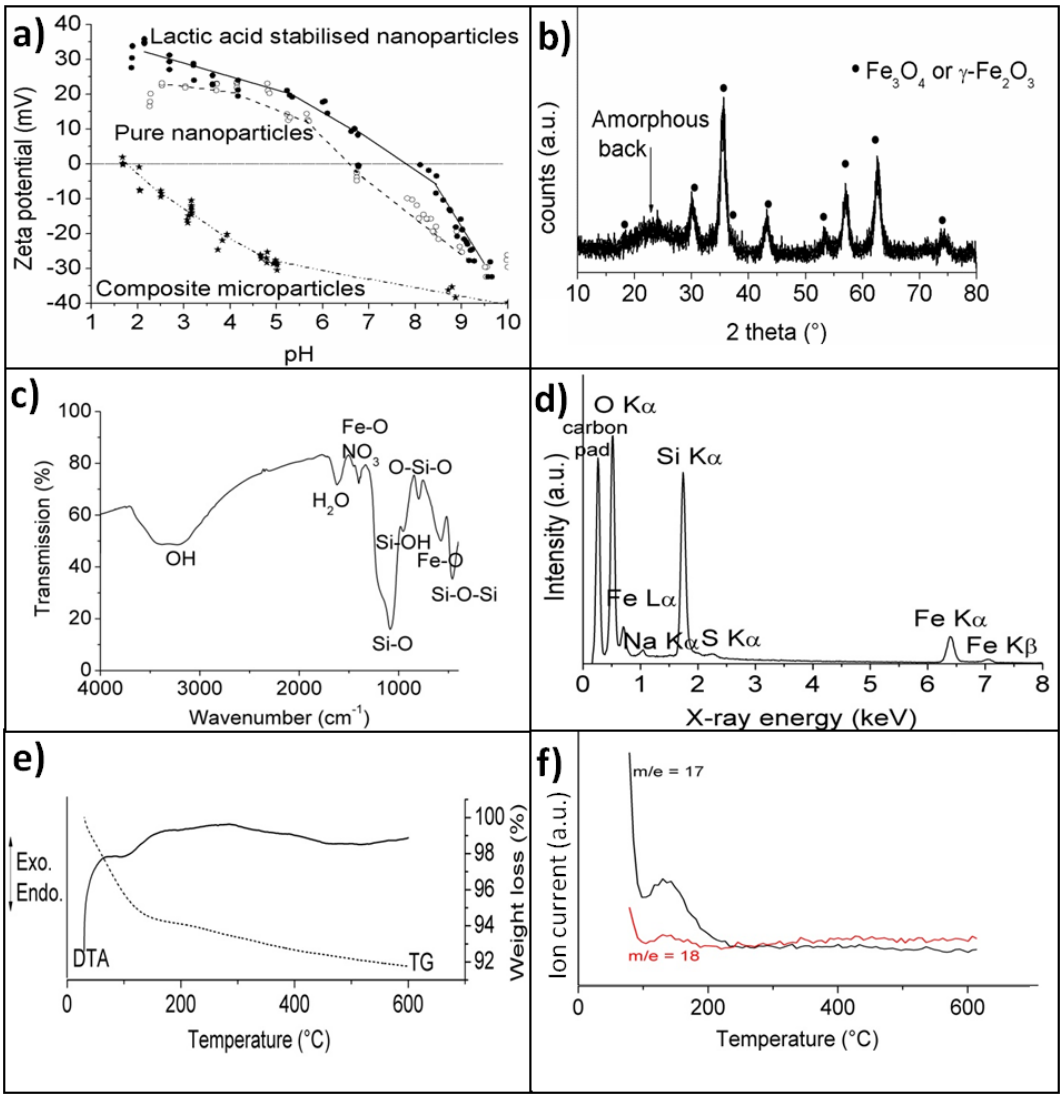

Figure 42: Superparamagnetic composite microparticles (a: Zeta potentials versus pH for magnetite nanoparticles, stabilised nanoparticles and composite microparticles; b: XRD; c: IR spectrum; d: EDX analysis, e: DTA-TG and f: mass spectrometry from released substances indicating only water release).

The superparamagnetic composite microparticles are easily separated from an aqueous suspension with a permanent magnet within 10 s (figures 43a-c). The necessity for engineering micrometer-sized composite particles in order to obtain a magnetically separable particle system becomes evident by comparison to dispersed magnetite nanoparticles that behave like a ferrofluid and cannot be separated from the liquid (figure 43d). The advantage of the present system over larger magnetite particles is demonstrated in figure 43e, where severe magnetic agglomeration of 500 nm sized magnetite particles, which do not possess the nano-effect of superparamagnetism, i.e., have a remanent magnetisation, renders it impossible to properly redisperse the particles once they have been magnetised. The superparamagnetic composite particles, however, can easily be redispersed with just a gentle shake to a fairly stable suspension (figure 43f).

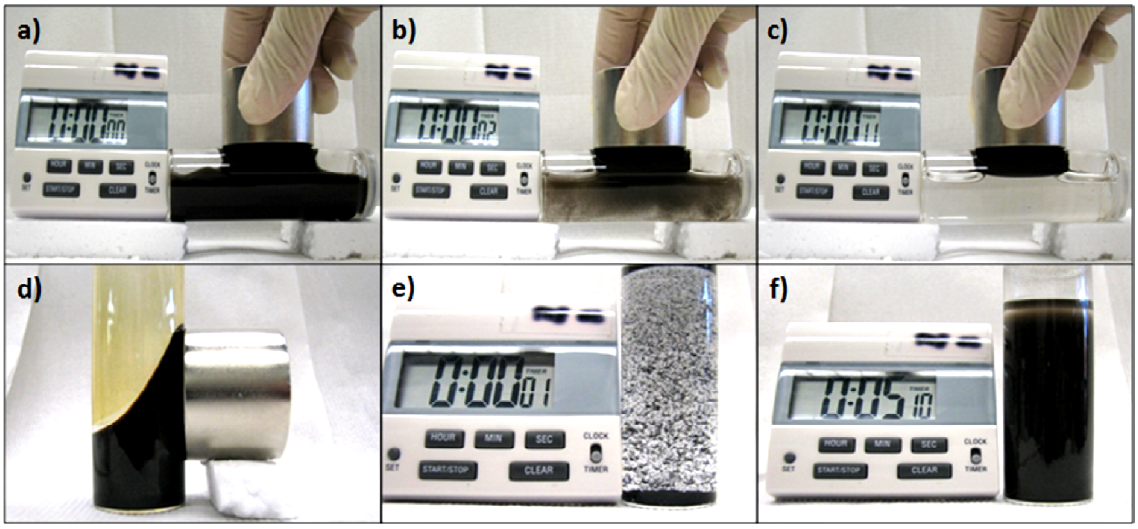

Figure 43: Magnetic separation of superparamagnetic nanocomposite microparticles (a–c). Individual nanoparticles cannot be magnetically separated from a fluid (d). Larger particles of magnetite bear remanent magnetisation and immediately agglomerate if tried to redisperse in water (e). Redispersion of superparamagnetic nanocomposite microparticles does not face the problem of magnetic agglomeration (f).

Light microscopy observations (figure 44) reveal that as soon as composite particles in water are exposed to an external magnetic field gradient, they start to arrange and align in this magnetic field. Chains of particles immediately self-assemble (figure 44, images b-c), before the particles actually start to move towards the external magnet (figure 44, image d). This chain formation is likely to improve the magnetic separability, as the magnetic moments of several composite particles sum up, while the viscous drag probably does not increase in the same way. The drag force acts on the front of the moving object and this front size hardly increases, as the chain arranges with its length along the direction of movement.

The chemical stability of the composite microparticles was tested by stirring in an aqueous suspension (1.2 wt%) at pH 2 (HCl) and 12 (NaOH) for 24 h at RT. After magnetic separation of the particles, the iron and silicon contents were analysed by ICP-OES of the resulting clear, colourless solution. Almost no release of iron was detected in relation to pH. A total of 0.16 wt% at pH 2 and 0.04 wt% at pH 12 of iron were found with respect to the total particle mass and 0.14 wt% at pH 2 and 15 wt% at pH 12 of silica, respectively. Stability against dissolution is slightly better than for silica synthesised from TEOS (18 wt% silica dissolved at pH 12 under the same conditions). It is well known that silica dissolution increases above pH 10.[316] Despite this partial dissolution magnetic separation of the microparticles was possible. The excellent acid resistance of the microparticles ensures that the magnetite nanoparticles are well protected at low pH. Even when particles were stirred for 2 h in concentrated HCl (36 wt%), no changes of the particle sizes were

detected by Fraunhofer diffraction (not shown). The mechanical stability of the microparticles was tested by a 1 h ultrasound treatment of a 2 wt% suspension. Despite their filigree structure, the mean particle size increased only slightly, possibly by particles hooking together, and no breakage of the particles was observed by Fraunhofer diffraction (not shown).

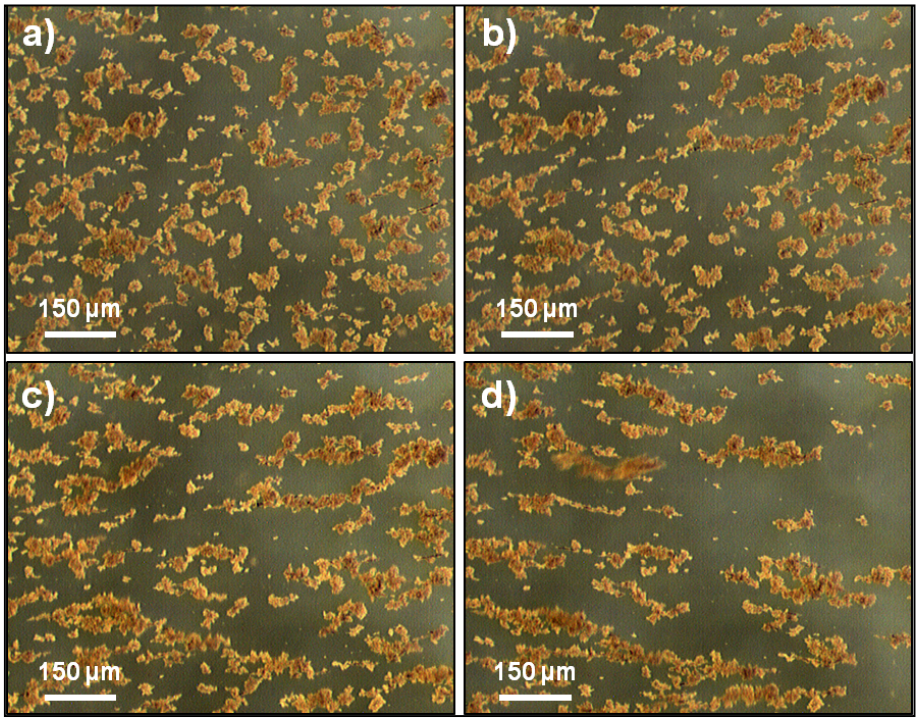

Figure 44: Light microscopy images of composite particles in water: Without an external magnetic field (a); while approaching a magnet from the left (b, c); moving chains of particles (image d, taken 1 second after image c).

A further advantage of the microparticles for any adsorption application is their large specific surface area of around 75 m^2/g (BET). Hence, because of the filigree structure of the nanocomposite, the particles' specific surface area comes close to the surface area of the 10 nm magnetite nanoparticles (100 m^2/g).

The large surface area of the microparticles makes them very promising candidates for modifications, necessary for specific adsorption applications. Table 2 summarises the characteristics of the nanocomposite microparticle system.

Table 2: Characteristics of the nanocomposite microparticle system.

Magnetic material	Superparamagnetic magnetite nanoparticles ~10 nm; continuous synthesis
Matrix confining nanoparticles	Amorphous SiO_2
Matrix synthesis	Precipitation at 70 °C from water glass solution with ammonia in presence of NO_3^- ions
Content of magnetic nanoparticles	45 wt%
Mean microparticle diameter	20 µm
Saturation magnetisation	30 emu/g
Specific surface area (BET)	75 m^2/g
Stability	Thermal: up to 600 °C (max. tested) Mechanical: ultrasound stable Chemical: pH 0 -12

4.2.2 Nanoparticle stabilisation effects on clustering and magnetics in nanocomposites[22]

This chapter describes the influence of different stabilisations and distributions of nanoparticles in a silica matrix on the magnetic properties of such composites. The magnetic effects were studied by means of zero field cooled / field cooled (ZFC / FC) measurements

For this study, the coprecipitated superparamagnetic magnetite nanoparticles were dispersed with nitric acid and stabilised with MP (Melpers4343) or LA (lactic acid). Nanoparticle sizes are independent of stabilisation.

Modification of the magnetite nanoparticles with a silica matrix, to form nanocomposite microparticles, was done by two chemical routes. To this effect, two different silica precursors were used: TEOS (tetraethoxysilane) and SS (sodium silicate / water glass). Four types of nanocomposite microparticles resulted:

- MPTEOS = MP stabilised nanoparticles in a TEOS based silica matrix
- MPSS = MP stabilised nanoparticles in a SS based silica matrix
- LATEOS = LA stabilised nanoparticles in a TEOS based silica matrix
- LASS = = LA stabilised nanoparticles in a SS based silica matrix

[22] This chapter has been published and is reused in this work by courtesy of Elsevier.
Original article: K. Mandel et al., *J. Magn. Magn. Mater.*, 2013, **331**, 269.

SS based nanocomposites can be produced in large scale, TEOS based composites suffer from uncontrolled gelation when syntheses are performed in larger reactors (for instance exceeding volumes of 500 ml).

Figure 45 shows SEM images of the four particle types. The iron oxide content analysed by ICP-OES in weight% for the samples is 32 wt% (MPTEOS), 35 wt% (LATEOS), 46 wt% (MPSS) and 42 wt% (LASS). A fraction of 3-8 wt% in each sample originates from residual water and organic molecules, while the remaining mass fraction is silica.

Particle size distribution measured with Fraunhofer diffraction for all sample types is in the range of 1-60 µm (figure 46).

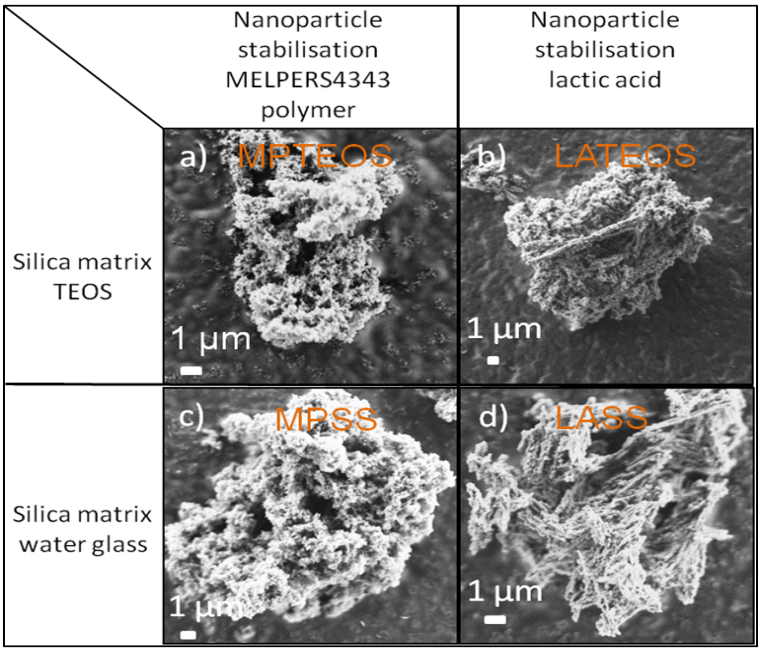

Figure 45: SEM images of nanocomposite particles: a) MPTEOS, 32 wt% Fe_3O_4, b) LATEOS 35 wt% Fe_3O_4, c) MPSS, 46 wt% Fe_3O_4, d) LASS, 42 wt% Fe_3O_4.

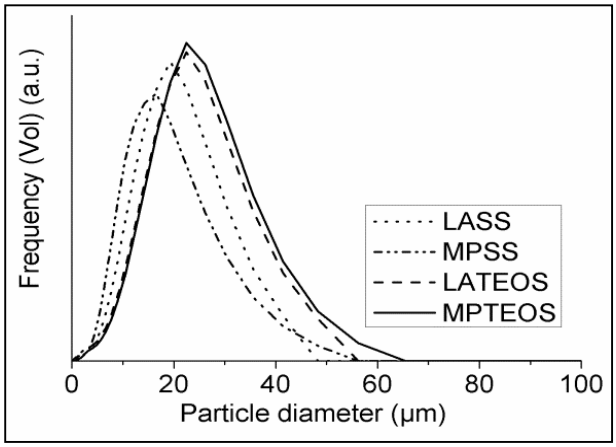

Figure 46: Size distribution of the composite particle systems MPTEOS, LATEOS, MPSS and LASS.

Morphologies of composites with MP stabilised nanoparticles seem to be somewhat more filigree than those with LA stabilisation, independent of the silica matrix. The iron oxide contents in the TEOS derived samples are approximately 10 wt% lower than with SS. The weight content of nanoparticles within the composite does not correlate to the nanoparticle stabilisation. In TEOS derived samples, LA stabilised nanoparticles are incorporated at a slightly higher amount (3 wt%) than MP stabilised nanoparticles. In SS samples, it is vice-versa. MP stabilised nanoparticle amount is 4 wt% higher.

All particle systems (the as-precipitated and the stabilised nanoparticles, as well as the composite particles) behave superparamagnetically at room temperature (figure 47: *M* versus *H* at moderate field). The saturation magnetisation drop (in emu/g; not visible in figure 47) compared to as-precipitated magnetite nanoparticles is proportional to the content of non-magnetic mass in the composite particles (which reduces the measured emu/g due to increased mass) within the range of errors (see *experimental section chapter 7.4*). At 60 K, the as-precipitated and the composite particles show a hysteretic magnetisation behaviour, indicating that the superparamagnetic relaxation of the particles is blocked (within the time of measurement) due to the low thermal energy available. Figure 48 shows the hysteresis of the as-precipitated nanoparticles and exemplarily of two samples of the composite particles. For convenience, the magnetisation for each sample in figure 48 was normalised by the respective system's saturation magnetisation at 60 K. Hystereses measurements (figure 47 and 48) were conducted with 100 Oe/s and as detailed analyses with 5 Oe/s and yielded the same curves.

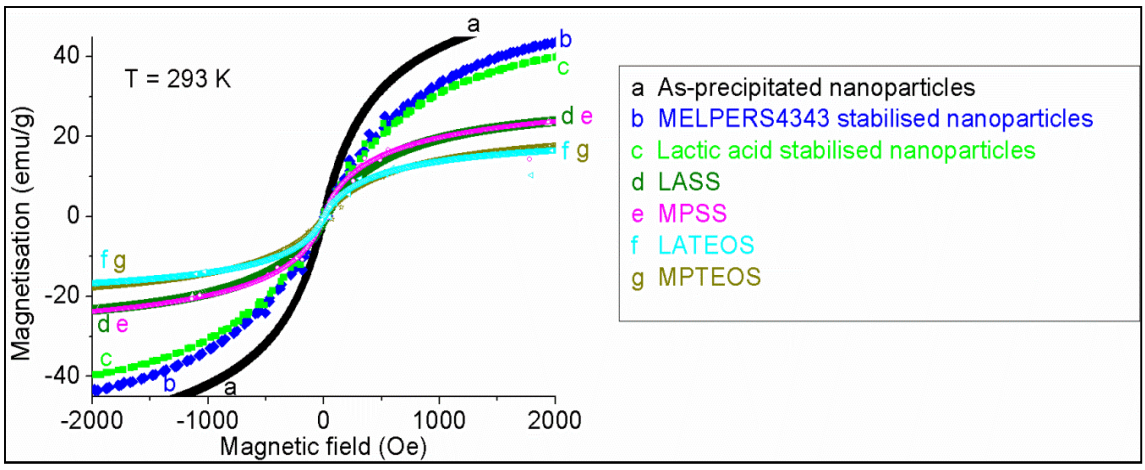

Figure 47: Magnetic curves of all particle systems studied at room temperature (293K).

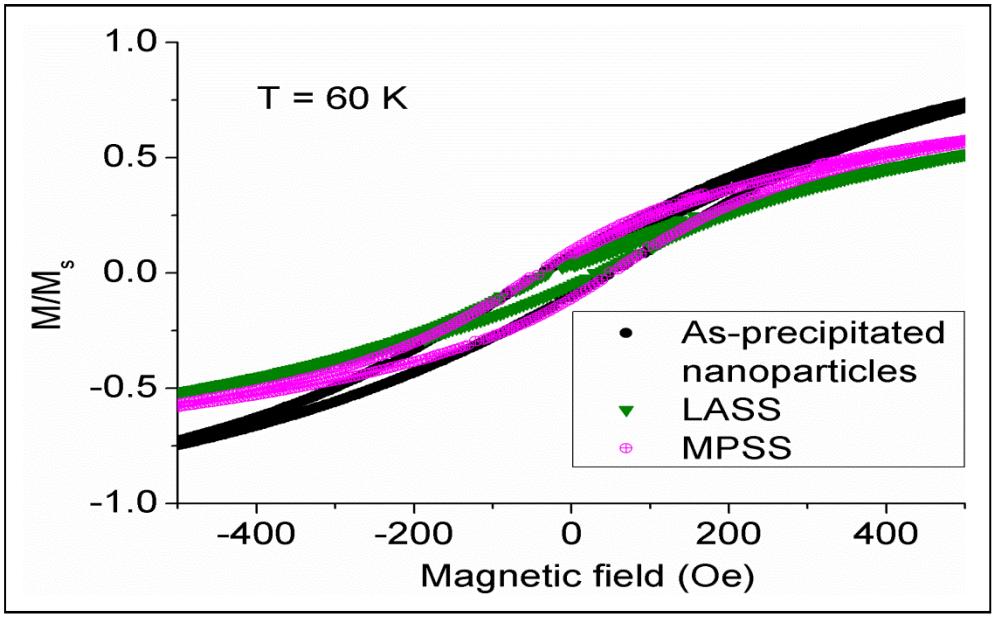

Figure 48: As-precipitated nanoparticles and nanocomposites show a hysteretic magnetic behaviour at 60 K. The magnetisations are shown as normalised to the respective saturation magnetisations to facilitate a comparison of the samples.

ZFC and FC measurements (figure 49) were carried out on vacuum-dried, as-precipitated and stabilised (MP and LA) nanoparticles. For the as-precipitated nanoparticles T_B and T_{ir} of (255 ± 10) K were measured ($\Delta T_{ir,B} \approx 0$). For both samples of stabilised (MP and LA) nanoparticles, ZFC and FC curves from 75 to 300 K are superimposed as is typical for superparamagnetic systems. M decays with increasing T for ZFC and FC experiments.[202,203] The blocking temperature of these particles is below 70 K.

The blocking temperature T_B of nanoparticles without mutual interaction (intrinsic $T_B < 70$ K) has to be determined in a dispersed state, e.g., in a sol after surface modification. Recently,[203] intrinsic T_B was found to be as low as 40 K for dispersed (individual) particles (magnetite, 8 nm) confined in a wax for measuring purpose.

ZFC and FC measurements on the four types of nanocomposite microparticles are shown in figure 50. In all cases, T_B is lower than for the as-precipitated nanoparticles (255 K) but higher than for LA or MP stabilised nanoparticles (< 70 K). This indicates that nanoparticles in silica matrix are less interacting than agglomerated, as-precipitated nanoparticles in direct contact to each other. On the other hand, the matrix-confined particles show a non-negligible dipole-dipole interaction as their blocking temperatures (125 to 210 K) are remarkably higher than the T_B of the stabilised nanoparticles (< 70 K).

Assuming that an increased T_B is related to a stronger dipole-dipole interaction,[212-215] the interaction intensity order is:
as-precipitated nanoparticles > nanoparticles in composites > stabilised nanoparticles.

The four types of composite particles also differ in T_B. MP stabilisation lowers T_B by 43 to 85 K in comparison to LA stabilisation. According to the mainly accepted theory this indicates stronger dipole-dipole interaction of the LA stabilised nanoparticles. As discussed earlier, the content of nanoparticles within the composites does not depend on stabilisation. Therefore, it can be excluded that the shift of T_B in the samples is related to the magnetite concentration in the composites.

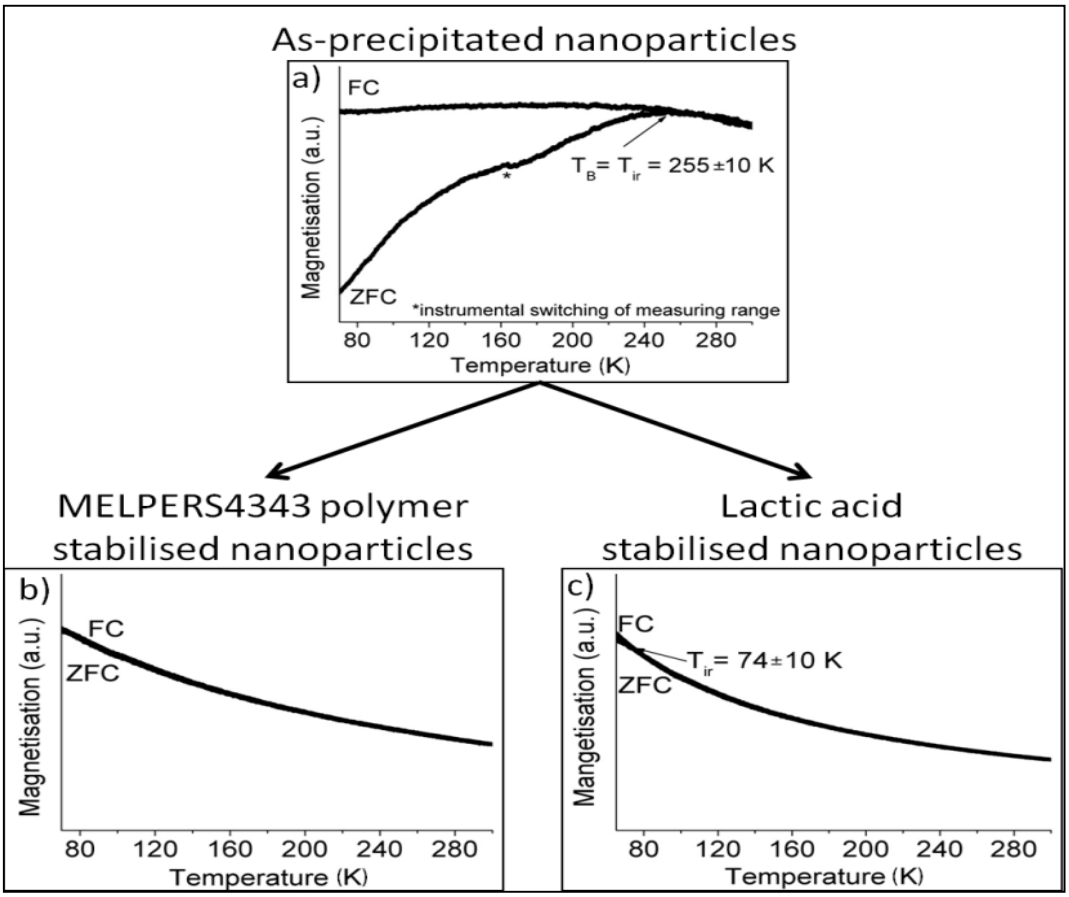

Figure 49: ZFC and FC measurements of magnetite nanoparticles: a) as-precipitated, b) MP stabilised, c) LA stabilised (splitting of the ZFC / FC curves at (74±10) K).

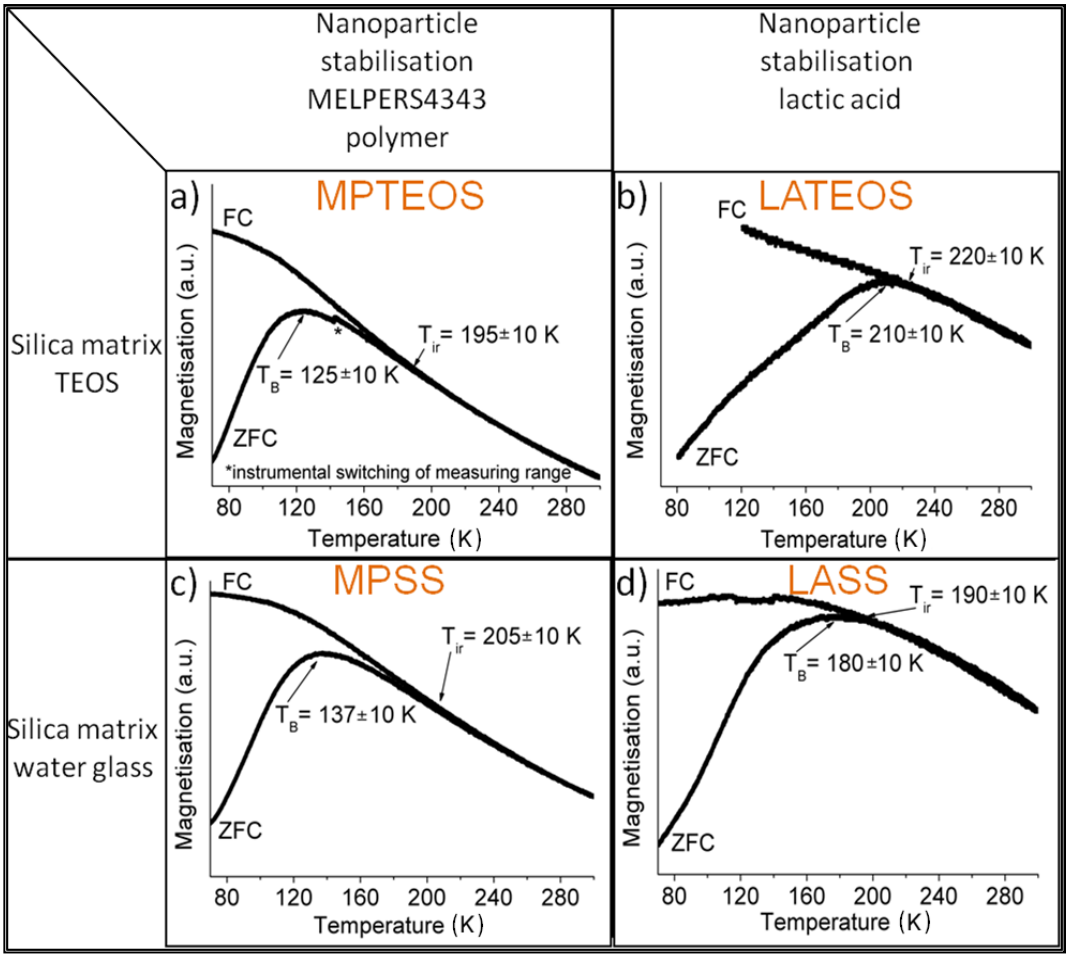

Figure 50: ZFC and FC measurements of nanocomposite particles: a) MPTEOS, 32 wt% Fe_3O_4, b) LATEOS 35 wt% Fe_3O_4, c) MPSS, 46 wt% Fe_3O_4, d) LASS, 42 wt% Fe_3O_4.

Figure 51 shows TEM cuts of the four composite particle systems. Obviously, the stabilisation of the nanoparticles (MP or LA) is most important for their distribution in the silica matrix. LA stabilised particles are packed in large clusters (sizes of several hundred nm) in the matrices. MP stabilised nanoparticles are prevailing as much smaller clusters (approximately 10 to 200 nm). Less agglomeration as for the MP stabilised nanoparticles is in accordance with a lower T_B (figure 50). The stabilisation does not influence the content of nanoparticles but their distribution in the composites.

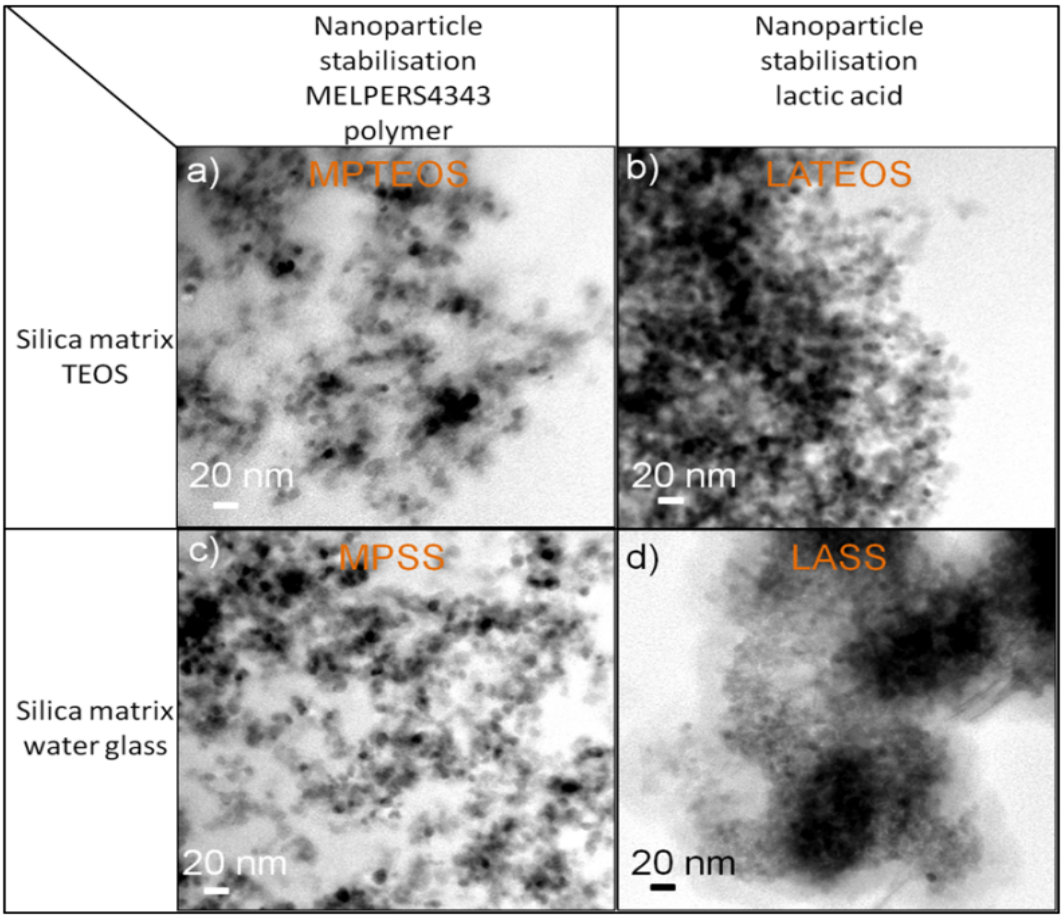

Figure 51: TEM images (bright field: dark spots are nanoparticle clusters. Fringes of silica (brighter grey) are partly visible) of nanocomposite particles: a) MPTEOS, 32 wt% Fe_3O_4, b) LATEOS 35 wt% Fe_3O_4, c) MPSS, 46 wt% Fe_3O_4, d) LASS, 42 wt% Fe_3O_4.

$\Delta T_{ir,B}$ equals zero (within the accuracy of measurement) for LATEOS and LASS (figure 50). $\Delta T_{ir,B}$ is around 70 K for MPTEOS and MPSS. Usually large values for $\Delta T_{ir,B}$ are attributed to a broad size distribution of nanoparticles.[200,210,211] Here, however, nanoparticles in all samples have the same size distribution. Thus, a higher $\Delta T_{ir,B}$ has to be interpreted in terms of a stronger magnetic dipole-dipole interaction.[210,218] But then, T_B should also be higher for MPTEOS and MPSS which, however, is not the case.

A possible explanation is in the different cluster sizes of nanoparticles in the samples. An increasing number of nanoparticles in a cluster intensifies the interaction and shifts T_B to higher values. A broader size distribution of clusters leads to a wider splitting of T_B and T_{ir} ($\Delta T_{ir,B}$ increases), because the clusters behave like nanoparticles of different sizes. This is illustrated in figure 52 by TEM micrographs that are generic for MPSS and MPTEOS composite particles. Clusters of varying numbers of nanoparticles are distributed in size over a wide range (from approximately 10 to 200 nm).

But above a certain cluster size (e.g. > 100 nm), distribution effects on $\Delta T_{ir,B}$ vanish. Clusters can be considered as a bulk material in which each nanoparticle is surrounded by so many others that dipolar interaction is at a maximum and thus it does no longer have any measurable effect when the cluster sizes are different (i.e., once the clusters are really large, different sizes of such large clusters cannot be resolved by ZFC / FC measurements anymore and the nanoparticle ensembles yield a signal equal to what would be obtained from an infinitely expanded ensemble). This is the case in LATEOS and LASS (figure 51), where nanoparticles are agglomerated to large clusters (> 100 nm).

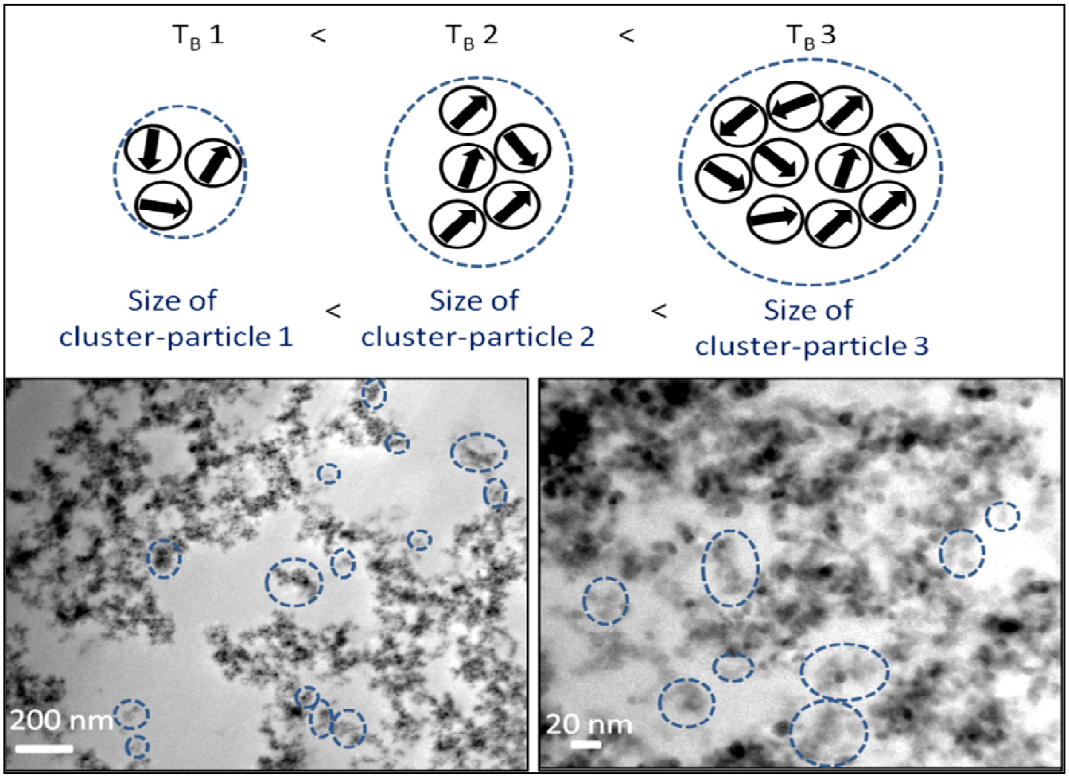

Figure 52: Superparamagnetic nanoparticles sized ~10 nm (black circles with arrows that indicate the magnetisation direction) grouped in different sizes may behave like larger magnetic cluster particles (upper scheme). The size distribution of such clusters of several nanoparticles (highlighted with circles in two TEM micrograph examples (bottom) from the MPSS sample) might lead to an increased $\Delta T_{ir,B}$.

In conclusion it can be stated that stabilisation of superparamagnetic magnetite nanoparticles with LA (lactic acid) or MP (MELPERS4343) lowers the blocking temperature T_B compared to as-precipitated and agglomerated nanoparticles (T_B = 255 K) by at least 180 K. Confining the stabilised nanoparticles in composite microparticles by formation of a silica matrix leads to clusters of various sizes. This influences the structure and the magnetic behaviour of the composite microparticles. Mutual magnetic blocking in the composites is less than in as-precipitated nanoparticles. T_B decreases in dependence of the stabilisation (45 or 65 K for LA stabilisation and 118 or 130 K for MP stabilisation).

LA stabilised nanoparticles in microcomposites are packed in dense, large clusters (> 100 nm) of many hundreds of particles. MP stabilised nanoparticles are packed in smaller clusters (approximately 10 to 200 nm) with only few nanoparticles. This is revealed by TEM images and related to ZFC / FC magnetic measurements. LA stabilisation causes a higher T_B and nearly no shift to T_{ir} ($\Delta T_{ir,B} \approx 0$). A lower T_B and a higher shift ($\Delta T_{ir,B} \approx 70$ K) are observed for MP stabilised nanoparticles in microcomposites. An explanation might be that smaller clusters act like particles of various sizes. $\Delta T_{ir,B}$ increases due to this "size distribution".

Preparation of the silica matrix from different precursors (TEOS or SS) has no detectable effects. ZFC / FC measurements of composites seem to be influenced by clustering of nanoparticles and size distributions in these clusters – an effect that should not be neglected if ZFC / FC studies are carried out.

4.3 Modified nanocomposite particles for adsorption / recovery of target substances

The nanocomposite microparticle system, compromising nano-magnetite particles in a silica matrix obtained from an inexpensive sodium silicate solution, represents a platform for various applications. In this work, focus was put on adsorption and recovery of dissolved substances from water by using the switchable magnetic particles with appropriate surface functionalities as carrier vehicles. The surface modifications and application results of the particles for the chosen targets mercury, copper, phosphate, and heavy metals in general, are discussed in the following chapters.

4.3.1 Microparticle modification for selective Hg(II) or Cu(II) separation and recovery[23]

Unmodified composite microparticles adsorb metal ions from an aqueous solution unselectively to some extent, but recovery of the metals in acid is not possible. For selectivity for specific metal ions in solution and their subsequent recovery, the particles' surface was modified. To demonstrate the potential of modified particles in this respect, Hg(II) and Cu(II) ions were chosen as target substance, respectively.

For Hg(II) recovery, the particle surface was modified with thiol groups using a simple reaction with a mercaptosilane. The diffuse reflectance infrared Fourier transformed (DRIFT) spectrum of the modified particles (figure 53a) shows C-H and S-H vibrations.[97] Saturation magnetisation drops from 30 to 22 emu/g, indicating a 27 wt% thiosilane modification. For selective Cu(II) extraction, the particles were impregnated (after silanisation with propylsilane) with 2-hydroxy-5-nonylacetophenone ketoxime (LIX84, which is dissolved in kerosene), a molecule developed as a highly selective Cu(II) chelating agent. Modifying magnetic particles with a selective Cu(II) binding agent designed for solvent extraction could result in a material that is applicable for a process overcoming the disadvantages of conventional solvent extraction.

The DRIFT spectrum of modified particles (figure 53b) shows absorptions between 3200 and 3600 cm^{-1} (p- and m-hydroxyl groups), at 1400 to 1500 cm^{-1} (substituted benzene), and at 1600 cm^{-1} (carbon-nitrogen bond).[109] Magnetisation drops to 16 emu/g, indicating a 47 wt% loading of the particles with LIX84 (probably including some residual kerosene). LIX84 modified composite microparticles are rather hydrophobic but disperse fairly well in water if vigorously shaken. Subsequent redispersion steps (e.g. after magnetic extraction) are easily achieved by gentle shaking.

[23] This chapter has been published and is reused in this work by courtesy of the American Chemical Society. Original article: K. Mandel et al., *ACS Appl. Mater. Interfaces*, 2012, **4**, 5633.

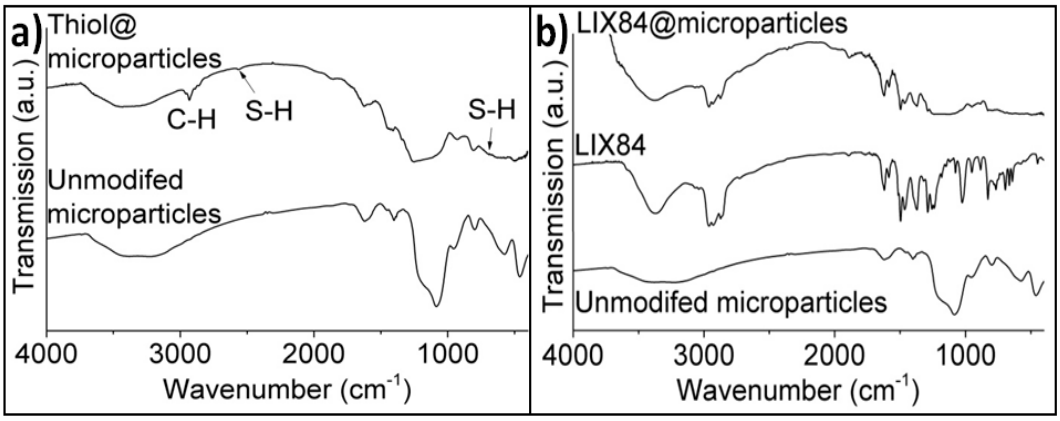

Figure 53: DRIFT spectra of thiol (a) and LIX84 (b) modified magnetic particles (assignment of peaks for unmodified microparticles as in figure 42c).

The LIX84, as well as the mercapto modified particle system was dispersed at a concentration of 1 g/l in water which contained approximately 10 mg/l of As(V), Cd(II), Cr(III), Hg(II), Cu(II), Zn(II), Pb(II), Ca(II) and Mg(II) ions. The initial pH of the heavy metal solution was set to 4 to avoid uncontrolled metal hydroxide precipitations. Particles were magnetically separated after a few seconds with a handheld magnet after they were stirred for 10 minutes in the water. Recovery (desorption) of metal ions was carried out in 10 ml 0.1 M HCl within 10 minutes before the particles were again magnetically separated, washed, and used for adsorption. The adsorption / desorption cycles were repeated three times. Concentrations of metal ions in the adsorption / desorption solutions were determined by ICP-OES. Data are given as percentages of the ideal (maximum possible) result (10 mg of the respective ion is adsorbed or desorbed; figure 54).

65 % Cu(II) was adsorbed in each cycle and recovered by 66 % (first cycle) to 90 % (third cycle). Recovery of Hg(II) was not possible by acid treatment alone. The addition of 2 % thiourea, as suggested for modified silica,[317] seems to be the key step in the recovery of Hg(II). Removal of Hg(II) of > 99 % was achieved for each adsorption cycle and recovered by 33 %, which could not be increased by a prolonged desorption time (30 min).

As can be seen from figure 54, adsorptions and desorptions for all other metal ions are much lower, especially in the case of Cu(II)-adsorbing particles, which are nearly 100 % selective over all other heavy metals studied. The performance of the particles did not drop within three cycles.

Cu(II) adsorption can be increased by a longer adsorption time (30 min) to 88 %. The maximum Cu(II) capacity of the particle system is 30 mg/g (adsorption saturation reached after 1 h in 100 mg/l aqueous heavy metal solution). Hg(II) adsorption was found to be > 99 % even after only 1 min adsorption time. The Hg(II) adsorption capacity of the thiolmodified particles was 74 mg/g (after 10 min of adsorption in a 100 mg/l aqueous heavy metal solution). Only when particles are in great excess to Hg(II) concentration (> 2 g/l per 1 mg/l Hg(II)) are Cd(II), Cu(II), and Pb(II) ions adsorbed as well. Hg(II) adsorption therefore has to be considered as very fast and selective.

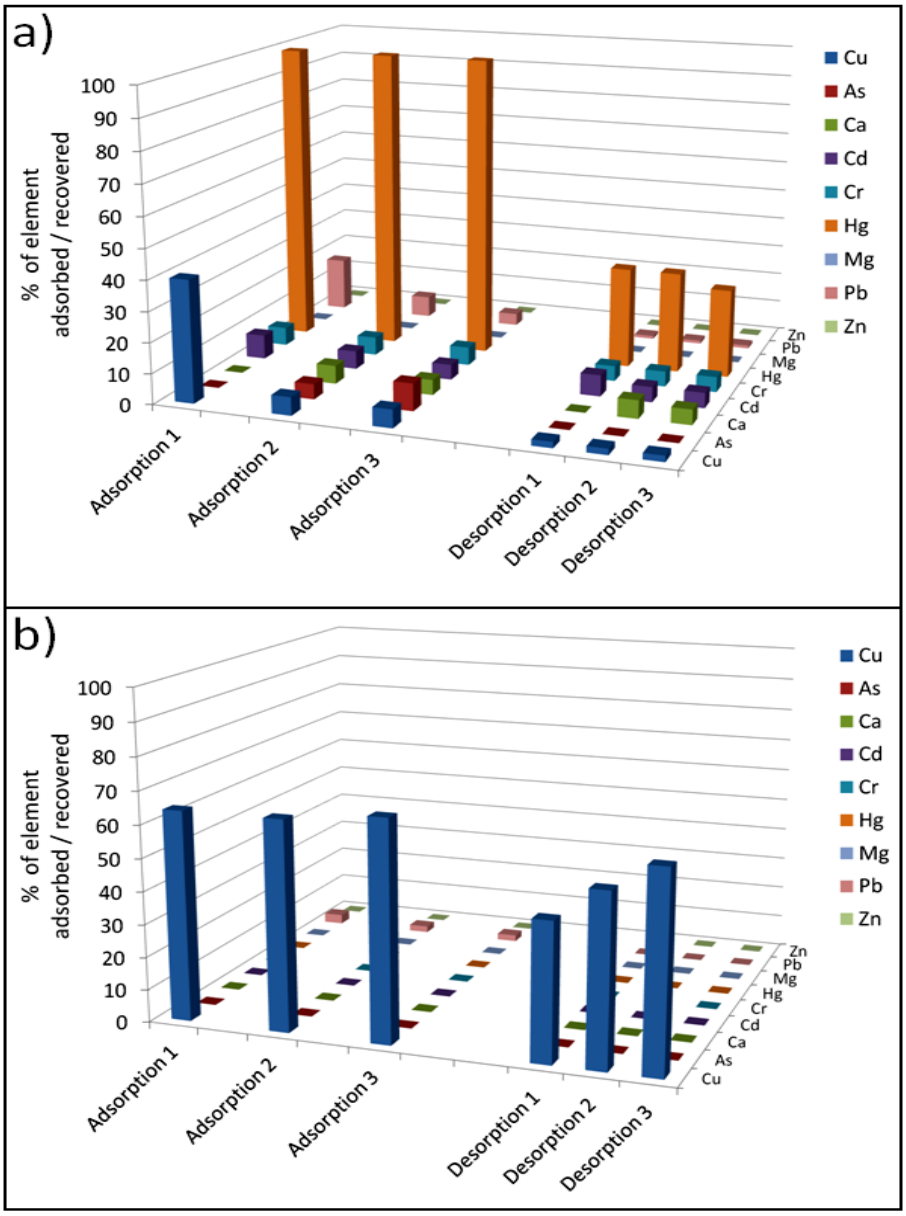

Figure 54: Result of adsorption / desorption cycles of metal ions on a) thiol and b) LIX84 modified magnetic microparticles. 100 % corresponds to the ideal (maximum possible) result.

4.3.2 Layered double hydroxides @ nanocomposite particles for phosphate recovery[24]

Besides silanisation or impregnation techniques for the modification of nanocomposite microparticles, it is also possible to deposit other solid material on these particles. Intertwining of magnetic particles with layered double hydroxides (LDH) was envisaged for a selective phosphate recovery from waste water. In this chapter, the material synthesis results will be described, followed by a chapter on the application of the particles in waste water.

Layered double hydroxides (LDH) as selective phosphate ion exchangers

LDHs were precipitated by a fast (within 5 min) and simple reaction (without pH variations, aging steps or air protection) by pouring an aqueous solution of metal salts into a sodium hydroxide solution (pH 10) under stirring. The mixtures were neutralised (pH 7) with HCl after 5 min to stop precipitations and to prepare the next step of composite synthesis. Thereby some shift in the composition of LDH from the stoichiometry of the precursors may occur, also by redissolution of Mg ions due to the acid treatment.

The well known MgAl and MgFe LDH systems were prepared and doped with Zr (MgAl-Zr and MgFe-Zr LDH) to improve their selectivity as phosphate ion exchangers.[130,131] For comparison, a precipitate (no LDH) from a pure $ZrOCl_2$ solution was prepared as well.

The LDHs were analysed by differential thermal analyses – thermogravimetry coupled with mass spectroscopy (DTA-TG-MS, figure 55) and inductively coupled plasma optical emission spectroscopy (ICP-OES). All LDH samples showed two endothermic peaks between 40 to 200 °C and 300 to 500 °C. MS revealed loss of H_2O only (adsorbed and interlayer water)[130] up to 200 °C. From TG the water content of an LDH is estimated. Up to 500 °C, H_2O and CO_2 are lost. Between 300 and 500 °C, dehydroxylation of LDH and decomposition of interlayer carbonate are observable.[130] At higher temperatures also HCl was lost. The $ZrOCl_2$ precipitation showed only loss of H_2O up to about 400 °C. An exothermic peak observed between 450 °C and 500 °C is attributed to crystallisation which takes place upon rapid release of H_2O from bound hydroxyls.[318]

[24] This chapter has been published and is reused in this work by courtesy of the Royal Society of Chemistry. Original article: K. Mandel et al., *J. Mater. Chem. A*, 2013, **1**, 1840.

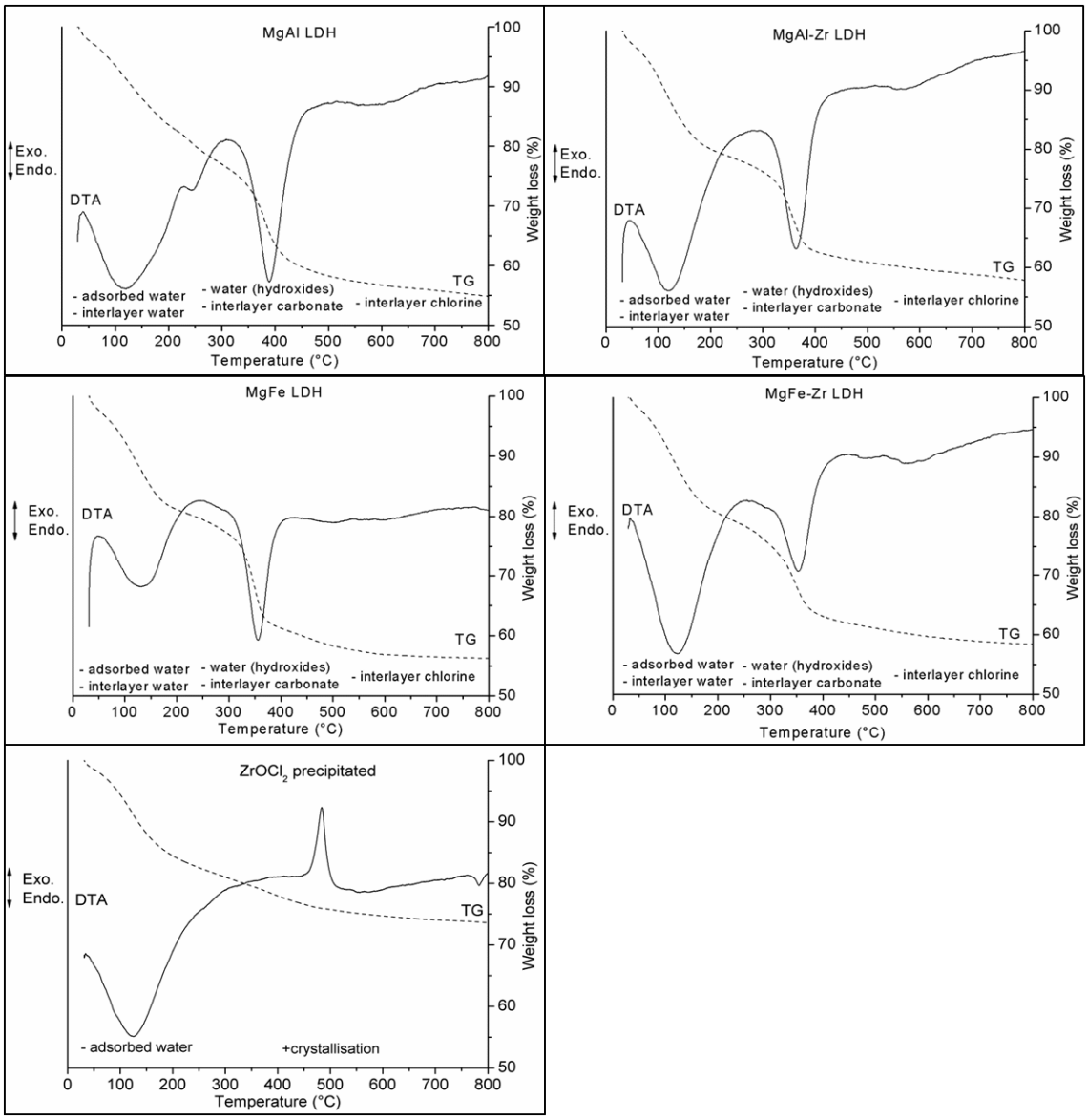

Figure 55: DTA-TG measurements for different LDHs prepared by fast coprecipitation.

The content of Fe, Zr, Mg, Al and Cl in the samples was measured by ICP-OES. The summarised masses of all metal oxides and chloride plus the weight loss (up to 500 °C) determined by TG was set to 100 %. Thereby atomic ratios of the LDHs were calculated and inserted in the general formula:[130]

$$[M^{2+}_{(1-x-y)}M^{3+}_{x}M^{4+}_{y}(OH)^{-}_{2}]\ [\text{interlayer anion}]^{-}_{(x+2y)} \cdot z\ [\text{interlayer } H_2O] \qquad (29)$$

H_2O, Cl^- and CO_3^{2-} were assumed as interlayer compounds. Chloride content is given by ICP-OES analysis. Carbonate was only measured qualitatively and quantitatively calculated from the charge balance of the LDH.

All weight loss up to 200 °C was attributed to the total water content of the LDH. A distinction between adsorbed and interlayer water is not possible.

In table 3, the atomic ratios of precursor compounds are compared to values calculated from analyses. MgAl LDH is completely soluble at pH 4; therefore its analysed Mg content is about 15 % too low and the Al content exceeds 0.33 due to partial leaching of Mg ions by the neutralisation reaction (to pH 7) with acid after precipitation. Zr and Fe containing LDH dissolve at pH 3. Shifts in the Mg contents are lower (about 9 %), three and four valent metal content sums up to less than 0.33, an upper empirically found limit before precipitation of other, separate hydroxides begins.[135] Zr is incorporated with the same shifts in the precursor stoichiometry and in conformable ratios as recently reported.[130,131] Indication of Zr incorporation into the LDH structure is found by combining XRD and DTA-TG results as described below.

Table 3: Derived LDH formulas in comparison to precursor ratios.

LDH Type	Precursor metal ratio	Determined formula
MgAl	$Mg_{0.67}Al_{0.33}$	$[Mg_{0.57}Al_{0.43}(OH)_2][Cl_{0.13}(CO_3)_{0.15}\cdot 1.27H_2O]$
MgAl-Zr	$Mg_{0.75}Al_{0.125}Zr_{0.125}$	$[Mg_{0.67}Al_{0.15}Zr_{0.18}(OH)_2][Cl_{0.11}(CO_3)_{0.20}\cdot 1.18H_2O]$
MgFe-Zr	$Mg_{0.75}Fe_{0.125}Zr_{0.125}$	$[Mg_{0.69}Fe_{0.14}Zr_{0.17}(OH)_2][Cl_{0.07}(CO_3)_{0.205}\cdot 1.15H_2O]$
MgFe	$Mg_{0.67}Fe_{0.33}$	$[Mg_{0.72}Fe_{0.28}(OH)_2][Cl_{0.10}(CO_3)_{0.09}\cdot 1.09H_2O]$

Figure 56 shows the X-ray diffractograms for the LDH systems and the precipitate from $ZrOCl_2$. Reflections of NaCl (without indication) were used for calibration of *d* values. Precipitated $ZrOCl_2$ seems to be X-ray amorphous. The structure of LDHs is confirmed by the reflections (003), (006) and (009).[31,130,131,136] The reflections (110) and (113), related to the distances and ordering of the metal hydroxide layers, are distinct for MgAl and MgFe LDH. In Zr containing systems, these reflections are no longer resolved, indicating a poor stacking order of the layers[319] and a potentially random distribution of Zr. There is no increased background in these X-ray diffractograms as observed for solely precipitated $ZrOCl_2$, i.e., there is no indication for a separate amorphous Zr containing phase in the LDH systems.

In all Zr containing systems reflections ((110), (003), (006), (009)) are shifted towards higher *d* values indicating an increased distance between the metal ions in the rhombohedral unit cell. Its lattice constants can be obtained by $a = 2\cdot d_{110}$ and $c = 3\cdot d_{003}$.[131] Table 4 lists values for *d*, *a* and *c* for the LDHs.

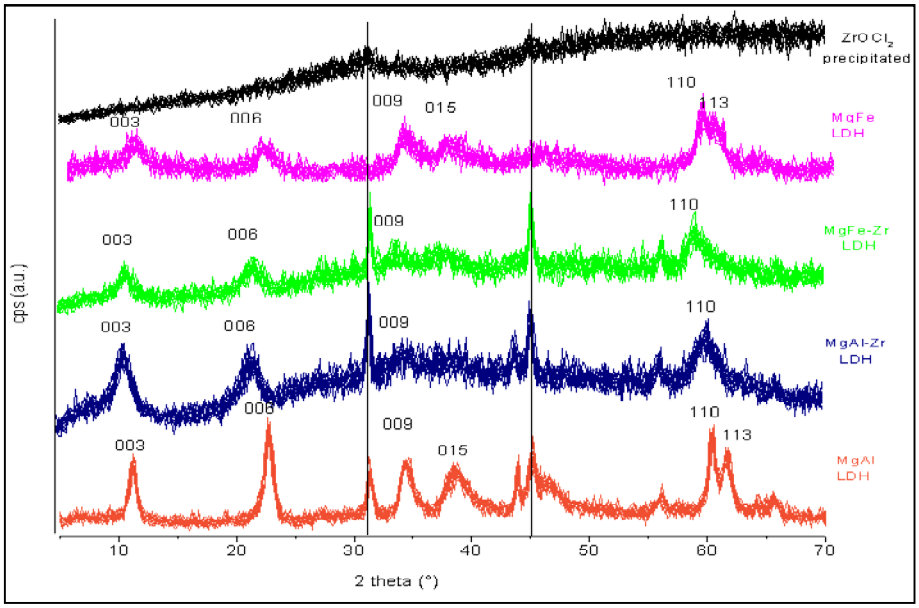

Figure 56: X-ray diffractograms of LDHs and $ZrOCl_2$ precipitation (reflections of NaCl without indices).

Table 4: *d* values and lattice constants (in Å**)** for LDH samples.

LDH Type	d_{110}	d_{003}	*a*	*c*
MgAl	1.530	7.878	3.061	23.633
MgAl-Zr	1.542	8.571	3.085	25.715
MgFe-Zr	1.570	8.613	3.140	25.840
MgFe	1.552	7.892	3.105	23.679

Both lattice constants (*a* and *c*) are increased by Zr doping of the LDHs. Usually the interlayer spacing (proportional *c*) should be reduced with increasing charge of the layers (which is the case if Fe^{3+} or Al^{3+} is replaced by Zr^{4+}).[320] However, analysis (table 3) of interlayer anions shows an enhanced content of carbonate causing an increase of interlayer spacing. The lattice constant *a* depends on the sizes of metal cations (in Å: Mg^{2+}: 0.74, Zr^{4+}: 0.72, Fe^{3+}: 0.55, Al^{3+}: 0.54)[135,321]. As shown for the MgAl LDH system the lattice constant *a* decreases linearly with an increasing stoichiometric content of Al^{3+}:[321]

$$(\Delta a = (-2.8\ \text{Å}) \cdot (Al^{3+}/(Al^{3+}+Mg^{2+})) \qquad (30)$$

Taken into account that Zr^{4+} and Mg^{2+} are equal in size, the lattice constant *a* can be calculated for the MgAl-Zr LDH (table 3) to be 3.085 Å, which perfectly fits the measured value (table 4). For the MgFe LDH the measured value of *a* fits well to published results (3.10 Å).[322] Substituting Al^{3+} by Fe^{3+} (which are nearly the same size) in the above

equation (30), the lattice constant *a* for MgFe-Zr LDH is calculated to be 3.144 Å, which also closely fits the measured value (table 4). Thus, calculation results suggest that Zr is part of the LDH.

DTA-TG measurements give a further indication for Zr incorporation into the LDH structures. The precipitate from the $ZrOCl_2$ solution shows an exothermic crystallisation peak at 450 °C to 500 °C, which cannot be found in Zr containing LDHs (figure 55), supporting the idea that Zr is not precipitated as a separate phase but as part of the LDH.

Fraunhofer diffraction (FD; figure 57a) and SEM (figure 57b and c) show that LDHs consist of agglomerated flakes 1 to 60 µm in size. Using the transmission electron microscope (TEM; figure 57d) hexagonally shaped crystallites, about 100 nm laterally sized, can be seen.

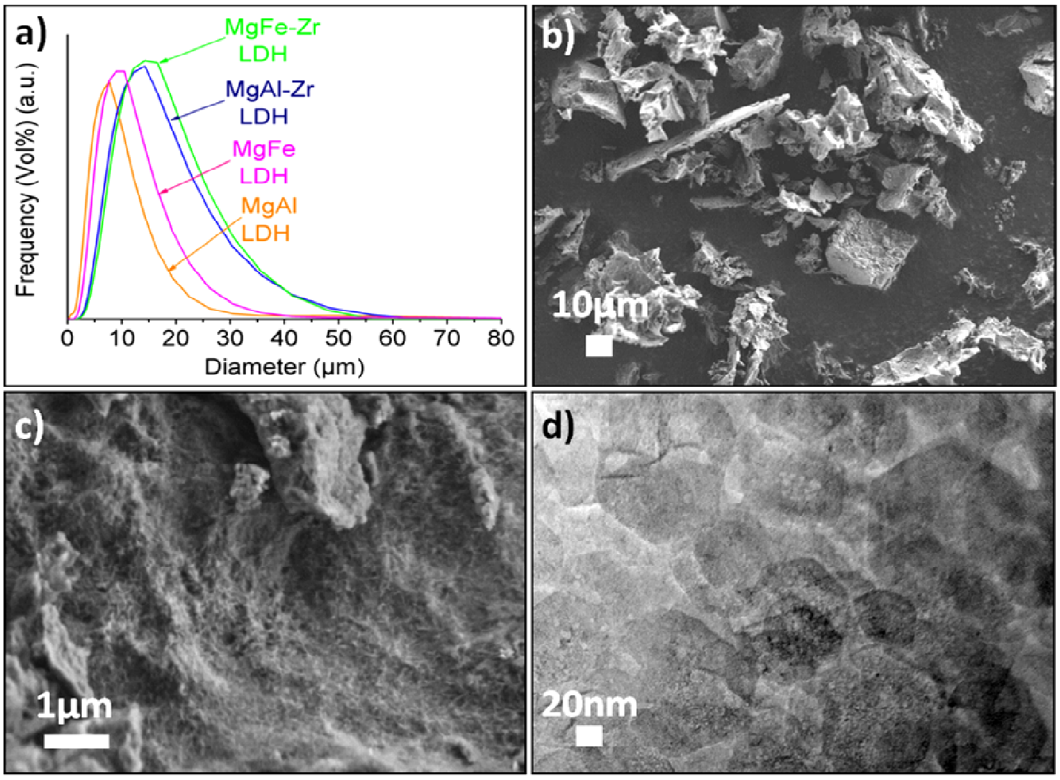

Figure 57: a) Fraunhofer diffraction on LDH dispersions; SEM (b, c) and TEM (d) micrographs of MgFe-Zr LDH.

LDH agglomerates were tried to be dispersed as nanosized crystals by refluxing dispersions in water for 8 h.[323] This was envisaged to potentially facilitate a subsequent composite formation with the magnetic particles. However, only for MgAl LDH a stable sol could be obtained. All other samples did not change in crystallinity or particle size. Thus, for a proper combination of LDH with magnetic particles, a different method had to be used.

Composite formation: LDHs on superparamagnetic microparticles

In LDHs the layers are positively charged. Their zeta potentials are strongly positive over a wide range of pH (figure 58). In contrast to this, the superparamagnetic microparticles show a negative zeta potential over a very wide range of pH as their surface completely consists of silica (figure 58). A strong attraction between the LDHs and the superparamagnetic particles is expectable.

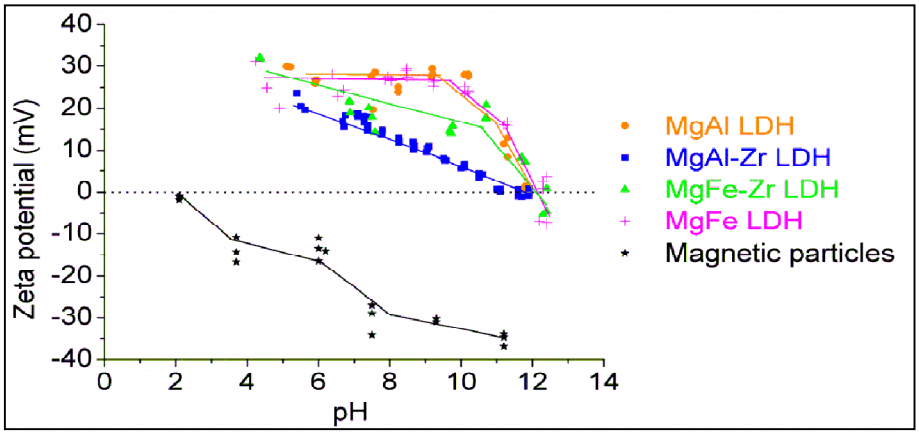

Figure 58: pH dependence of zeta potentials of superparamagnetic particles and LDHs.

By simply mixing dispersion batches of LDH and of superparamagnetic particles a slight flocculation could be seen at pH 7 on a lab scale. Only fractions of the suspension were magnetically separated. However, mixing under ultrasonic treatment leads to stronger flocculation (or even coagulation) and complete magnetic separability of the composite particles that formed.

On a larger scale, composite formation under ultrasonic assistance was carried out continuously in an ultrasonic flow cell. Figure 59 shows the principle of composite formation for both mixing procedures.

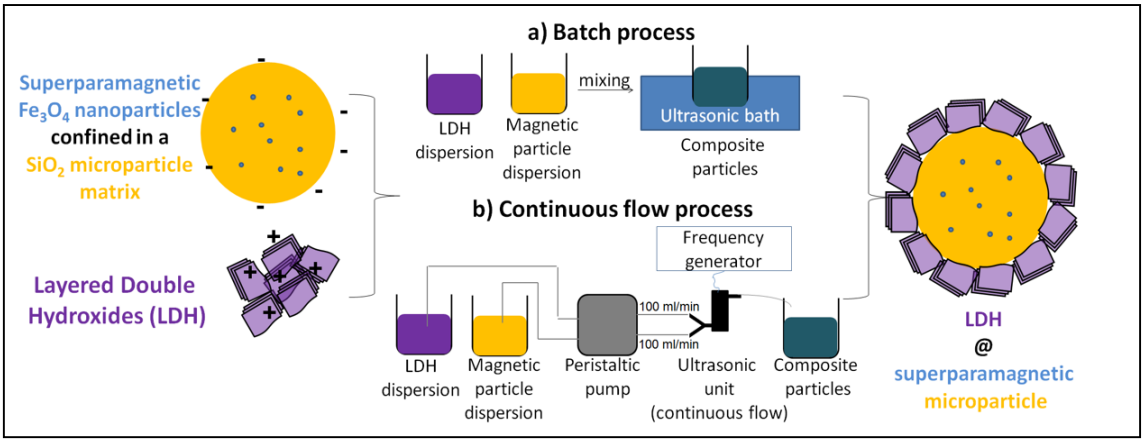

Figure 59: Scheme for composite formation by ultrasonic treatment in a batch and in a continuous process.

If not indicated otherwise, following characterisations discussed in this work were done on batch samples.

FD measurements of composite particles (figure 60) reveal that these are slightly larger than the pure magnetic particles. Ultrasonic treatment on a pure LDH suspension showed only very slightly reduced agglomerate sizes (not shown). Therefore, it is assumed that by ultrasonic treatment LDH agglomerates break and re-arrange, but are deposited as distributed parts on magnetic particles if these are present.

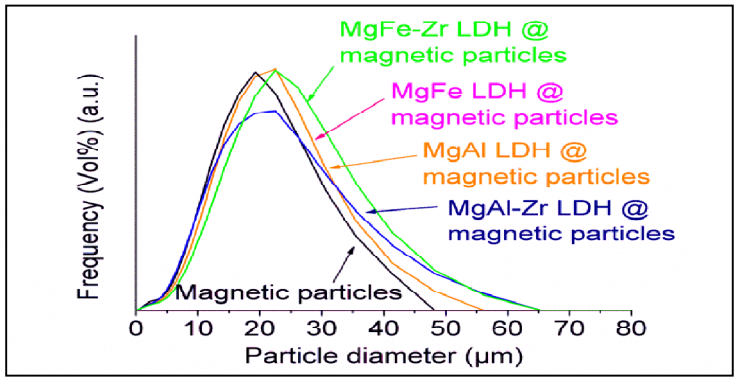

Figure 60: Particle size distributions measured by Fraunhofer diffraction on suspensions of superparamagnetic microparticles and composite particles with 20 wt% LDH (note: distribution curves for MgFe and MgAl LDH @ magnetic particles are superimposed).

Deposition of LDH on the superparamagnetic particles was confirmed by X-ray diffraction of washed, magnetically separated and dried composite particles (figure 61). Reflections of LDH and for magnetite could be detected.

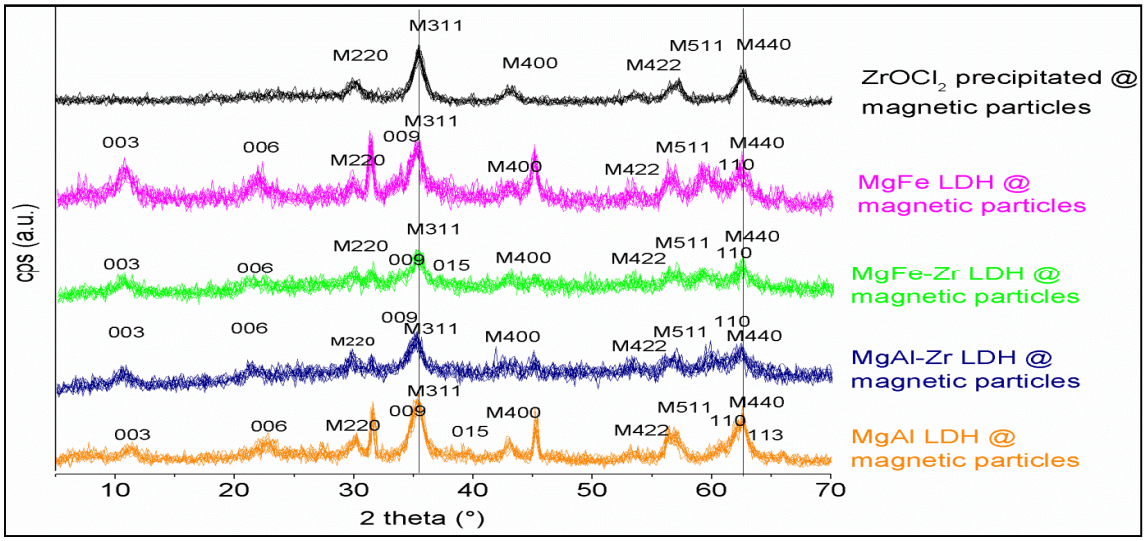

Figure 61: X-ray diffractograms of composite particles (60 wt% LDH). Reflections of magnetite nanoparticles from the superparamagnetic microparticles are labelled with *Mhkl.* Reflections of NaCl remain unlabelled.

SEM images of composite particles (figure 62) show the same LDH structures (figure 62b) as in figure 57c. SEM and TEM micrographs (figure 62c-f) of a cross section through a composite particle (obtained via focused ion beam technique) reveal the intertwined local arrangement of LDH and the superparamagnetic particle. The composition of the different phases (LDH, SiO_2, Fe_3O_4) was also confirmed by scanning transmission electron microscopy combined with energy dispersive X-ray analysis (STEM-EDX; not shown).

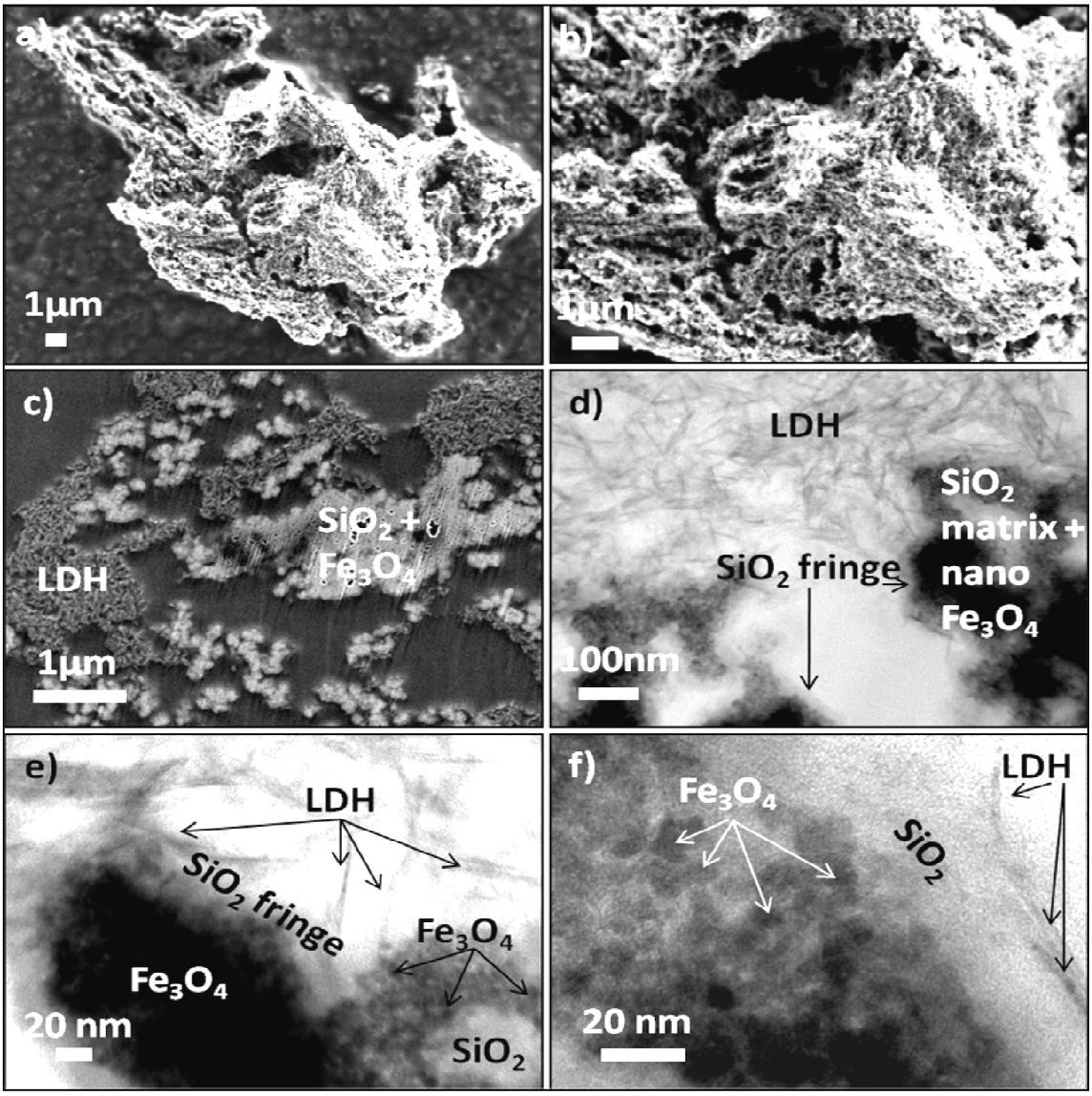

Figure 62: SEM images (a, b) of a composite particles; SEM (c) and TEM (d-f) images at different magnifications of a cross section through the composite particle including the LDH on the silica fringe of the microparticles that host superparamagnetic Fe_3O_4 nanoparticles (~10 nm) in a silica matrix.

The LDH content in composite particles could be varied (20, 40, 60 wt%). After ultrasonic deposition, particles were magnetically separated with a handheld magnet and washed twice.

Only the MgAl LDH was washed off if more than 20 wt% LDH was initially provided. A determination of the LDH load on composite particles was conducted from DTA-TG measurements and vibrating sample magnetometer measurements (VSM).

From DTA-TG measurements, total weight loss (in wt%) up to 500 °C of pure superparamagnetic microparticles (*B*) was compared to weight losses of pure LDH (*A*) and composite particles (*C*). The fraction *x* of LDH on the composite can be calculated:

$$A \cdot x + B \cdot (1-x) = C \;\; ; x = \frac{C-B}{A-B} \tag{31}$$

Using VSM, saturation magnetisation of pure superparamagnetic microparticles and composite particles - that are superparamagnetic as well - can be compared (figure 63). Loss of magnetisation per mass is caused by the added LDH content. Pure LDHs without Fe behave diamagnetically (magnetisation at 3 T is less than 0.5 emu/g). Fe containing LDHs are weakly paramagnetic (MgFe-Zr LDH magnetisation at 3 T is 0.6 emu/g, MgFe LDH is 1.6 emu/g). These contributions lead to a maximal error of 5 % for the LDH content.

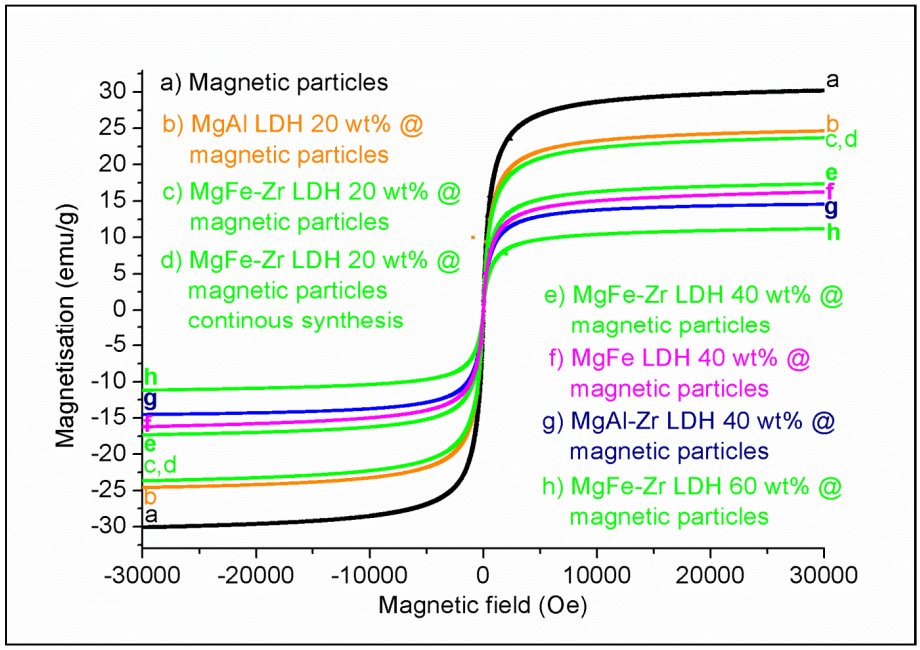

Figure 63: Vibrating sample magnetometer measurements (at 293 K) of superparamagnetic particles and composite particles (LDH deposited on superparamagnetic particles).

LDH weight fractions at preparation of the composites and determined by DTA-TG and VSM measurements are given in table 5. Deviations of measured values and values at preparation are small.

Table 5: LDH weight fraction (in wt%) in composite particles determined from DTA-TG and VSM measurements compared to weight fraction at preparation.

Sample	At preparation	VSM	DTA-TG
MgAl LDH@ magnetic particles	20	19	21
MgFe LDH@ magnetic particles	40	47	40
MgAl-Zr LDH@ magnetic particles	40	52	49
MgFe-Zr LDH@ magnetic particles	20	22	18
MgFe-Zr LDH@ magnetic particles	40	43	41
MgFe-Zr LDH@ magnetic particles	60	63	60
MgFe-Zr LDH@ magnetic particle continous synthesis	20	18	16

For adsorption or ion exchange processes, a large surface area is desired. All pure LDHs considered in this work have specific surface areas (N_2 adsorption, BET method) of 1 to 7 m^2/g.

These comparably low values are reported in the literature[131] for non-porous as-precipitated LDH materials. The interlayer-space filled with anions is not accessible for N_2 molecules.[131] Furthermore agglomeration of LDH flakes after precipitation diminishes the surface area.

Superparamagnetic particles have a surface area of 50 to 75 m^2/g and composite particles have 90 to 105 m^2/g (for all types of LDH with a fraction of 40 wt% LDH of the composite). The composite with MgAl LDH was even measured to have a surface area of 232 m^2/g. This increase in surface areas indicates a deposition of *dispersed* LDH agglomerates onto the superparamagnetic particles by ultrasonic treatment.

The $ZrOCl_2$ precipitate could not be deposited on superparamagnetic particles in the same way as LDH. Therefore it was directly precipitated onto the magnetic particles. However, the resulting product was hardly magnetically separable as the formed product was very voluminous. From DTA-TG analyses a deposition of 20 wt% was estimated. The surface area of this composite was 70 m^2/g.

4.3.3 Applied phosphate recovery from municipal waste water[25,26]

Initial experiments for phosphate recovery with the different composite particles were performed in distilled water and in real municipal waste water. The respective starting phosphate concentrations were adjusted to 10 mg/l PO_4-P [27] (36.65 mg/l PO_4^{3-}, corresponding 100 %) with phosphoric acid (H_3PO_4), to test the particles' performance for phosphate concentrations typically encountered in municipal waste water streams.[34] All water samples had a pH in the neutral range of 7 to 8. Composite particle concentrations were adjusted to a corresponding LDH concentration of 200 mg/l.

After suspending the particles in 100 ml of the solutions for a given contact time up to 24 h (20 °C, stirring), particles were separated in the field gradient of a permanent magnet. The remaining phosphate concentrations were measured photometrically according to the ammonium molybdate spectrometric method. Independent of water and contact time the MgFe-Zr LDH showed the highest first adsorption (figure 64a).

Regeneration of LDH ion-exchangers ("desorption") of composite particles was performed in 100 ml solution of 0.1 M NaOH and 2.0 M NaCl. After magnetic separation, particles could be used again. In recycling experiments with composite particles contact times for complete adsorption and desorption were set to 24 h, arbitrarily.

In real waste water, after the first two desorption steps, MgFe-Zr LDH performed best (highest adsorptions, figure 64b), however, MgAl-Zr and MgFe LDH composites also showed good performance. MgFe-Zr showed the highest desorption rates in steps 1 to 4 (figure 64c, 100 % corresponds to all phosphate initially adsorbed on the particles). Phosphate desorption of Zr based precipitate @ magnetic particles was hardly possible (only 20 % after 24 h); so these particles were not tested in subsequent repetition cycles. For all LDH samples, no clear performance drop was observed during the recycling tests.

The LDH composites were finally compared based on their PO_4-P uptake (in mg) per g LDH on the particles after 24 h adsorption in waste water. The MgFe-Zr LDH adsorbed 30 mg PO_4-P per g LDH, followed by MgFe and MgAl-Zr LDH with approximately 20 mg/g. The Zr based system showed an adsorption of 15 mg/g and the MgAl LDH of 12 mg/g. Thus, the Zr doping of a MgFe LDH is most promising for a high and selective uptake of phosphate in waste water.

[25] The first part of this chapter up to figure 64 has been published and is reused in this work by courtesy of the Royal Society of Chemistry. Original article: K. Mandel et al., *J. Mater. Chem. A*, 2013, **1**, 1840.
[26] The second part of this chapter has been submitted to *Water Research* for publication. The submitted title is "*Phosphate recovery from wastewater using engineered superparamagnetic particles modified with layered double hydroxide ion exchangers*". The main author and thus contributer to the work illustrated here is Asya Drenkova-Tuhtan (University Stuttgart).
[27] The term PO_4-P is generally used in this work to address the amount of elemental P that is present as phosphate (dependend on the pH P is present as H_3PO_4, $H_2PO_4^-$, HPO_4^{2-} or PO_4^{3-}).

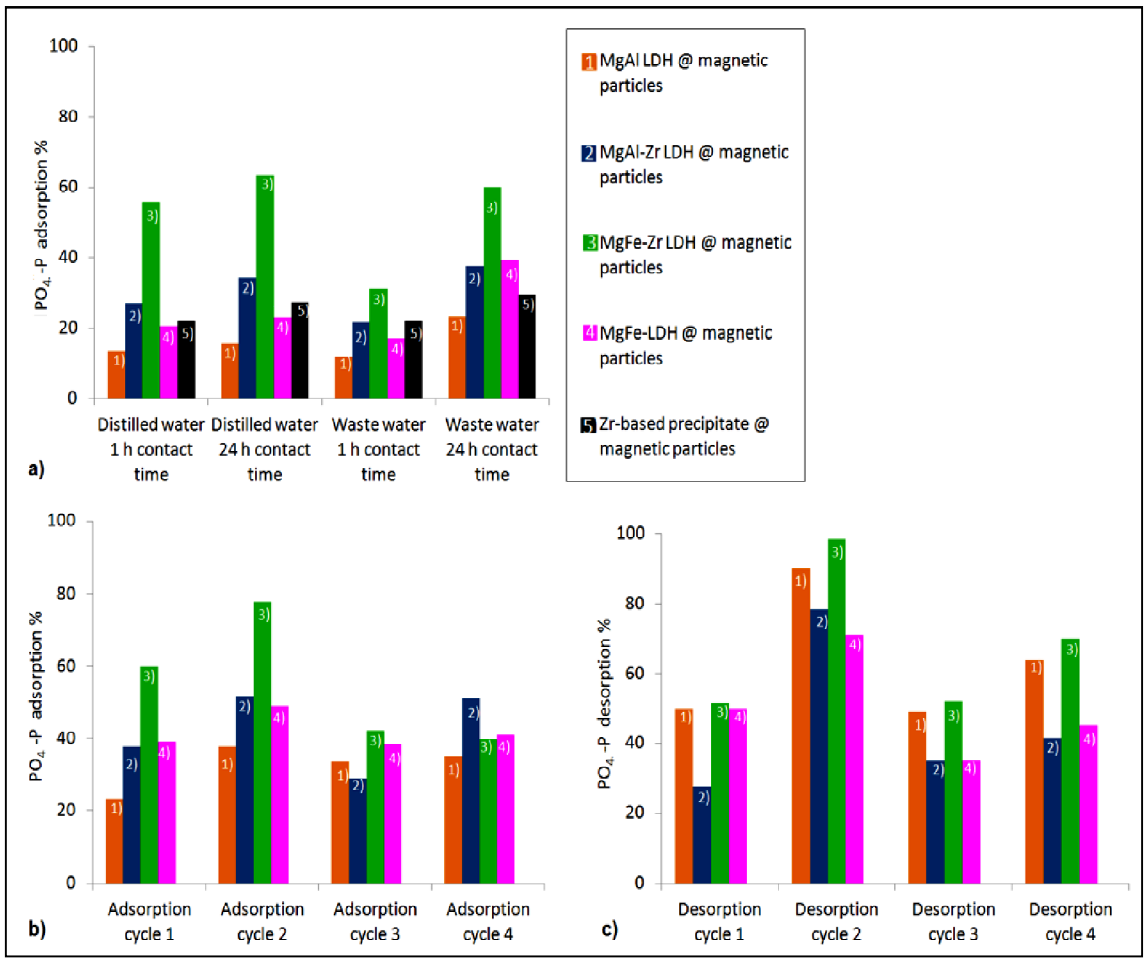

Figure 64: Phosphate recovery experiments with composite particles; a) in distilled water and waste water; 1 h and 24 h contact time; b, c) four adsorption and desorption (24 h contact time each) cycles in waste water.

However, good phosphate adsorption does not necessarily imply good selectivity. Therefore, the effect of other potentially competing anions in waste water was studied as a further criterion for selection of the best performing particle system.[28] Predominantly total inorganic carbon (TIC) (40-50 %), followed by phosphate (40-45 %) and some adsorption of sulfate (5-8 %) and nitrate (2-10 %) in all systems was observed. A detailed discussion on these results is beyond the scope of this work.[29] Also from these tests, MgFe-Zr LDH on magnetic particles seems to be the most promising combination and therefore further studies concentrated on this sample.

[28] See following footnote
[29] Experimental concept design, measurements and data evaluation were performed by Asya Drenkova-Tuhtan (University Stuttgart) and the results are submitted to *Water Research* for publication. The submitted title is "*Phosphate recovery from wastewater using engineered superparamagnetic particles modified with layered double hydroxide ion exchangers*".

Reaction kinetics and adsorption isotherm of the MgFe-Zr LDH @ magnetic particles [30]

Figure 65 illustrates the specific phosphate adsorption (mgP/gLDH) from the liquid phase on the LDH surface at different contact times and three different pH ranges (4.5-5; 5.5-6 and 7-8). In order to enhance the reaction kinetics and the adsorption efficiency, LDH concentration was increased up to 400 mg/l, corresponding to 1 g/l particles (40 wt% LDH @ magnetic particles).

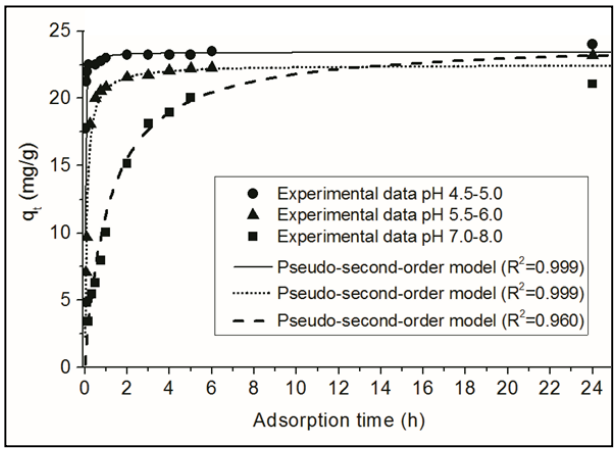

Figure 65: Adsorption kinetics of phosphate for 400 mg/l MgFe-Zr LDH @ magnetic particles as a function of pH at room temperature. Initial concentration of PO_4-P = 10 mg/l.

There is a rapid phosphate adsorption in the first 1 h and equilibrium is reached after approximately 2 h contact time for pH 4.5-5 and pH 5.5-6. Phosphate adsorption at pH 7-8 is much slower and the system is getting close to equilibrium after more than 6 hours of reaction. The fastest kinetics is observed at pH 4.5-5 where more than 90 % of the total phosphate was adsorbed already within the first 45 min and at equilibrium a capacity of 23 mgP/gLDH was achieved.

To model the adsorption kinetics, initially it was considered that the measured data follows a pseudo-first-order model, based on the differential equation:

$$\frac{dq_t}{dt} = k_1 \cdot (q_e - q_t) \tag{32}$$

which can be linearised in the form:

$$\ln(q_e - q_t) = \ln(q_e) - k_1 \cdot t \tag{33}$$

[30] The text of this chapter was written jointly by Asya Drenkova-Tuthan (University Stuttgart) and Karl Mandel; Experimental concept design and data was acquired by Asya Drenkova-Tuhtan (University Stuttgart) and modeled by Karl Mandel. The chapter is part of the work submitted to *Water Research* for publication. The submitted title is "*Phosphate recovery from wastewater using engineered super-paramagnetic particles modified with layered double hydroxide ion exchangers*".

where q_e and q_t is the amount of adsorbed phosphate at equilibrium and at time t, k_1 is the rate constant and t the adsorption time.[129] The pseudo-first-order model, however, did not result in a good fit. Therefore, the kinetic data were further analysed by testing a pseudo-second-order model, developed by Y. S. Ho and G. McKay for describing the sorption of divalent metals.[324] It resembles the pseudo-first-order model but the adsorbed amount of analyte is a function of the squared concentration difference instead:

$$\frac{dq_t}{dt} = k_2 \cdot (q_e - q_t)^2 \tag{34}$$

where k_2 is the reaction rate constant.

The equation can be solved and rewritten as follows:

$$\frac{t}{q_t} = \frac{1}{q_e^2 \cdot k_2} + \frac{1}{q_e} \cdot t \tag{35}$$

The model was developed under the assumptions that sorption follows the Langmuir mechanism: only a monolayer is adsorbed, the energy at each site is the same and there is no mutual interaction between the ions. As demonstrated later in figure 66, the phosphate adsorption isotherm indeed follows the Langmuir model. The pseudo-second-order equation was successfully applied by others as well, describing the adsorption kinetics of phosphate on various materials [121,325] and also on LDH.[129]

For the studied MgFe-Zr LDH modified magnetic particles, the phosphate adsorption kinetics most closely followed the pseudo-second order model with the highest correlation coefficient $R^2 = 0.999$ at pH 4.5-5 and pH 5.5-6. At pH 7-8, the correlation was still good ($R^2 = 0.960$), however, the fitting of the measured values in the linear section does not resemble an ideal straight line anymore.

Adsorption isotherm of phosphate on 40 wt% MgFe-Zr LDH @ magnetic particles is presented in figure 66. Freundlich and Langmuir equilibrium adsorption models were introduced to study the isotherm.

The Langmuir model follows the mathematical formulation:

$$q_e = \frac{b \cdot C_e}{1 + b \cdot C_e} \cdot Q_{max} \tag{36}$$

The Freundlich equation is represented as:

$$q_e = K \cdot C_e^u \tag{37}$$

where Q_{max} and q_e are the maximum and equilibrium amount (mg/g) of phosphate adsorbed on the particles, and C_e denotes the phosphate concentration in the solution at

equilibrium. *K*, *u* and *b* are constants which are obtained from fitting the model to the measured data. Linearisation for fitting the data with the Freundlich model can be done by a double logarithmic plot. The Langmuir linear regression was used to fit the Langmuir model to the experimental data. Both regressions have the advantage to be only slightly sensitive to data errors. They show a certain bias towards fitting in the higher concentration range. The best possible fit resulted in K = 9.855, u = 0.172 and b = 2.27 l/mg. The correlation coefficient R^2 was determined to be 0.997 for the Langmuir and 0.905 for the Freundlich model. The experimental data seems to rather follow the Langmuir model (figure 66). The maximum capacity of the particles, determined from the Langmuir model, is 14 mgPO_4-P/g particles, corresponding to 35 mgPO_4-P/gLDH, which is a bit higher than what was achieved at pH 7 for MgFe-Zr LDH (30 mgPO_4-P/g).

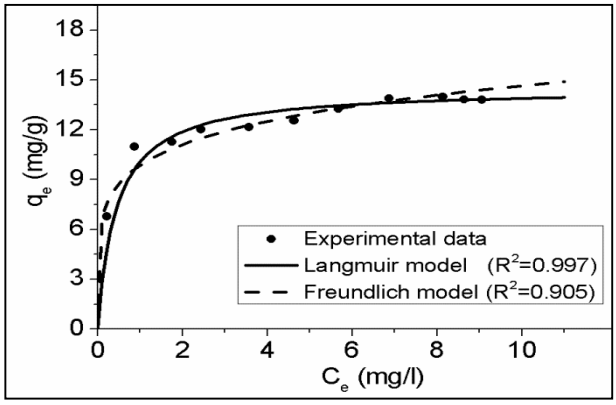

Figure 66: Phosphate adsorption isotherm for MgFe-Zr LDH @ magnetic particles at room temperature and pH 4.5. Remark: results are presented as mgP/g particles; multiplication with a factor of 2.5 is necessary for conversion to mgP/gLDH.

Reusability of the particles[31]

Stability and reusability of the magnetic composite particles is most important for a technical application. The superparamagnetic nanoparticles in silica matrix are chemically stable over a wide range of pH (pH 0-12). However, at pH values below 4 dissolution of the LDH starts and at pH 1 the LDH is dissolved. In the lab scale experiments performed, particle loss after four adsorption / desorption cycles (dry weight) for 20 and 40 wt% LDH @ magnetic particles was about 3-5 % (for experiments as depicted in figure 64), indicating that particles can be magnetically recovered and LDH is slightly detached or dissolved from the magnetic particles. For 60 wt% LDH load losses are significantly higher.

[31] The content of this chapter is the work of Asya Drenkova-Tuhtan (University Stuttgart) and is reprinted here with the permission of her. The chapter is part of the work submitted to *Water Research* for publication. The submitted title is "*Phosphate recovery from wastewater using engineered superparamagnetic particles modified with layered double hydroxide ion exchangers*".

For a technical application, e.g. in a waste water treatment plant, less LDH loading (e.g. 10-20 wt%) might be favourable to ensure that particles are not lost and can fully be magnetically recovered after each cycle.

To further demonstrate the reusability potential of the particles, a laboratory experiment with 15 adsorption / desorption cycles was designed and performed with two 1 l reactors, operated in parallel under the same conditions, with the only difference that in one case a fresh desorption solution was used in each cycle, and in the other case the same desorption solution was reused every time targeting phosphate enrichment. Particles concentration in each reactor was 1 g/l (400 mg/l LDH), pH was maintained at 4.5 and adsorption contact time was set to 1 h. Desorption took place for 30 min in 1M NaOH + 1M NaCl in a separate reactor with the same volume. This desorption solution was identified to achieve the highest desorption rates.[32]

Figure 67a shows the adsorption of phosphate for the 15 cycles, and figure 67b the desorption. Adsorption of 100 % corresponds to complete removal of the initial 10 mg/l PO_4-P. Desorption rates were calculated as a ratio of the desorbed to the adsorbed amount of phosphate. The adsorption rates slightly dropped to finally 76 %, respectively 62 % efficiency for the last cycle in each reactor. The desorption rates in the reactor with the fresh solution fluctuated between 62 % and 98.5 % with an average of 86 %. At the same time, phosphate was cumulatively concentrated by a factor of 11 in the desorption solution that was repeatedly reused in every cycle, corresponding to 95 % recovery of the total adsorbed phosphate, i.e., 83.5 % of the total mass of PO_4-P (133 mg) dosed into the system.

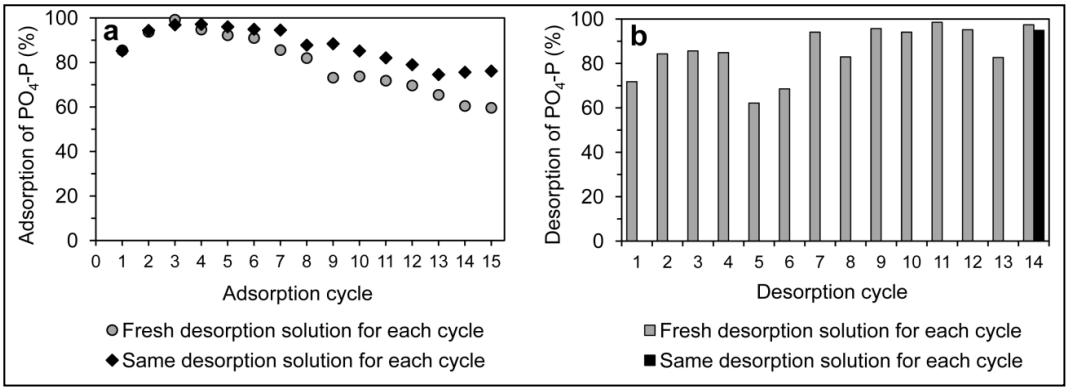

Figure 67: Reusability of the particles in (a) 15 adsorption and (b) 14 desorption cycles with enrichment of the desorption solution.

[32] Experimental design, measurements and evaluation of desorption solutions were performed by Asya Drenkova-Tuhtan (University Stuttgart) and results are submitted to *Water Research* for publication. The submitted title is "*Phosphate recovery from wastewater using engineered superparamagnetic particles modified with layered double hydroxide ion exchangers*".

Pilot-scale tests with MgFe-Zr LDH @ magnetic particles[33]

As a first approach to upscale the method developed in this work, particles were used to treat a total of 125 l waste water in 5 consecutive cycles under the already established optimal reaction conditions via application of a high gradient magnetic filter (HGMF). The pilot-scale setup and a photograph is shown in figure 68.

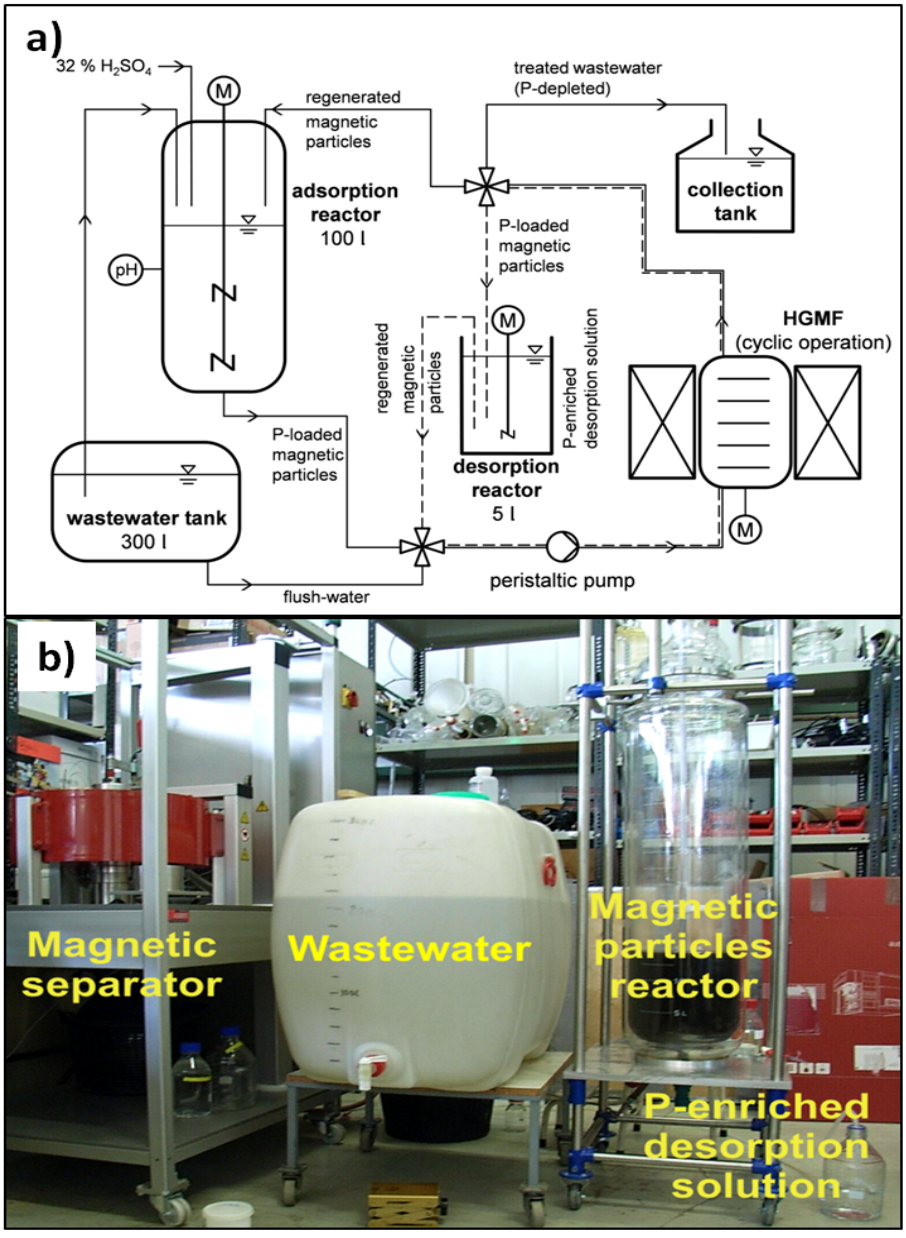

Figure 68: Principle sketch of the pilot-scale setup with HGMF (a) and a photograph of the real setup (b).

[33] The content of this section is the joint work of Asya Drenkova-Tuhtan (University Stuttgart), Karl Mandel and Anja Paulus (Karlsruhe Institute of Technology). Figure 68a is used with permission of Anja Paulus (Karlsruhe Institute of Technology), Figure 69 is used with permission of Asya Drenkova-Tuhtan (University Stuttgat). The chapter is part of the work submitted to *Water Research* for publication. The submitted title is "*Phosphate recovery from wastewater using engineered superparamagnetic particles modified with layered double hydroxide ion exchangers*".

The waste water was spiked with phosphoric acid (15 mg PO_4-P/l) and in every cycle 25 l of waste water were introduced into a well-mixed adsorption reactor and left in contact with the composite magnetic particles (concentration 400 mg/l LDH) for 45 min, where pH was continuously maintained at 4.5. Then the 25 l mixture of waste water and phosphate loaded particles was pumped for 15 min through the HGMF by retaining the particles inside the separator and discharging the phosphate depleted waste water into a side collection tank. The first three desorption cycles took place directly inside the small HGMF chamber (1 l desorption solution, 1M NaOH + 1M NaCl). The regenerated particles were flushed with fresh waste water and re-introduced into the adsorption reactor for a new cycle. It is obvious from figure 69a that this strategy did not result in good desorption rates (< 30 %), therefore the following two cycles were performed in an exterior desorption tank with 2.5 l of solution, which improved the desorption efficiency to almost 70 % in the last cycle.

The magnetic separation efficiency of the particles in every cycle was always > 99 %. The loss on particles was calculated based on the measured dry substance concentration. The total loss of dry substance after 5 cycles was only 3 %, most likely due to partial detachment of LDH from the particle surface.

The adsorption rate was relatively high in cycle 1 (75 %), followed by a sharp reduction in the following two cycles probably due to incomplete desorption in cycles 1-3. In cycle 4, adsorption was deliberately carried out overnight for 14 hours at pH 7 to test if P-uptake is possible at neutral pH and longer contact time. This had a positive impact and improved the adsorption by almost 15 % (figure 69a). The last adsorption cycle was performed in the same manner like cycles 1-3 and again a drop in performance was observed.

In total, only 277 mg PO_4-P were recovered out of almost 1900 mg PO_4-P dosed into the system (figure 69b). The total efficiency of the pilot-scale test after 5 cycles is much lower (46 % adsorption and 32 % desorption) compared to the lab-scale experiment after 14 cycles (88 % adsorption and 95 % desorption). There might be several reasons for this. The waste water used for this pilot-scale experiment had a higher total suspended solids concentration (16 mg/l TSS) and a higher conductivity (1595 µS/cm) than the waste water used in the lab-scale tests (4 mg/l TSS and 820 µS/cm). This implies more suspended solids and ions (especially SO_4^{2-} and Cl^-), which compete with phosphate for the adsorption sites in the LDH structure. On the other hand, certain amount of LDH might have been detached and lost from the particles due to stronger shear forces inside the HGMF or dissolved due to local corrosive conditions during acid dosage into the reactor.

Last but not least, the worse performance might be attributed to incomplete desorption, probably due to insufficient contact volume, especially in the first three cycles where the ratio of the adsorption vs. desorption volume was 25:1, resulting in a 25 times increase of the particles concentration in the desorption phase and fast depletion of the desorption solution.

Suggestions for improvement of the performance may involve reduction of the LDH fraction attached on the particles to 10 wt%, which might make the loss of LDH due to shear forces in a HGMF more unlikely. This might even allow the use of a drum separator with permanent magnets that would make the process cheaper compared to the HGMF which requires strong electromagnets and cooling. As a further improvement, an LDH system has to be developed which allows fast P-adsorption kinetics even at neutral pH to avoid the need for acid treatment of the waste water, possibly causing LDH dissolution and subsequent performance drop.

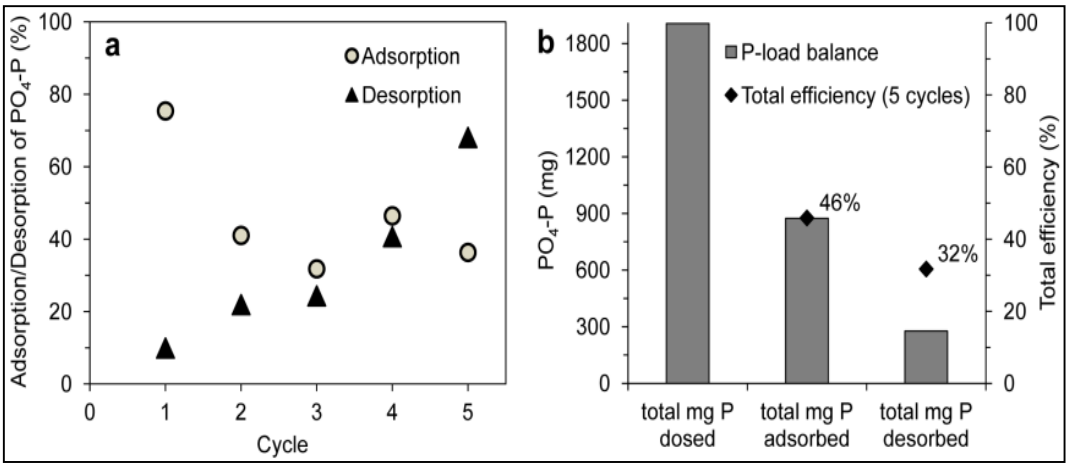

Figure 69: Pilot-scale test results: a) phosphate adsorption / desorption rates of each cycle and b) total efficiency after 5 cycles.

4.3.4 Heavy metal removal via magnetic seedparticles for floc-precipitation[34]

Superparamagnetic nanocomposite particles are not only useful magnetic scavengers if their surface is modified with dedicated adsorbers. This last chapter is intended to demonstrate their potential also as seeds to carry precipitates, formed in waste water. Exploiting the acid stability of the particles, a process was developed to enrich heavy metals, originally highly diluted in water, via magnetic seeding-flocculation and recovery in an acid solution. Following this strategy, a reusability of the magnetic particles is achievable. Water cleaning is possible and the concentration of heavy metals in acid might pave the way to apply a recently published method to electrowinning and thus recycle the metals from this acid solution for further use.[37]

The nanocomposite microparticles are negatively charged due to their silica surface over a wide range of pH. Precipitated iron hydroxide flocs possess a positive zeta potential from pH 2 to around 7.5. Thus, electrostatic attraction may contribute to hydroxide precipitation on the silica surface (figure 70).

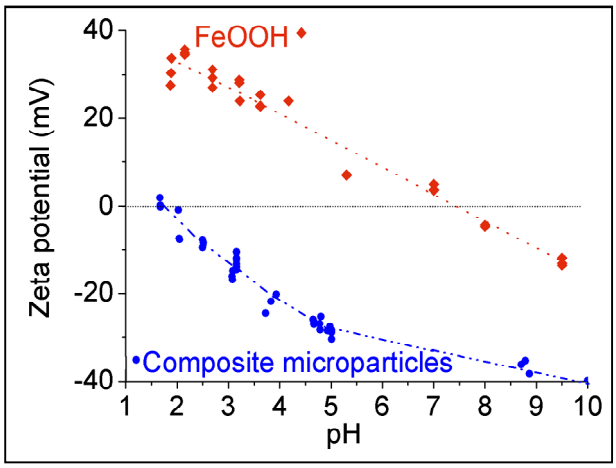

Figure 70: pH dependence of zeta potentials of magnetic seed particles (composite microparticles) and precipitated iron hydroxide.

Flocculation of added (dissolved) iron salt in a heavy metal containing solution (mixture of Cd, Cr, Cu, Pb, Zn, As, Hg) in presence of suspended superparamagnetic composite particles, by raising the pH of the solution from 4 to approximately 8, yields a completely magnetically separable product after 1 to 5 min (figure 71). A visibly clear aqueous solution remains (figure 71d). Without the magnetic particles the flocculated precipitate cannot be separated magnetically.

[34] This chapter has been published and is reused in this work by courtesy of Elsevier.
Original article: K. Mandel et al., *Sep. Purif. Technol.*, 2013, **109**, 144.

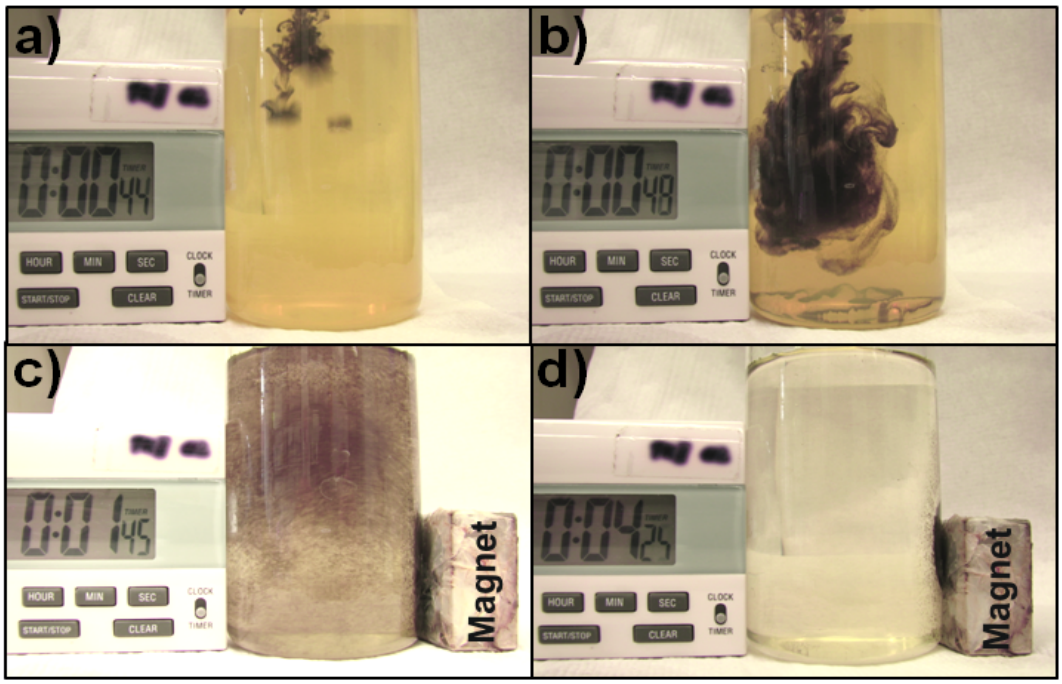

Figure 71: a) and b): Addition of Fe(III) salt solution and magnetic composite particles to a heavy metal ion solution, c) and d): Magnetic separation of the precipitates after pH increase to 8.

The magnetically separated product is treated in a small volume of hydrochloric acid to dissolve iron hydroxide and coprecipitated heavy metal ions. Cleaned magnetic composite particles are again magnetically separated and then reused in the next precipitation step (figure 72).

It should be mentioned that before reusing the particles as seeds again, an additional washing step (with a very small amount of deionised water) is applied to avoid any carry over of the acidic heavy metal solution into the water that shall be purified. This might be critical in a technical (large scale) process: Adding the acidic heavy metal containing wash water to the recovery solution will lead to dilution; discharging it into the water, that is meant to be purified, will lead to acidification of this water and a circulation of heavy metal ions. The latter also holds if the washing step is completely skipped. However, process solutions might be found to minimise this problem.

Figure 72 also shows two scanning electron microscopy (SEM) images of individual superparamagnetic nanocomposite microparticles. In the top image the particle is covered with the flocculated iron hydroxide containing heavy metals. Energy dispersive X-ray analyses (EDX) of the flocculated product on the particle confirms its heavy metal load (inset figure 72). The bottom SEM image depicts a magnetic particle after acid treatment where the heavy metals were successfully removed (EDX inset).

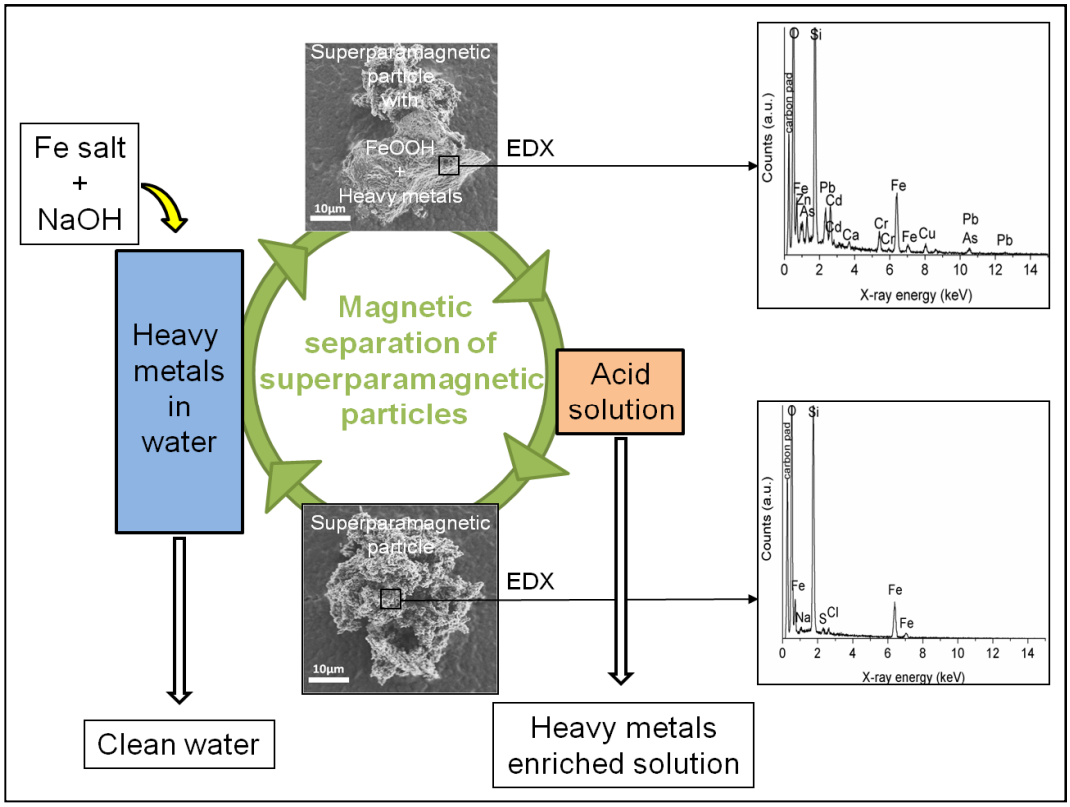

Figure 72: Scheme for removal and recovery of heavy metal ions from an aqueous solution (SEM images and EDX analyses show the precipitate of iron hydroxide and heavy metal ions on a magnetic composite particle and their absence after acid treatment).

Remaining concentrations (given in percent of starting concentrations, equal to approximately 1 mg/l for each ion) of heavy metal ions after precipitation and magnetic separation are shown in figure 73a for three water cleaning cycles with the same magnetic particles. With the exception of Hg, more than 95 % (often more than 99 %) of the heavy metals could be removed. Remaining concentrations are below 10 ppb. The difficulties to remove Hg might be related to a prevailing polyhydroxy complexe for this element. Such complexes are known to hardly precipitate with the ferric floc.[24]

Very similar results were also observed for starting concentrations of 100 mg/l for each kind of ion and with the same dosed amount of Fe(III) salt solution and magnetic composite particles, indicating the good precipitation and separation capacity. The remaining concentration of Fe ions in water after magnetic separation was typically 0.04 mg/l in all cases.

It is worth noting that when magnetic particles had been modified with precipitated iron hydroxide *before* being added to the heavy metal solution, the removal of the heavy metal ions (after 10 min) was considerably less effective. The same holds for adsorption on the nanocomposite particles (without any iron hydroxide). Furthermore, only less than 20 % of

heavy metal ions could be removed by the nanocomposite particles, if the pH of the water, after addition of the iron salt solution, was too low for the setting in of flocculation of iron hydroxides. Therefore, it seems that it is the *incorporation / coprecipitation* of heavy metals during the in situ flocculation of iron hydroxide that leads to scavenging of heavy metals rather than any surface adsorption processes.

After each of the three precipitation / separation steps, the magnetic composite particles were recovered in a small volume (10 ml) of hydrochloric acid. The acid dissolved the precipitates from the surface of the composite particles, but not the particles themselves due to their acid resistant silica surface. Using the same acid solution over and over again, it was possible to concentrate the heavy metals in this small amount of solution. Ion concentrations in the acid were determined exemplarily after the third cleaning step. The factors of concentration increase for each kind of metal ion are given in figure 73b (for comparison, the heavy metal concentration in water, set to 1, is also shown). Concentrations increase typically by factors of 20 to 23 after only three cycles, indicating the impressive potential of the process to concentrate formerly highly diluted heavy metals. Unavoidably, Fe ions are enriched in the cleaning solution up to 250 mg/l. A separation of the different heavy metals from the iron content in the cleaning solution might be possible by electrowinning, as recently published.[37]

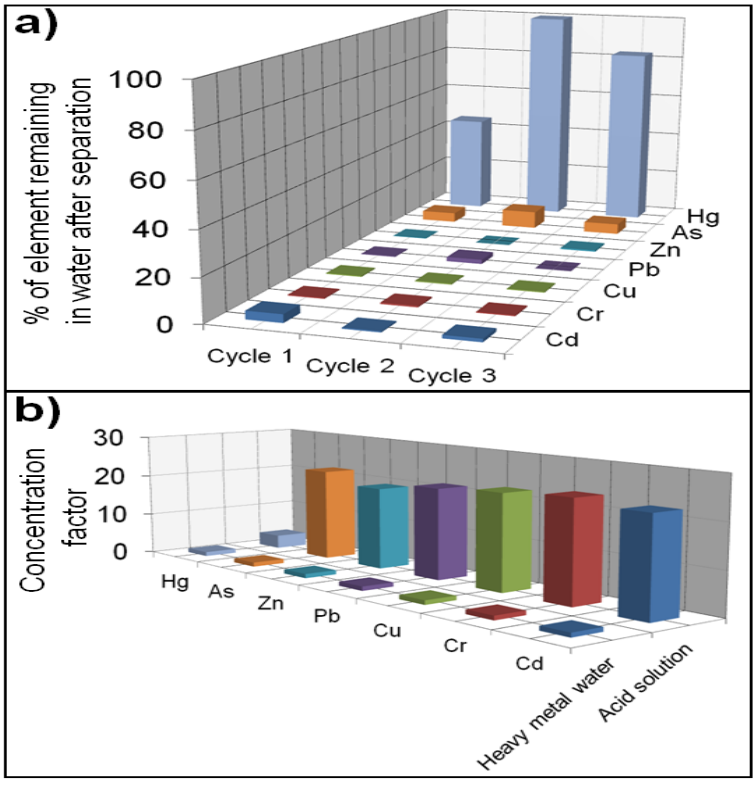

Figure 73: a) Percentage of remaining ion concentrations after three precipitation / separation cycles with the same magnetic composite particles. b) Factors of concentration-increase in the cleaning acid after three recovery steps.

5. SUMMARY AND OUTLOOK

Increasing living standards and a growing global population are linked to a rising demand of resources, for instance, among others, of precious metals or nutrients such as phosphate. Their natural deposits are increasingly exploited to satisfy the growing demand. This will lead to scarcity of many important elements in the future, unless processes are developed to regain the substances from all kinds of drains, they are dissipated to, during or after their use.

One of these drains is water, which might be a considerable future source from which to recover dissolved substances again for reuse. The extraction of diluted substances might furthermore not only help to stop their dissipative loss, but also to purify water, which, after all, is our most important and most valuable resource that needs to be kept clean for being drinkable.

In this work, the use of dedicated magnetic carrier particles for this challenge is suggested and their development and a proof of concept was the topic of this thesis.

Novel, superparamagnetic nanocomposite microparticles with a chemically modified surface were designed to act as scavengers for dissolved substances in water when the particles are dispersed in it. Magnetic separation of the particles with their load allows purification of the water and by subsequent regeneration of the particles the recovery of the substances, e.g. valuable resources, is rendered possible. The nano effect superparamagnetism is exploited to use such particles as switchable magnets: In presence of an external magnetic field, they behave like reasonably strong magnets and are attracted by a magnetic gradient, but as soon as the field is removed, no magnetisation remains. Due to their superparamagnetic behaviour, an agglomerate-free redispersion in water is easily feasible so that the whole procedure can be repeated.

In a batch, as well as in a continuous process, undefined, loose agglomerates (with a broad size distribution of 1-200 µm) of superparamagnetic nanoparticles (diameter ~10 nm) were precipitated from dissolved iron salts. These agglomerates were dispersed to a sol (dispersion of individual nanoparticles, hydrodynamic diameters 10-20 nm) with nitric acid.

The structure of the as-precipitated and moreover of the nitric acid peptised particles was investigated with X-ray methods (XRD, XANES, EXAFS, SAXS). Both types of nanoparticles (as-precipitated and nitric acid stabilised) were found to have the same formal valence as magnetite (Fe_3O_4).

By X-ray studies, in combination with HRTEM investigations, it was possible to state that the nitric acid treated particles are surface-etched.

Randomly directed Brownian forces exceed the force of a magnetic field gradient (e.g. from a handheld magnet) acting on individual nanoparticles, therefore preventing their separation from a fluid. Instead, the whole sol (a so-called ferrofluid) is magnetically responding to a magnetic field gradient. For the envisaged application of water purification and resources recovery however, separable carrier particles are needed. Therefore, well-defined nanocomposite microparticles were prepared by confining the nanoparticles into a silica matrix. The nano property superparamagnetism is thereby successfully transferred to the micron scale and the particles are, due to their size, easily magnetically separable from a fluid.

For the preparation of the microparticles, the nitric acid dispersed nanoparticles were at first stabilised with either lactic acid (LA) or the polycarboxylate ether polymer MELPERS4343 (MP) to avoid uncontrolled agglomeration during change of pH or addition of other chemicals in the course of the microparticle synthesis. The electrosteric repulsion mechanism for MP modified nanoparticles was studied in detail.

The stabilised sols were reacted with two silica precursors (TEOS: tetraethoxysilane or SS: sodium silicate (water glass) solution). Not only from a hydrolysis and condensation reaction with TEOS (which is well known), but also via precipitation of silica from SS in an alkaline, ammonia and nitrate containing environment, it was possible to obtain chemically (pH 0-12) and mechanically stable superparamagnetic microparticles (average size 20 µm, saturation magnetisation 30 emu/g, specific surface area 75 m^2/g). This preparation process from SS is facile, fast, inexpensive and can be upscaled, which could be shown for the first stage.

The magnetic behaviour of the nanocomposite microparticles was characterised in dependence of the nanoparticle stabilisation (LA or MP) and silica matrix (from TEOS or SS). The stabilisation determines the distribution of the nanoparticles in the composite (as revealed by TEM) and their magnetic interactions (examined by ZFC / FC measurements). Independent of the silica matrix, a stabilisation with LA results in a more homogenous distribution and a more uniform magnetic interaction of nanoparticles than is the case for MP stabilisation. In the latter case, clustered regions of nanoparticles were found in the composites. It is argued that the magnetic interaction of nanoparticles within clusters of different sizes can be revealed by ZFC / FC measurements and that, therefore, such measurements could be used to deduce information on nanoparticle distribution in composites.

For applications as magnetically separable scavengers the surfaces of nanocomposite microparticles were modified in following ways.

A silanisation of the particles with (3-mercaptopropyl)trimethoxysilane yielded selective Hg(II) scavengers. From the impregnation with 2-hydroxy-5-nonylacetophenone ketoxime (LIX84), a particle system was obtained that was highly selective for Cu(II). Both modifications were tested in a solution of different heavy metals to demonstrate their selectivity. Regenerability and reusability of the particles were demonstrated.

Superparamagnetic microparticles were furthermore intertwined with an ion exchange system for the recovery of phosphate from waste water. Layered double hydroxides (LDH), clay minerals which can intercalate anions selectively, were precipitated from an aqueous solution in different compositions (MgAl, MgFe, MgAl-Zr and MgFe-Zr LDH) and investigated in detail with XRD, ICP-OES and DTA-TG. Deposition of the LDHs on the superparamagnetic microparticles was conducted by ultrasonic treatment in a batch process as well as in a continuous way, the latter by using an ultrasonic flow cell. The obtained composite particles show good magnetic separability and possess a specific surface area of around 100 m^2/g.

The particle systems were tested for selective phosphate removal from waste water. MgFe-Zr LDH @ magnetic particles showed the best phosphate uptake behaviour and selectivity and for this system, the adsorption kinetics (at different pH values) and the adsorption isotherm for phosphate were determined. Reusability of the particles was demonstrated for 15 adsorption / desorption cycles in a laboratory experiment. A first pilot-scale testing was conducted with 125 l waste water.

Moreover, superparamagnetic nanocomposite microparticles were applied as seeds for iron hydroxide precipitates. Flocculation of iron hydroxide is suitable to adsorb and entrap heavy metal ions dissolved in water. The flocculation product gets deposited on the surface of the nanocomposite microparticles. The switchable magnets can be separated from water together with their load by an external magnetic field gradient. In an acidic solution, particles are cleaned by dissolution of the iron hydroxide precipitate. The silica surface protects the superparamagnetic microparticles from dissolution, thus rendering their reuse as seeds and magnetic carriers possible. Repetition of the separation and recovery process leads to a significant increase in concentration of heavy metals in the acid cleaning solution, which paves the way for further recycling procedures of these elements.

In this work, the principle applicability of nanocomposite microparticles for water purification and resources recovery was demonstrated. As a prerequisite for real, technical application of the particles, their synthesis process must be optimised for a large scale production. Moreover, focus must be put on systematic research on the particles' surface functionalities. It will be necessary to monitor the loss of the functional surface molecules, or in case of phosphate recovery, of the LDH, during a repeated use of the particles and furthermore to gain a better understanding of the bonding mechanism of the functional molecules (or compounds) with the particle surface. With these studies, it might be possible to improve the stability of the surface modifications and reduce their losses. This is particularly important for the LDH system, where a drop in adsorption performance, observed during the first pilot-scale test, might have had one cause in the partial depletion of LDH. Moreover, the influence of the composition of different waste waters on the particles' adsorption performance and selectivity needs to be studied more systematically. Last but not least, it has to be demonstrated how the recovered resources in solution can actually be finished to a new product, for instance how separated phosphate can be turned into fertiliser or concentrated heavy metal solutions into solid metals. In this connection, it will be crucial at first to optimise the desorption and recovery process to obtain enriched resources in quantity and quality beyond what has been obtained by the first proof of concept results, presented in this work.

As a general future prospect, it can be stated that the particles could serve as a technology platform for a wide variety of all kinds of applications (figure 74). Suitable, novel, surface modifications might equip the particles with (selective) scavenging potential for a wide variety of inorganic (e.g. heavy metals) or organic (drugs, pesticides etc.) trace substances. Valuable resources could be recovered from process waters especially when the magnetic separation principle is combined with electrowinning techniques. In the field of biotechnology, modified particles might also find their application, despite of the competition with other, already existing particle systems, as the production of the developed particles might be possible on a larger scale and with less expensive chemicals than yet employed. Another interesting field of research is the augmentation of a sensing signal with the aid of the particles: highly diluted substances could be trapped by the particles and subsequently transported and concentrated at a sensor spot where a signal (fluorescence, light absorption, electrochemical potential shift etc.) is monitored and related to a specific substance bound to the particles, which is thereby detected.

Finally, but by no means the last conceivable application, it might be promising to immobilise valuable inorganic (e.g. metals from the platinum group) or bio-organic (e.g. enzymes) catalysts on the particles' surface. Finely dispersed heterogeneous catalysts in a fluid might be suitable to promote fast reactions as diffusion pathways of reactants are kept short. By using magnetic separation, the recovery and reuse of the catalyst could be possible.

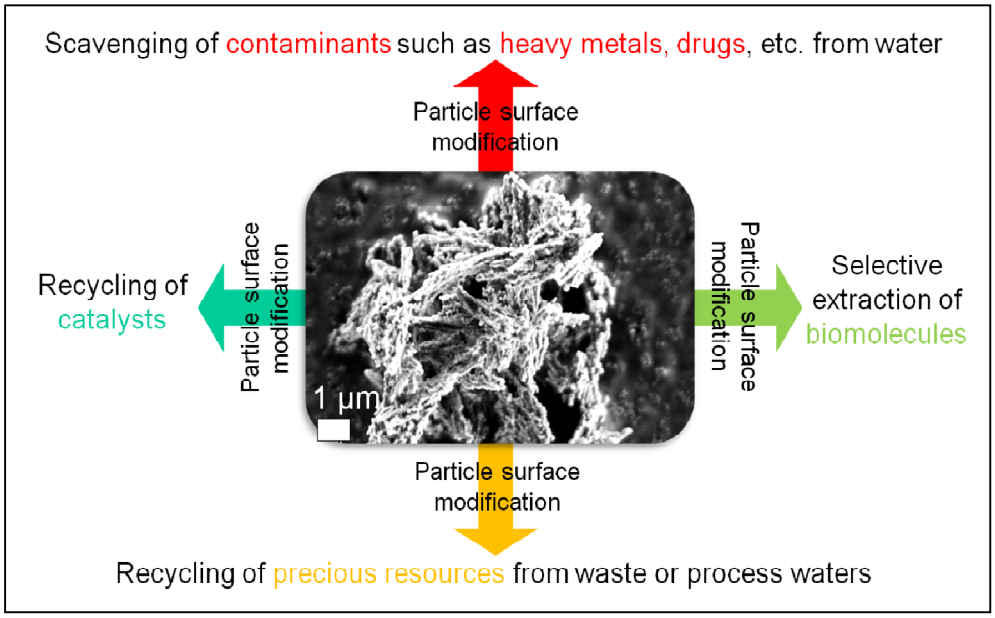

Figure 74: Examples of potential application fields of superparamagnetic nanocomposite microparticles.

6. ZUSAMMENFASSUNG UND AUSBLICK

Ein weltweit steigender Lebensstandard und eine immer weiter wachsende Bevölkerung gehen einher mit einem zunehmenden Bedarf an Rohstoffen, unter anderem beispielsweise an wertvollen Metallen oder Nährstoffen wie Phosphat. Deren natürliche Reserven werden mehr und mehr ausgebeutet, um die Nachfrage zu befriedigen. Dies kann in Zukunft zu einer Verknappung vieler wichtiger Elemente führen. Um dem entgegen zu wirken, müssen Prozesse entwickelt werden, durch die eine Dissipation dieser Stoffe verhindert und eine Rückgewinnung ermöglicht wird.

Eine der Senken für Wertstoffe in gelöster Form ist Wasser, welches damit zu einer beachtenswerten zukünftigen Quelle rückgewinnbarer Rohstoffe werden könnte. Die Extraktion darin gelöster Stoffe würde zudem nicht nur dazu beitragen, deren Dissipation und damit Verlust zu stoppen, sondern auch das Wasser selbst – welches letztendlich unser wertvollster Rohstoff ist – zu reinigen und so beispielsweise als Trinkwasser wieder nutzbar zu machen.

Eine Möglichkeit dieser Herausforderung zu begegnen, ist der Einsatz von maß-geschneiderten Magnetträgerpartikeln. Deren Entwicklung und Nachweis ihrer prinzipiellen Einsetzbarkeit für Wasserreinigung und Wertstoffrückgewinnung war die Zielsetzung dieser Arbeit.

Dafür wurden neuartige, mikrometergroße, superparamagnetische Nanokomposit-mikropartikel synthetisiert. Mit einer entsprechenden chemischen Modifikation ihrer Oberfläche können solche Partikel genutzt werden, um im Wasser gelöste Substanzen einzufangen. Nach einer magnetischen Abtrennung ist das Wasser von diesen Stoffen befreit. Durch eine anschließende Regeneration der Partikel werden z.B. Wertstoffe zurückgewonnen. Der Nanoeffekt Superparamagnetismus wird ausgenutzt, um solche Partikel magnetisch zu schalten. In einem äußeren Magnetfeld werden sie magnetisiert und von einem Feldgradienten angezogen; ohne Feld aber verschwindet die Partikel-magnetisierung vollständig. Dadurch sind die Partikel ohne magnetische Agglomeration redispergierbar, so dass der gesamte Prozess mehrfach wiederholt werden kann.

In einem Batch-, sowie einem kontinuierlichen Syntheseverfahren wurden undefinierte, lose Agglomerate (mit einer breiten Größenverteilung von 1-200 µm) von superparamagnetischen Nanopartikeln (Durchmesser ~10 nm) aus einer Eisensalzlösung gefällt. Die Agglomerate wurden mit verdünnter Salpetersäure zu einem Sol (Dispersion von Nanopartikeln, mit einem hydrodynamischen Durchmesser von 10-20 nm) dispergiert.

Die Struktur der gefällten, sowie der salpetersauer peptisierten Nanopartikel wurde mit Röntgenmethoden (XRD, XANES, EXAFS, SAXS) untersucht. In beiden Fällen liegt Magnetit (Fe_3O_4) vor. Durch Röntgenanalysen, in Kombination mit HRTEM Untersuchungen, konnte zudem aufgezeigt werden, dass die peptisierten Partikel oberflächlich angeätzt sind.

Ungerichtete Brown‘sche Kräfte, die auf dispergierte Nanopartikel wirken, sind (normalerweise) deutlich größer als die eines Magnetfeldgradienten (z.B. eines Handmagneten), weshalb eine Abtrennung der Nanopartikel aus einem Fluid so nicht möglich ist. Vielmehr wandert das gesamte Sol - ein sogenanntes Ferrofluid – im Magnetfeldgradienten. Im Hinblick auf die angestrebte Anwendung der Wasserreinigung und Wertstoffrückgewinnung werden jedoch separierbare Trägerpartikel benötigt. Aus diesem Grund wurden die Nanopartikel in eine Silicamatrix eingebunden, um so mikrometergroße Kompositpartikel zu erhalten. Der Superparamagnetismus wird dabei auf die Mikrometerskala übertragen. Die Partikel dieser Größe sind sehr gut abtrennbar.

In Vorbereitung auf die Mikropartikelherstellung wurden die dispergierten Nanopartikel zunächst mit Milchsäure (LA) oder dem Polycarboxylatetherpolymer MELPERS4343 (MP) stabilisiert, um eine unkontrollierte Agglomeration bei der Synthese der Silicamatrix (durch pH-Änderung oder Chemikalienzugabe) möglichst zu verhindern.

Der elektrosterische Abstoßungsmechanismus der MP modifizierten Nanopartikel wurde im Detail untersucht.

Die stabilisierten Sole wurden mit zwei Silicaprekursoren zur Reaktion gebracht (TEOS: Tetraethoxysilan bzw. SS: Natriumsilikatlösung (Wasserglas)). Nicht nur durch die Hydrolyse-Kondensationsreaktionen von TEOS, sondern auch durch Fällung von Silica aus SS in einer ammoniakalischen Umgebung in Anwesenheit von Nitrat können chemisch (pH 0-12) und mechanisch stabile, superparamagnetische Nanokompositmikropartikel erhalten werden (durchschnittliche Größe: 20 µm; Sättigungsmagnetisierung: 30 emu/g; spezifische Oberfläche: 75 m^2/g). Das dafür entwickelte, wasserglasbasierte Verfahren ist einfach, schnell, kostengünstig und aufskalierbar.

An den verschiedenen Nanokomposit-Partikelsystemen wurde untersucht, in wieweit die Stabilisierung (LA oder MP) und die Silicamatrix (basierend auf TEOS oder SS) Einfluss auf magnetische Eigenschaften haben. Die Stabilisierung der Nanopartikel bestimmt deren Verteilung in der Matrix (TEM) und damit deren magnetische Wechselwirkungen (ZFC / FC Messungen). Unabhängig von der Silicamatrix lagen LA stabilisierte Nanopartikel homogener verteilt vor, woraus eine einheitlichere magnetische Interaktion im Vergleich zu MP stabilisierten Nanopartikeln resultierte. Bei MP modifizierten

Nanopartikeln wurde eine Clusterung in den Kompositen beobachtet. Es konnten Indizien für eine Polydispersität der Cluster anhand von Messung der magnetischen Interkationen mittels ZFC / FC Untersuchungen gefunden werden. Solche Messungen könnten generell genutzt werden, um die Verteilung von Nanopartikeln in Kompositen zu ermitteln.

Für Anwendungen als magnetisch abtrennbare Fängerpartikel wurden die Oberflächen der Nanokompositmikropartikel auf folgende Weise modifiziert.

Selektive Adsorption von Hg(II)-Ionen wurde durch eine Silanisierung mit 3-Mercapto-propyl-trimethoxysilan erreicht. Eine hohe Selektivität für Cu(II)-Ionen wurde durch Imprägnierung der Partikel mit 2-Hydrox-5-Nonylacetophenon Ketoxim (LIX84) erzielt. Die Affinität beider Modifikationen zu ihren Zielionen gegenüber anderen Elementen wurde in einer Lösung von unterschiedlichen Schwermetallionen getestet. Die Partikel wurden regeneriert und mehrfach wiederverwendet.

Für die Rückgewinnung von Phosphat aus Abwasser wurde ein Ionentauscher auf die Partikel aufgebracht. Dazu wurden Layered double hydroxides (LDH), Tonminerale welche selektiv Anionen interkalieren können, aus wässrigen Lösungen in verschiedenen Zusammensetzungen ausgefällt (MgAl, MgFe, MgAl-Zr, MgFe-Zr LDH), mit XRD, ICP-OES und DTA-TG untersucht und durch Ultraschallbehandlung auf den Mikropartikeln deponiert. Dies war sowohl im Batch- als auch in einem kontinuierlichen Verfahren (Ultraschalldurchflusszelle) möglich. Die so erhaltenen Kompositpartikel sind gut magnetisch separierbar und haben eine spezifische Oberfläche von ca. 100 m^2/g. Die Partikelsysteme wurden in Abwasser auf ihre Phosphatadsorptions-Kapazität und -Selektivität getestet. Für das beste System (MgFe-Zr-Mikopartikelsystem) wurde die Adsoprtionskinetik bei verschiedenen pH-Werten, sowie die Adsorptionsisotherme bestimmt. Die Wiederverwendbarkeit der Partikel wurde in 15 Adsorptions-Desorptions-zyklen im Labormaßstab demonstriert. Zudem wurde ein erstes Pilotanlagenexperiment mit 125 l Abwasser durchgeführt.

Unmodifizierte Nanokompositmikropartikel wurden als Flockungshilfsmittel für eine Eisenhydroxid-Fällung verwendet. Durch sie werden in Wasser gelöste Schwermetallionen mitgefällt und eingefangen. Der Niederschlag bildet sich bzw. adsorbiert auf der Oberfläche der Mikropartikel und wird zusammen mit ihnen in einem Magnetfeld-gradienten abgetrennt. In einer sauren Regenerationslösung werden die Partikel durch Auflösen der Hydroxidflocken gereinigt. Dabei schützt die Silicaoberfläche die superparamagnetischen Magnetitpartikel vor der Säure. Die Mikropartikel werden erneut eingesetzt. Eine Wiederholung des Abtrenn- und Regenerationsprozesses führt zu einer Anreicherung der Schwermetallionen in der Waschlösung, wodurch der Weg für ein anschließendes Recylcingverfahren bereitet wird.

In der vorliegenden Arbeit wurde die prinzipielle Funktionalität von superparamagnetischen Nanokompositmikropartikeln für die Wasserreinigung und Rückgewinnung von Wertstoffen gezeigt. Eine Voraussetzung für eine technische Anwendung der Partikel ist die Optimierung des Syntheseprozesses für ihre großmaßstäbliche Herstellung. Des Weiteren ist die systematische Untersuchung der Oberflächenfunktionalisierungen wichtig. In diesem Zusammenhang sollte der Verlust an funktionellen Gruppen, bzw. im Falle von Phosphatrecycling der Verlust an LDH, genau nachverfolgt werden. In Kombination mit einem besseren Verständnis der Verknüpfungsmechanismen der funktionellen Moleküle (oder Verbindungen) mit der Oberfläche der Partikel könnte es so möglich sein, die Verknüpfungsstabilität zu verbessern und damit Verluste zu verringern oder zu vermeiden. Das gilt vor allem für das LDH System, da Ablösen von LDH, während der Durchführung des ersten Pilot-Versuchs zur Phosphatrückgewinnung, eine der möglichen Ursachen für eine Verminderung der Phosphatadsorptionsleistung gewesen sein könnte. Darüber hinaus sollte der Einfluss unterschiedlicher Abwasserchemie auf das Adsorptionsverhalten und die Selektivität der Partikel untersucht werden. Zu guter Letzt gilt es einen Weg zu finden, wie die angereicherten Wertstofflösungen tatsächlich in nutzbare Produkte überführt werden können, beispielsweise Phosphat in Düngemittel oder Schwermetalllösungen in Metalle. In diesem Zusammenhang wird es entscheidend sein, zunächst den Desorptions- und Rückgewinnungsprozess zu optimieren um angereicherte Wertstoffe in einer Quantität und Qualität zu bekommen, die über das, was in den ersten Ergebnissen in der vorliegenden Arbeit zur prinzipiellen Machbarkeit des Verfahrens gezeigt wurde, hinausgeht.

Grundsätzlich stellen die Partikel eine Technologieplattform für eine Vielzahl von Anwendungsfeldern dar (Abbildung 1). Geeignete (neue) Oberflächenmodifikationen der Partikel machen diese zu (selektiven) Fängern für eine Vielzahl anorganischer (z.B. Schwermetalle) oder organischer (z.B. Medikamentrückstände, Pestizide, etc.) Spurenstoffe in Wässern. Rückgewinnung von Wertstoffen aus Prozesswässern ist denkbar; in diesem Zusammenhang wäre es möglicherweise besonders attraktiv, wenn es gelänge das Prinzip der Magnetpartikelabtrennung mit elektrochemischen Abscheideverfahren zu kombinieren. Im Bereich der Biotechnologie könnten die Partikel ebenfalls Anwendung finden und - aufgrund der Kostengünstigkeit der Chemikalien, die zu ihrer Herstellung benötigt werden, sowie ihrem Aufskalierungspotential - zu anderen bereits bestehenden Partikelsystemen konkurrenzfähig sein. Ein weiterer interessanter Forschungsbereich ist Signalverstärkung mit Hilfe der Partikel: Hierbei ist angedacht, dass eine hochverdünnte Substanz in Lösung von den Partikeln eingefangen und durch ein Magnetfeld zu einem Sensor transportiert wird. Die Aufzeichnung eines Signals (Fluoreszenz, Lichtabsorption, elektrochemische Potentialänderung etc.), zurückgeführt auf den an die Partikel gebundenen Stoff, würde dessen Nachweis ermöglichen.

Als ein letztes Einsatzfeld das hier Erwähnung finden soll (neben noch vielen weiteren Möglichkeiten) könnte es lohnend sein, teure anorganische (z.B. Platingruppenmetalle) oder bioorganische (z.B. Enzyme) Katalysatoren auf den Partikeloberflächen zu immobilisieren. Feinverteilte Katalysatorpartikel in einem Fluid würden zu schnellen Reaktionsumsätzen führen, da die Diffusionswege der Reaktanten kurz sind. Durch Magnetseparation wäre die Rückgewinnung und Wiederverwendbarkeit der Katalysatoren aus den Reaktorlösungen auf einfache Weise möglich.

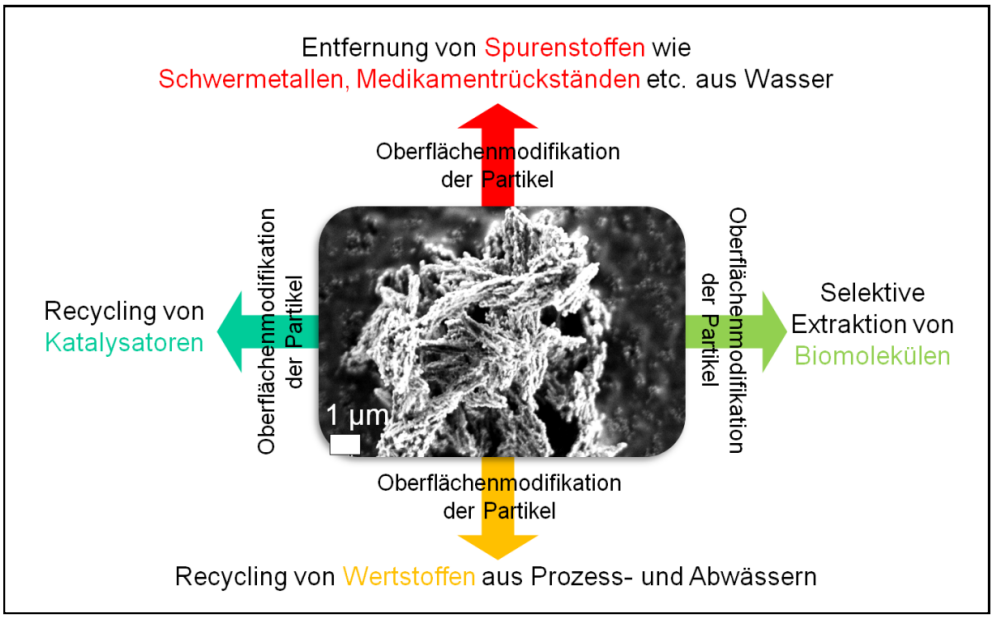

Abbildung 1: Beispiele potentieller Anwendungsfelder superparamagnetischer Nanokompositmikropartikel.

7. EXPERIMENTAL

7.1 Materials and Chemicals

All chemicals, if not otherwise indicated, were purchased from Sigma-Aldrich, Germany.

Separation of magnetic particles, if not otherwise indicated, was done with a handheld magnet (Supermagnet Q404020N, energy product: 330 kJ/m^3; or Supermagnet S4530N, energy product: 340 kJ/m^3; purchased from supermagnete.de).

Carbonyl iron particles (CIP)

Carbonyl iron powders were purchased from BASF (Germany):
CIP HS (D50 1.8-2.3 µm), pure Fe powder, no coating
CIP HQ (D50 2.0 µm), pure Fe powder, no coating
CIP EM (D50 4.5-6.0 µm), pure Fe powder, no coating
CIP EL (D50 5-6.5 µm), pure Fe powder, no coating
CIP CM (D50 9.5 µm), pure Fe powder, no coating
CIP SQ (D50 3.7-4.7 µm), Fe powder coated with SiO_2

Coating agents

tetraethoxysilane (TEOS, 98 %)
zirconium(IV) oxychloride octahydrate ($ZrOCl_2 \cdot 8H_2O$, 99.5 %)

Chemicals for the synthesis of nano zero valent iron (NZVI)

iron(III) chloride hexahydrate ($FeCl_3 \cdot 6H_2O$, >99 %)
sodium borohydride ($NaBH_4$, 99.99 %)

Chemicals for the synthesis and stabilisation of iron oxide nanoparticles

iron(III) chloride hexahydrate ($FeCl_3 \cdot 6H_2O$, >99 %)
iron(II) chloride tetrahydrate ($FeCl_2 \cdot 4H_2O$, >99 %)
ammonia solution (NH_3(aq), 28 wt%)
nitric acid (HNO_3, 1 M)
amino acids: L-arginine (>98 %), L-asparagine (>98 %), L-glutamine (>99 %)
sugars: D-glucose (>99 %), D-sucrose (>99 %)
hydroxy carboxylic acids: DL-malic acid (>99 %), L-tartaric acid (>99 %),
DL-lactic acid (90 wt% in water)
polycarboxylate ether MELPERS4343 42.9 wt% aqueous solution (BASF, Germany)

Chemicals for the synthesis of nanocomposite microparticles

tetraethoxysilane (TEOS, 98 %)
sodium silicate solution (water glass solution, 36 wt%, molar ratio of SiO_2:Na_2O = 3:1, corresponding $Na_2O \cdot 3SiO_2$, Fischar Chemicals, Germany)

For the larger scale (100 g composite particles) synthesis (Fischar Chemicals, Germany):
ammonia solution (NH_3(aq), 25 wt%)
nitric acid (HNO_3, 1 M, diluted from a 53 wt% solution)
L-lactic acid (80 wt% in water)

Chemicals for surface modification of nanocomposite particles

(3-aminopropyl)triethoxysilane (98 %)
(3-mercaptopropyl)trimethoxysilane (95 %)
trimethoxy(propyl)silane (97 %)
2-hydroxy-5-nonylacetophenone ketoxime (LIX84; 10 % in kerosene, BASF, UK)

Chemicals for the synthesis of layered double hydroxide

iron(III) chloride hexahydrate ($FeCl_3 \cdot 6H_2O$, >99 %)
magnesium chloride hexahydrate ($MgCl_2 \cdot 6H_2O$, >99 %)
aluminium chloride hexahydrate ($AlCl_3 \cdot 6H_2O$, >99 %)
zirconium(IV) oxychloride octahydrate ($ZrOCl_2 \cdot 8H_2O$, 99.5 %)

Chemicals for heavy metal adsorption tests

As(V) (H_3AsO_4)
$Cd(NO_3)_2 \cdot 4H_2O$, $Zn(NO_3)_2 \cdot 6H_2O$, $Cu(NO_3)_2 \cdot 3H_2O$, $Hg(NO_3)_2 \cdot H_2O$, ($Pb(NO_3)_2$)
$CrCl_3 \cdot 6H_2O$, $MgCl_2 \cdot 6H_2O$, $CaCl_2$ (all chemicals in high purity grade)
thiourea (>99 %) (regeneration agent), $FeCl_3 \cdot 6H_2O$ (>99 %) (flocculation agent)

Chemicals for phosphate recovery

orthophosphoric acid (H_3PO_4, 85 %), Merck KGaA, Germany
NaCl (>99 %), Merck KGaA, Germany

Chemicals for pH adjustment in solutions and ethanol as solvent

hydrochloric acid (HCl, 36 wt%)
sodium hydroxide (NaOH, solutions prepared from pellets, 98 %)
ammonia solution (NH_3(aq), 28 wt%)
ethanol (absolute, containing 1 % methyl ethyl ketone, CSC Jäklechemie, Germany)

7.2 Synthesis

All syntheses were conducted under normal atmosphere, i.e., without any inert conditions such as oxygen free environment. Wet-chemical syntheses were generally carried out in deionised water. All chemicals were used without further purification as received.

7.2.1 Synthesis and modification of micro and nano iron particles

SiO_2 coating of carbonyl iron

In a typical experiment to coat carbonyl iron particles with silica, 2 g CIP HS was stirred in 100 ml ethanol and 10 ml deionised water and 7 ml 28 % ammonia solution. 6.25 g (30 mmol) tetraethoxysilane (TEOS) were added. After 10 minutes, the dark grey suspension turned light grey, indicating the formation of SiO_2. The dispersion was stirred for 1 h before the particles were magnetically removed and washed three times with deionised water. Experimental variations included different amounts of CIP (1–8 g), different reaction times (0.5-2 h) and reaction temperatures (RT or 50 °C). Variations had no influence on the coating quality (acid dissolution tests) and were therefore not discussed in detail.

SiO_2-ZrO_2 coating

Typically, 2 g (6.2 mmol) $ZrOCl_2 \cdot 8H_2O$ dissolved in 10 ml ethanol and 10 ml deionised water were added dropwise 15 minutes after TEOS was added to CIP HS particles (see above). Experimental variations included different amounts of CIP (1-8 g), different reaction times (0.5-2 h) and reaction temperatures (RT or 50 °C). Variations had only negligible influence on the coating quality (acid dissolution tests) and were therefore not discussed in detail.

Evaluation of coating quality

Best experimental coating parameters were determined by ranking the samples according to their dissolution resistance in concentrated hydrochloric acid (36 %). The best samples were chosen for further investigation.

Quantitative comparison of the coating quality of the most promising samples was done by adding a known amount of particles to 1 l 1 M HCl. The particles were mechanically stirred for 2 h at 500 rpm. After 10, 30, 60 and 120 minutes, the magnetic particles were held in the solution with a magnet and 5 ml of the solution were taken for analysis of the dissolved Fe with ICP-OES.

Synthesis of nano zero valent iron (NZVI)

Synthesis attempts followed.[52] Typically, 1.8 g (47 mmol) $NaBH_4$ dissolved in a minimum of water were added to 3.24 g (12 mmol) $FeCl_3 \cdot 6H_2O$ dissolved in 250 ml water under stirring (300 rpm) at RT. Black, magnetically self-attracting precipitates immediately formed.

7.2.2 Synthesis and stabilisation of superparamagnetic iron oxide nanoparticles

Coprecipitation of superparamagnetic iron oxide nanoparticles

Following,[279] 2.16 g (8 mmol) $FeCl_3 \cdot 6H_2O$ and 795 mg (4 mmol) $FeCl_2 \cdot 4H_2O$ were dissolved in 100 ml water in air at 20 °C. 5 ml of aqueous ammonia solution (NH_3(aq), 28 %) were quickly added under stirring (300 rpm). Approximately 0.93 g of black precipitate was magnetically separable with a permanent handheld magnet after 1 min.

Continuous precipitation of superparamagnetic nanoparticles

Typically, 8.64 g (32 mmol) of $FeCl_3 \cdot 6H_2O$ and 3.18 g (16 mmol) of $FeCl_2 \cdot 4H_2O$ were dissolved in 100 ml water at 20 °C. 20 ml aqueous ammonia solution (25 %) were diluted with 100 ml water. The two solutions were mixed by pumping through 5 mm diameter silicon tubes using a peristaltic pump (Istatec BV-GES) into a Y-shaped gas tube connection (total length 31 mm) acting as a simple continuous flow reactor. Each arm (inner diameters 3 mm) of the connector had a length of 18 mm, the two supporting arms met at an angle of 55 °. The flow rate in each supporting channel was 100 ml/min. A black suspension formed in the outlet, from which the precipitate was separated using a handheld permanent magnet. Approximately 3.7 g nanoparticles were collected once the starting solutions had been totally consumed. A scale-up is possible by simply increasing the amount of starting solutions; there is no upper limit for the amount of particles that can be produced this way.

Preliminary in situ stabilisation

Preliminary in situ stabilisation experiments were carried out with amino acids (L-arginine, L-asparagine, L-glutamine), sugars (D-sucrose, D-glucose) or α-hydroxycarboxylic acids (DL-lactic acid, DL-malic acid, L-tartaric acid). Per usual, the respective stabiliser was added in amounts of 0.5-5 g to 2.16 g (8 mmol) $FeCl_3 \cdot 6H_2O$ and 795 mg (4 mmol) $FeCl_2 \cdot 4H_2O$ dissolved in 100 ml water and was present during precipitation with 5 ml aqueous ammonia solution (28 %). Temperature was varied between RT and 70 °C.

Sol formation with nitric acid

As-precipitated particles were typically washed 1-3 times with water and redispersed via stirring (300 rpm) in 0.5 M HNO_3. 0.93 g particles were normally dispersed in 5-20 ml. The colour of the dispersion turned black-brown.

Stabilisation of nitric acid dispersed nanoparticle sols

Amino acids (L-arginine, L-asparagine, L-glutamine), sugars (D-sucrose, D-glucose) or α-hydroxycarboxylic acids (DL-lactic acid, DL-malic acid, L-tartaric acid) were added in amounts of 0.5-2 g to 0.93 g nanoparticles dispersed in nitric acid. For DL-lactic acid, the added amounts were between 0.3 and 5 ml (3.6 and 60 mmol). Between 0.1 and 5 g of the MELPERS4343 solution were used. Optionally, mixtures were placed into an ultrasonic bath (Bandelin Sonorex Super RK103 Ultrasonic bath: 180 W, 35 kHz) for 20 min.

Evaluation of colloidal stability of nanoparticle sols

The stability of modified nanoparticle sols was evaluated qualitatively by raising the pH by addition of aqueous ammonia or sodium hydroxide solution or dropping the sols into ethanol or ethanol-ammonia solutions and observing potential flocculation / agglomeration. Quantitative evaluation was carried out by measuring the hydrodynamic radii of particles in the dispersions via DLS.

7.2.3 Synthesis of nanocomposites with a silica matrix from water glass or TEOS

Precipitation of unstable silica from water glass solution in an acidic medium

5 ml sodium silicate solution were added under stirring (300 rpm) to 10 ml 1 M nitric acid and 10 ml deionised water (at RT). Immediately, a solid precipitate formed that was filtered and washed three times and vacuum dried (50 °C, approx. 0.1 mbar, 2 h) for further analyses.

Nanocomposite particles with an unstable water glass based silica matrix

To a sol of stabilised nanoparticles (typically 0.93 g in 200 ml at pH 1, obtained from an aqueous nitric acid solution), 2 ml of sodium silicate solution were added under stirring (300 rpm). The resulting precipitate was separated magnetically after 60 s and washed three times with water. Variations included different dilutions of nanoparticle sols (0.93 g nanoparticles in 20-200 ml nitric acid solution) and different amounts of water glass solutions (0.2-13 ml) for precipitation.

Precipitation of stable silica from water glass solution in a basic medium

Stable silica from water glass was precipitated as follows: 20 ml 0.5 M of HNO_3 solution were mixed by stirring (300 rpm) with 20 ml ammonia solution (25 %) to increase the pH to 11-12. Sodium silicate (water glass) solution was slowly added under stirring (300 rpm) (molar ratios NH_3 : HNO_3 : $Na_2O{\cdot}3SiO_2$ = 27 : 1 : 0.4). The precipitate was filtered and washed three times. Precipitations were performed at RT and at 70 °C. The solid was vacuum dried (50 °C, approx. 0.1 mbar, 2 h) for further analyses.

Nanocomposite particles with a stable water glass based silica matrix

Well-defined water glass based silica nanocomposite microparticles were prepared as follows: 88 ml of ammonia solution (25 %) diluted in 80 ml deionised water were added to a stabilised nanoparticle sol (containing approximately 3.7 g nanoparticles). The mixture was heated to 70 °C in air with stirring (300 rpm). A sodium silicate solution (molar ratios NH_3 : HNO_3 : $Na_2O{\cdot}3SiO_2$ as before) was added slowly through a syringe needle. The reaction mixture was stirred for 5 min at 70 °C whereupon the product was magnetically removed and washed. Scale-up of the procedure by a factor of ten has been successfully conducted.

Experimental variations included different dilutions of nanoparticles (0.93 g nanoparticles stabilised with MELPERS4343 or lactic acid in 20-200 ml solution) different amounts of water glass (0.2-13 ml) and a variation of the temperature during silica precipitation (RT to 80 °C).

Nanocomposite particles with a TEOS based silica matrix

0.93 g nanoparticles, as agglomerates or dispersed in 20 ml 0.5 M nitric acid solution stabilised with either lactic acid (between 0.3 and 5 ml (3.6 and 60 mmol)) or MELPERS4343 solution (between 0.1 and 5 g), were reacted with 6.25 g (30 mmol) TEOS in 100 ml ethanol, 10 ml deionised water and 7 ml aqueous ammonia solution (28 %) by stirring (300 rpm) for 60 min.

Synthesis of nanocomposite particles for structural and magnetic characterisations

For structure and magnetic property studies, as discussed in *chapter 4.2.2*, four types of magnetic nanocomposite particles were synthesised from a stable ferrofluid (magnetite sol, see "*Sol formation with nitric acid*"): Nanoparticles were stabilised either with Melpers4343 (MP) or lactic acid (LA) and then incorporated into a silica matrix formed either from tetraethoxysilane (TEOS) or sodium silicate (SS), yielding the four types of

composite particles MPTEOS, LATEOS, MPSS and LASS. The synthesis protocol is as follows:

0.93 g nanoparticle agglomerates were dispersed via stirring (300 rpm) in 10 ml deionised water and 10 ml 1 M nitric acid (HNO_3) to obtain a stable ferrofluid (magnetite sol). Four samples were treated this way.
To two samples, 120 mg MP solution was added under stirring (300 rpm). The mixture was placed into an ultrasonic bath (Bandelin Sonorex Super RK103 Ultrasonic bath: 180 W, 35 kHz) for 20 min. A golden brown dispersion (dMP) resulted.
To the other two samples, instead of MP, 360 mg (4.3 mmol) LA were added under stirring (300 rpm) (dLA).

The nanocomposites MPTEOS and LATEOS were prepared by adding 100 ml ethanol, 7 ml aqueous ammonia solution and 6.25 g (30 mmol) TEOS either to dMP or dLA. The mixtures were stirred (300 rpm) for 1 h at RT. The resulting nanocomposite particles were magnetically separated and washed with ethanol and water.

The nanocomposites MPSS and LASS were prepared by adding 40 ml of ammonia solution diluted with 40 ml deionised water to dMP or dLA. The mixtures were heated to 70 °C under stirring (300 rpm) in air. Sodium silicate solution (molar ratios $NH_3 : HNO_3 : Na_2O{\cdot}3SiO_2$ = 27 :1 : 0.4) was added and the resulting reaction mixtures were stirred for 5 min at 70 °C. Precipitated particles were magnetically removed and washed.

Chemical stability of nanocomposite particles

The chemical stability of the nanocomposite particles was evaluated by stirring (200 rpm) the particles for 24 h at pH 2 and pH 12, adjusted via HCl and NaOH, respectively, and analysing (ICP-OES) the supernatant after magnetic separation of the particles. Particles of the LASS type were furthermore stirred for 2 h in concentrated hydrochloric acid (36 wt%) and the change of their size was measured with Fraunhofer diffraction. The mechanical stability of the particles was tested by suspending the composites in water with a Bandelin Sonorex Super RK103 Ultrasonic bath (180 W, 35 kHz) for 60 minutes and measuring their sizes with Fraunhofer diffraction.

7.2.4 Functionalisation of nanocomposites with Hg(II) or Cu(II) selective molecules

All functionalisations were conducted on nanocomposite particles with a stable silica matrix obtained from water glass solution precipitated in a basic medium (type LASS).

Modification of nanocomposites for selective Hg(II) adsorption

Thiol functionalisation was achieved by addition of 2 ml (9.7 mmol) of (3-mercaptopropyl)trimethoxysilane 5 min after silica precipitation (based on a synthesis of 8.2 g composite particles). The mixture was stirred for 1 h before magnetic separation and washing in ethanol and water.

Modification of nanocomposites for selective Cu(II) adsorption

Particle modification with a Cu(II) ion exchanger was carried out as follows: 2 g of magnetic microparticles were dispersed in 100 ml ethanol. 8 ml aqueous ammonia (28 %) were added together with 0.5 ml (2.8 mmol) of trimethoxy(propyl)silane. After stirring for 1 h (300 rpm), the particles were magnetically separated and washed with acetone. Wet particles were immersed in 2-hydroxy-5-nonylacetophenone ketoxime (10 wt% LIX84 in kerosene) and shaken for 1 h. Subsequently, particles were magnetically separated, washed with acetone, dried for 6 h at 130 °C and redispersed in water by heavy shaking.

Variations of the method included initial functionalisation of the composite particles with (3-aminopropyl)triethoxysilane or (3-mercaptopropyl)trimethoxysilane in the same way as described for trimethoxy(propyl)silane before modification with LIX84. Furthermore, LIX84 in kerosene was diluted in several experiments to 1-10 vol% LIX84-kreosene in acetone before particles were stirred in it. However, all these variations turned out to yield an inferior modification of the particles as, typically, LIX84 was not properly attached to the particles initially or immediately lost once the particles were shaken and magnetically separated in water.

7.2.5 Synthesis of layered double hydroxides and intertwining with magnetic particles

Synthesis of layered double hydroxides (LDH)

The synthesis of the LDH is based on a published recipe,[323] and was used with the modifications of treatment and composition as described as follows.

Metal ion precursor solutions for the different LDHs were prepared by dissolving the respective metal salts in 100 ml deionised water:

MgAl LDH: 4.16 g (20 mmol) $MgCl_2 \cdot 6H_2O$ and 2.41 g (10 mmol) $AlCl_3 \cdot 6H_2O$.

MgAl-Zr LDH: 3.65 g (18 mmol) $MgCl_2 \cdot 6H_2O$, 0.72 g (3 mmol) $AlCl_3 \cdot 6H_2O$ and 0.98 g (3 mmol) $ZrOCl_2 \cdot 8H_2O$.

MgFe-Zr LDH: 3.66 g (18 mmol) $MgCl_2 \cdot 6H_2O$, 0.81 g (3 mmol) $FeCl_3 \cdot 6H_2O$ and 0.98 g (3 mmol) $ZrOCl_2 \cdot 8H_2O$.

MgFe LDH: 3.66 g (18 mmol) $MgCl_2 \cdot 6H_2O$ and 1.62 g (6 mmol) $FeCl_3 \cdot 6H_2O$.

Each precursor solution was slowly added to 400 ml of 0.15 M NaOH under stirring (300 rpm). The resulting turbid suspension was stirred for 5 minutes and afterwards adjusted to pH 7 with hydrochloric acid (36 %) for further processing.

Initially, precursor ratios were varied for the synthesis of LDHs. To keep results clear and concise, only the most important LDH systems, as listed above, are discussed in this work. In further experimental variations, LDH systems were subjected to thermal treatment: LDHs, left in their mother solution as precipitated, or filtered and washed in deionised water, were boiled at 100 °C under reflux for 1-8 h. Furthermore, as-precipitated LDHs in their mother solution, or filtered and washed LDHs redispersed in deionised water, were hydrothermally treated in an autoclave at 125 °C for 2 h. These treatment variations were studied for their influence on the colloidal stability of the LDH dispersions (and subsequent intertwinability with the magnetic particles) and on phosphate adsorption behaviour. Preliminary phosphate adsorption studies in waste water revealed that there was no difference between thermally treated and non-thermally treated LDH samples. Details on these LDH systems were therefore omitted in the results and discussion part of this work.

For chemical structure quantification, LDH samples were centrifuged and washed twice in deionised water and dried in a vacuum oven (50 °C, approx. 0.1 mbar, 2 h) before they were analysed with ICP-OES and DTA-TG-MS.

Deposition of LDHs on superparamagnetic microparticles

Magnetic microparticles (type LASS) were dispersed in 500 ml water. The concentration was adapted to the concentration of the respective LDH suspension (500 ml from the reaction suspension) to yield the desired ratio of LDH and magnetic microparticles.

In batch process, the two dispersions were mixed for 60 s under stirring (300 rpm) and subsequently placed into an ultrasonic bath (Bandelin Sonorex Super RK103 Ultrasonic bath: 180 W, 35 kHz) for 100 s. On a larger scale the mixed dispersions were exposed to a 110 W Branson Sonifier II Model 450 sonifier horn for 120s, 50 % duty cycle.

In a continuous deposition process, the two dispersions were pumped through silicon tubes (Ø 5 mm) using a peristaltic pump (Istatec BV-GES) into a Y-shaped gas tube connection (total length 31 mm) as continuous flow reactor. Each arm (Ø 3 mm) of the connector had a length of 18 mm, the two supporting arms met at an angle of 55 °. The flow rate in each supporting channel was 100 ml/min. The mixed suspensions flowed through the outlet tube (50 cm, 200 ml/min) into a continuous flow ultrasonic cell. In this device (Branson Sonifier II Model 450 continuous ultrasound flow cell) the suspension was signified (duty cycle of 50 %, resulting output power for the used ½ ” sonifier horn of 110 W, approximately 5 s exposure time to the reactants).

Precipitation of zirconium dioxide on magnetic particles (type LASS)

In a typical experiment 1.7 g nanocomposite particles were dispersed in 50 ml 0.15 M NaOH under stirring (300 rpm). 0.4 g (2.5 mmol) $ZrOCl_2$ were dissolved in 25 ml deionised water and slowly added to the nanocomposite particle dispersion in NaOH under stirring (300 rpm). The resulting precipitate was stirred for 60 s and additionally ultrasonicated (Bandelin Sonorex Super RK103 Ultrasonic bath: 180 W, 35 kHz) for 100 s before it was magnetically separated and washed three times with water.

7.3 Adsorption and separation studies with selective composite particles

7.3.1 Heavy metal removal and recovery studies

Salts (of nitrates and chlorides, see *chapter 7.1*) of the heavy metals As(V), Cd(II), Cr(III), Zn(II), Pb(II), Cu(II), Hg(II), as well as Mg(II) and Ca(II) ions were dissolved in 1 l deionised water to yield concentrations of approximately 1 mg/l, respectively 10 mg/l or 100 mg/l for each element. To avoid premature precipitations, the pH was adjusted to 4 by hydrochloric acid. Exact concentrations were analysed by ICP-OES.

Hg(II) and Cu(II) removal and recovery experiments

A defined amount of modified composite microparticles was added to 100 ml of a heavy metal solution and stirred for a given time at RT to selectively adsorb Hg(II) and Cu(II), respectively. The particles were separated with a handheld magnet within 60 s and the remaining solution was reanalysed for its heavy metal content.

The magnetically removed particles were stirred for a given time at RT in 10 ml of hydrochloric acid of a given molarity. For Hg(II) recovery, additionally 2 % thiourea was added to the recovery solution.

Magnetic seeding for heavy metal removal and recovery

A flocculation solution was prepared by dissolving 500 mg (1.9 mmol) $FeCl_3 \cdot 6H_2O$ and 200 mg (1.8 mmol) $CaCl_2$ in 100 ml deionised water. The addition of Ca was necessary to promote flocculation.

1 ml of the flocculation solution and 100 mg of superparamagnetic nanocomposite microparticles were added to 100 ml of the heavy metal ion solution under stirring. The pH was raised to 7.5-8 by addition of NaOH (e.g. 0.2 ml 1 M NaOH). After stirring the solution at 300 rpm for 1 to 5 min, the precipitate was separated with a handheld magnet. Concentrations of ions in the remaining solution were analysed. Concentrations of ions in the remaining solution were analysed by ICP-OES. It should be pointed out, that it was deliberately avoided to carry out any filtering operations (e.g. with a membrane filter as it is often done in a standard ICP-OES analysis routine) of the solutions before analysis, to guarantee that the purification of the water is only achieved due the magnetic separation process.

The separated particles were suspended in 10 ml 0.1 M HCl and stirred for 10 minutes. The acid-treated particles were magnetically separated again, washed once with deionised water and used as seeds for the next precipitation.

7.3.2 Phosphate removal and recovery studies[35]

Waste water

All waste water samples for the lab-scale experiments were collected from the effluent of the waste water treatment plant for education and research (LFKW) at the Institute for Sanitary Engineering, Water Quality and Solid Waste Management, University of Stuttgart. The pilot-scale experiments were carried out with municipal waste water effluent from the treatment plant Karlsruhe Institute of Technology (KIT) – Campus Nord. The waste water had a relatively low phosphorus concentration due to its earlier removal in the treatment process and they were therefore spiked with a known amount of orthophosphoric acid to reach concentrations of about 10-15 mg/l PO_4-P.

[35] Lab-scale experiments were designed, carried out and evaluated by Asya Drenkova-Tuhtan (University Stuttgart) and the description is reprinted here. The pilot-scale experiments were designed jointly by Asya Drenkova-Tuhtan (University Stuttgart), Karl Mandel and Anja Paulus (Karlsruhe Institute of Technology). The descriptions here are part of the work submitted to *Water Research* for publication. The submitted title is "*Phosphate recovery from wastewater using engineered superparamagnetic particles modified with layered double hydroxide ion exchangers*".

Adsorption and desorption of phosphate on LDH @ magnetic particles

All adsorption studies were carried out as batch experiments with an initial PO_4-P concentration of 10 mg/l in waste water.

Phosphate desorption was carried out in all experiments with a 1M NaOH + 1M NaCl solution for 30 min, except for the initial experiments at pH 7, where the desorption time was 24 h.

The preliminary screening of the different systems with LDHs on composite particles was performed in 100 ml of spiked municipal waste water and dosed 200 mg/l LDH at pH 7-8. The samples were mixed magnetically at room temperature for 24 h to reach adsorption equilibrium. The supernatant was decanted with the help of a permanent magnet and analysed for phosphate and other competing anions. The adsorption capacity was determined from the decrease of phosphate concentration relative to the initial concentration in the waste water. For subsequent experiments, the particle concentration was doubled to 400 mg/l LDH (1 g/l particles with 40 wt% LDH), due to insufficient adsorption in the first experimental series. Phosphate adsorption kinetics study was conducted by treating 1 l municipal waste water with 400 mg/l LDH at three pH ranges (4.5-5.0, 5.5-6.0 and 7.0-8.0). The pH in the contact tank was adjusted using minimum volumes of 1M HCl or 1M NaOH. Aliquot amount (10 ml) of the water-particle working solution was sampled at different time intervals between 0 and 24 h, so that the total particle concentration remained undisturbed, the particles were separated magnetically and the residual phosphate concentration in the supernatant was analysed spectrophotometrically. The specific phosphate adsorption values were plotted against time. An adsorption isotherm was obtained in 100 ml scale by stirring different concentrations of particles with waste water at room temperature and pH 4.5 for 24 h until adsorption equilibrium was achieved based on the foregoing investigation.

Reusability of the particles was tested first on a lab-scale with 1 l of spiked municipal waste water within 15 adsorption / desorption cycles. Based on optimised reaction conditions from the earlier experiments, the particles concentration was set to 1 g/l (400 mg/l LDH), pH 4.5 and adsorption contact time 1 h. The supernatant was separated magnetically from the particle fraction, analysed for phosphate and the adsorption rate of each cycle was calculated as mentioned earlier.

Desorption was performed either by using 1 l of fresh desorption solution each time (reactor 1) or by using the same 1 l of desorption solution for each regeneration cycle (reactor 2). The phosphate desorption rates were determined for each cycle in reactor 1 and after the last cycle in reactor 2.

For the pilot-test a total of 60 g particles with 20 wt% LDH fraction (corresponding to 400 mg/l LDH concentration) were applied to 125 l of waste water effluent (25 l per cycle) spiked with phosphoric acid with 15 mg/l initial PO_4-P concentration. The waste water was stirred for 45 min with the magnetic particles modified with MgFe-Zr LDH in a propeller mixed glass reactor at pH 4.5. Adjustment of pH was performed with 32 wt% H_2SO_4. The only exception was cycle 4 when the adsorption was deliberately carried out overnight at pH 7 for 14 hours. Adsorption / desorption cycles were repeated 5 times.

In the pilot-scale experiment the particles were regenerated with the same solution of 1M NaOH + 1M NaCl as in the laboratory tests. Adsorption was carried out with 25 l of fresh waste water in every cycle and only 2.5 l of recovery solution was used for desorption, targeting P-enrichment. The same desorption solution was applied five times leading to further accumulation of phosphate.

Pilot-scale magnetic separation with a HGMF

The high gradient magnetic filter (HGMF) used in this work is a rotor-stator device which was developed at KIT in cooperation with the companies chemagen (Baesweiler, Germany), now part of the PerkinElmer family and Abbis, part of Vulkan Technic Maschinen-Konstruktions GmbH (Wiesbaum, Germany).[326] The separation chamber (1 l) contains 25 fixed stainless steel discs which are aligned in a rotor-stator fashion with 25 rotating discs to enhance particle release. It is surrounded by an electromagnet that generates a magnetic field of 0.25 T. The filter has a retaining capacity of approximately 100 g of particles depending on particle type and surrounding medium. A peristaltic pump and two valves are used for flow generation, allowing a flow rate up to 1.4 l/min.

The principle of magnetic separation via HGMF in the pilot-scale experiment can be described by the following four steps:

(1) Adsorption (45 min): Functionalised magnetic particles are loaded with phosphate in an exterior adsorption tank.

(2) Separation I (15 min): The suspension is pumped into the separator where the product-loaded magnetic particles are collected in the filter, while the product-depleted solution passes through. The magnet is turned on during this step.

(3) Desorption (30 min): A desorption solution is pumped through the chamber into an exterior desorption tank together with the phosphate loaded particles. The release of the particles is supported by operation of the rotor-stator arrangement. The magnet is turned off during desorption.

(4) Separation II (15 min): The unloaded particles and the desorption solution, rich in phosphate product, are pumped back into the HGMF device where the regenerated particles are collected. Then they are flushed with fresh waste water from the HGMF and introduced into the adsorption tank to be reused in a new cycle.

Depending on the desired volume, adsorption and desorption can also be performed inside the separation chamber which has a limited capacity. In this work 5 adsorption / desorption cycles were done. In the first 3 cycles desorption took place inside the separation chamber, but due to its limited volume and insufficient regeneration of the particles, the following 2 cycles were carried out in an exterior desorption tank with 2.5 l of solution.

7.4 Analytical methods

Scanning electron microscopy (SEM) and energy dispersive X-ray spectroscopy (EDX)

An electron beam scanned over a sample triggers a variety of processes. Detection of remitted secondary electrons yields topographic information of the sample.[327] A gray-scale translated *current versus x-y-position* image can be obtained with a resolution much better than from light microscopy.[327] Detection and energy resolution of X-rays, emitted by the sample, with a Li doped Si crystal p-i-n diode reveals the elemental composition of the sample (energy dispersive X-ray spectroscopy, EDX).[328]
Scanning electron microscopy (SEM) was carried out with a Zeiss Supra 25 SEM at 3 keV (field emission). EDX was done with 15 keV at a working distance of 8 mm.

Transmission electron microscopy (TEM) and energy dispersive X-ray spectroscopy (EDX)

Detection of diffraction (and also mass and thickness) contrast for electrons, transmitted through a thin (< 100 nm) sample allows to image structures of a few nm in size (the best resolution achieved with a transmission electron microscope to date is as good as 0.7 nm)[329]. It is also possible to obtain a diffraction pattern of a sample region by focusing the post-specimen (projector) lenses of the microscope to the back focal plane of the objective lens.[330] Furthermore, the electron beam can be scanned and characteristic X-rays, emitted by the sample, can be detected for highly space resolved elemental analysis (STEM-EDX).
Size and shape of nanoparticles were studied with a Jeol JEM 2010 transmission electron microscope (TEM). Their crystallinity was confirmed with high resolution TEM images and by diffraction imaging. Samples of nanocomposite particles for transmission electron microscopy were obtained by embedding composite particles in an epoxy resin, generating a flat surface by cross section polishing (JEOL Cross Section Polisher SM-09010) and

cutting a lamella with a focused Ga ion beam (FEI Company Focused Ion Beam Quanta 200 3D). TEM, high resolution TEM (HRTEM) and scanning transmission electron microscopy with energy dispersive X-ray analysis (STEM-EDX) on the composites were also conducted on the JEOL JEM2010.

X-ray absorption fine structure spectroscopy (XAFS)

X-ray absorption fine structure spectroscopy (XAFS) compromises data of X-ray absorption near edge structure (XANES) as well as extended X-ray absorption fine structure (EXAFS).[331,332] Using a tunable X-ray source from synchrotron radiation allows probing the local atomic environment of an element in a solid. An element specific X-ray energy leads to excitation of an inner core electron (to an available empty state). This results in a steep absorption edge at this X-ray energy that can be visualised by monitoring either the X-ray intensity transmitted *through* the sample or the fluorescent X-ray intensity radiated *from* the sample. The exact position of the absorption edge (and the occurrence of other pre-edge absorption peaks) depends on the valence state of the element that can thereby be determined (XANES).[333] Absorption of X-rays with energies typically 50-1000 eV higher than the necessary excitation energy at the absorption edge creates photoelectrons that propagate from the excited atom and are scattered by neighbouring atoms (that might be different elements).[334] The outgoing and the back scattered photoelectron waves interfere with each other. Whether this interference is constructive or destructive depends (among other contributions) on the path difference of the waves which is a function of their *k*-vector and the distance of the excited atom to the scatter atoms. Tuning of the incident X-ray energy therefore leads to recordable modulatory absorption intensities of the X-rays in the post-edge region as the *k*-vector of the photoelectrons is varied that way. The Fourier transformation of this periodic absorption signal as function of *k*, from the *k*-space into the *R*-space, gives the quasi radial distribution of neighbouring atoms. [331,333,335]

An exact expression for the absorption variation as function of the incident X-ray energy can be obtained from perturbation theory for the interaction Hamiltonian (initial state: incident X-ray, undisturbed atom; final state: photoelectron created, excited atom) modified with a term taking into account the backscattered photoelectron wave. The expression obtained that way is generally used for analysing (modelling) EXAFS data.[336]

X-ray absorption fine structure (XAFS) experiments were carried out at BAMline beamline[337] installed at the synchrotron light source BESSY II, Berlin, Germany. The beam was monochromatised using a double-crystal monochromator, DCM, Si(111) with an energy resolution of about $2 \cdot 10^{-4}$. Higher harmonics were suppressed by a preinstalled multilayer mirror. The spectra were measured in the fluorescence yield in the standard 45°

geometry at the K-edge of iron (E_0 = 7112 eV) using an energy dispersive silicon drift detector (X-Flash by Bruker Nano). The spectra were recorded with a 10 eV step in the pre-edge region ranging from E_0 - 150 eV to E_0 - 20 eV below the edge. The near-edge region was scanned with a 0.5 eV step. The extended X-ray absorption fine structure (EXAFS) region, above E_0 + 50 eV was measured with a constant step in the *k*-space (momentum) of 0.05 $Å^{-1}$ extending up to 15 $Å^{-1}$.

The XAFS data were processed using the free software package Ifeffit ver. 1.2.11d[338] with the GUI extensions Athena and Artemis,[339] whereas the *ab initio* calculations of the EXAFS spectra have been carried out using the FEFF 8.4 code[340] (refer to [290] for fit parameters used for the calculations). The background subtraction and normalisation procedure of the measured XAFS has been done using the AutoBK routine implemented in Ifeffit applying default parameters, notably R_{bkg} = 1.0.

Small angle X-ray scattering (SAXS)

Small angle X-ray scattering (SAXS) can determine the primary size of nanoparticles and their agglomerate sizes. Unlike in laser light scattering techniques (e.g. DLS), the particles do not have to be in solution but can be in form of powders, i.e., primary particle sizes can be compared independently of their dispersability / agglomeration state in solution.

A monochromatic X-ray beam transmitted through a sample gets scattered dependent on encountered charge densities (related to the electron clouds of the atoms) and their distribution in a sample.[341] A nanoparticle sample can be considered as consisting of regions with high charge densities (the dense, spherical nanoparticles) and low densities (the spacing between the particles). The X-rays are scattered at low angles into a detector. The radial intensity distribution at the detector plane is related to the scattering vector *q*. A larger radial distance from the central beam axis corresponds to a larger *q*. As the scattering intensity is the Fourier transform of the scatterer densities in the sample (e.g. the nanoparticles), information such as size of the nanoparticles and the agglomerates can be gained. Typically, there are two regimes in the *intensity I(q) versus q double logarithmic plot*: A region of a slope $\sim q^{-2}$ at low *q* values (the Guinier regime) and a region where $I(q) \sim q^{-4}$ (the Porod regime).[342] G. Beaucage developed an approach to extract information such as primary particle size and agglomerate size from the scattering function of a "*complex system that contains multiple levels of related structural features*" (e.g. primary particles and their agglomerates).[292]

Probing of the in situ nanoparticle structure was carried out with small angle X-ray scattering (SAXS) Saxsess by Anton Paar (Graz, Austria) with a Cu anode x-ray tube (K_α radiation; λ = 0.15406 nm) on a length scale between π/q_{max} = 0.5 nm and π/q_{min} = 45 nm.

X-ray diffraction (XRD)

The X-ray diffraction technique can be used to determine the crystalline structure of a material as incident X-rays are diffracted by crystal planes in a constructive or destructive manner, depending on the incident angle of the X-rays and the arrangement of the crystal planes. The diffraction pattern obtained for a certain range of 2θ (0°-90°) follows Bragg´s law and is a finger print for the crystalline material.[343]

XRD was performed on dried powder samples of nano- and microparticles. A Phillips PW 1730/10 employing Cu K_α radiation (λ = 0.15406 nm) was used (step size 0.02 2θ, typical count time 1 s). Indication of reflections was carried out relying on the International Centre for Diffraction Data PDF-4 database[286] and on published work as quoted. For particle size determination using the Scherrer equation,[281] an instrumental peak broadening of 0.2 ° was taken into account.

Vibrating sample magnetometry (VSM)

In 1959, S. Foner proposed an instrumental setup that is based on the principle of a perpendicularly vibrating sample that is magnetised in a field between two pole pieces and that at the same time induces a voltage via induction in so-called pick-up coils that are traversed by this sample while being moved up and down in the magnetic field.[344] Electrically multiplying the vibration frequency of the sample with the frequency of the voltage signal recorded by the pick-up coils due to the periodical induction is a simple way of obtaining a lock-in amplified signal of high quality which renders measurement of very low sample magnetisation values possible.[345] Improved noise reduction is achieved by more sophisticated arrangements of pick-up coil pairs.[346] Hysteresis curves can be obtained by looping the magnetic field between the two pole pieces using electromagnets. A coolable / heatable sample chamber renders measurements of magnetisation at different temperatures possible.

Magnetic properties of vacuum-dried particles were studied with a vibrating sample magnetometer (VSM, VersaLabTM 3T, Cryogenfree Vibrating Sample Magnetometer). The system allows cooling down to 60 K. For zero field cooled (ZFC) and field cooled (FC) measurements, vacuum dried samples were demagnetised at 293 K by setting an initial field of 10 000 Oe and decreasing the field stepwise to zero by oscillating at 200 Oe/s. Samples were cooled down to 70 K via a cryocooler system at zero field. Then an external field of 10 Oe was applied and the samples were heated to 300 K with 1 K/min and again cooled down to 70 K at 1 K/min in the 10 Oe field. *M* was measured by vibrating the samples at 40 Hz. One data point was delivered for *M* measured within 1 s (averaging time).

Hystereses measurements were carried out at 60 K and 293 K respectively for each sample by cycling the applied field from −30 to +30 kOe for two times at a step rate of 100 Oe/s. Detailed analyses were carried out by cycling the applied field from -5 to +5 kOe with 5 Oe/s.

Drying procedures of washed (water) particles (drying: typically 50 °C, approx. 0.1 mbar, 2 h) and subsequent sample preparation is a non-negligible but also non-avoidable source of error in the determination of the mass magnetisation of samples. Incompletely dried samples or moisture uptake during sample preparation (filling of the powder into small capsules by hand in a non-moisture free environment) cannot be excluded. Resulting deviations in determined masses can be up to 5-10 %. The comparably high percental error is due to the very small amount of measured particle mass (typically 3-10 mg). This inaccuracy must always be taken into account when saturation magnetisations are compared.

Differential thermal analysis – thermogravimetry – mass spectroscopy (DTA-TG MS)

Thermally induced changes and reactions in a sample can be analysed by heating in e.g. synthetic air while monitoring the sample's weight as well as its temperature change in comparison to a reference. Endothermic and exothermic reactions can be detected and the products can be analysed by a mass spectrometer coupled to the exhaust air stream.[347]

Differential thermogravimetric analyses (DTA-TG) were carried out from RT to 600 °C or 800 °C with a Netzsch STA 449 C Jupiter DTA-TG coupled with a Netzsch Aeolos QMS403C mass spectrometer (MS) by heating pre-dried (50 °C, approx. 0.1 mbar, 2 h) samples in synthetic air (80 vol% nitrogen, 20 vol% oxygen).

Inductively coupled plasma – optical emission spectroscopy (ICP-OES)

Elements in solution, sprayed as aerosol into an inductively generated Ar plasma torch emit characteristic radiation when excited in this extremely energetic plasma field. The characteristic radiation can be detected for many elements almost simultaneously by a grating spectrometer system. The integral area of a characteristic emission peak (calibrated to a standard) permits the quantitative analysis of a detected element.[348]

Measurements were carried out with a Varian Vista-Pro CCD Simultaneous Inductive Coupled Plasma - Optical Emission Spectroscope (ICP-OES). Solid samples were analysed after dissolution in hot hydrofluoric acid. Dissolved samples (solutions) were measured directly without further treatment.

Specific surface area measurement by nitrogen adsorption according the Brunauer, Emmett and Teller theory (BET)

The determination of the amount of adsorbed nitrogen allows the calculation of the specific surface area of a solid by assuming an area demand of 16.2 $Å^2$ per nitrogen molecule.[349] Characteristic (multilayer) isotherms can be obtained that furthermore contain information on the sample's porosity. Measurements with a Quantachrome Instruments Autosorb-3B were performed on degassed and dried samples (110 °C, 10^{-3} mbar, 16 h). BET analysis follows DIN66131.[350]

Fourier transformed infrared spectroscopy (FTIR)

Molecular vibrations can be induced by absorption of infrared radiation and "*must give rise to a change in the molecular electric dipole moment to be infrared active*"[351]; if however it is the polarisability of the molecules that is altered due to the irradiation, the vibrational mode is said to be Raman active (the complementary method to IR vibrational spectroscopy).[351] Analyses of a Fourier transformed frequency spectrum of IR radiation transmitted through (or reflected from) a sample reveals characteristic absorption bands which can be related to chemical bonds (functional groups) of the molecules in the sample.[352] The FTIR method was used to prove successful chemical functionalisation / modification of particles.

Nanoparticles were analysed as KBr pellets with a Fourier transformation infrared spectrometer (FTIR, Nicolet Magna-IR 760 Spectrometer E.S.P.). Composites and their surface modifications were investigated by diffuse reflectance FTIR (DRIFT) on powder samples using the same spectrometer.

^{29}Si nuclear magnetic resonance spectroscopy (^{29}Si-NMR)

Certain nuclear isotopes possess a permanent magnetic moment (nuclear spin *I*). In a strong external magnetic field (applied in *z*-direction) the rotational axis of the spinning nucleus cannot orient exactly parallel to this direction but precesses around the *z*-axis with an angular velocity proportional to the applied magnetic field strength.[353] For a single nucleus with $I = ½$, there are (only) two energy states for the system (generally: $2I+1$ states): the magnetisation direction is either parallel to the external field (low energy) or antiparallel (high energy). More states populate the lower level leading to a measurable net magnetic moment of the system. Electromagnetic irradiation on the system with the same frequency as the precession speed (the resonance frequency) can disturb the system, i.e., deflect the axis of the magnetic moment away from the *z*-direction.[353] If this is done by a short radio frequency pulse (such a pulse contains a broad spectrum of frequencies

around the resonant frequency), applied perpendicularly to the direction of the permanent magnetic field, the evolution of the off-resonance precession and free induction decay of the magnetic moment of the nucleus can be recorded by pick-up coils. The Fourier transform of this exponential decay gives access to the resonant frequencies.[354] These are dependent on the local magnetic field the nucleus is exposed to. This local field is the weakened external field as electron clouds from neighbouring atoms electromagnetically partly shield the nucleus. The resonant frequency is denoted as chemical shift δ to an external standard (e. g. TMS: tetramethylsilan) given in ppm. Information on the local environment (chemical bonds) for the resonating nucleus (atom) can be obtained from these shifts.[354,355] ^{29}Si solid state NMR is particularly suitable to quantify the structural Si configuration, i.e., to resolve the fraction of Q1, Q2, Q3 and Q4 ($\equiv Si(OSi)_1$ to $Si(OSi)_4$) groups in a silica solid by quantifying the absorption peak areas at the different δ positions.[356] High frequency spinning of a sample at an angle of 54.7° (magic angle, MAS) relative to the magnetic field drastically improves the spectral resolution as anisotropy effects are cancelled out, that would otherwise strongly broaden the peaks.[357]

^{29}Si-MAS-NMR spectra were recorded at 22 °C on 100 mg samples with a Bruker DSX-400 NMR (9.4 Tesla) spectrometer using bottom layer rotors of ZrO_2 (diameter 4 mm) (spinning rate 13 kHz; pulse length 2.0 µs; repetition time 180 s; external standard TMS: 79.5 MHz, $\delta = 0$).

Dynamic light scattering (DLS)

The dynamic light scattering (DLS) method is a way to determine the hydrodynamic radii of nanoparticles that are immersed in a liquid. Scattering of incident laser light by the particles that undergo Brownian motion leads to a time variant interference signal that can be resolved if a high frequency photodetector is used. The exponential decay (as the simplest approximation for the decay) of the autocorrelation function of the signal intensity (as function of time) can be related to the diffusion constant from which the particle radii are obtained using the Einstein-Stokes equation (compare[358]).
Nanoparticle samples were measured using a DLS Malvern Instruments Zeta Sizer Nano.

Fraunhofer diffraction (FD)

Light scattering of a laser beam shone on small, micron sized particles in solution results in diffraction rings on a screen that is placed behind the particle solution (in transmission direction). This circular pattern is the Fourier transform of the observed objects. The spacing width of the diffraction rings is reciprocally related to the particle size. Detection with circularly arranged photodiodes renders it possible to determine the size of the particles.[359,360]

Particle sizes of microparticles dispersed in deionised water were determined via Fraunhofer diffraction (FD) with a Malvern Mastersizer S.

Zeta potential measurement

The electrophoretic mobility of surface charged particles in dispersion, induced by applying an electric field, can be detected similarly to DLS. The mobility is directly related to the particle's zeta potential, i.e., the electric potential at the plane of shear in a diffuse double layer of ions surrounding a charged particle.[361] Typically, the pH dependence of the zeta potential is measured. The iso electric point (i.e.p.) is the pH value of a vanishing zeta potential (no electrophoretic mobility). Zeta potential curves and the position of the i.e.p. depend on the surface modification of particles.

Zeta potential measurements were performed on a Malvern Instruments Zeta Sizer Nano; pH was adjusted by 0.1 M NaOH and 0.1 M HCl (titration).

Photometric determination of phosphate concentrations

Phosphate concentrations were determined spectrophotometrically with the ammonium molybdate method:[362] In a first step an antimony-phosphorus-molybdate complex is formed that is subsequently reduced with ascorbinic acid to a deeply coloured molybdenum blue complex. Its concentration is determined photometrically at a wavelength of 880 nm by comparing the extinction to a calibration curve obtained from known PO_4-P concentrations.[362]

Viscosimetry and gel permeation chromatography

Possible changes of the MELPERS4343 polymeric chain lengths due to ultrasonic treatment were examined with a Anton Paar Physica MC R301 viscosimeter and a gel permeation chromatograph (GAT TC1900 oven with a Schambeck RI2000 detector) using polystyrene as standard. Both methods are suitable to determine the chain lengths of polymers.[363]

8. LITERATURE

The following references are formatted according to the standards of the Royal Society of Chemistry (RSC style).

[1] S. Pappas, *7 Population Milestones for 7 Billion People* www.livescience.com/16489-7-population-milestones-7-billion-people.html (Accessed: 22 December 2012).

[2] *United Nations Human Development Report 2011,* United Nations http://hdr.undp.org/en/reports/global/hdr2011/ (Accessed: 22 December 2012).

[3] *Rohstoffsituation Bayern –keine Zukunft ohne Rohstoffe Strategien und Handlungsoptionen Ein aktualisierter Bericht der IW Consult GmbH Köln unter Mitwirkung von Prof. Reller (WZU Augsburg) im Auftrag der vbw – Vereinigung der Bayerischen Wirtschaft e. V. Stand Juli 2011* www.rohstoffstrategie-bayern.de/neue-rohstoffstrategie/publikationen/ (Accessed: 22 December 2012).

[4] B. Achzet, A. Reller, V. Zepf, C. Rennie, M. Ashfield, J. Simmons, *Materials critical to the energy industry. An introduction,* ON Communication, 2011.

[5] G. Sextl, T. Brämer, C. Gellermann, A. Reller, *Chem. Ing. Tech*., 2012, **84**, 977.

[6] D. Cordell, J. O. Drangert, S. White, *Global Environ. Change*, 2009, **19**, 292.

[7] D. Cordell, *8 reasons why we need to rethink the management of phosphorus resources in the global food system, The Story of P,* Information Sheet 1, Global Phosphorus Research Initiative, Institute for Sustainable Futures, University of Technology, Sydney (UTS) Australia and Department of Water and Environmental Studies, Linköping University (LiU), Sweden, 2008.

[8] S. von der Weiden, *Klärwerke sind unerschöpfte Goldgruben,* Die Welt, 18 July 2011.

[9] S. Neumann, *Colloquium Produktionsintegrierte Wasser-/Abwassertechnik*, LANXess, Bremen, 2009.

[10] A. Zehnsdorf, P. Hoffmann, H. Seidel, U. Schlenker, R. A. Müller, *Chem. Ing. Tech*., 2012, **84**, 1255.

[11] M. Boller, *Fachgespräch "Freisetzung von Schwermetallen aus Materialien in die Umwelt"*, Umweltbundesamt Deutschland, Berlin, 2004.

[12] B. G. Lottermoser, *Elements*, 2001, **7**, 405.

[13] V. Inglezakis, S. Poulopoulos, *Adsorption, Ion Exchange and Catalysis: Design of Operations and Environmental Applications*, Elsevier Science, Amsterdam, 2006, p. 26.

[14] *Technical Resource Document: Extraction and Beneficiation of Ores and Minerals: Copper*, U.S. Environmental Protection Agency, Washington DC, 1994.

[15] *Water supply, sanitation and hygiene development*, World Health Organisation www.who.int/water_sanitation_health/hygiene/en/ (Accessed: 22 December 2012).

[16] *Making Water a part of economic development The economic benefits of improved water management and services A report commissioned by the Governments of Norway and Seweden as input to the Commission on Sustainable Devolopment (CSD) and its 2004-2005 focus on water, sanitation and related issues*, World Health Organisation www.who.int/water_sanitation_health/economic/en/ (Accessed: 22 December 2012).

[17] *WHO guidelines for drinking water quality*, World Health Organisation www.who.int/water_sanitation_health/dwq/guidelines/en/index.html (Accessed: 22 December 2012).

[18] P. D. Johnson, P. Girinathannair, K. N. Ohlinger, S. Ritchie, L. Teuber, J. Kirby, *Water Environ. Res.*, 2008, **80**, 472.

[19] H. Strathmann, *Introduction to Membrane Science and Technology*, Wiley-VCH, Weinheim, 2011.

[20] V. K. Gupta, P. J. M. Carrott, M. M. L. Ribeiro Carrott, *Crit. Rev. Env. Sci. Technol*., 2009, **39**, 783.

[21] S. E. Kentish, G. W. Stevens, *Chem. Eng. J.*, 2001, **84**, 149.

[22] A. A. Zagorodni, *Ion exchange Materials Properties and Applications,* Elsevier, Amsterdam, 2007, pp. 1-9.

[23] F.H. Frimmel, A. Gorenflo, F. Saravia, *Aufbereitung wässriger Lösungen durch Memebranverfahren*, Engler-Bunte-Institut Bereich Wasserchemie Universität Karlsruhe (TH), 2006.

[24] R. D. Ambashta, M. Sillanpää, *J. Hazard. Mater*., 2010, **180**, 38.

[25] C. P. Bean, J. D. J. Livingston, *J. Appl. Phys. Suppl*., 1959, **30**, 120S.

[26] M. Zborowski, in *Magnetic Cell Separation,* ed. M. Zborowski, J. J. Chalmers, Elsevier, Oxford, 2008, pp. 63-79.

[27] D. D. Zhang, in *Dekker Encyclopedia of Nanoscience*, ed. C. I. Contescu, K. Putyera, Taylor & Francis, Florida, 2nd edn., 2009, p. 1951.

[28] E. P. Pluddemann, *Silane coupling agents*, Plenum Press, New York, 1982.

[29] P. K. Jal, S. Patel, B. K. Mishra, *Talanta*, 2004, **62**, 1005.

[30] K. Y. Park, J. H. Song, S. H. Lee, H. S. Kim, *Environ. Eng. Sci.*, 2010, **27**, 805.

[31] J. Das, B.S. Patra, N. Baliarsingh, K.M. Parida, *Appl. Clay Sci.*, 2006, **32**, 252.

[32] U. Teipel, R. Schmidt, *Rohstoffeffizienz und Rohstoffinnovationen*, Fraunhofer Verlag, Band 2, 2011.

[33] L. Hermann, *Rückgewinnung von Phosphor aus der Abwassereinigung. Eine Bestandesaufnahme,* Umwelt-Wissen Nr. 0929, Bundesamt für Umwelt, Bern, 2009.

[34] G. Tchobanoglous, F. L. Burton, H. D. Stensel, *Metcalf & Eddy Inc., Wastewater Engineering: Treatment and Reuse,* McGraw-Hill, 4th edn., New York, 2003.

[35] DWA 22, *Leistungsvergleich kommunaler Kläranlagen*, 2009.

[36] J. G. Dean, F. L. Bosqui, K. H. Lanouette, *Environ. Sci. Technol*., 1972, **6**, 518.

[37] P. Grimshaw, J. M. Calo, G. Hradil, *Chem. Eng. J*., 2011, **175**, 103.

[38] J. M. D. Coey, *Magnetism and Magnetic Materials*, Cambridge University Press, New York, 2010, pp. 375-376.

[39] J. M. D. Coey, *Magnetism and Magnetic Materials*, Cambridge University Press, New York, 2010, p. 17.

[40] J. M. D. Coey, *Magnetism and Magnetic Materials*, Cambridge University Press, New York, 2010, p. 385.

[41] D. L. Huber, in *Dekker Encyclopedia of Nanoscience*, ed. C. I. Contescu, K. Putyera, Taylor & Francis, Florida, 2nd edn., 2009, p. 1681.

[42] R. M. Cornell, U. Schwertmann, *The Iron Oxides*, Wiley-VCH, Weinheim, 2nd edn., 2003, p. 28.

[43] R. M. Cornell, U. Schwertmann, *The Iron Oxides*, Wiley-VCH, Weinheim, 2nd edn., 2003, pp. 14-27.

[44] C. K. Vogt, *Herstellung und Anwendung von Aggregaten aus oberflächenaktiven Nanopartikeln und Magnetit für den Einsatz in der Magnetseparation*, Ph.D. thesis, Universität Fridericiana zu Karlsruhe (TH), 2006.

[45] R. M. Cornell, U. Schwertmann, *The Iron Oxides*, Wiley-VCH, Weinheim, 2nd edn., 2003, p. 123.

[46] R. M. Cornell, U. Schwertmann, *The Iron Oxides*, Wiley-VCH, Weinheim, 2nd edn., 2003, pp. 29-36.

[47] R. M. Cornell, U. Schwertmann, *The Iron Oxides*, Wiley-VCH, Weinheim, 2nd edn., 2003, p. 126.

[48] S. Laurent, D. Forge, M. Port, A. Roch, C. Robic, L. Vander Elst, R. N. Muller, *Chem. Rev.*, 2008, **108**, 2064.

[49] X. Q. Li, D. W. Elliott, W. X. Zhang,
Crit. Rev. Solid State Mater. Sci., 2006, **31**, 111.

[50] B. L. Cushing, V. L. Kolesnichenko, C. J. O'Connor,
Chem. Rev., 2004, **104**, 3893.

[51] S. Sun, H. Zeng, *J. Am. Chem. Soc.*, 2002**, 124**, 8204.

[52] Y. P. Sun, J. Cao, W. X. Zhang, H. P. Wang,
Adv. Colloid Interface Sci., 2006, **120**, 47.

[53] M. J. Lefort, *C. R. Acad. Sci. Paris*, 1852, **55**, 488.

[54] X. Sun, C. Zheng, F. Zhang, Y. Yang, G. Wu, A. Yu, N. Guan,
J. Phys. Chem. C, 2009, **113**, 16002.

[55] D. Patel, Y. Chang, G. H. Lee, *Curr. Appl. Phys.*, 2009, **9**, S32.

[56] M. H. Sousa, J. C. Rubim, P. G. Sobrinho, F. A. Tourinho,
J. Magn. Magn. Mater., 2001, **225**, 67.

[57] S. L. Tie, Y. Q. Lin, H. C. Lee, Y. S. Baea, C. H. Lee,
Colloids Surf., A, 2006, **273**, 75.

[58] C. Hui, C. Shen, T. Yang, L. Bao, J. Tian, H. Ding, C. Li, H. J. Gao,
J. Phys. Chem. C, 2008, **112**, 11336.

[59] C. L. Lin, C. F. Le, W. Y. Chiu, *J. Colloid Interface Sci.*, 2005, **291**, 411.

[60] J. Yan, S. Mo, J. Nie, W. Chen, X. Shen, J. Hu, G. Hao, H. Tong,
Colloids Surf., A, 2009, **340**, 109.

[61] G. Goloverda, B. Jackson, C. Kidd, V. Kolesnichenko,
J. Magn. Magn. Mater., 2009, **321**, 1372.

[62] M. T. Klem, M. Young, T. Douglas, *Mater. Today*, 2005, **9**, 28.

[63] Y. H. Deng, C. C. Wang, J. H. Hu, W. L. Yang, S. K. Fu,
Colloids Surf., A, 2005, **262**, 87.

[64] S. Kralj, D. Makovec, S. Čampelj, M. Drofenik,
J. Magn. Magn. Mater., 2010, **322**, 1847.

[65] K. D. Kim, S. S. Kim, H. T. Kim, *J. Ind. Eng. Chem.*, 2005, **11**, 584.

[66] M. Arruebo, R. Fernández-Pacheco, B. Velasco, C. Marquina, J. Arbiol, S. Irusta, M. R. Ibarra, J. Santamaría, *Adv. Funct. Mater.*, 2007, **17**, 1473.

[67] F. Mahtab, Y. Yu, J. W. Y. Lam, J. Liu, B. Zhang, P. Lu, X. Zhang, B. Z. Tang, *Adv. Funct. Mater.*, 2011, **21**, 1733.

[68] V. Salgueiriño-Maceira, M. A. Correa-Duarte, M. Spasova, L. M. Liz-Marzán, M. Farle, *Adv. Funct. Mater.*, 2006, **16**, 509.

[69] C. Y. Haw, C. H. Chia, S. Zakaria, F. Mohamed, S. Radiman, C. H. Teh, P. S. Khiew, W. S. Chiu, N. M. Huang, *Ceram. Int.*, 2011, **37**, 451.

[70] Y. Piao, A. Burns, J. Kim, U. Wiesner, T. Hyeon, *Adv. Funct. Mater.*, 2008, **18**, 3745.

[71] Z. Huang, F. Tang, *J. Colloid Interface Sci*., 2004, **275**, 142.

[72] Z. Cao, W. Jiang, X. Ye, X. Gong, *J. Magn. Magn. Mater.* 2008, **320**, 1499.

[73] D. Niu, Y. Li, X. Qiao, L. Li, W. Zhao, H. Chen, Q. Zhao, Z. Mac, J. Shi, *Chem. Commun.*, 2008, 4463.

[74] M. D. Butterworth, S. P. Armes, A. W. Simpson, *J. Chem. Soc., Chem. Commun.*, 1994, 2129.

[75] D. Niu, Y. Li, Z. Ma, H. Diao, J. Gu, H. Chen, W. Zhao, M. Ruan, Y. Zhang, J. Shi, *Adv. Funct. Mater.*, 2010, **20**, 773.

[76] H. Tan, J. M. Xue, B. Shuter, X. Li, J. Wang, *Adv. Funct. Mater.*, 2010, **20**, 722.

[77] A. B. Fuertes, M. Sevilla, S. Álvarez, T. Valdés-Solís, P. Tartaj, *Adv. Funct. Mater.*, 2007, **17**, 2321.

[78] D. Horák, M. Babič, H. Macková, M. Beneš, *J. Sep. Sci.*, 2007, **30**, 1751.

[79] I. J. Bruce, J. Taylor, M. Todd, M. J. Davies, E. Borioni, C. Sangregorio, T. Sen, *J. Magn. Magn. Mater.*, 2004, **284**, 145.

[80] www.magneticmicrosphere.com/suppliers/magnetic_microspheres.php (Accessed: 09 March 2013).

[81] D. Amara, J. Grinblat, S. Margel, *J. Mater. Chem.*, 2010, **20**, 1899.

[82] R. N. Grass, E. K. Athanassiou, W. J. Stark, *Angew. Chem. Int. Ed.*, 2007, **46**, 4909.

[83] I. K. Herrmann, R. N. Grass, D. Mazunin, W. J. Stark, *Chem. Mater.*, 2009, **21**, 3275.

[84] www.chemagen.com (Accessed: 09 March 2013).

[85] www.chemicell.com (Accessed: 09 March 2013).

[86] M. Pridöhl, *Kleben und Entkleben mit MagSilica®*, Degussa AG (Evonik) Advanced Nanomaterials, 2005.

[87] www.magnamedics.com (Accessed: 09 March 2013).

[88] www.millipore.com/diagnostics_cap/flx4/estapor_microspheres (Accessed: 09 March 2013).

[89] www.merckmillipore.com/germany/life-science-research/magprep-silica-particles/EMD_BIO-70912/p_uuid (Accessed: 09 March 2013).

[90] www.miltenyibiotec.com/Products-and-Services/MACS-Cell-Separation/MACS-Technology.aspx (Accessed: 09 March 2013).

[91] www.qiagen.com (Accessed: 09 March 2013).

[92] www.turbobeads.com (Accessed: 09 March 2013).

[93] J. Liu X. Du, *J. Mater. Chem.*, 2011, **21**, 6981.

[94] Y. Zhai, S. Duan, Q. He, X. Yang, Q. Han, *Microchim. Acta*, 2010, **169**, 353.

[95] B. Y. Song, Y. Eom, T. G. Lee, *Appl. Surf. Sci.*, 2011, **257**, 4754.

[96] S. Shin, J. Jang, *Chem. Commun.*, 2007, 4230.

[97] F. He, W. Wang, J. W. Moon, J. Howe, E. M. Pierce, L. Liang, *ACS Appl. Mater. Interfaces*, 2012, **4**, 4373.

[98] Y. J. Jiang, X. T. Li, J. Gao, X. C. Guo, J. Guan, X. D. Mu, . *J. Nanopart. Res*,. 2011, **13**, 939.

[99] W. Yantasee, C. Warnern, T. Sangvanich, R. S. Addleman, T. G. Carter, R. J. Wiacek, et al., *Environ. Sci. Technol.*, 2007, **41**, 5114.

[100] H. Yong-Mei, C. Man, H. Zhong-Bo, *J. Hazard. Mater.*, 2010, **184**, 392.

[101] J. Y. Tseng, C. Y. Chang, C. F. Chang, Y. H. Chen, C. C. Chang, D. R. Ji, C. J. Chiu, P. C. Chiang, *Hazard. Mater.*, 2009, **171**, 370.

[102] Y. Lin, H. Chen, K. Lin, B. Chen, C. Chiou, *J. Environ. Sci*., 2011, **23**, 44.

[103] Y. T. Zhou, H. L. Nie, C. Branford-White, Z. Y. He, L. M. Zhu, *J. Colloid Interface Sci.*, 2009, **330**, 29.

[104] H. Yan, L. Yang, Z. Yang, H. Yang, A. Li, R. Cheng, *J. Hazard. Mater.*, 2012, **229– 230**, 371.

[105] Y. Ren, M. Zhang, D. Zhao, *Desalination*, 2008**, 228**, 135.

[106] J. Y. Tseng, C. Y. Chang, Y. H. Chen, C. F. Chang, P. C. Chiang, *Colloids Surf., A*, 2007, **295**, 209.

[107] J. L. Gong, X. Y. Wang, G. M. Zeng, L. Chen, J. H. Deng, X. R. Zhang, Q. Y. Niu, *Chem. Eng. Journal*, 2012, **185– 186**, 100.

[108] G. A. J. Kordosky, *Afr. Inst. Min. Metall.*, 2002, **11**, 445.

[109] C. Cooper, Y. S. Lin, M. Gonzalez, *Ind. Eng. Chem. Res*., 2003, **42**, 1253.

[110] Y. Qian, *Copper Recovery and spent etchant regeneration based on supported liquid membrane technology*, Ph.D. thesis, Department of Chemical and Biomolecular Engineering National University of Signapore, 2007.

[111] J. S. Kim, J. Yi, *J. Chem. Technol. Biotechnol.*, 1999, **74**, 544.

[112] C. A. Cooper, Y. S. Lin, M. Gonzalez, *J. Membr. Sci.*, 2004, **229**, 11.

[113] J. S. Kim, S. Chah, J. Yi, *Korean J. Chem. Eng.*, 2000, **17**, 118.

[114] N. V. Deorkar, L. L. Tavlarides, *Ind. Eng. Chem. Res.*, 1997, **36**, 399.

[115] E.A. Deliyanni, E.N. Peleka, N. K. Lazaridis, *Sep. Purif. Technol.*, 2007, **52**, 478.

[116] S. Tanada, M. Kabayama, N. Kawasaki, T. Sakiyama, T. Nakamura, M. Araki, T. Tamura, *J. Colloid Interface Sci.*, 2003, **257**, 135.

[117] N. Kawasaki, F. Ogata, H. Tominaga, *J. Hazard. Mater.*, 2010, **181**, 574.

[118] R. Chitrakar, S. Tezuka, A. Sonoda, K. Sakane, K. Ooi, T. Hirotsu, *J. Colloid Interface Sci.*, 2006, **297**, 426.

[119] X. Zhu, A. Jyo, *Water Res.*, 2005, **39**, 2301.

[120] A. Sarkar, S. K. Biswas, P. Pramanik, *J. Mater. Chem.*, 2010, **20**, 4417.

[121] N. I. Chubar, V. A. Kanibolotskyy, V. V. Strelko, G. G. Gallios, V. F. Samanidou,T. O. Shaposhnikova, V. G. Milgrandt, I. Z. Zhuravlev, *Colloids Surf., A*, 2005, **255**, 55.

[122] S. M. Onyango, D. Kuchar, M. Kubota, H. Matsuda, *Ind. Eng. Chem. Res.*, 2007, **46**, 894.

[123] D. Chandra, A. Bhaumik, *J. Mater. Chem.*, 2009, **19**, 1901.

[124] L. M. Blaney, S. Cinar, A. K. SenGupta, *Water Res.*, 2007, **41**, 1603.

[125] A. Kugimiya, H. Takei, *Anal. Chim. Acta*, 2006, **564**, 179.

[126] K. Kuzawa, Y. J. Jung, Y. Kiso, T. Yamada, M. Nagai, T. G. Lee, *Chemosphere, 2006*, **62**, 45.

[127] H. He, H. Kang, S. Ma, Y.g Bai, X. Yang, *J. Colloid Interface Sci.*, 2010, **343**, 225.

[128] R. Chitrakar, S. Tezuka, A. Sonoda, K. Sakane, K. Ooi, T. Hirotsu, *J. Colloid Interface Sci.*, 2005, **290**, 45.

[129] X. Cheng, X. Huang, X. Wang, B. Zhao, A. Chen, D. Sun, *J. Hazard. Mater.*, 2009, **169**, 958.

[130] R. Chitrakar, S. Tezuka, J. Hosokawa, Y. Makita, A. Sonoda, K. Ooi, T. Hirotsu, *J. Colloid Interface Sci.*, 2010, **349**, 314.

[131] R. Chitrakar, S. Tezuka, A. Sonoda, K. Sakane, K. Ooi, T. Hirotsu, *J. Colloid Interface Sci.*, 2007, **313**, 53.

[132] N. K. Lazaridis, *Water Air Soil Pollut.*, 2003, **146**, 127.

[133] A. Legouri, M. Badreddine, A. Barroug, A. de Roy, J. P. Besse, *J. Mater. Sci. Lett.*, 1999, **18**, 1077.

[134] Y. Seida, Y. Nakano, *Water Res.*, 2002, **36**, 1306.

[135] P. S. Braterman, Z. P. Xu, F. Yarberry, in *Handbook of Layered Materials*, ed. S. M. Auerbach, K. A. Carrado, P. K. Dutta, Marcel Dekker Ink., New York, 2004, pp. 363-458.

[136] V. Rives, M. A. Ulibarri, *Coord. Chem. Rev.*, 1999, **181**, 61.

[137] X. L. Wu, L. Wang, C. L. Chen, A. W. Xuc, X. K. Wang, *J. Mater. Chem.*, 2011, **21**, 17353.

[138] C. Chen, P. Gunawan, R. Xu, *J. Mater. Chem.*, 2011, **21**, 1218.

[139] L. Li, Y. Feng, Y. Li, W. Zhao, J. Shi, *Angew. Chem. Int. Ed.*, 2009, **48**, 5888.

[140] Y. Xu, H. Zhang, X. Duan, Y. Ding, *Mater. Chem. Phys.*, 2009, **114**, 795.

[141] H. Zhang, R. Qi, D. G. Evans, X. Duan, *J. Solid State Chem.*, 2004, **177**, 772.

[142] A. N. Ay, B. Zümreoglu-Karan, A. Temel, V. Rives, *Inorg. Chem.*, 2009, **48**, 8871.

[143] Q. Chang, L. Zhu, Z. Luo, M. Lei, S. Zhang, H. Tang, *Ultrason. Sonochem.*, 2011, **18**, 553.

[144] A. M. H Shaikh, S. G. Dixit, *Water Res.*, 1992, **26**, 845.

[145] M. Franzreb, W. H. Höll, *IEEE Trans. Appl. Supercond.*, 2000, **10**, 923.

[146] A. Merino-Martos, J. de Vicente, L. Cruz-Pizarro, I. de Vicente, *J. Hazard. Mater.*, 2011, **186**, 2068.

[147] I. de Vicente, A. Merino-Martos, F. Guerrero, V. Amores, J. de Vicente, *J. Hazard. Mat.*, 2011, **192**, 995.

[148] J. Duan, J. Gregory, *Adv. Colloid Interface Sci.*, 2003, **100**, 475.

[149] R. Lehane, *A tidier way to clean up water*, ECOS Magazine, 1982, **31**, 25.

[150] M. Franzreb, *Magnettechnologie in der Verfahrenstechnik wässriger Medien* Forschungszentrum Karlsruhe Wissenschaftliche Berichte FZKA 6916, 2003, pp. 139-149.

[151] N. Karapinar, *Int. J. Miner. Process.*, 2003, **71**, 45.

[152] Y. Li, J. Wang, Y. Zhao, Z. Luan, *Sep. Purif. Technol.*, 2010, **73**, 264.

[153] Y. Terashima, H. Ozaki, M. Sekine, *Water Res.*, 1986, **20**, 537.

[154] J. Y. Hwang, G. Kullerud, M. Takayasu, F. J. Friedlaender, P. C. Wankat, *IEEE Trans. Magn.*, 1982, **18**, 1689.

[155] J. Waynert, C. Prenger, L. Worl, B. Wingo, T. Ying, J. Stewart, D. Peterson, J. Bernard, C. Rey, M. Johnson, *Superconductivity for Electric Systems Program Review*, Los Alamos National Laboratory, 2003.

[156] E. Barrado, F. Prieto, J.Ribas, F.A. Lopez, *Water Air Soil Pollut.*, 1999, **115**, 385.

[157] www.miexresin.com/index.asp?page=7 (Accessed: 22 December 2012).

[158] B. M. Moskowitz, *Guide to Magnetism*, Environmental Magnetism Workshop Institute for Rock Magnetism University of Minesota, 1991, p. 5.

[159] B. Hillebrands, S. Blügel, in *Bergmann / Schaefer, Lehrbuch der Experimentalphysik Band 6 Festkörper*, ed. R. Kassing, de Gruyter, Berlin, 2nd edn., 2005, pp. 402-405.

[160] M. Lambeck, in *Bergmann / Schaefer, Lehrbuch der Experimentalphysik Band 4 Teil 1 Aufbau der Materie,* ed. H. Gobrecht, de Gruyter, Berlin, 2nd edn., 1980, pp. 830-833.

[161] M. Lambeck, in *Bergmann / Schaefer, Lehrbuch der Experimentalphysik Band 4 Teil 1 Aufbau der Materie,* ed. H. Gobrecht, de Gruyter, Berlin, 2nd edn., 1980, p. 834.

[162] B. Hillebrands, S. Blügel, in *Bergmann / Schaefer, Lehrbuch der Experimentalphysik Band 6 Festkörper,* ed. R. Kassing, de Gruyter, Berlin, 2nd edn., 2005, p. 414.

[163] B. Hillebrands, S. Blügel, in *Bergmann / Schaefer, Lehrbuch der Experimentalphysik Band 6 Festkörper,* ed. R. Kassing, de Gruyter, Berlin, 2nd edn., 2005, pp. 407-414.

[164] B. M. Moskowitz, *Guide to Magnetism,* Environmental Magnetism Workshop Institute for Rock Magnetism University of Minesota, 1991, p. 6.

[165] J. M. D. Coey, *Magnetism and Magnetic Materials,* Cambridge University Press, New York, 2010, p. 76.

[166] W. Heisenberg, *Z. Angew. Phys.*, 1928, **49**, 619.

[167] C. Kittel, *Introduction to Solid State Physics,* John Wiley and Sons, New York, 1953, p. 162.

[168] B. Hillebrands, S. Blügel, in *Bergmann / Schaefer, Lehrbuch der Experimentalphysik Band 6 Festkörper,* ed. R. Kassing, de Gruyter, Berlin, 2nd edn., 2005, pp. 417-421.

[169] B. M. Moskowitz, *Guide to Magnetism,* Environmental Magnetism Workshop Institute for Rock Magnetism University of Minesota, 1991, pp. 7-13.

[170] J. M. D. Coey, *Magnetism and Magnetic Materials,* Cambridge University Press, New York, 2010, p. 374.

[171] S. P. Gubin, in *Magnetic Nanoparticles,* ed. S. P. Gubin, Wiley-VCH, Weinheim, 2009, p. 9.

[172] Y. A. Koksharov, in *Magnetic Nanoparticles,* ed. S. P. Gubin, Wiley-VCH, Weinheim, 2009, p. 199.

[173] B. Hillebrands, S. Blügel, in *Bergmann / Schaefer, Lehrbuch der Experimentalphysik Band 6 Festkörper,* ed. R. Kassing, de Gruyter, Berlin, 2nd edn., 2005, pp. 424-428.

[174] M. Lambeck, in *Bergmann / Schaefer, Lehrbuch der Experimentalphysik Band 4 Teil 1 Aufbau der Materie,* ed. H. Gobrecht, de Gruyter, Berlin, 2nd edn., 1980, p. 853.

[175] Y. A. Koksharov, in *Magnetic Nanoparticles,* ed. S. P. Gubin, Wiley-VCH, Weinheim, 2009, p. 203.

[176] R. Skomski, *Simple Models of Magnetism,* Oxford University Press, Oxford, 2008, p. 130.

[177] M. Lambeck, in *Bergmann / Schaefer, Lehrbuch der Experimentalphysik Band 4 Teil 1 Aufbau der Materie,* ed. H. Gobrecht, de Gruyter, Berlin, 2nd edn., 1980, p. 861.

[178] M. Lambeck, in *Bergmann / Schaefer, Lehrbuch der Experimentalphysik Band 4 Teil 1 Aufbau der Materie,* ed. H. Gobrecht, de Gruyter, Berlin, 2nd edn., 1980, pp. 855-856.

[179] R. Skomski, *Simple Models of Magnetism,* Oxford University Press, Oxford, 2008, p. 125.

[180] M. Lambeck, in *Bergmann / Schaefer, Lehrbuch der Experimentalphysik Band 4 Teil 1 Aufbau der Materie,* ed. H. Gobrecht, de Gruyter, Berlin, 2nd edn., 1980, p. 862.

[181] M. Lambeck, in *Bergmann / Schaefer, Lehrbuch der Experimentalphysik Band 4 Teil 1 Aufbau der Materie,* ed. H. Gobrecht, de Gruyter, Berlin, 2nd edn., 1980, p. 854.

[182] B. Hillebrands, S. Blügel, in *Bergmann / Schaefer, Lehrbuch der Experimentalphysik Band 6 Festkörper,* ed. R. Kassing, de Gruyter, Berlin, 2nd edn., 2005, pp. 440-441.

[183] C. Kittel, *Introduction to Solid State Physics,* John Wiley and Sons, New York, 1953, p. 351.

[184] F. Heider, A. Zitzelsberger, K. Fabian,
Pyhs. Earth Planet. Inter., 1996, **93**, 239.

[185] R. Skomski, *Simple Models of Magnetism,* Oxford University Press,
Oxford, 2008, p. 126.

[186] J. M. D. Coey, *Magnetism and Magnetic Materials,*
Cambridge University Press, New York, 2010, p. 300.

[187] M. Lambeck, in *Bergmann / Schaefer, Lehrbuch der*
Experimentalphysik Band 4 Teil 1 Aufbau der Materie,
ed. H. Gobrecht, de Gruyter, Berlin, 2nd edn., 1980, pp. 871-872.

[188] S. Mørup, M. F. Hansen, C. Frandsen,
Beilstein J. of Nanotechnol., 2010, **1**, 182.

[189] D Zhang, in *Dekker Encyclopedia of Nanoscience,* ed. C. I. Contescu,
K. Putyera, Taylor & Francis, Florida, 2nd edn., 2009, p. 1955.

[190] Y. A. Koksharov, in *Magnetic Nanoparticles,* ed. S. P. Gubin,
Wiley-VCH, Weinheim, 2009, p. 211.

[191] Y. A. Koksharov, in *Magnetic Nanoparticles,* ed. S. P. Gubin,
Wiley-VCH, Weinheim, 2009, p. 212.

[192] L.Néel, *Ann. Geophys.*, 1949, **5**, 99.

[193] Y. Park, S. Adenwalla, G.P. Felcher, S.D. Bader,
Phys. Rev. B: Condens. Matter., 1995, **52**, 12779.

[194] B. M. Moskowitz, *Guide to Magnetism,* Environmental Magnetism
Workshop Institute for Rock Magnetism
University of Minesota, 1991, p. 26.

[195] J. M. D. Coey, *Magnetism and Magnetic Materials,*
Cambridge University Press, New York, 2010, p. 295.

[196] P. Ziemann, Lecture notes from Solid State Physics II
Ulm University, 2009.

[197] Y. A. Koksharov, in *Magnetic Nanoparticles,* ed. S. P. Gubin,
Wiley-VCH, Weinheim, 2009, p. 210.

[198] X. Batlle, A. Labarta, *J. Phys. D: Appl. Phys.*, 2002, **35**, R15.

[199] J. J. Lu, H. Y. Deng, H. L. Huang, *J. Magn. Magn. Mater.*, 2000, **29**, 37.

[200] S. P. Gubin, Y. A. Koksharov, G. B. Khomutov, G. Y. Yurkov, *Russ. Chem. Rev.*, 2005, **74**, 489.

[201] O. Petracic, *Superlattices Microstruct.*, 2010, **47**, 569.

[202] Y. Cai, Y. Shen, A. Xie, S. Li, X. Wang, *J. Magn. Magn. Mater.*, 2010, **322**, 2938.

[203] T. Yang, C. Shen, Z. Li, H. Zhang, C. Xiao, S. Chen, Z. Xu, D. Shi, J. Li, H. Gao, *J. Phys. Chem. B*, 2005, **109**, 23233.

[204] B. D. Plouffe, D. K. Nagesha, R. S. DiPietro, S. Sridhar, D. Heiman, S. K. Murthy, L. H. Lewis, *J. Magn. Magn. Mater.*, 2011, **323**, 2310.

[205] C. de Julián, C. Sangregorio, G. Mattei, G. Battaglin, E. Cattaruzza, F. Gonella, S. Lo Russo, F. D'Orazio, F. Lucari, G. De, D. Gatteschi, P. Mazzoldi, *J. Magn. Magn. Mater.*, 2001, **226-230**, 1912.

[206] G. S. Rajan, S. L. Stromeyer, K. A. Mauritz, G. Miao, P. Mani, M. Shamsuzzoh, D. E. Nikles, A. Gupta, *J. Magn. Magn. Mater.*, 2006, **299**, 211.

[207] M. J. Kim, Y. H. Choa, D. H. Kim, K. H. Kim, *IEEE Trans. Magn.*, 2009, **45**, 2446.

[208] D. Kumar, J. Narayan, A.V. Kvit, A.K. Sharma, J. Sankar, *J. Magn. Magn. Mater.*, 2001, **232**, 161.

[209] S. Gangopadhyay, G. C. Hadjipanayis, B. Dale, C. M. Sorensen, K. J. Klabunde, V. Papaefthymiou, A. Kostikas, *Phys. Rev. B: Condens. Matter*, 1992, **45**, 9778.

[210] M. Tadic, V. Kusigerski, D. Markovic, I. Milosevic, V. Spasojevic, *J. Magn. Magn. Mater.*, 2009, **321**, 12.

[211] E. Pollert, K. Knížek, M. Maryško, K. Závěta, A. Lančok, J. Boháček, D. Horák, M. Babič, *J. Magn. Magn. Mater.*, 2006, **306**, 241.

[212] X. X. Zhang, G. H. Wen, G. Xiao, S. Sun, *J. Magn. Magn. Mater.*, 2003, **261**, 21.

[213] M. Mikhaylova, D. K. Kim, N. Bobrysheva, M. Osmolowsky, V. Semenov, T. Tsakalakos, M. Muhammed, *Langmuir*, 2004, **20**, 2472.

[214] A. Poddar, R.N. Bhowmik, A. De, P. Sen, *J. Magn. Magn. Mater.*, 2009, **321**, 2015.

[215] M. González, I. Martín-Fabiani, J. Baselga, J. Pozuelo, *Mater. Chem. Phys.*, 2012, **132**, 618.

[216] S. Mørup, E. Tronc, *Phys. Rev. Lett.*, 1993, **72**, 3278.

[217] S. Mørup, *Europhys. Lett.*, 1994, **28**, 671.

[218] P. Granitzer, K. Rumpf, A.G. Roca, M.P. Morales, P. Poelt, M. Albu, *J. Magn. Magn. Mater.*, 2010, **322**, 1343.

[219] J. L. Dormann, D. Fiorani, E.Tronc, *Adv. Chem. Phys.*, 1997, **XCVIII**, 283.

[220] R. L. Johntson, *Atomic and Molecular Clusters,* Taylor & Francis, London and New York, 2002, p. 6.

[221] Y. A. Koksharov, in *Magnetic Nanoparticles,* ed. S. P. Gubin, Wiley-VCH, Weinheim, 2009, p. 219.

[222] Y. A. Koksharov, in *Magnetic Nanoparticles,* ed. S. P. Gubin, Wiley-VCH, Weinheim, 2009, p. 230.

[223] Y. A. Koksharov, in *Magnetic Nanoparticles,* ed. S. P. Gubin, Wiley-VCH, Weinheim, 2009, pp. 215-218.

[224] D. L. Huber, in *Dekker Encyclopedia of Nanoscience,* ed. C. I. Contescu, K. Putyera, Taylor & Francis, Florida, 2nd edn., 2009, p. 1683.

[225] R. M. Cornell, U. Schwertmann, *The Iron Oxides,* Wiley-VCH, Weinheim, 2nd edn., 2003, p. 32.

[226] J. M. D. Coey, *Magnetism and Magnetic Materials,* Cambridge University Press, New York, 2010 p. 422.

[227] R. M. Cornell, U. Schwertmann, *The Iron Oxides,* Wiley-VCH, Weinheim, 2nd edn., 2003, p. 129.

[228] H. U. Worm, *Geophys. J. Int.*, 1998, **133**, 201.

[229] T. Atsumi, B. Jeyadevan, Y. Sato, K. Tohji, *J. Magn. Magn. Mater.*, 2007, **310**, 2841.

[230] M. Zborowski, in *Magnetic Cell Separation,* ed. M. Zborowski, J. J. Chalmers, Elsevier, Oxford, 2008, pp. 427-440.

[231] E. P. Furlani, Y. Sahoo, K. C. Ng, J. C. Wortman, T. E. Monk, *arXiv*:0612.092 [physics].

[232] M. Zborowski, in *Magnetic Cell Separation,* ed. M. Zborowski, J. J. Chalmers, Elsevier, Oxford, 2008, p. 71.

[233] M. Franzreb, *Magnettechnologie in der Verfahrenstechnik wässriger Medien* Forschungszentrum Karlsruhe Wissenschaftliche Berichte FZKA 6916, 2003, p. 2.

[234] M. Zborowski, in *Magnetic Cell Separation,* ed. M. Zborowski, J. J. Chalmers, Elsevier, Oxford, 2008, p. 106.

[235] C. T. Yavuz, J. T. Mayo, W. W. Yu, A. Prakash, J. C. Falkner, S. Yean, L. Cong, H. J. Shipley, A. Kan, M. Tomson, D. Natelson, V. L. Colvin, *Science*, 2006, **314**, 964.

[236] L. Marshall, C. F. Zukoski, J. W. Goodwin, *J. Chem. Soc. Faraday Trans. 1 F*, 1989, **85**, 2785.

[237] M. Ocalan, G. H. McKinley, *J. Intell. Mater. Syst. Struct.*, 2012, **23**, 969.

[238] V. Sharma, K. Park, M. Srinivasarao, *Mater. Sci. Eng.*, 2009, **R 65**, 1.

[239] M. Franzreb, *Magnettechnologie in der Verfahrenstechnik wässriger Medien*, Forschungszentrum Karlsruhe Wissenschaftliche Berichte FZKA 6916, 2003, p. 28.

[240] M. Zborowski, in *Magnetic Cell Separation,* ed. M. Zborowski, J. J. Chalmers, Elsevier, Oxford, 2008, p. 50.

[241] M. Zborowski, in *Magnetic Cell Separation*, ed. M. Zborowski, J. J. Chalmers, Elsevier, Oxford, 2008, p. 93.

[242] G. D. Moeser, K. A. Roach, W. H. Green, T. A. Hatton, P. E. Laibinis *AlChE Journal*, 2004, **50**, 2835.

[243] M. Zborowski, in *Magnetic Cell Separation*, ed. M. Zborowski, J. J. Chalmers, Elsevier, Oxford, 2008, p. 82.

[244] M. Zborowski, in *Magnetic Cell Separation*, ed. M. Zborowski, J. J. Chalmers, Elsevier, Oxford, 2008, p. 83.

[245] M. Franzreb, *Magnettechnologie in der Verfahrenstechnik wässriger Medien*, Forschungszentrum Karlsruhe Wissenschaftliche Berichte FZKA 6916, 2003, p. 13.

[246] M. Franzreb, *Magnettechnologie in der Verfahrenstechnik wässriger Medien*, Forschungszentrum Karlsruhe Wissenschaftliche Berichte FZKA 6916, 2003, p. 35.

[247] J. H. P Watson, *High gradientmagnetic separation*, Butterworth, London, 1989, pp. 661–670.

[248] M. Zborowski, in *Magnetic Cell Separation*, ed. M. Zborowski, J. J. Chalmers, Elsevier, Oxford, 2008, p. 86-88.

[249] M. Zborowski, in *Magnetic Cell Separation*, ed. M. Zborowski, J. J. Chalmers, Elsevier, Oxford, 2008, p. 91.

[250] M. Franzreb, *Magnettechnologie in der Verfahrenstechnik wässriger Medien*, Forschungszentrum Karlsruhe Wissenschaftliche Berichte FZKA 6916, 2003, p. 121.

[251] M. Franzreb, *Magnettechnologie in der Verfahrenstechnik wässriger Medien*, Forschungszentrum Karlsruhe Wissenschaftliche Berichte FZKA 6916, 2003, p. 120.

[252] J. N. Lalena, D. A. Cleary, E. E. Carpenter, N. F. Dean, *Inorganic Materials Synthesis and Fabrication*, Jon Wiley and Sons, New Jersey, 2008.

[253] J. Blackman, *Metallic Nanoparticles*, Elsevier, Amsterdam, 2009.

[254] C.N.R. Rao (ed.), A. Müller (ed.), AK. Cheetham (ed.), *Nanomaterials Chemistry*, Whiley-VCH, Weinheim, 2007.

[255] G.P. Demopoulos, *Hydrometallurgy*, 2009, **96**, 199.

[256] C. Burda, X. Chen, R. Narayanan, M. A. El-Sayed, *Chem. Rev*., 2005, **105**, 1027.

[257] G. Nichols, S. Byard, M. J. Bloxham, J. Botterill, D. J. Dawson, A. Dennis, V. Diart, N. C. North, J. D. Sherwood, *J. Pharm. Sci.*, 2002, **91**, 2103.

[258] P. Atkins, J. de Paula, *Physical Chemistry*, Oxford University Press, Oxford, 9th edn., 2010, p. 673.

[259] W.B. Russel, D.A. Saville, W.R. Schowalter, *Colloidal Dispersions*, Cambridge University Press, New York, 1989.

[260] S. Gyergyek, D. Makovec, M. Drofenik, *J. Colloid Interface Sci.*, 2001, **354**, 498.

[261] B. K. Coltrain, L. W. Kelts, in *Colloidal Silica Fundamentals and Applications*, ed. H. E. Bergna, W. O. Roberts, Taylor and Francis, Florida, 2006, p. 637.

[262] W. O. Roberts, in *Colloidal Silica Fundamentals and Applications*, ed. H. E. Bergna, W. O. Roberts, Taylor and Francis, Florida, 2006, p. 133.

[263] J. E. Otterstedt, D. A. Brandreth, *Small Particles Technology*, Plenum Press New York, 1998, p. 50.

[264] J. E. Ottersted, P. Greenwood, in *Colloidal Silica Fundamentals and Applications*, ed. H. E. Bergna, W. O. Roberts, Taylor and Francis, Florida, 2006, p. 748.

[265] V. Inglezakis, S. Poulopoulos, *Adsorption, Ion Exchange and Catalysis: Design of Operations and Environmental Applications*, Elsevier Science, Amsterdam, 2006, p. 31.

[266] V. Inglezakis, S. Poulopoulos, *Adsorption, Ion Exchange and Catalysis: Design of Operations and Environmental Applications*, Elsevier Science, Amsterdam, 2006, p. 32.

[267] C. C. E. Housecroft, A. G. Sharpe, *Inorganic Chemistry*, Pearson Education Limited, Essex, 3rd edn., 2008, p. 198.

[268] R. G. Pearson, *J. Am. Chem. Soc.*, 1963, **85**, 3533.

[269] G. N. Lewis, *Valence and the structure of atoms and molecules*, The Chemical Catalog Company, inc., 1923.

[270] W. B. Jensen, *Chem. Rev.*, 1978, **78**, 1.

[271] C. E. Housecroft, A. G. Sharpe, *Inorganic Chemistry*, Pearson Education Limited, Essex, 3rd edn., 2008, p. 207.

[272] C. E. Housecroft, A. G. Sharpe, *Inorganic Chemistry*, Pearson Education Limited, Essex, 3rd edn., 2008, p. 205.

[273] C. E. Housecroft, A. G. Sharpe, *Inorganic Chemistry*, Pearson Education Limited, Essex, 3rd edn., 2008, p. 203.

[274] V. Inglezakis, S. Poulopoulos, *Adsorption, Ion Exchange and Catalysis: Design of Operations and Environmental Applications*, Elsevier Science, Amsterdam, 2006, p. 288.

[275] P. Atkins, J. de Paula, *Physical Chemistry*, Oxford University Press, Oxford, 9th edn., 2010, pp. 889-894.

[276] Z. Kechrid, F. Dahdouh, R. M. Djabar, N. Bouzerna, *J. Environ. Health. Sci. Eng.*, 2006, **3**, 65.

[277] Y. D. Liu, F. F. Fang, H. J. Choi, *Colloid. Poylm. Sci.*, 2011, **289**, 1295.

[278] R. Shen, S. N. Shafrir, C. Miao, M. Wang, J. C. Lambropoulos, S. D. Jacobs, H. Yang, *J. Colloid Interface Sci.*, 2010, **342**, 49.

[279] R. Massart, *IEEE Trans. Magn.*, 1981, **17**, 1247.

[280] C. E. Housecroft, A. G. Sharpe, *Inorganic Chemistry*, Pearson Education Limited, Essex, 3rd edn., 2008, p. 721.

[281] A. Patterson, *Phys. Rev.*, 1939, **56**, 978.

[282] K. Mandel , F. Dillon , A. A. Koos , Z. Aslam , F. Cullen , H. Bishop , A. Crossley, N. Grobert, *RSC Adv.*, 2012, **2**, 3748.

[283] K. Mandel , F. Dillon , A. A. Koos , Z. Aslam , K. Jurkschat , F. Cullen, A. Crossley , H. Bishop , K. Moh , C. Cavelius , E. Arzt, N. Grobert, *Chem. Commun.*, 2011, **47**, 4108.

[284] K. Mandel, *Wet Chemical Synthesis of Transaition Metal Nanoparticles for Carbon Nanotube Growth*, M.Sc. Thesis, University of Oxford, Ulm University, 2010.

[285] M. Liu, K. Stierstadt, in *Colloidal Magnetic Fluids*, ed. S. Odenbach, Springer-Verlag, Berlin Heidelberg, 2009, p. 114.

[286] International Centre for Diffraction Data, PDF4+ Database.

[287] E. Sobczak, Y. Swilem, N. N. Dorozhkin, R. Nietubyć, P. Dłużewski, A. Ślawska-Waniewska, *J. Alloy Compd.*, 2001, **328**, 57.

[288] B. A. Wechsler, D. H. Lindsley, C. T. Prewitt, *Am. Min.*, 1984, **69**, 754.

[289] R. M. Cornell, U. Schwertmann, *The Iron Oxides*, Wiley-VCH, Weinheim, 2nd edn., 2003, p. 12.

[290] K. Mandel, W. Szczerba, A. F. Thünemann, H. Riesemeier, M. Girod, G. Sextl, *J. Nanopart. Res.*, 2012, **14**, 1066, supporting information.

[291] O. Glatter, O. Kratky, *Small-Angle X-ray Scattering*, Academic Press, London, 1982.

[292] G. Beaucage, *J. Appl. Cryst.*, 1995, **28**, 717.

[293] J. Als-Nielsen, D. McMorrow, *Elements of Modern X-ray Physics*, John Wiley & Sons, Ltd., West Sussex, 2nd edn., 2011, p. 139.

[294] J. Oberdisse, A. El Harrak, G. Carrot, J. Jestin, F. Boué, *Polymer*, 2005, **46**, 6695.

[295] M. P. Morales S. V. Verdaguer, M. I. Montero, C. J. Serna, *Chem. Mater.*, 1999, **11**, 3058.

[296] Y. de Hazan, D. Werner, M. Z'graggen, M. Groteklaes, T. Graule, *J. Colloid Interface Sci.*, 2008, **328**, 103.

[297] Y. de Hazan, T. Reuter, D. Werner, R. Clasen, T. Graule, *J. Colloid Interface Sci.*, 2008, **323**, 293.

[298] M. Hesse, H. Meier, B. Zeeh, *Spektroskopische Methoden in der organischen Chemie*, Thieme Verlag, Stuttgart, 1979, pp. 55-94.

[299] M. Ma, Y. Zhang, W. Yu, H. Y. Shen, H. Q.Zhang, N. Gu, *Colloids Surf., A*, 2003, **212**, 219.

[300] T. Ohya, M. Ito, K. Yamada, T. Ban, Y. Ohya, Y. Takahashi, *J. Sol-Gel Sci. Technol.*, 2004, **30**, 71.

[301] M. Liu, K. Stierstadt, in *Colloidal Magnetic Fluids*, ed. S. Odenbach, Springer-Verlag, Berlin Heidelberg, 2009, p. 115.

[302] A. P. Philipse, M. P. B. van Bruggen, C. Pathmamanoharan, *Langmuir*, 1994, **10**, 92.

[303] C. Chanéac, E. Tronc, J. P. Jolivet, *Mater. Chem.*, 1996, **6**, 1905.

[304] C. Yang, G. Wang, Z. Lu, J. Sun, J. Zhuang, W. Yang, *J. Mater. Chem.*, 2005, **15**, 4252.

[305] D. Y. Ju, P. Bian, G. L. Qing, D. Lu, H. He, *Key Eng. Mater.*, 2008, **368**, 1366.

[306] X. Liu, Z. Ma, J. Xing, H. Liu, *J. Magn. Magn. Mater.*, 2004, **270**, 1.

[307] M. Ettlinger, in *Ullmann`s encyclopedia, Industrial inorganic chemicals and products Vol 5*, Wiley-VCH, Weinheim, 1998, p. 4113-4114.

[308] P. Nauroth, R. Kuhlmann, G. Turk, A. Becker, US Pat., 4857289 A, 1989.

[309] A. P. Legrand, H. Hommel, J. B. d'Espinose de la Caillerie, in *Colloidal Silica Fundamentals and Applications*, ed. H. E. Bergna, W. O. Roberts, Taylor and Francis, Florida, 2006, pp. 855-856.

[310] H. E. Bergna, in *Colloidal Silica Fundamentals and Applications*, ed. H. E. Bergna, W. O. Roberts, Taylor and Francis, Florida, 2006, p. 24.

[311] A. Minihan, in *Ullmann`s encyclopedia, Industrial inorganic chemicals and products Vol 5*, Wiley-VCH, Weinheim, 1998, p. 4223.

[312] J. G. Vail, *Soluble Silicates in Industry*, American Chemical Society Monograph Series, The Chemical Catalog Company Inc., New York, 1928, p. 85.

[313] R.K. Iler, *The chemistry of silica*, John Wiley and Sons, New York, 1997, p. 367.

[314] D. J. Shaw, *Introducation to Colloid & Surface Chemistry*, Butterworth-Heinemann, Oxford, 1992, pp. 180-181.

[315] S. Dembski, S. Rupp, C. Gellermann, M. Batentschuk, A. Osvet, A. Winnacker, *J. Colloid Interface Sci.*, 2011, **358**, 32.

[316] P. V. Brady, J. V. Walther, *Geochim. Cosmochim. Acta*, 1989, **53**, 2823.

[317] A. Walcarius, C. Delacôte, *Anal. Chim. Acta*, 2005, **547**, 3.

[318] M. Z. C. Hu, R. D. Hunt, E. A. Payzant, C. R. Hubbard, *J. Am. Ceram. Soc.*, 1999, **82**, 2313.

[319] J. Breu, W. Seidl, A. Stoll, *Z. Anorg. Allg. Chem.*, 2003, **629**, 503.

[320] S. K. Yun, T. J. Pinnavaia, *Chem. Mater.*, 1995, **7**, 348.

[321] S. Miyata, *Clays Clay Miner.*, 1980, **28**, 50.

[322] A. V. Radha, P. V. Kamath, *Bull. Mater. Sci.*, 2003, **26**, 661.

[323] Z. P. Xu, G. S. Stevenson, C. Q. Lu, G. Q. (Max) Lu, P. F. Bartlett, P. P. Gray, *J. Am. Chem. Soc.*, 2006, **128**, 36.

[324] Y. S. Ho, G. McKay, *Water Res.*, 2000, **34**, 735.

[325] L. Ruixia, G. Jinlong, T. Hongxiao, *J. Colloid Interface Sci.*, 2002, **248**, 268.

[326] M. Franzreb, C. Reichert, US Pat., 7506765 B2, 2009.

[327] C. R. Brundle, C. A. Evans, Jr., S. Wilson, *Encyclopedia of Materials Characterization*, Butterworth-Heineman, Massachusetts, 1992, pp. 70-84.

[328] C. R. Brundle, C. A. Evans, Jr., S. Wilson, *Encyclopedia of Materials Characterization*, Butterworth-Heineman, Massachusetts, 1992, pp. 120-134.

[329] B. Freitag, M. Bischoff, H. Mueller, P. Hartel, H.S. von Harrach, *Sub-nanometer resolution in field-free imaging using a Titan80-300 with Lorentz lens and image Cs-corrector at 300kV acceleration voltage*, FEI.com, 2009.

[330] C. R. Brundle, C. A. Evans, Jr., S. Wilson, *Encyclopedia of Materials Characterization*, Butterworth-Heineman, Massachusetts, 1992, pp. 107-109.

[331] C. R. Brundle, C. A. Evans, Jr., S. Wilson, *Encyclopedia of Materials Characterization*, Butterworth-Heineman, Massachusetts, 1992, pp. 214-215.

[332] J. Als-Nielsen, D. McMorrow, *Elements of Modern X-ray Physics*, John Wiley & Sons, Ltd., West Sussex, 2nd edn., 2011, p. 251.

[333] M. Newville, *Fundamentals of XAFS*, University of Chicago, 2004.

[334] J. Als-Nielsen, D. McMorrow, *Elements of Modern X-ray Physics*, John Wiley & Sons, Ltd., West Sussex, 2nd edn., 2011, p. 252.

[335] S. D. Kelly, D. Hesterberg, B. Ravel, *Methods of Soil Anlysis Part 5 Mineralogical Methods*, Soil Science Society of America, Wisconsin, 2008, pp. 387-463.

[336] J. Als-Nielsen, D. McMorrow, *Elements of Modern X-ray Physics*, John Wiley & Sons, Ltd., West Sussex, 2nd edn., 2011, pp. 255-257.

[337] M. Newville, *J. Synchrotron Radiat.*, 2001, **8**, 322.

[338] H. Riesemeier, K. Ecker, B. R. Müller, W. Görner, M. Radtke, M. Krumrey, *X-Ray Spectrom.*, 2005, **34**, 160.

[339] B. Ravel B, M. Newville, *J. Synchrotron Rad.*, 2005, **12**, 537.

[340] J. J. Rehr, R. C. Albers, *Rev. Mod. Phys.*, 2000, **72**, 621.

[341] J. Als-Nielsen, D. McMorrow, *Elements of Modern X-ray Physics*, John Wiley & Sons, Ltd., West Sussex, 2nd edn., 2011, pp. 134-137.

[342] J. Als-Nielsen, D. McMorrow, *Elements of Modern X-ray Physics*, John Wiley & Sons, Ltd., West Sussex, 2nd edn., 2011, pp. 137-139.

[343] C. R. Brundle, C. A. Evans, Jr., S. Wilson, *Encyclopedia of Materials Characterization*, Butterworth-Heineman, Massachusetts, 1992, pp. 198-213.

[344] S. Foner, *Rev. Sci. Instrum.*, 1959, **30**, 548.

[345] M. Urbaniak, *Lecture 3 Magnetic hysteresis and basic magnetometry*, Institute of Molecular Physics Polish Academy of Sciences, 2012.

[346] A. Zieba, S. Foner, *Rev. Sci. Instrum.*, 1982, **53**, 1344.

[347] D. Campbell, J. R. White, *Polymer Characterization*, Chapman and Hall, New York, 1989, pp. 301-326.

[348] C. R. Brundle, C. A. Evans, Jr., S. Wilson, *Encyclopedia of Materials Characterization*, Butterworth-Heineman, Massachusetts, 1992, pp. 633-644.

[349] C. R. Brundle, C. A. Evans, Jr., S. Wilson, *Encyclopedia of Materials Characterization*, Butterworth-Heineman, Massachusetts, 1992, p. 739.

[350] German standard DIN 66131: 1993-07, *Bestimmung der spezifischen Oberfläche von Feststoffen durch Gasadsorption nach Brunauer, Emmett und Teller (BET).*

[351] C. E. Housecroft, A. G. Sharpe, *Inorganic Chemistry*, Pearson Education Limited, Essex, 3rd edn., 2008, p. 101.

[352] C. R. Brundle, C. A. Evans, Jr., S. Wilson, *Encyclopedia of Materials Characterization*, Butterworth-Heineman, Massachusetts, 1992, pp. 416-427.

[353] J. C. Edwards, *Principles of NMR*, Process NMR Associates LLC, Danbury Connecticut, 2006.

[354] C. R. Brundle, C. A. Evans, Jr., S. Wilson, *Encyclopedia of Materials Characterization*, Butterworth-Heineman, Massachusetts, 1992, pp. 460-467.

[355] H. Hart, L. E. Craine, D. J. Hart, *Organische Chemie*, Wiley-VCH, Weinheim, 10th edn., 2002, pp. 431-435.

[356] K. J. D. MacKenzie, *Br. Ceram. Trans.*, 2000, **99**, 231.

[357] C. R. Brundle, C. A. Evans, Jr., S. Wilson, *Encyclopedia of Materials Characterization*, Butterworth-Heineman, Massachusetts, 1992, p. 468.

[358] K. Mandel, *Wet Chemical Synthesis of Transaition Metal Nanoparticles for Carbon Nanotube Growth*, M.Sc. Thesis, University of Oxford, Ulm University, 2010, Appendix III.

[359] J. Hoffmann, *Taschenbuch der Messtechnik*, Fachbuchverlag Leipzig im Carl Haner Verlag, Leipzig, 4th edn., 2004, pp. 312-314.

[360] H. J. Eichler, in *Bergmann / Schaefer, Lehrbuch der Experimentalphysik Band 3 Optik*, ed. H. Niedrig, de Gruyter, Berlin, 9th edn., 1993, p. 367.

[361] W. Stumm, *Chemistry of the Solid-Water Interface,* John Wiley & Sons, Inc., New York, 1992, pp. 50-56.

[362] German standard DIN EN ISO 6678:2004, *Bestimmung von Phosphor – Photometrisches Verfahren mittels Ammoniummolybdat.*

[363] D. Campbell, J. R. White, *Polymer Characterization*, Chapman and Hall, New York, 1989, pp. 26-35.

9. APPENDIX

CALCULATIONS ON MAGNETIC PARTICLE SEPARATION BEHAVIOUR IN FLUIDS

Separation of magnetic particles from fluids in a magnetic field gradient is a highly complex process. Design of magnetic separators based on fluid and magnetodynamics is far beyond the scope of this work.

However with some simplifying assumptions, forces acting on magnetic particles dispersed in a fluid and exposed to a magnetic field gradient can be described. It is possible to compare the order of magnitude of these forces and estimate separation velocities. Besides the *magnetic, gravitational* and *Brownian force,* the *force of viscous drag* has to be taken into account. Three different particle types, relevant in this work, were chosen for calculations:

System 1: Iron particles (saturation magnetisation: 217 emu/g, density: 7.9 g/cm^3, particle diameter: 2 µm) were considered as alternatives to superparamagnetic nanocomposite particles due to their high saturation magnetisation and soft magnetic properties.

System 2: Magnetite nanoparticles (saturation magnetisation: 60 emu/g, density: 5 g/cm^3, particle diameter: 10 nm) correspond to the nanoparticles synthesised in this work.

System 3: Magnetite nanoparticles in a silica matrix, sphere like nanocomposites with a 45 wt% content of magnetite (saturation magnetisation: 30 emu/g (average value for composite particles), density: 3.5 g/cm^3 (estimated value from particles composition and porosity)). As the size distribution of nanocomposites synthesised in this work is rather broad, three diameters are considered: 1 µm, 20 µm and 50 µm.

For all calculations, spherical particles in the state of magnetic saturation were assumed. Particle-particle interactions were neglected, i.e., calculations only considered forces on individual particles. This simplification leads to miscalculations (presumably too small values for separation velocities), as microscopically it can be observed that particles form chains during separation (interparticle interaction). Magnitudes of magnetic gradients ($gradB = \mu_0 \cdot gradH$) were chosen for a handheld magnet (23 T/m, low gradient) and for a strong magnetic field (10 000 T/m, high gradient). These values were considered as constant, which is again a simplification as the gradients usually change with distance (e.g. exponentially for a handheld magnet).

Figure A1 shows the order of magnitude of the calculated forces for the different particle systems on a logarithmic scale plot. Calculations were done using *equations (17-21)* (*chapter 3.2)*. Calculations for the magnetic forces hold for a magnetic field considered in only one dimension (compare *equation (17), chapter 3.2.1*).

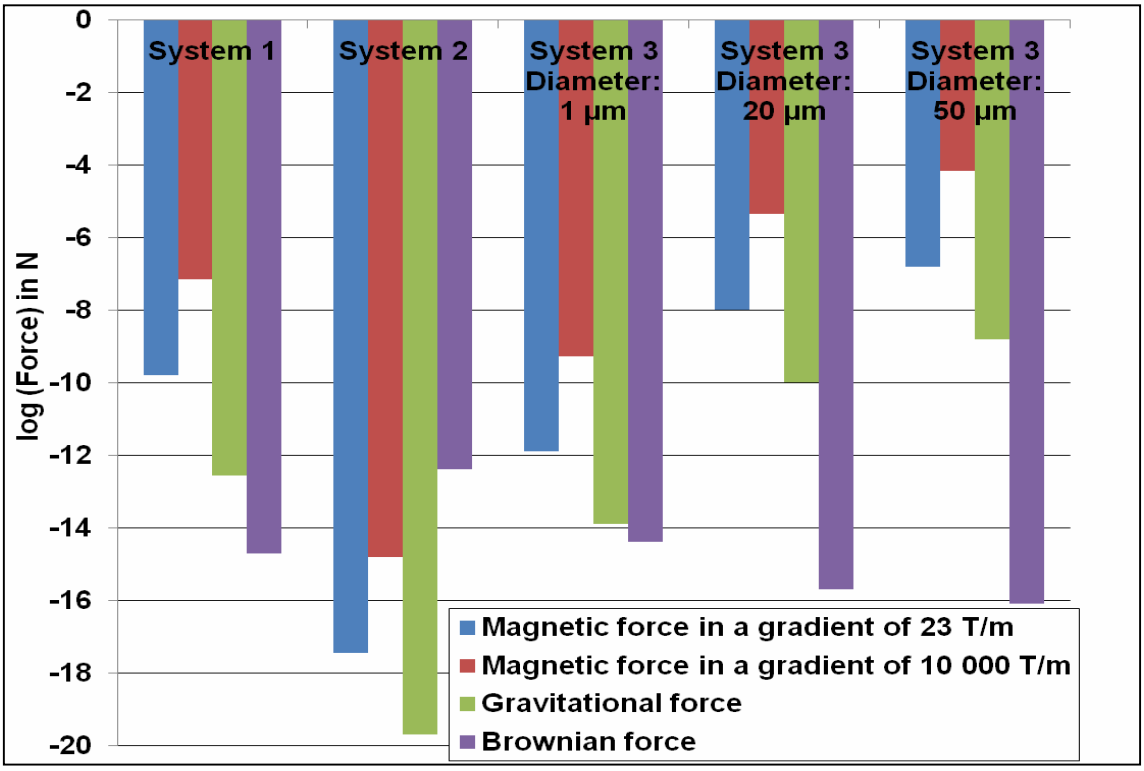

Figure A1: Magnetic, gravitational and Brownian forces, calculated for micron sized iron particles (*System 1*), magnetite nanoparticles (*System 2*) and nanocomposite particles of different sizes (*System 3*).

Brownian (randomly directed) forces are dominant for individual nanoparticles (*System 2*) and exceed all other forces. This explains why in a ferrofluid nanoparticles neither sediment nor can be magnetically separated from the fluid with a handheld magnet. Even high gradient magnetic separation seems to be difficult. For all micron sized particle systems the Brownian force is several orders of magnitude lower than the magnetic force and can be neglected. Gravitational force increases for larger particles. The magnetic force increases with particle size and magnetic gradient. The magnetic and the gravitational force for *System 3* spread over five orders of magnitude for particles sized 1 µm in comparison to 50 µm sized particles.

Magnetic separation velocities can be estimated for all micron sized particle systems (*Systems 1* and *3*) by using simplified equations. The dominance of the Brownian force in *System 2*, even in high magnetic field gradients, needs a more sophisticated mathematical treatment. *System 2* is therefore not further considered.

Gravitational or magnetic force lead to solid-liquid separation of micron sized particles (*Systems 1* and *3*). Separation velocities are determined by the counteracting fluid drag forces. The direction of particle motion is defined by the directions of the gravitational and the magnetic force. These two forces might be oriented to each other depending on the actual separator configuration. In the following, a perpendicular force arrangement will be considered. In this case, the gravitational force neither increases nor reduces the magnetic gradient force. The gravitational force is neglected, thereby.

In reality, a particle that is attracted by a magnet, horizontally, will also be exposed to a downward-pointing gravitational force, resulting in a more complex trajectory.

Using the simplified assumptions, calculated separation velocities in a one dimensional direction (using *equation (20)*, see *chapter 3.2.2*) for particles of *System 1* in water are 0.002 m/s (low gradient) and 0.92 m/s (high gradient). For particles of *System 3* separation velocities can be as low as $3.2 \cdot 10^{-5}$ m/s (1 µm; low gradient) respectively 0.014 m/s (1 µm; high gradient) and as high as 0.08 m/s (50 µm; low gradient) respectively 34.8 m/s (50 µm; high gradient). Thus, a broad “separation front” has to be expected in a real separation application.

DECLARATION

I declare that the present thesis was written by myself independently using only allowed resources. Furthermore, all sentences in the text, whose words or idea is adopted from other work, are denoted as citation with declaration of the original reference.

ERKLÄRUNG

Hiermit erkläre ich, dass ich die vorliegende Arbeit selbständig und nur mit erlaubten Hilfsmitteln angefertigt habe und dass alle Stellen, die im Wortlaut oder dem Sinne nach anderen Werken entnommen sind, durch Angabe der Quellen als Entlehnung kenntlich gemacht worden sind.

Karl Mandel, Würzburg im Juni 2013